UNIVERSITY OF CALIFORNIA
SANTA CRUZ

ILLUMINATING THE GAS CYCLING IN AND OUT OF GALAXIES

A dissertation submitted in partial satisfaction of the
requirements for the degree of

Doctor of Philosophy

in

ASTRONOMY AND ASTROPHYSICS

by

Camille N. S. Leibler

March 2022

The Dissertation of Camille N. S. Leibler is approved:

Enrico Ramirez-Ruiz, Chair

Constance Rockosi

Evan Kirby

Peter Biehl
Vice Provost and Dean of Graduate Studies

Table of Contents

List of Figures

List of Tables

Abstract

Illuminating the gas cycling in and out of galaxies

by

Camille N. S. Leibler

In this dissertation, we combine two different approaches — chemical evolution modeling and direct observations of the gas distributed around a galaxy — to study the gas cycling into and out of galaxies. The interplay of fundamental astrophysical processes that drive this baryon cycle, such as star formation and evolution, gas accretion from the cosmic web, and galactic winds, shapes the evolution of galaxies. These processes also determine the galactic gas enrichment history which is preserved in the stellar abundances of low mass stars that are still alive today. Therefore, stellar chemical abundance patterns can be used to indirectly illuminate the evolution of gas in and around galaxies.

For the first part of this thesis, we build a flexible one-zone chemical evolution model to decode the star-by-star abundance patterns of nearby galaxies or the average abundance ratios derived from the integrated-light of distant galaxies. We characterize how and why these processes affect the observed stellar abundances and validate our code by modeling the stellar abundances of the Milky Way's geometrically-selected thick disk. We then utilize our chemical evolution model to help elucidate how the stellar populations of elliptical galaxies can simultaneously exhibit greater α-enhancement and higher metallicities with increasing galaxy mass. Recent papers suggest that more massive ellipticals require more top-heavy IMFs. In contrast, we find that while a

galaxy-mass dependent IMF is not precluded, the abundance patterns of these galaxies can also be explained if more massive ellipticals form their stars on shorter timescale and have outflows that are less enriched and/or are less efficiently driven by supernovae.

In the second part of this thesis, we present direct observations of emission from a very bright enormous Lyman-α nebula (the Slug) that is illuminated by a nearby quasar at $z \sim 2.3$. This is a rare opportunity to examine the physical properties of gas surrounding a galaxy that even extends beyond the halo into the intergalactic medium. We successfully detect Hα emission from the Slug, indicating that the observed Lyα is produced in situ by hydrogen recombination and traces highly-ionized, optically-thick, dense clumps of cool gas.

For my family, the ones I was born with and the ones I've been lucky enough to find along the way. Je vous adore.

Acknowledgments

I would never have made it through this PhD if not for the incredible people that have supported me, cheered me on, picked me up when I repeatedly stumbled, advocated for me, and helped keep me (mostly) sane. I have learned so much from you all and while this has not been an easy journey, I am unbelievably lucky to have had you all by my side.

First, I am so grateful to my thesis committee members, Enrico Ramirez-Ruiz, Connie Rockosi, and Evan Kirby. Enrico, you have been the fil conducteur of my graduate school journey. Thank you for being there through all the twists and turns, for seeing my potential and not giving up on me, for picking up the pieces and guiding me to the finish line. Evan, thank you for your expertise and thoughtful feedback and most especially your patience and flexibility as everything came together over the winter holidays. Connie, I'm really happy that I got to work so closely with you over the past six months. Your feedback and encouragement got me through the worst of the dissertation writing process. Thank you for somehow always finding the time to meet with me; your advising was invaluable and it was such a joy to get to talk about chemical evolution with you.

I would also like to profusely thank those that have at various times been kind enough to step into the role of unofficial science advisor and/or mentor, particularly Bradford P. Holden, Ryan Cooke, and Sebastiano Cantalupo.

I would be remiss if I did not acknowledge a few other people who were integral supports in my path through graduate school. Lindsay, I cannot thank you enough

for your encouragement, for checking in on me weekly over the past two years, for doing endless pomodoros with me and helping me navigate the nightmare that is UCSC bureaucracy. You are a treasure. I am also so happy to have had Jenn in my life this past year to help add some structure to the blur that is the pandemic graduate student life. Thank you for coworking with me, for strategizing with me, for helping me identify what worked and did not work for me, and for tirelessly cheering me on! Thank you also to Paula who guided me through the ups and downs of my twenties and helped me see my worth while sanding off some of my rough edges.

I am also very fortunate to have truly stellar friends that I will never be able to thank enough:

To my brain twin Brad who shares my voracious curiosity and with whom I've had the best meandering conversations about anything and everything. You've taught me most of what I know about astronomy and helped me transition from student to scientist. Thank you for being one of my best friends and for taking on the role of mentor and advisor when I did not have one. I look forward to having epically long conversations again that have nothing to do with graduate school.

To my best friend Marianna who showed me how expansive friendship can be. Thank you for being the sort of person who offers to fly across the country when your friend gets her heart broken, who hears someone say that that are thinking about getting their ears pierced and says "Ok, let's do that right now!", who knows that if a friend calls twice in a row, it's important and will pick up even if she doesn't really have bandwidth at that moment. Thank you for your creativity, for your passion for doing

what is right even when it isn't easy, for your deep love of science even when other parts of the job aren't great; you are a never-ending source of inspiration. Oh and there is absolutely no way I could have made it through grad school or finished this dissertation without you. So thank you for that as well.

To Elizabeth who I actually met two years prior to grad school when the summer REU students kindly adopted me. I feel so privileged to have had you as my first-year roommate and as my first friend in grad school. You are so insightful, conscientious, compassionate and fiercely driven about the things that matter and I admire you tremendously. Thank you for your unwavering friendship, for your excellent book recommendations and scrumptious cooking projects, for introducing me to critical role and learning to knit during the pandemic, and for making me think deeply about so many things. The list could go on and on but I think you'd prefer that I get some sleep instead.

To Caitlin — I knew I wanted to be friends with you as soon as I saw you so I'm glad you forgave me for that time I actually served myself some water after you told me that I could help myself. From doing yoga with you outside the remote observing room during long exposures to profound conversations or sleepy silence as we carpooled over 17 to endless afternoons working at coffee shops to being in each other's weddings, so many of the memorable and mundane moments were with you. Thank you for being my steadfast companion, stabilizing third wheel, and partner in silliness for the first 6.5 years of grad school.

To Tiffany, who shares my love of tea and nail polish. Our office was always

an oasis amid the craziness thanks to you and it was such a joy to have you as an office mate for so many years. Please move back to the Bay Area soon.

To Emily Martin — I am so glad Marie told me that we'd get along and that I decided to brazenly seek you out and knock on your office door to introduce myself once I found out you were also a knitter. I only met you a few years ago but it feels like I've known you forever. I am in awe of the friendship you have shown me and I cannot wait to spend so much time hanging out now that this is done!

To my knitting crew — Diana, Maggie, Louisa, Sarah and of course, the aforementioned Emily and Elizabeth, you have brought so much joy to these dark times (and probably enabled way too many yarn purchases). I look forward to a great many more knit nights to come.

To my college roommates Ashley, Cara, and Emma, who somehow all converged in the Bay Area for a few years, thank you for being such amazing friends! You are all brilliant and hilarious and I'm so glad I got to spend this time near you.

To Ragnhild, Anders, and Rebekah, I'm so glad that astronomy brought you into my life.

Special thanks to so many other current and former UCSC graduate students. Most particularly my former roommate Emily Cunningham and my other year-mates Zach, Marie, Alex, Jieun, and Phil.

Finally, to my family — je vous adore infiniment! To Maman et Papa who fostered such a deep sense of curiosity and a profound love of learning in me. Thank you for your unfaltering belief that I could do this, for your love and unending support, for

the pomodoros, the pep talks, the long phone calls and the endless supply of "<3" and "jtminf" and "TEG" text messages to encourage me and keep me going. To mon bébé Alexandre, nobody gets you like a sibling and I am so lucky to have you as my brother! I am so incredibly proud of you and I look forward to the time I will soon get to spend with you. To Babcia who instilled in me a love of sweets and math by giving me math problems to do when I would get home from school and rewarding me with a lollipop once they were completed. I wish that you were here to see me follow in your footsteps. To Mamie who I have not seen in much too long and who will be so excited that I am finally finished. I love you so very much. And of course to the two best kitties in the world — to Leo, my sweet boy that I adopted as soon as I moved out to Santa Cruz for graduate school and to Lyra, my little demon princess. You have been my steadfast companions, the best snuggle buddies, and bring me joy every single day.

Lastly and probably most importantly, to the funniest and most supportive person I know, Gene. I cannot count the number of teas you've made me, breakfasts you've brought me in bed, dinners you've cooked me or loads of dishes you have done as I've shambled my way along. Thank you for being the most amazing partner I could have ever imagined, for being my constant cheerleader, and for somehow putting up with me, even at my (frequent) worst. We did it!

Published Material

The text of this dissertation includes reprints of the following published material led by Leibler, with the permission of the listed coauthors.

Chapter 4 was published in the literature as Leibler et al. (2018). I was re-

sponsible for obtaining, reducing, and analyzing the LRIS spectroscopic observations of the Slug Nebula as well as reducing and analyzing the MOSFIRE spectra. I created all of the figures and wrote the paper text with the exception of Section 4.4.3 which was written by Bradford P. Holden and some of the introduction text in Section 4.1 was written by Sebastiano Cantalupo. I wish to thank my coauthors Bradford P. Holden, Sebastiano Cantalupo, and Piero Madau for their support and guidance in the course of this research.

Scientific Acknowledgments

I appreciatively acknowledge support from the National Science Foundation (NSF) Graduate Research Fellowship under Grant No. NSF DGE1339067. This dissertation includes data obtained at the W. M. Keck Observatory, which is operated as a scientific partnership among the California Institute of Technology, the University of California and the National Aeronautics and Space Administration. The Observatory was made possible by the generous financial support of the W. M. Keck Foundation.

I wish to recognize and acknowledge the very significant cultural role and reverence that the summit of Mauna Kea has always had within the indigenous Hawaiian community. We are most fortunate to have the opportunity to conduct observations from this mountain. I would also like to thank the support astronomers and observing assistant at Keck Observatory without whom this work would not have been possible.

Chapter 1

Introduction

The evolution of many core galaxy properties such as size, luminosity, color, metallicity, stellar mass, stellar ages, and gas masses of the cold and hot components of the interstellar medium (ISM) and circumgalactic medium (CGM), is shaped by the interplay of fundamental astrophysical processes that cause gas to be cycled into and out of galaxies (see Somerville & Davé 2015, for a review). The fundamental processes that drive this "baryon cycle" (e.g., Shapiro & Field 1976; Davé et al. 2012) include star formation and evolution, stellar feedback and galactic winds, and gas accretion.

Galaxies do not evolve in isolation and instead, according to models of large-scale structure formation in our ΛCDM Universe, are embedded in dark matter filaments that form the cosmic web (de Lapparent et al. 1986; Bond et al. 1996; Vogelsberger et al. 2014; Libeskind et al. 2018). Streams of cold dense metal-poor gas flowing along these filaments are able to penetrate the hot halos of galaxies, allowing galaxies to refresh their reservoirs of cold gas and sustain star-formation over long periods of time (e.g., Dekel

et al. 2009). In addition to these very low-metallicity inflows from the intergalactic medium (IGM), galaxies can also re-accrete gas previously ejected in galactic winds (wind recycling; Oppenheimer et al. 2010) or accrete gas that was pre-processed by external galaxies, for example in gas-rich mergers or gas removal from satellite galaxies by ram-pressure and/or tidal stripping (Anglés-Alcázar et al. 2017).

This accretion of cold gas, which we also refer to as gas inflow or infall, serves as the fuel for future star formation (e.g., White & Frenk 1991). Though direct observational evidence of galactic gas accretion remains rare, cool gas inflows in the form of high velocity clouds have been detected in the Milky Way's halo (e.g., Lehner & Howk 2011; Putman et al. 2012; Fox et al. 2019). Moreover, whereas molecular gas depletion timescales[1] for nearby galaxies ($z \sim 0$) are around $\sim 1-2$ Gyr (Leroy et al. 2013; Querejeta et al. 2021), these timescales become rapidly shorter with increasing redshift. For instance, Scoville et al. (e.g., 2016) measure the average molecular gas depletion timescale of $\tau_{\rm dep}^{\rm mol} \sim 0.84$ Gyr at $z \sim 1.1$ which decreases to $\tau_{\rm dep}^{\rm mol} \sim 0.56$ Gyr at $z \sim 2.2$ (consistent with the $\tau_{\rm dep}^{\rm mol} \sim 0.7$ Gyr found by Tacconi et al. 2013, for galaxies at $z \sim 1-2.5$) and becomes shorter still ($\tau_{\rm dep}^{\rm mol} \sim 0.31$ Gyr) at $z \sim 4.4$[2]. Yet, many galaxies are still star-forming at $z \sim 0$ despite the fact that these observations imply that they should have run out of gas long ago. This serves as further evidence that galaxies must be accreting fresh gas over the course of their lifetimes.

[1] The molecular gas depletion timescale is defined as the time it would take for a galaxy to convert its current reservoir of cold molecular gas into stars assuming it continued forming stars at its current rate. Therefore, $\tau_{\rm dep}^{\rm mol} = \frac{\rm M_{mol}}{\rm SFR}$, where $\rm M_{mol}$ is the molecular gas mass.

[2] A comparison of the cold gas depletion timescale (neutral+ molecular) to the molecular gas deplection timescale as a function of redshift can be found in Péroux & Howk (2020).

As the continued accretion of fresh gas fuels new star formation, the more massive of these recently-formed stars will soon end their lives as core-collapse supernovae (CCSN). These violent explosions can heat the nearby interstellar medium (ISM) or even drive galactic-scale winds that entrain the surrounding interstellar medium (ISM) gas (e.g., Hopkins et al. 2012). That CCSNe are capable of launching gas outflows is well substantiated by the many observations of outflowing gas associated with actively star-forming regions within galaxies for a broad range of galaxy masses and redshifts (Weiner et al. 2009; Rubin et al. 2010; Martin et al. 2012; Rubin et al. 2014; Chisholm et al. 2015; McQuinn et al. 2019; see Veilleux et al. 2020 for a review). In either case, whether some of the ISM gas is simply heated and thus prevented from cooling and forming stars or is removed entirely in winds and deposited into the circumgalactic medium (CGM) or even the intergalactic medium (IGM) [3], this gas is no longer available to be converted into stars. It is therefore likely that stellar feedback and gas outflows in general are also essential in determining the star formation histories of galaxies and by extension, the aforementioned core galaxy properties (e.g., Hopkins et al. 2014).

These same astrophysical processes influence the galactic chemical enrichment history: The primordial gas initially present in a galaxy is converted to stars which in turn can produce elements heavier than hydrogen and helium as they undergo nucleosynthesis. During the late stages of stellar evolution, this metal-enriched material is recycled back into the ISM, thereby increasing the metallicity of the gas. Subsequent generations of stars formed out of this increasingly metal-rich gas will therefore have

[3]This happens if the outflow velocity exceeds the escape velocity of the galaxy.

progressively higher metallicities. However, as the more massive of these stars explode as CCSNe, the outflows they drive expel enriched ISM gas from the galaxy and, if some of the very metal-rich SN ejecta is also removed in these galactic winds prior to being recycled back into the gas reservoir, the chemical enrichment of the galaxy will be significantly slowed. Moreover, as the galaxy's cold gas reservoir is depleted by star formation and SN-driven outflows, it will need to be replenished by the accretion of new gas which is usually of much lower metallicity gas than the ISM gas that was converted into stars or lost in outflows. Therefore, gas inflows will generally lower the metallicity of the ISM, though this dilution of the metals in the galaxy's cold gas reservoir due to the infall of metal-poor IGM gas may be mitigated by the accretion of enriched gas from external galaxies or the re-accretion of formerly expelled gas (i.e., wind recycling).

Thus, the chemical evolution history of a galaxy is determined by the interplay between 1) *star formation and evolution*, which depletes the cold gas reservoir but also enriches it with metal-rich stellar winds and SN ejecta, 2) *galactic outflows*, which expel enriched ISM and, possibly, very metal-rich SN ejecta, depositing metals into the CGM and IGM, and likely slowing future star formation, and 3) *gas accretion* from the IGM, wind recycling, and already enriched (externally processed) gas from other galaxies, which can change the metallicity of the ISM and replenish the cold gas reservoir to fuel future star-formation.

The time-dependent behavior of these fundamental processes is imprinted on the chemical evolution of the gas and is preserved as gas is converted into stars in the stellar abundances of low mass, long lived stars that are still observable today.

In particular, signatures of these processes and their interaction are encoded in the stellar abundance patterns (especially [α/Fe] vs [Fe/H]) and the metallicity distribution function (MDF) of a galaxy which can be observationally derived from star-by-star measurements of stellar abundance ratios for the Milky Way and other nearby galaxies for which high-resolution spectra of individual stars can be obtained. The comparison of these observed stellar abundance patterns to predictions from simple galactic chemical evolution models can be used to infer important constraints on, or insights into, these processes and serves as a powerful tool for studying the galactic baryon cycle.

This is demonstrated in Chapter 2, where we build just such a simple chemical evolution model and combine it with the wealth of high-quality spectroscopic observations available for the Milky Way to constrain and characterize the fundamental processes that have shaped our Galaxy's evolution. The goal of Chapter 2, however, is not to model the full complexity of the Milky Way's chemical evolution history but rather to:

1. Present our flexible one-zone galactic chemical evolution model.

2. Develop a general framework for understanding *why* different physical processes (and their parametrization within a chemical evolution model) impact the present-day stellar abundances in the way they do. In particular, we find that the effect of a model ingredient (or parameter) on the chemical evolution of a galaxy can be characterized with respect to its influence on two key terms that we call the "effective gas returns", $R_{\rm eff}$ and the "gas removal efficiency", $\epsilon_{\rm rm}$.

3. Establish the manner in which different galaxy ingredients affect characteristic

features in the stellar abundance patterns we observe today.

4. Validate our chemical evolution code by generating simulated [Mg/Fe]–[Fe/H] tracks and MDFs that adequately reproduce the observed star-by-star abundance patterns and [Fe/H] distribution function of the Milky Way's thick disk.

Unfortunately, with current observational capabilities, star-by-star abundances that enable the inference of detailed histories for individual histories are only measurable for the most nearby galaxies. However, for galaxies beyond the Local Group but still within the local universe, it is possible to obtain sufficiently high-quality spectra of the integrated light of galaxies, from which galaxy-wide average stellar abundance ratios can be calculated. The further away the galaxy, the more difficult it becomes to acquire spectra with the necessary signal-to-noise to measure even galaxy-averaged stellar abundance ratios. However, while this precludes studying the chemical evolution of individual distant galaxies, stacking their spectra with those of similar galaxies produces a higher signal-to-noise spectrum from which average stellar abundance ratios — that are representative of the chemical evolution of this population of galaxies as a whole — can be determined (e.g., Conroy et al. 2014).

As we show in Chapter 3, in the case of low-redshift elliptical galaxies, these average abundance ratios — in conjunction with chemical evolution modeling — can still be used to gain valuable insights into the fundamental astrophysical processes that govern the evolution of an entire population of galaxies. In Chapter 3 we use an updated version of the chemical evolution code described in Chapter 2 to explore how various physical processes influence the average abundance ratios (particularly $\langle$[Mg/Fe]$\rangle$ and

$\langle$[Fe/H]$\rangle$) of elliptical galaxies. We highlight the difficulty in simultaneously reproducing the mass-metallicity relation and the positive correlation between elliptical galaxy α-enhancement and mass which continues to present a severe challenge for galaxy evolution models. Although, in recent years, this has frequently been interpreted as evidence for a non-universal IMF (Fontanot et al. 2017; De Masi et al. 2018; Yan et al. 2019), we present a reasonable alternative explanation for these average abundance trends.

We also find that despite its simplicity, our chemical evolution code is particularly well suited to modeling the elliptical galaxy populations described in Chapter 3. Unlike many traditional chemical evolution models which relate the star-formation rate to the gas mass, we implement a predetermined star-formation history that decouples these two quantities. Consequently, we can easily incorporate a priori knowledge about elliptical galaxies, such as their lack of recent star formation, without having to determine the underlying physical drivers that cause it. In our code, this elliptical galaxy property can easily be represented by a truncated star-formation history without making assumptions about what caused the quenching (such as a rapid gas consumption timescale or a reduction in the accretion of gas from the IGM) and allows us to consider gas depletion (or gas fraction) independently from star formation quenching.

Since the gas that is cycled into and out of galaxies shapes the core properties of galaxies, direct observations of this gas are essential to further our understanding of how galaxies evolve across cosmic time. The CGM and IGM are most commonly observed in absorption, either using a sight-line to a bright background source like a quasar that traverses the gas near a galaxy (e.g., Rudie et al. 2012; Lau et al. 2016) or using the

"down the barrel" technique which employs the light emitted by the host galaxy itself as the background source (e.g., Rubin et al. 2012, 2014; Henry et al. 2015). These pencil-beam measurements are sensitive to a wide range of gas column densities but probe only a small region of the gas. Due to the rarity of sufficiently bright background sources, it is only possible to get a very limited number of sight-lines through the gas of any given galaxy (usually only one for galaxies beyond the local Universe). Consequently, absorption-line studies are best used to statistically sample the gas around galaxies as a whole rather than to build a picture of the CGM or IGM properties near a specific galaxy (for a review, see Tumlinson et al. 2017).

To study the gas around individual galaxies and map properties such as its surface brightness, geometry, kinematics, ionization, metallicity, volume density and mass, it is necessary to observe the gas in emission, though the low typical densities expected for the CGM and IGM make such observations challenging (e.g., Dijkstra 2017). However recent discoveries of enormous Lyman-α nebulae (ELANe; Cantalupo et al. 2014; Hennawi et al. 2015; Cai et al. 2017) around quasars at $z \approx 2$ that extend over several hundred kpc provide an excellent opportunity for the detailed study of gas in emission around individual galaxies at this cosmic epoch. One of the brightest ($L_{Ly\alpha} = 2.2 \pm 0.2 \times 10^{44}$ erg s^{-1}) such ELANe is the "Slug Nebula" (Cantalupo et al. 2014), which was discovered around the radio-quiet quasar UM287 ($z = 2.283$) using narrow-band imaging. This nebula has a projected size of ~ 460 kpc that extends well beyond the viral radius of the quasar's dark matter halo, thus tracing not only the CGM but also the IGM.

Cantalupo et al. (2014) propose two possible mechanisms for producing the Slug's Ly α emission that have very different implications for the physical properties of the gas. In the first case, the nearby quasar photoionizes the Slug's cool, very high-density hydrogen gas resulting in Lyα emission from hydrogen recombination. In the second case, the gas is mostly neutral and the Lyα emission of the Slug is primarily Lyα emission produced by the quasar broad-line region that has been resonantly scattered into our line-of-sight by the Nebula. However, Ly α imaging alone cannot differentiate between these two scenarios, and observations of the Slug's emission from a non-resonant transition such as Hα are needed to distinguish them.

In Leibler et al. (2018), reprinted in Chapter 4, we analyze deep long-slit Ly α and H α spectroscopy of the brightest regions of Slug Nebula taken with Keck I/LRIS and Keck I/MOSFIRE. We then calculate the Ly α and H α flux and consider their respective kinematics in order to compare them with predictions from case B hydrogen recombination. Finally, having identified the mechanism by which the Ly α is being generated, we discuss the implications of our results for the physical properties of the Slug Nebula's gas, including its density, spatial distribution, and ionization state.

Chapter 5 summarizes our findings and explores possible future work towards understanding the baryon cycle in galaxies and the physical processes that drive it.

Chapter 2

The Chemical Evolution of the Milky Way

2.1 Introduction

The abundances of elements of a galaxy's stars form a sort of fossil record wherein each star is imprinted with the gas abundance at the time (and place) of its birth. Thus, present-day, long-lived, low-mass stars preserve a snapshot of the chemical enrichment history which reflects a range of physical processes that affected the evolution of the galaxy as a whole. A visual representation of the process through which a galaxy becomes chemically enriched is shown in Figure 2.1, which we will refer to as "the diagram" below. Conceptually, a galaxy's baryonic matter can be partitioned into three components: stars, stellar remnants, and a gas reservoir. The galaxy's star-formation history (SFH; label **A** in the diagram) is established and its stellar component built up

as cold, dense gas from the reservoir collapses to form stars whose masses are distributed according to the stellar initial mass function (IMF; label **B** in the diagram).

As time passes, stars of increasingly lower masses evolve off of the main sequence and return a portion of their initial mass to the gas reservoir in the form of stellar winds and/or supernova (SN) ejecta as they die off. Stars that end their lives as asymptotic giant branch (AGB; depicted in pink in the diagram) stars or as core-collapse supernovae (CCSNe; depicted in dark blue in the diagram), will release nucleosynthetic by-products (shown as the dark gray arrow in the diagram) that will enrich the initially pristine gas reservoir with e.g., α-elements (shown in cyan) like oxygen (O), magnesium (Mg), and silicon (Si). The white dwarfs, neutron stars, or black holes that are left behind are no longer considered to contribute to the stellar mass and are instead added to the stellar remnant component. A number of these white dwarf remnants will eventually explode as thermonuclear Type Ia SNe (SNIa), as determined by the SNIa delay-time distribution (DTD; label **C**). The ejecta from these SNIa, which also serves to enrich the gas reservoir, is particularly rich in iron (Fe) peak elements (shown in green) while being nearly devoid of α-elements (as seen in insert **D** of the diagram).

Thus, as subsequent generations of stars are born, they are formed out of increasingly enriched gas [4]. This is known as the stellar age-metallicity relation (Twarog 1980; Casagrande et al. 2011; Haywood et al. 2013; Hayden et al. 2017). In addition, the [α/Fe] abundance ratio of the gas reservoir will also evolve and be imprinted on

[4]In this work, the gas enrichment is usually characterized by the [Fe/H] abundance ratio, which is defined as the logarithm of the ratio of iron to hydrogen in the gas to the ratio found in the Sun. The solar ratios are taken from Lodders et al. (2009).

subsequent stellar generations as ejecta from the SNIa pollute the α-element rich returns from massive stars with copious amounts of Fe. Since these massive stars have short lifetimes of about 10 million years (Myr) while SNIa take on the order of billions of years (Gyr) to explode after the formation of their progenitor stellar generation, the evolution of [α/Fe] and [Fe/H] encodes important information about e.g., the galaxy's SFH that is preserved in the abundance ratios of long-lived low mass stars. However, the interpretation of [α/Fe] as being simply an indicator of the star-formation timescale is complicated by the fact that these abundance ratios can also be affected by other galactic phenomena such as inflows and outflows (represented in the diagram by the white and light gray arrows, respectively).

Therefore, in order to relate chemical abundance patterns of stars to information about the specific physical processes taking place in a galaxy at the time of their birth, it is necessary to use models. A wide variety of methods have been used to approach this problem: for example, analytical solutions, one-zone galactic chemical evolution models (GCEM), cosmological semi-analytical models, and complex hydrodynamical simulations have all provided various insights about the assembly history of the Milky Way.

These very different approaches have their advantages as well as specific limitations. Analytical solutions are easy to understand but commonly require unrealistic simplifying assumptions (such as gas never entering nor leaving galaxies), and therefore are at odds with current observational constraints. Hydrodynamical simulations include the most realistic physics but are computationally expensive, complex to inter-

pret given the various assumptions made to parameterize the physics at small scales, and still cannot self consistently model the vast range of temporal and spatial scales involved in galaxy evolution. Finally, one-zone GCEM use physically motivated analytic prescriptions for or simple relations between different galaxy components. They are therefore inexpensive to run and enable exploration of a large parameter space and, as such, can isolate the effects of different physical processes. Despite their inability to incorporate all the physics included in more complex three-dimensional models, these relatively simple simulations are the most useful tool when attempting to decipher the principal physical drivers behind the observed stellar abundance patterns.

Historically, one-zone galactic chemical evolution models have been used extensively to try to understand the assembly of our own Galaxy, as stars in the Milky Way are uniquely well characterized and a wealth of abundance data is available with which to compare and constrain the models. Understanding the assembly of external galaxies is complicated by the limited data available and, in particular, the lack of star-by-star abundances, but these relatively simple models are still able to provide valuable insight into their overall history and evolution (see Chapter 3). To be able to represent the formation history of a large sample of galaxies, we have developed a flexible code for chemical evolution. In this chapter, we validate its implementation and explore its parameter space with data from the Milky Way, in the tradition of many simple modelling studies.

The goal of this work, however, is not to perfectly reproduce all the peculiarities of the Milky Way. Instead, the aim of this chapter is to present a framework

with which to understand the role of different physical processes in altering the chemical composition of the gas and successive generations of stars in galaxies over time. The details of the implementation of our chemical evolution model and its model parameters are described in Section 2.2. The fiducial "Closed Box", "Inflows-Only, and "Inflows+Outflows" models are presented in Section 2.3.1 and the Milky Way data to which all simulations in this chapter are compared is described in Section 2.3.2. The results are presented in Section 2.4: we first identify two key quantities that can be used to characterize the impact of any physical process on the chemical evolution of a galaxy in Section 2.4.1. In Section 2.4.2 we investigate the stellar abundance features produced by a galaxy that evolves as a closed box and broadly consider how these features change in the presence of galactic inflows and outflows (summarized in Section 2.4.2.4). Next, in Section 2.4.3, we examine the role of a number of galaxy model ingredients and their associated parameters in shaping the metallicity distribution function and the stellar [Mg/Fe] and [Fe/H] abundance patterns. Finally, in Section 2.4.4 we summarize the challenges in replicating the Milky Way's observed stellar abundance patterns. We then present two simulations that, despite these difficulties, produce reasonable fits to the Milky Way comparison data, thereby validating our chemical evolution code. In the discussion in Section 2.5, we summarize the main results of this chapter, discuss the ways other aspects of the model would be expected to alter the [Mg/Fe] and [Fe/H] abundance patterns, and compare our results with previous studies. Limitations of this work and the ways in which our flexible model framework could enable interesting extensions are also considered.

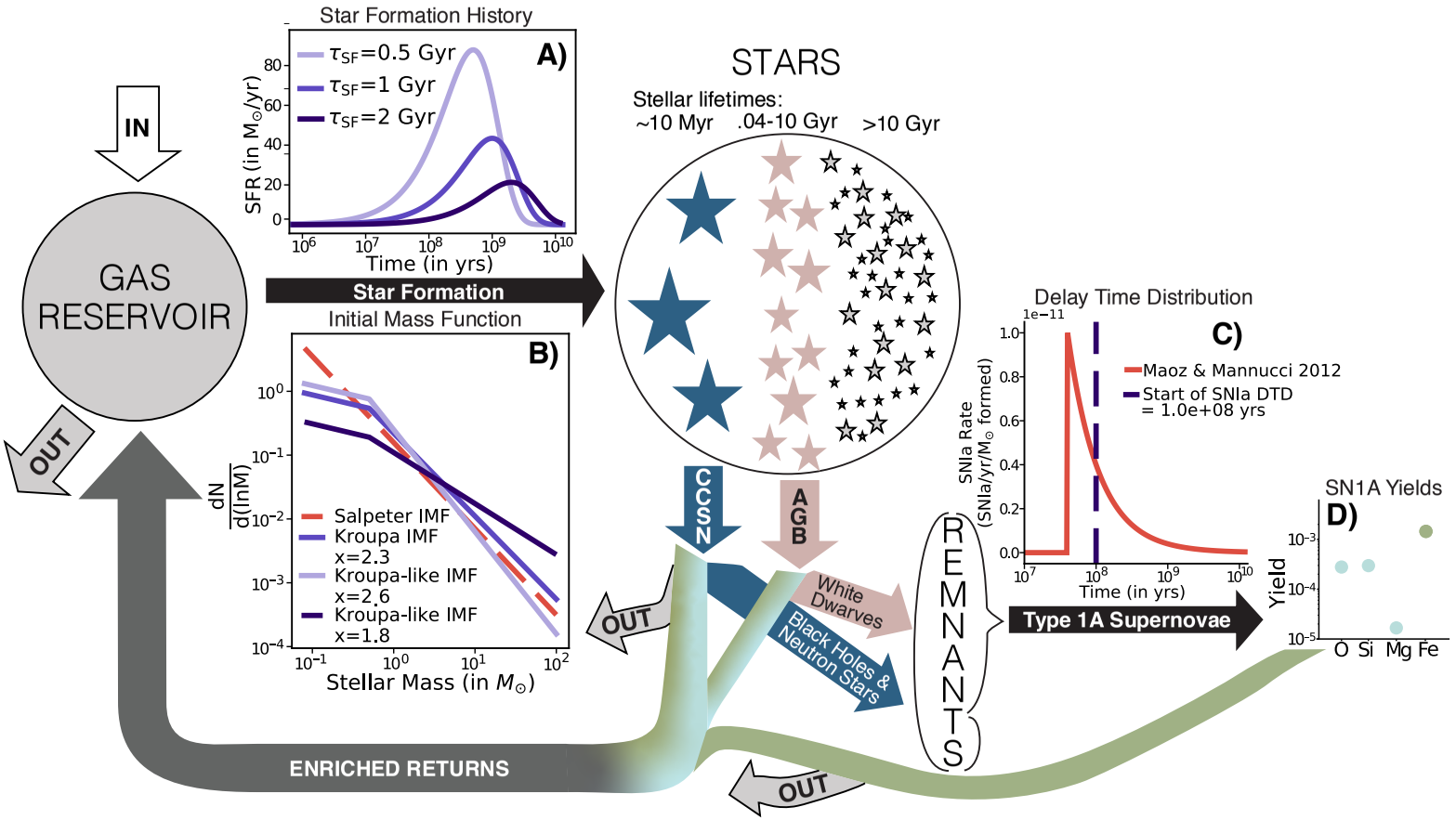

Figure 2.1: This diagram is a visual representation of the process by which a galaxy becomes chemically enriched. We refer the reader to the text in Section 2.1 for more details. In addition, a few key ingredients to the chemical evolution code described in Section 2.2 are shown as labeled insert panels. Insert **A** shows three examples of linear-exponential SFH. Insert **B** depicts the standard Salpeter (1955) IMF and Kroupa (2008) IMF as well as a top-heavy (α =1.8) and top-light (α =2.6) Kroupa-like IMF. The implemented Maoz & Mannucci (2012) SNIa DTD (red solid curve) is plotted in insert **C** as is the fiducial minimum time before SNIa explode of $t_{DTD} = 100$ Myr (purple dotted line) which approximately corresponds to the minimum lifetime of stars that produce CO white dwarf remnants (see Section 2.2.4). The Nomoto et al. (1997) SNIa yields for a small subset of elements is shown in insert **D**.

2.2 Model Description

We have built a flexible, one-zone galactic chemical evolution model (GCEM) in PYTHON including packages such as NUMPY, SCIPY, AND PANDAS (Van Rossum & Drake 2009; Walt et al. 2011; Jones et al. 2001; Team 2019; Wes McKinney 2010). The model includes simple, but physically-motivated, prescriptions for the main processes that influence the chemical evolution of galaxies such as the star-formation history (ref. Section 2.2.1), the stellar initial mass function (ref. Section 2.2.2), inflows (ref. Section 2.2.6), outflows (ref. Section 2.2.5), and enriched gas returns from dying stars (ref. Section 2.2.3). The code separately tracks the chemical evolution of all elements produced by AGB stars and in the explosions of CCSN and SNIa, with their theoretically-derived nucleosynthetic by-products included in the form of yield tables.As a default, elements with atomic number $1-32$ (H$-$Ge) are tracked, though fewer elements can be followed to speed up the calculations. The need for the often used 'instantaneous-recycling' assumption (Schmidt 1963) is eliminated by incorporating realistic stellar lifetimes which are determined from MIST models [5]. However, this code does implement the "instantaneous mixing approximation" (see e.g., Dalcanton 2007; Pagel 2009) which assumes that infalling gas and gas returns from various phases of stellar evolution are immediately and completely mixed back into the cold gas reservoir. Additionally, we adopt a 'mono-phase' interstellar medium whereby no attempt is made to distinguish between cold and hot gas throughout the simulated galaxy. In the following subsections, we

[5] http://waps.cfa.harvard.edu/MIST/ (Dotter 2016; Choi et al. 2016; Paxton et al. 2011, 2013, 2015, 2018)

detail the different components (also referred to as galaxy ingredients) included in the code along with the equations that govern the chemical evolution of our model galaxies.

2.2.1 Star Formation History

Galactic chemical evolution models commonly implement a star-formation (SF) prescription akin to the Kennicutt-Schmidt law (Schmidt 1959; Kennicutt 1998). Instead of the observed power-law relationship between surface density of star-formation and the gas surface density: $\Sigma_* \propto \Sigma_{\rm gas}^n$ with $n = 1.4$ from Kennicutt (1998), the stellar mass formed is assumed to be linearly proportional to the gas reservoir mass ($M_{\rm gas}(t)$), $\Psi(t) = \dfrac{1}{\tau_{\rm dep}} M_{\rm gas}(t) = \epsilon_{\rm SF} M_{\rm gas}(t)$ (as in, e.g. Schmidt 1963; Andrews et al. 2017). Here, $\Psi(t)$ is the star-formation rate (SFR), $\tau_{\rm dep}$ is the gas depletion timescale and $\epsilon_{\rm SF} \equiv \tau_{\rm dep}^{-1}$ is known as the star-formation efficiency.

Although this description of the SFR is mathematically convenient (as mentioned in e.g., Recchi et al. 2008), it does not actually match the observed slope of $n \approx 1.4$ nor does it account for how total gas mass can differ from surface density. In addition, this parametrization forces the star-formation efficiency to be constant. However, given that the observed Kennicutt-Schmidt law is non-linear, it is likely that as galaxies become less gas rich at later times, the star-formation efficiency is also declining. Furthermore, this relation makes the star-formation rate implicitly dependent on the inflows, outflows, and IMF-weighted yields, making it extremely challenging to disentangle the effects of each of these physical processes on the chemical evolution. Finally, this parametrization makes it difficult to produce simulations that match a particular final stellar mass and final gas fraction (to match observations).

In order for this code to remain as broadly applicable as possible, we have instead chosen to characterize the SFH of our model Milky Way-like galaxies as a linear-exponential function, which has been shown to be a good parametrization to the SFHs of galaxies in cosmological simulations and hydrodynamical zoom-in simulations (e.g, De Lucia et al. 2006; Lee et al. 2010; Simha et al. 2014):

$$\Psi(t) = \Psi_0 t e^{\left(-t/\tau_{\rm SF}\right)} \tag{2.1}$$

where $\Psi(t)$ is the star-formation rate at time t, $\tau_{\rm SF}$ is the star-formation timescale, and Ψ_0 is the normalization factor chosen such that the stellar mass at the end of the simulation, $t = T_{\rm gal}$, is the user-provided final stellar mass of the galaxy, $M_{\rm star,f}$. This normalization is easily calculated since it only additionally depends on the IMF and the lifetime of stars. The stellar mass of the Milky Way that is usually reported in the literature actually refers to the stellar mass + remnant mass (denoted as $M_*(t) = M_{\rm star}(t) + M_{\rm rem}(t)$, which for an end-of-simulation galaxy is simply $M_{*,\rm f} = M_{\rm star,f} + M_{\rm rem,f}$). Therefore, we choose $M_{\rm star,f}$ such that the final stellar+remnant mass is close to $M_{*,\rm f} \approx 5.4 \times 10^{10} \mathrm{M}_\odot$ that is reported for the Galaxy in Bland-Hawthorn & Gerhard (2016).

In addition, we assume a fiducial value of $T_{\rm gal} = 13$ Gyr, as in Kobayashi et al. (2006), though other comparable Milky Way chemical evolution models sometimes use slightly shorter simulation lengths; e.g. 12 Gyr for Andrews et al. (2017) and 12.5 Gyr for Freudenburg et al. (2017) and Weinberg et al. (2017). These small differences in the assumed age of the Galaxy should have no appreciable impact on the predicted chemical

abundance patterns.

2.2.2 Initial Mass Function

The mass of each stellar generation is distributed according to the stellar initial mass function (IMF):

$$\frac{dN(M)}{dM} \propto M^{-\alpha} \tag{2.2}$$

We have implemented a generalized prescription for the IMF so that it takes the form of either a single power-law, as in the case of the Salpeter (1955) IMF, or a broken power-law, as suggested by Kroupa (2008). The canonical form of the Salpeter IMF has a slope $\alpha = 2.35$, while the Kroupa IMF has different slopes for low-mass stars and high-mass stars:

$$\alpha = \begin{cases} 1.3 \pm 0.3 & \text{for } 0.08 \leq \mathrm{M/M_{\odot}} \leq 0.5 \\ 2.3 \pm 0.5 & \text{for } 0.5 \leq \mathrm{M/M_{\odot}} \leq 100 \end{cases} \tag{2.3}$$

As a default, we assume the standard Kroupa IMF over the mass range 0.08 $\mathrm{M_{\odot}} \leq M \leq 100\ \mathrm{M_{\odot}}$, though we also explore the impact of using a Salpeter IMF, a top-heavy Kroupa-like IMF, and a top-light Kroupa-like IMF in Section 2.4.3.3.

Table 2.1: Variables Used in this Chapter

Variable Name	Variable Description	Section
$T_{\rm gal}$	Duration of simulation (final galaxy age)	Section 2.2.1
$M_{\rm star}(t)$	The stellar mass as a function of time	Section 2.2.1
$M_*(t)$	The stellar mass + remnant mass as a function of time	Section 2.2.1
$M_{\rm gas}(t)$	The gas reservoir mass as a function of time	Section 2.2.1
$M_{\rm in}(t)$	The inflow mass as a function of time	Section 2.2.6
$M_{\rm out}(t)$	The outflow mass as a function of time	Section 2.2.5
$M_{\rm tot}(t)$	The total mass of the galaxy as a function of time $M_{\rm gas}(t) + M_*(t) + M_{\rm in}(t) - M_{\rm out}(t)$	Section 2.2.6
$f_{\rm gas}(t)$	The gas fraction as a function of time —$\frac{M_{\rm gas}}{M_{\rm tot}}$	Section 2.2.6
$M_{\rm star,f}$	The mass that remains in stars at the end of the simulation —$M_{\rm star}(t = {\rm T_{gal}})$	Section 2.2.1
$M_{*,\rm f}$	The final stellar mass + remnant mass —$M_*(t = T_{\rm gal})$	Section 2.2.1
$M_{\rm gas,0}$	The initial mass present in the gas reservoir at the start of the simulation	Section 2.2.6
$f_{\rm gas,f}$	The final gas fraction —$\frac{M_{\rm gas}}{M_{\rm tot}}\,(t = T_{\rm gal})$	Section 2.2.6
$\Psi\,(t)$	The star-formation rate	Section 2.2.1
Ψ_0	The star-formation normalization (to get $M_{\rm star,f}$ at $t = T_{\rm gal}$)	Section 2.2.1
$\tau_{\rm SF}$	The star-formation timescale	Section 2.2.1
I_0	The inflow normalization (to get $f_{\rm gas,f}$ at t=$\rm T_{gal}$)	Section 2.2.6
$\tau_{\rm in}$	The inflow timescale	Section 2.2.6
α	IMF slope	Section 2.2.2
$\Phi\,(t)$	The SNIa delay-time distribution (number of SNIa/$\rm M_\odot$ produced t yrs post generation formation)	Section 2.2.4
$\rm t_{DTD}$	The minimum delay-time for SNIa	Section 2.2.4
$\epsilon_{\rm out}$	The outflow parameter	Section 2.2.5
$f_{\rm SN}$	The fraction of supernova ejecta that is removed in the outflow	Section 2.2.5
$t_{\rm step}$	The length of a simulation time-step	Section 2.2.7
$N_{\rm step}$	The number of time-steps in a simulation —$T_{\rm gal}/t_{\rm step}$	Section 2.2.7

2.2.3 Nucleosynthetic Yields

Here we adopt the Kobayashi et al. (2006) core-collapse supernova (CCSN) nucleosynthetic yields for our chemical evolution models though we do not include their hypernova yield tables since the hypernova rate is thought to be around 100 times lower than the present-day rate of CCSN (Podsiadlowski et al. 2004; Guetta & Della Valle 2007). Kobayashi et al. (2006) provides yield tables for four different metallicities; $Z = Z_{\odot}$, Z =0.004, Z =0.001, Z =0. These tables include seven initial stellar progenitor masses (spanning 13 $M_{\odot}$ to 40 $M_{\odot}$), their corresponding final stellar mass prior to explosion, the remnant mass left behind after the CCSN, and the mass of each elemental isotope found in the SN ejecta. We linearly interpolate each table to calculate the yields for a more finely sampled initial stellar mass range and assume that stars above $40M_{\odot}$ collapse directly to black holes without enriching the ISM. Stellar mass lost as winds prior to the CCSN explosion[6] is assumed to be returned to the gas reservoir with the initial birth metallicity of the star.

Stars with initial masses 1 $M_{\odot} \leq M_{i} \leq 6$ $M_{\odot}$ end their lives as asymptotic giant branch (AGB) stars that generate metal-enriched winds. We adopt the Karakas (2010) yields for Z = 0.02, 0.008, 0.004 and 0.0001 and the Fishlock et al. (2014) for Z=0.001. For intermediate-mass stars with initial masses above 6 $M_{\odot}$ (up to $7.5-9$ $M_{\odot}$, depending on the stellar metallicity), which evolve into super-AGB stars, we use the Doherty et al. (2014a,b) yield tables. These tables cover Z = 0.02, 0.008, 0.004 and Z = 0.0001, 0.001, respectively.

[6]The mass lost as winds is determined by taking the difference between the initial and final stellar mass given in the Kobayashi et al. (2006) yield tables.

Table 2.2: Default metallicity thresholds and corresponding yield table choices

Metallicity Range	**AGB**	**Super-AGB**	**CCSN**	**SNIa**
$\mathbf{0 \leq Z < 5 \times 10^{-4}}$	Karakas 2010 Z = 0.0001	Doherty et al. 2014b Z = 0.0001	Kobayashi et al. 2006 Z = 0	Nomoto et al. 1997
$\mathbf{5 \times 10^{-4} \leq Z < 5.5 \times 10^{-4}}$	Karakas 2010 Z = 0.0001	Doherty et al. 2014b Z = 0.0001	Kobayashi et al. 2006 Z = 0.001	Nomoto et al. 1997
$\mathbf{5.5 \times 10^{-4} \leq Z < 2.5 \times 10^{-3}}$	Fishlock et al. 2014 Z = 0.001	Doherty et al. 2014b Z = 0.001	Kobayashi et al. 2006 Z = 0.001	Nomoto et al. 1997
$\mathbf{2.5 \times 10^{-3} \leq Z < 6 \times 10^{-3}}$	Karakas 2010 Z = 0.004	Doherty et al. 2014a Z = 0.004	Kobayashi et al. 2006 Z = 0.004	Nomoto et al. 1997
$\mathbf{6 \times 10^{-3} \leq Z < 0.012}$	Karakas 2010 Z = 0.008	Doherty et al. 2014a Z = 0.008	Kobayashi et al. 2006 Z = 0.004	Nomoto et al. 1997
$\mathbf{0.012 \leq Z < 0.014}$	Karakas 2010 Z = 0.008	Doherty et al. 2014a Z = 0.008	Kobayashi et al. 2006 Z = 0.02	Nomoto et al. 1997
$\mathbf{0.014 \leq Z}$	Karakas 2010 Z = 0.02	Doherty et al. 2014a Z = 0.02	Kobayashi et al. 2006 Z = 0.02	Nomoto et al. 1997

In general, the fates of stars with initial masses between $8 - 13$ $M_\odot$ are still poorly understood (see Nomoto et al. 2013; Doherty et al. 2017; Gil-Pons et al. 2018) and their nucleosynthetic contribution remains very uncertain. This is even true for super-AGB stars, which are the subset of stars within this mass range for which theoretical yield tables exist (and whose nucleosynthesis is included in our code). For instance, the nucleosynthetic calculations for low metallicity super-AGBs disagree to such an extent that it is not even clear whether crucial elements like O and Mg are created or destroyed in these stars (cf. Siess 2010; Ventura et al. 2013; Doherty et al. 2014b at Z=0.0001 and see Doherty et al. 2017 for a more detailed review). Therefore, rather than using methods like extrapolating the CCSN yields to lower masses or interpolating between the CCSN and the super-AGB stellar yield tables (as in Andrews et al. (2017) but see Doherty et al. (2017) for why this would cause significant errors), which would likely add difficult to quantify errors to our chemical evolution model, we instead assume that stars with intermediate masses not covered by these yield tables evolve passively. As such, these stars undergo no net element production and the winds that are returned to the gas reservoir retain the original birth metallicity of the star.

Low-mass stars with $M_\mathrm{i} < 1$ $M_\odot$ also evolve passively in our models. Over their lifetimes, these stars lose mass in the form of stellar winds, eventually becoming remnants with masses determined by the Renzini & Ciotti (1993) initial-final mass relation (IFMR): $M_\mathrm{f} = 0.077 M_\mathrm{i} + 0.48$. Note that though this is an older IFMR prescription, it is implemented in Conroy & Gunn (2010) (see Conroy et al. 2009), which is used to measure the elliptical galaxy abundances (Conroy et al. 2014) in Chapter 3.

Additionally, it is similar to other more modern characterizations of the IFMR such as Kovetz et al. (2009); Salaris et al. (2009); Zhao et al. (2012). As with the winds from massive stars, the winds returned by passively evolving stars have Z corresponding to their birth metallicity such that they produce no net yields.

This effect as well as our choice to have intermediate-mass stars (that are not covered by the Doherty et al. (2014a,b) super-AGB yield tables) return no net nucleosynthetic yields means that our models likely underestimate the total production of metals. Even though we do not expect this to be a large effect, this could be relevant for our predictions of [Fe/H], see Section 2.5.

We do not interpolate the yield tables for CCSN and AGB stars to intermediate metallicities, choosing instead to transition to a higher-metallicity yield table when the gas reservoir crosses particular metallicity thresholds (see Table 2.2.3). Since Kobayashi et al. (2006) does not provide net yields or the initial metallicities of their model stars, we choose to implement absolute (or gross) yields. This means that the masses of stellar ejecta or wind that are returned from dying stars are taken directly from the (mass-interpolated) yield tables. The element mass returned is not adjusted to account for differences between the star's original birth metallicity and the metallicity assumed by the yield table. For instance, we use the same Kobayashi et al. (2006) Z=0.001 yield table for a stellar population born from gas with Z=0.001 and Z=0.0015. The stars with a birth metallicity of Z=0.0015 would contain higher masses of metals (e.g. Mg and Fe) than the Z=0.001 stars but CCSN from both stellar populations will return the exact same element masses as their stellar ejecta. Thus, the Z=0.0015 population

effectively produces lower net returns, since the difference between the initial element mass and the element mass returned after death is now smaller.

Finally, for the nucleosynthetic yields of Type Ia supernovae (SNIa), we adopt the W7 model from Nomoto et al. (1997). In the future, we plan to implement the metallicity-dependent updated W7 models from Leung & Nomoto (2018). For now, we simply note that according to the updated solar metallicity W7 model, a slightly higher Fe mass ($\approx$ 8.7 % increase) would be produced per SNIa explosion as compared to what is predicted by the Nomoto et al. (1997) solar metallicity W7 model. The SNIa Leung & Nomoto (2018) W7 models for lower metallicities produce slightly more Fe than even the Leung & Nomoto (2018) W7 solar metallicity SNIa models (representing an $\approx$ 18.6 % increase as compared to our default Nomoto et al. (1997) W7 model for the Z=0.1 $Z_{\odot}$ W7 models from Leung & Nomoto (2018)). We expect that for the simulations that we show in this chapter, this would result in a relatively small increase in [Fe/H] after the onset of SNIa of up to a few hundredths of a dex and that the decline in [Mg/Fe] could also be more slightly more pronounced. This would not significantly impact the results we present in this chapter or Chapter 3.

For this work, all the abundance ratios are calculated using the Lodders et al. (2009) solar abundance scale.

2.2.4 Type Ia Supernova Delay-Time Distribution

Type Ia supernovae (SNIa) are produced by a stellar generation at a rate characterized by the SNIa delay-time distribution (DTD). We adopt the power-law SNIa DTD from Maoz & Mannucci (2012) (c.f. Weinberg et al. 2017; Heringer et al.

2019, for other descriptions and implementations of the SNIa DTD), of the form:

$$\Phi(t) = \begin{cases} 0 & \text{for } t < \mathrm{t_{DTD}} \\ 4 \times 10^{-13}\ \mathrm{SNyr^{-1}M_{\odot}^{-1}} \left(\frac{t}{1\mathrm{Gyr}} \right)^{-1} & \text{for } t \geq \mathrm{t_{DTD}} \end{cases} \tag{2.4}$$

Since SNIa require at least one white dwarf (WD) progenitor (generally assumed to be a CO WD), and WDs are remnants produced by stars of mass $\mathrm{M_i} \lesssim 8\ \mathrm{M_{\odot}}$ that have lifetimes $\gtrsim$ 40 Myr, the minimum delay-time should be no shorter than $\mathrm{t_{DTD}} \sim 40$ Myr. However, stars with initial masses $5.5\ \mathrm{M_{\odot}} \lesssim \mathrm{M} \lesssim 8\ \mathrm{M_{\odot}}$ likely produce O+Ne WDs (Chen et al. 2014; Doherty et al. 2015) that either do not explode as SNIa, or if they do, are not a dominant channel of SNIa (Marquardt et al. 2015). Therefore, as suggested in Heringer et al. (2017), we assume a fiducial minimum delay-time of $\mathrm{t_{DTD}} = 100$ Myr that corresponds to the approximate lifetime of 5.5 $\mathrm{M_{\odot}}$ stars. As discussed in Weinberg et al. (2017), a longer minimum delay-time could also be justified in order to account for the time needed for the SNIa ejecta to cool and be reincorporated into the gas reservoir. We explore the effect of changing $\mathrm{t_{DTD}}$ on the Galactic chemical evolution in Section 2.4.3.2.

A limitation of using an SNIa DTD that is a fit to observed SNIa rates, as is the case for Maoz & Mannucci (2012), rather than one that is derived theoretically, is that we cannot easily account for the change in the SNIa rate due to changes in the IMF. We therefore do not attempt to quantitatively correct for this and instead mention the qualitative implications when relevant. Additionally, we do not account for how initial stellar metallicity could affect the SNIa rate. This might have an important impact on

the chemical evolution of a galaxy for which we do not account.

2.2.5 Outflow Prescription

The standard "bathtub" model representation of galaxy evolution (Bouché et al. 2010; Davé et al. 2011; Krumholz & Dekel 2012; Lilly et al. 2013; Andrews et al. 2017) assumes that the mass removed from the gas reservoir in outflows is proportional to the star formation rate, $M_{\rm out}(t) = \eta \times \Psi(t)$, where the constant of proportionality, η, is known as the mass loading factor. Though this dependence on the SFR is mathematically convenient and observationally motivated (Martin 1999, 2005; Rupke et al. 2005; Martin et al. 2012), it implicitly assumes that SNIa — especially SNIa with longer delay times — do not drive outflows. As an alternative to this classic outflow parametrization, we assume that galactic outflows are driven by either momentum or energy imparted by supernovae and that $M_{\rm out}(t)$ is therefore proportional to the mass ejected by SNe, $M_{\rm SN,ej}(t)$. This results in a more physically-motivated outflow implementation that also accounts for SNIa-driven winds and allows us to separately track the contribution of CCSN and SNIa to the outflow mass and metallicity:

$$M_{\rm out}(t) = \epsilon_{\rm out} \times M_{\rm SN,ej}(t) \tag{2.5}$$

where the total SN ejecta mass at a given time is the sum of the ejecta mass returned by CCSN and SNIa:

$$M_{\rm SN,ej}(t) = M^{\rm CCSN}_{\rm SN,ej}(t) + M^{\rm SNIa}_{\rm SN,ej}(t). \tag{2.6}$$

The contribution of SNIa to galactic outflows is particularly important at later

times when the current star-formation rate is low and the classic bathtub model would predict hardly any outflows. In reality, more significant outflows might still be driven by longer delay-time SNIa from stellar generations that were born when the star-formation rate was high. It may also be more realistic to allow $\epsilon_{\rm out}$ to vary with time to reflect possible changes in the properties of the ISM (such as density), we have not yet implemented this functionality.

Although it is usually assumed that the outflow metallicity is simply the metallicity of the ISM, this may not be the case. In order to separately track all elements self-consistently, without assuming all the metals are in solar ratios, we decompose the outflow into a combination of enriched gas from the SN ejecta and unenhanced gas from the ISM such that:

$$M_{\rm out}(t) = M_{\rm ISM}(t) + M_{\rm enriched}(t) \tag{2.7}$$

and

$$M_{\rm enriched}(t) = f_{\rm SN} \times M_{\rm SN,ej}(t) \tag{2.8}$$

where $f_{\rm SN}$ is the fraction of the supernova ejecta that is swept up in the outflow. Therefore, $f_{\rm SN} = 0$ corresponds to an outflow that is purely ISM while $f_{\rm SN} = 1$ implies a maximally enriched outflow where the entire SN ejecta is removed in the outflow and thus, the SN ejecta does not contribute to the chemical enrichment of the ISM. [7]

[7] Note that Dalcanton (2007) parametrizes the outflow enrichment as $x = Z_{\rm out} \,/\, Z_{\rm ISM}$ (which we will refer to as $f_{\rm entrain}$ to avoid confusion) and assumes that a mass fraction ϵ of the wind is entrained gas from the ISM. Our two outflow parameters $\epsilon_{\rm out}$ and $f_{\rm SN}$ are related to $f_{\rm entrain}$ as follows: $f_{\rm entrain} = 1 - \frac{f_{\rm SN}}{\epsilon_{\rm out}}$.

2.2.6 Inflow Prescription

To account for the cold gas accreted onto our simulated galaxies (see Anglés-Alcázar et al. 2017, and references therein) from sources such as the intergalactic medium (IGM) (e.g., Dekel et al. 2009), gas from other galaxies in wet mergers or tidal stripping (e.g., Lin et al. 2008; Perez et al. 2011), or even cooled gas that was previously expelled from the galaxy as outflows (i.e., wind-recycling: Oppenheimer et al. 2010) we must include an inflow prescription. We adopt a linear-exponential functional form that mirrors that of our star-formation history and is commonly adopted in other GCEM (e.g., Yoshii et al. 1996; Kobayashi et al. 2006; Andrews et al. 2017):

$$\mathrm{M_{in}(t) = I_0 te^{\left(-t/\tau_{in}\right)}} \tag{2.9}$$

where $\tau_{\rm in}$ is the inflow timescale. The inflow mass is normalized to produce the user-specified final gas fraction, $f_{\rm gas,f}$. In this work, we define the galaxy's gas fraction as:

$$f_{\rm gas}(t) \equiv \frac{M_{\rm gas}(t)}{M_{\rm tot}(t)} \tag{2.10}$$

where $M_{\rm gas}(t)$ is the gas mass and $M_{\rm tot}(t)$ is the total mass of the galaxy at a given time t (where $M_{\rm tot}(t) = M_{\rm star}(t) + M_{\rm rem}(t) + M_{\rm gas}(t) + M_{\rm in}(t) - M_{\rm out}(t)$). Thus, the final gas fraction is simply

$$f_{\rm gas,f} \equiv \frac{M_{\rm gas}(t = \mathrm{T_{gal}})}{M_{\rm tot}(t = \mathrm{T_{gal}})} \equiv \frac{M_{\rm gas,f}}{M_{\rm tot,f}}. \tag{2.11}$$

The final gas mass, $M_{\rm gas,f}$, can be rewritten in terms of gas source and sink terms as:

$$M_{\rm gas,f} = M_{\rm gas,0} + M_{\rm in,tot} + M_{\rm ret,tot} - M_{\rm out,tot} - \int_0^{\rm T_{gal}} \Psi(t)dt \tag{2.12}$$

where $M_{\rm gas,0} \equiv M_{\rm gas}(t=0)$ is the initial gas mass, $M_{\rm in,tot} = \int_0^{\rm T_{gal}} M_{\rm in}(t)dt$ is the total inflow mass, $M_{\rm ret,tot}$ is the total gas returned from dying stars, $M_{\rm out,tot}$ is the total outflow mass, and the last term is the total gas mass that was converted into stars. Similarly, the total final galaxy mass, $M_{\rm tot,f}$, is simply the starting mass of the galaxy, which is assumed to initially be just gas, plus the difference between the total gas mass that enters the galaxy as inflows and the mass that is lost via outflows:

$$M_{\rm tot,f} = M_{\rm gas,0} + M_{\rm in,tot} - M_{\rm out,tot} \tag{2.13}$$

Using these expanded expressions in the definition of $f_{\rm gas,f}$ and solving for the total inflow mass, we find:

$$M_{\rm in,tot} = (M_{\rm out,tot} - M_{\rm gas,0}) + \frac{\int_0^{\rm T_{gal}} \Psi(t)dt - M_{\rm ret,tot}}{(1 - f_{\rm gas,f})} \tag{2.14}$$

Additionally, we require that at every time-step, there is always enough reservoir gas to remove the current outflow mass (driven by SNe from older stellar generations) and to form the precalculated stellar generation mass. For a given combination of star-formation history, IMF-weighted yields, inflow timescale, outflow parameters, and $f_{\rm gas,f}$, this places a constraint on the minimum $M_{\rm gas,0}$ that can sustain the simulated galaxy.

Assuming the provided initial gas mass is large enough to avoid premature gas depletion, the inflow normalization I_0, which has units of $\mathrm{M}_\odot\ \mathrm{yr}^{-2}$, becomes:

$$I_0 = \frac{1}{\int_0^{\mathrm{T_{gal}}} te^{\left(-t/\tau_{\mathrm{in}}\right)} dt} \left[(M_{\mathrm{out,tot}} - M_{\mathrm{gas,0}}) + \frac{\int_0^{\mathrm{T_{gal}}} \Psi(t) dt - M_{\mathrm{ret,tot}}}{(1 - f_{\mathrm{gas,f}})} \right] \tag{2.15}$$

$M_{\mathrm{out,tot}}$ and $M_{\mathrm{ret,tot}}$ depend on the star-formation history (which is predetermined by the final stellar mass and the star-formation timescale) and the IMF-weighted yields, which dictate the gas returns and the mass ejected by SNe. The IMF-weighted yields are metallicity-dependent,and therefore, the exact amount of total outflow mass and total returned gas mass for a simulated galaxy will depend on its gas enrichment history. Since the inflow normalization is calculated prior to running the simulation and thus, prior to knowing the precise evolution of the gas metallicity, we must pick a yield table metallicity with which to estimate $M_{\mathrm{out,tot}}$ and $M_{\mathrm{ret,tot}}$. This can result in a final gas fraction for the simulated galaxy that differs slightly from the initially inputted $f_{\mathrm{gas,f}}$. For instance, choosing a lower metallicity for the yield tables will tend to underestimate the gas returns, leading to a higher than intended final gas fraction.

As discussed above, our inflow prescription can represent cold gas accreted from sources besides the IGM. Reaccretion of previously expelled outflows or gas added during a wet merger could result in inflow that is significantly enriched, unlike the pristine abundance inflows that are typically assumed by Galactic chemical evolution models (e.g., Matteucci & Greggio 1986; Kobayashi et al. 2006; Pagel 2009). In our implementation, the metallicity of the inflowing gas is controlled by the parameter Z_{in} and the ratios of the different elements are set according to the metal ratios of the IMF-

weighted Kobayashi et al. (2006) CCSN yields for the yield table whose metallicity (Z=0, Z=0.001, Z=0.004, and Z=$Z_{\odot}$) is closest to $Z_{\rm in}$. We assume a primordial abundance of X=0.75, Y=0.25, and Z=0, and when Z>0, the additional metal mass fraction is removed from the hydrogen mass fraction.

2.2.7 Equations governing the chemical evolution of our galaxy models (Evolution Equations)

At the beginning of the simulation, the gas reservoir is initialized with a gas mass of $\rm M_{gas,0}$, that is generally assumed to be pristine (though this can be modified if desired). Each time-step i, starts at time t[i] and ends at $t[i]+t_{\rm step}$, with the simulation being run until t =$\rm T_{gal}$, such that $t[i=0]=0$ and the total number of time-steps is $N_{\rm step}=\dfrac{\rm T_{gal}}{t_{\rm step}}$.

At the beginning of each time-step i, some amount of infalling cold gas, denoted as I[i] in Equation 2.16, is added to the gas reservoir according to the inflow prescription described in Section 2.2.6. Note that $I[i]=\int_{t[i]}^{t[i+1]} M_{\rm in}(t)dt$, where $M_{\rm in}(t)$ is the inflow mass at time t, as defined by Equation 2.9. As a default, the inflows are assumed to be nearly pristine, but the metallicity of the inflows, $\rm Z_{in}$, can be varied, and the effect of enriched inflows is explored in Section 2.4.3.2.

In addition, enriched gas is returned to the gas reservoir as stars die off and SNIa go off. The fraction of each generation of stars that die off as a function of time is set by a combination of the IMF (which determines how the generation mass is distributed among stars of different masses) and the lifetimes of stars as a function of stellar mass. A portion of this stellar mass will be locked away in the form of remnants

(as determined by the yield tables or the IFMR; see Section 2.2.3) while the rest will be returned as gas to the reservoir (denoted $R^*[i]$). These stellar gas returns will generally be a combination of CCSN yields from recent star formation, AGB yields from older stellar generations, and may also include winds from high mass stars ($\geq$ 8 $M_\odot$) and, at very late times, winds from passively evolving low mass stars ($<$ 1 $M_\odot$). Note that these two wind contributions will be returned with element abundances that match those of the gas from which they formed. The other gas return component comes from SNIa. The number of SNIa produced by each stellar generation as a function of time is dictated by the SNIa delay-time distribution described in Section 2.2.4 and the total number of SNIa that go off in a time-step is

$$N^{\mathrm{SNIa}}[i] = \sum_{j=0}^{t} S[j] \times \Phi[i-j]$$

where $S[j]$ is the mass of the stellar generation formed at time-step j, $i-j$ represents the number of time-steps since this stellar generation was formed (where $t[i-j]$ is the age of the stellar generation), and $\Phi[i-j] = \int_{t[i-j]}^{t[i-j+1]} \Phi(t)dt$ is the number of SNIa per stellar mass formed, produced this time-step by the stellar generation formed at time-step j.

Since each SNIa has the same mass, $\mathrm{m}^{\mathrm{SNIa}}$, the SNIa contribution to the gas mass return is $R^{\mathrm{SNIa}}[i] = N^{\mathrm{SNIa}}[i] \times \mathrm{m}^{\mathrm{SNIa}}$. The total return gas for each time-step is denoted $R[i]$ in Equation 2.16, where $R[i] = R^*[i] + R^{\mathrm{SNIa}}[i]$ and the returned gas mass of a particular element, elem, is denoted $R_{\mathrm{elem}}[i]$, such that $R[i] = \sum_{\mathrm{elem}} R_{\mathrm{elem}}[i]$.

Once inflows have occurred and stars have died off, the CCSN and SNIa pro-

duced that time-step drive outflows, as described by the equations provided in Section 2.2.5. Thus, the outflow mass for time-step i, is $O[i] = \epsilon_{\rm out} \times (R^{\rm CCSN}[i] + R^{\rm SNIa}[i])$, where $R^{\rm CCSN}[i]$ is the mass ejected by CCSN this time-step and $\epsilon_{\rm out}$ is our outflow parameter (see Equation 2.5 and note that $M_{\rm SN,ej}[i] = R^{\rm CCSN}[i] + R^{\rm SNIa}[i]$). If $f_{\rm SN} = 0$, then the composition of these outflows will match that of the gas reservoir (see Section 2.2.5).

Finally, a new stellar generation is formed out of the reservoir gas, according to the SFH (see Section 2.2.1). Therefore, the mass of this stellar generation, is $S[i] = \int_{t[i]}^{t[i+1]} \Psi(t)dt$, where $\Psi(t)$ is the star formation rate, as defined in Equation 2.1. The abundance patterns for a stellar generation will match those of the gas from which the stars are formed.

2.2.7.1 Gas reservoir mass at the end of each time-step

If we denote the gas reservoir mass at the end of time-step i, as $G[i]$, then:

$$G[i] = G[i-1] + I[i] + R[i] - O[i] - S[i] \tag{2.16}$$

2.2.7.2 Gas reservoir mass of element, elem, at the end of each time-step

We will denote the mass fraction of each element in the gas reservoir as $Z_{\rm elem}$. Note that for the sake of clarity, we will use this notation for H and He, such that the hydrogen mass fraction $X = Z_{\rm H}$ and the helium mass fraction is $Y = Z_{\rm He}$.

Therefore, the gas mass of a particular element, elem, at the end of time-step

i, denoted $G_{\rm elem}[i]$, can be defined as:

$$G_{\rm elem}[i] = G_{\rm elem}[i-1] + I_{\rm elem}[i] + R_{\rm elem}[i] - O_{\rm elem}[i] - S_{\rm elem}[i] \tag{2.17}$$

where, $R_{\rm elem}[i]$ is the gas return mass of elem, $I_{\rm elem}[i]$ is the element inflow mass, $S_{\rm elem}[i]$ is the gas mass of element, elem, that goes into forming this time-step's stellar generation, and $O_{\rm elem}[i]$ is the element gas mass that gets removed as a result of outflows.

2.2.7.3 The expanded gas reservoir mass equation for $f_{\rm SN} = 0$

When $f_{\rm SN} = 0$, the outflow gas and stars formed will both have the same composition as the gas reservoir, such that $O_{\rm elem}[i] = O[i] \times Z_{\rm elem}[i]$ and $S_{\rm elem}[i] = S[i] \times Z_{\rm elem}[i]$, where the element gas mass fraction is defined as:

$$Z_{\rm elem}[i] \equiv \frac{G_{\rm elem}(\text{right before outflows})}{G(\text{right before outflows})} = \frac{G_{\rm elem}[i-1] + I_{\rm elem}[i] + R_{\rm elem}[i]}{G[i-1] + I[i] + R[i]} \tag{2.18}$$

Thus, for $f_{\rm SN} = 0$, we can rewrite Equation 2.17 as:

$$\begin{aligned} G_{\rm elem}[i] &= G_{\rm elem}[i-1] + I_{\rm elem}[i] + R_{\rm elem}[i] - Z_{\rm elem} \times (O[i] + S[i]) \\ &= (G_{\rm elem}[i-1] + I_{\rm elem}[i] + R_{\rm elem}[i]) \left(1 - \frac{O[i] + S[i]}{G[i-1] + I[i] + R[i]}\right) \end{aligned} \tag{2.19}$$

Using the standard definition of star formation efficiency,

$$\epsilon_{\rm SF}[i] \equiv \frac{\rm SFR}{\text{Gas Mass}} = \frac{S[i]}{G[i-1] + I[i] + R[i]} \tag{2.20}$$

and defining an analogous outflow efficiency,

$$\psi_{\rm out}[i] \equiv \frac{\text{Outflow Mass}}{\text{Gas Mass}} = \frac{O[i]}{G[i-1] + I[i] + R[i]} \tag{2.21}$$

Equation 2.19 becomes:

$$\begin{aligned} G_{\rm elem}[i] &= (G_{\rm elem}[i-1] + I_{\rm elem}[i] + R_{\rm elem}[i]) \times (1 - \epsilon_{\rm SF[i]} - \psi_{\rm out}[i]) \\ &= (G_{\rm elem}[i-1] + R_{\rm elem,eff}[i]) \times (1 - \epsilon_{\rm rm}) \end{aligned} \tag{2.22}$$

Here, $R_{\rm elem,eff}[i] \equiv I_{\rm elem}[i] + R_{\rm elem}[i]$, which we refer to as the "effective gas return" for elem (at time-step i). Similarly, we define the "gas removal efficiency" (at time-step i) as:

$$\epsilon_{\rm rm}[i] \equiv \epsilon_{\rm SF}[i] + \psi_{\rm out}[i] = \frac{O[i] + S[i]}{G[i-1] + I[i] + R[i]} \tag{2.23}$$

Note that for the standard prescriptions for the star-formation rate and outflow rate that are generally adopted by traditional "bathtub" models, the gas removal efficiency becomes $\epsilon_{\rm rm} = \epsilon_{\rm SF}(1 + \eta)$, where η is the mass loading factor, defined such that $O[i] = \eta \times S[i]$. Since the star-formation efficiency and the mass loading factor are assumed to be constant throughout the simulation, the $(1 - \epsilon_{\rm rm})$ term in Equation 2.22 must also be constant with time.

2.2.7.4 The expanded gas reservoir mass equation for $f_{\rm SN} \neq 0$

If $f_{\rm SN} \neq 0$, then

$$G_{\rm elem}[i] = G_{\rm elem}[i-1] + I_{\rm elem}[i] + R_{\rm elem}[i] - f_{\rm SN}\left(R^{\rm CCSN}_{\rm elem}[i] + R^{\rm SNIa}_{\rm elem}[i]\right) \\ - Z_{\rm elem}\left(\left(O[i] - f_{\rm SN}\left(R^{\rm CCSN}[i] + R^{\rm SNIa}[i]\right)\right) + S[i]\right) \quad (2.24)$$

where $O^{\rm ISM}[i] = \left(O[i] - f_{\rm SN}\left(R^{\rm CCSN}[i] + R^{\rm SNIa}[i]\right)\right)$ is the ISM mass that is entrained by the SNe and removed as outflows this time-step. Note that this is just a retranscription of Equation 2.7, where $\rm M_{out}$ is O[i], $\rm M_{ISM}$ is equivalent to $O^{\rm ISM}[i]$ and $M_{\rm SN,ej}[i] = R^{\rm CCSN}[i] + R^{\rm SNIa}[i]$ such that $M_{\rm enrich}[i] = M_{\rm SN,ej}[i] \times f_{\rm SN} = f_{\rm SN}\left(R^{\rm CCSN}[i] + R^{\rm SNIa}[i]\right)$).

Using $O[i] = \epsilon_{\rm out} \times \left(R^{\rm CCSN}[i] + R^{\rm SNIa}[i]\right)$ from Equation 2.5, we can rewrite Equation 2.24 as:

$$G_{\rm elem}[i] = G_{\rm elem}[i-1] + I_{\rm elem}[i] + R_{\rm elem}[i] - f_{\rm SN}\left(R^{\rm CCSN}_{\rm elem}[i] + R^{\rm SNIa}_{\rm elem}[i]\right) \\ - Z_{\rm elem}\left(\left(\epsilon_{\rm out} - f_{\rm SN}\right)\left(R^{\rm CCSN}[i] + R^{\rm SNIa}[i]\right) + S[i]\right) \quad (2.25)$$

Here, the element mass fraction is defined slightly differently, as:

$$\begin{aligned} Z_{\rm elem}[i] &\equiv \frac{G_{\rm elem}(\text{right before outflows})}{G(\text{right before outflows})} \\ &= \frac{G_{\rm elem}[i-1] + I_{\rm elem}[i] + \left(R_{\rm elem}[i] - f_{\rm SN}\left(R^{\rm CCSN}_{\rm elem}[i] + R^{\rm SNIa}_{\rm elem}[i]\right)\right)}{G[i-1] + I[i] + \left(R[i] - f_{\rm SN}\left(R^{\rm CCSN}[i] + R^{\rm SNIa}[i]\right)\right)} \end{aligned} \quad (2.26)$$

Using the appropriate star formation efficiency,

$$\epsilon_{\rm SF} \equiv \frac{\rm SFR}{\rm Gas\ Mass} = \frac{S[i]}{G[i-1] + I[i] + (R[i] - f_{\rm SN}\left(R^{\rm CCSN}[i] + R^{\rm SNIa}[i]\right))} \tag{2.27}$$

Equation 2.25 becomes:

$$G_{\rm elem}[i] = \left(G_{\rm elem}[i-1] + I_{\rm elem}[i] + R_{\rm elem}[i] - f_{\rm SN}\left(R^{\rm CCSN}_{\rm elem}[i] + R^{\rm SNIa}_{\rm elem}[i]\right)\right) \left(1 - \epsilon_{\rm SF} - \frac{\left(\epsilon_{\rm out} - f_{\rm SN}\right)\left(R^{\rm CCSN}[i] + R^{\rm SNIa}[i]\right)}{G[i-1] + I[i] + (R[i] - f_{\rm SN}\left(R^{\rm CCSN}[i] + R^{\rm SNIa}[i]\right))}\right) \tag{2.28}$$

2.3 Simulation Suite and Observational Comparison Data

2.3.1 Suite of Galaxy Simulations

We create a suite of simulations to explore how a range of physical processes — and the parameters that characterize them — drive the chemical evolution of a galaxy. Using these simulations, we investigate in Section 2.4 how the galaxy ingredients described in Section 2.2 and the equations presented in Section 2.2.7 influence the observed present-day stellar abundances. Three increasingly-complex galactic chemical evolution scenarios are introduced in Sections 2.4.2.1 (closed box), 2.4.2.2 (inflows-only), and 2.4.2.3 (inflows and outflows). We establish a fiducial simulation for each scenario, which we refer to as the "Closed Box", "Inflows-Only", and "Inflows+Outflows" simulations, respectively. These fiducial simulations are presented in Figure 2.2 and their chosen parameter values are enumerated in Table 2.3.1.

All three simulations are run for 13 Gyrs and assume the same delayed-exponential star formation history (detailed in Section 2.2.1) with a star-formation timescale $\tau_{\rm SF} = 1$Gyr, a standard Kroupa IMF, a final gas fraction $f_{\rm gas,f} = 0.2$ and a final stellar mass $\rm M_{star,f} = 4.3 \times 10^{10} M_{\odot}$. The latter two default values were chosen to reproduce the current estimates of the Milky Way's cold gas fraction and its stellar+remnant mass, $\rm M_{*,f} \approx 5.4 \times 10^{10} M_{\odot}$ (see Bland-Hawthorn & Gerhard 2016, and references therein). The default values for $M_{\rm gas,0}$, $\tau_{\rm SF}$, $\tau_{\rm in}$, and $\epsilon_{\rm out}$ were chosen to allow the model sufficient dynamic range, ensuring that the impact of varying other parameters (as in Section 2.4.3) is not accidentally masked. While these fiducial parameters generally produce chemical evolution tracks (panel (a) of Figure 2.2) that are a decent match to the observed Milky Way stellar abundance data (discussed below in Section 2.3.2), they are distinct from the "best-fit" parameters presented in Section 2.4.4. As we generate our suite of simulations for Section 2.4.3, we modify only one parameter at a time, keeping the others at their fiducial value. The range explored for each parameter in our simulation suite and the figures in which they appear is also provided in Table 2.3.1.

Figure 2.2 *(next page)*: The chemical evolution of the fiducial Closed Box, Inflows-Only, and Inflows+Outflows simulations: (a) [Mg/Fe]–[Fe/H] (b) MDF, (c) [Mg/Fe] evolution, (d) [Fe/H] evolution, (e) $\epsilon_{\rm rm}$ evolution, and (f) gas mass evolution. The red lines correspond to the fiducial Closed Box simulation, the light blue lines to the fiducial Inflows-Only simulation, and the purple line to the fiducial Inflows+Outflows simulation. The colored squares in panel (a) denote the average abundances of each simulation. The gray circles are the Bensby et al. 2014 abundance ratios for the kinematically-selected thick disk stars described in Section 2.3.2. Two gray dashed lines corresponding to [Mg/Fe]=0 and [Fe/H]=0 have been added as visual guides. The Milky-Way MDF for the geometrically-selected thick disk stars at 3kpc $<$ R $<$ 5kpc from Hayden et al. 2015 (detailed in Section 2.3.2) is shown as a comparison as a slate gray dashed line in panel (b). In panels (c) and (d), the solid lines indicate the gas reservoir abundance ratios while the dotted lines indicate the gas return abundance ratios. The gray dot-dashed lines show the onset of SNIa at t = 100 Myr. In panels (e) and (f), the gray dotted lines mark the peak of the star-formation history at $t = \tau_{\rm SF} = 1$ Gyr. N.B.— For ease of comparison, in the figures presented in Section 2.4.3, the relevant fiducial simulation will always be plotted in the same color as is used here.

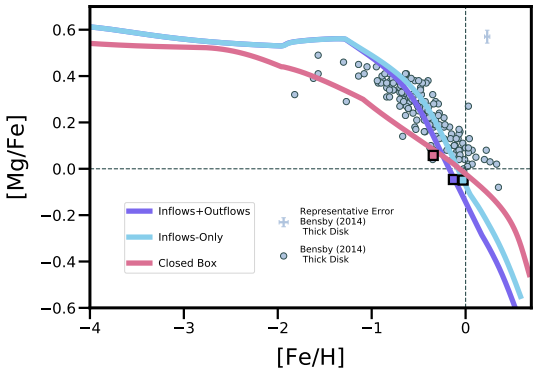

(a) [Mg/Fe]–[Fe/H]

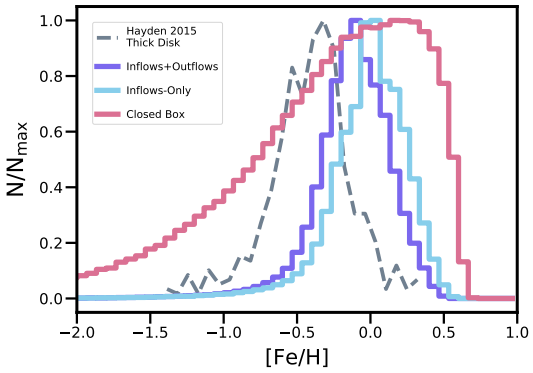

(b) Metallicity Distribution Function

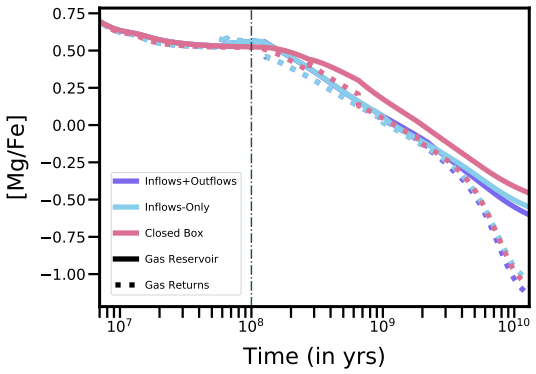

(c) [Mg/Fe] evolution

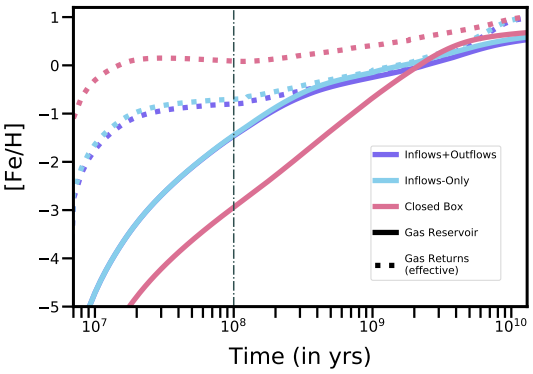

(d) [Fe/H] evolution

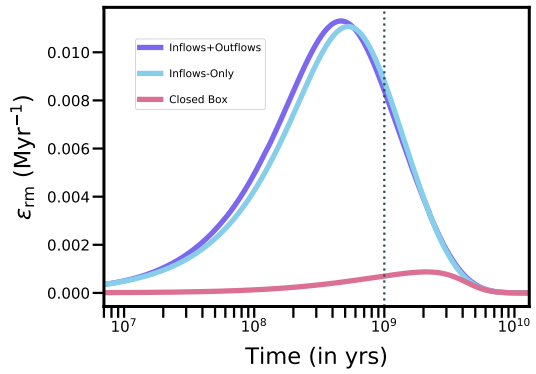

(e) Gas removal efficiency evolution

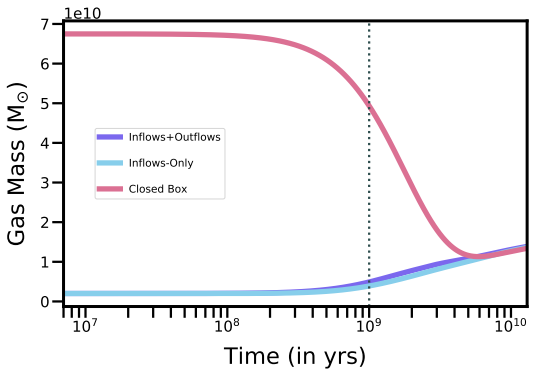

(f) Gas reservoir mass evolution

Figure 2.2: The chemical evolution of the fiducial Closed Box, Inflows-Only, and Inflows+Outflows simulations. See the previous page for the full caption text.

Table 2.3: The fiducial simulation parameters

	Closed Box	**Inflows-Only**	**Inflows+Outflows**	**Figure**	**Parameter Range**
IMF α	Kroupa: 2.3 (high-mass slope) 1.3 (low-mass slope)	Kroupa: 2.3 (high-mass slope) 1.3 (low-mass slope)	Kroupa: 2.3 (high-mass slope) 1.3 (low-mass slope)	Fig. 2.12	Kroupa: 1.8, 2.3, 2.6 Salpeter: 2.35
$\mathbf{M_{star,f}}$	$4.3 \times 10^{10} M_\odot$	$4.3 \times 10^{10} M_\odot$	$4.3 \times 10^{10} M_\odot$		
$\mathbf{M_{*,f}}$	$5.4 \times 10^{10} M_\odot$	$5.4 \times 10^{10} M_\odot$	$5.4 \times 10^{10} M_\odot$		
$\mathbf{M_{gas,0}}$	$6.75 \times 10^{10} M_\odot$	$2 \times 10^{9} M_\odot$	$2 \times 10^{9} M_\odot$	Fig. 2.6	$2 \times 10^{7} M_\odot$ $2 \times 10^{9} M_\odot$ $2 \times 10^{10} M_\odot$
$f_{\mathbf{gas,f}}$	0.2	0.2	0.2	Fig. 2.4 (CB) Fig. 2.5 (Inflows)	Closed Box: 0.05, 0.1, 0.2 Inflows: 0.07, 0.10, 0.2
$\mathbf{t_{DTD}}$	100 Myr	100 Myr	100 Myr	Fig 2.7	50 Myr 100 Myr 200 Myr
$\tau_{\mathbf{SF}}$	1 Gyr	1 Gyr	1 Gyr	Fig 2.13	0.5 Gyr, 1 Gyr, 2 Gyr
$\tau_{\mathbf{in}}$	···	0.9 Gyr	0.9 Gyr	Fig. 2.11	0.1 Gyr, 0.5 Gyr, 0.9 Gyr
$\mathbf{Z_{in}}$	···	10^{-10}	10^{-10}	Fig. 2.8	10^{-10}, 0.001, 0.005, 0.01
$\epsilon_{\mathbf{out}}$	···	···	3	Fig. 2.9	0, 3, 10
$f_{\mathbf{SN}}$	···	···	0	Fig. 2.10	0, 0.25, 0.5

2.3.2 The Milky Way Comparison Data

Traditionally, Galactic chemical evolution models (e.g., Schmidt 1963; Pagel & Patchett 1975; Chiosi 1980; Pagel & Tautvaisiene 1995) have focused on reproducing the abundance patterns of the local solar neighborhood (7kpc $<$ R $<$ 9kpc) since only nearby stars were bright enough to take the high resolution, high signal-to-noise spectra needed for measuring high-precision stellar abundances that could be used to constrain models. It has long been known that stars located at larger distances of $\sim 1-2$ kpc from the Galactic plane (known as the geometrically-defined thick disk, e.g. Yoshii (1982); Gilmore & Reid (1983)) tend to have hotter kinematics, have older ages, and be more metal-poor than stars in the Milky Way thin disk (e.g. Gilmore et al. 1989; Robin et al. 2014; Hayden et al. 2015; Kawata & Chiappini 2016, and references therein). However, it has also become clear in recent years that the Milky Way's disk can be separated into a high-[α/Fe] and low-[α/Fe] component (e.g., Fuhrmann 1998; Prochaska et al. 2000) that, at least in the solar neighborhood, does not simply correspond to the geometric or kinematic thick disk (e.g., Adibekyan et al. 2012; Bensby et al. 2014). For instance, the thick disk in the vicinity of the solar radius (7kpc $<$ R $<$ 9kpc, 1kpc $<$ |z| $<$ 2kpc) has a significant population of low-[α/Fe] stars. Furthermore, the relative proportion of stars in the high-[α/Fe] and low-[α/Fe] populations depends on Galactocentric radius, R, and vertical distance from the Galactic plane, $|z|$, (e.g., Anders et al. 2014; Nidever et al. 2014; Hayden et al. 2015).

More recent chemical evolution studies have found that the low [α/Fe] population cannot be well modeled as a single continuously-forming population with a simple

SFH (like the one assumed in our code). Instead, attempts at explaining the stellar abundance patterns of both the high-[α/Fe] and low-[α/Fe] stars in the solar neighborhood, using chemical evolution models, have required the assumption of a more complex Milky Way accretion history (e.g., the two-infall model Chiappini et al. 1997; Chiappini et al. 2001) or the inclusion of additional dynamical processes (e.g., radial migration Schönrich & Binney 2009). Thus, it is likely that the high-[α/Fe] and low-[α/Fe] disk components were formed differently, perhaps influenced by distinct dynamical processes (Chiappini 2009; Kawata & Chiappini 2016; Mackereth et al. 2019). Since the goal of this work is to validate our chemical evolution code rather than constraining the specific and detailed history of the Milky Way, we will only be considering the high-[α/Fe] sequence for our model comparisons, which is known to be well reproduced by one-zone chemical evolution models like ours.

Nidever et al. (2014) and Hayden et al. (2015) find that the distribution of stars that belong to the high-[α/Fe] sequence in the [α/Fe]-[Fe/H] plane varies very little with Galactocentric radius. Since high-[α/Fe] stars tend to dominate at higher vertical distances from the Galactic plane, we compare our Milky Way simulations to observed stellar abundances of stars at large distances from the plane (i.e., the geometrically selected thick disk). Unfortunately, Nidever et al. (2014) and Hayden et al. (2015) only provide an [α/Fe] that is computed using a complicated global fit to O, Mg, Si, S, Ca, and Ti, which does not directly correspond to the outputs of our simulations. We therefore choose to compare the [Mg/Fe] - [Fe/H] tracks of our models to the thick-disk

stellar abundances measured by Bensby et al. (2014)[8]. In their paper, Bensby et al. (2014) analyzed the high-resolution, high signal-to-noise spectra of 714 F and G dwarf and subgiant stars in the Solar neighborhood. These stars are sorted into thin disk, thick disk, halo, and transition stellar populations according to a kinematical criterion (see Bensby et al. (2003) and Appendix A of Bensby et al. (2014)). Using this criterion, they calculate thick-to-thin disk probability ratios (TD/D) finding that 203 of these stars are at least twice as likely to kinematically belong to thick disk rather than to the thin disk (TD/D$>$ 2). A final cut on the effective temperature is applied to these thick disk candidates to remove stars with high abundance uncertainties ($T_{\rm eff} \lesssim 5400$K).

Our final thick disk subsample from Bensby et al. (2014) contains 156 stars whose abundance ratios are shown as light gray circles in the top panel of Figure 2.3 (as well as in all [Mg/Fe] – [Fe/H] plots in Section 2.4). Since Bensby et al. (2014) intentionally aimed to trace the metal-poor and metal-rich ends of the local thick-disk stellar population, this thick disk subsample covers a wide range of metallicities ($-1.82 \leq$ [Fe/H] ≤ 0.35), enabling these data to provide useful constraints over the majority of the dynamic range of stellar metallicities formed by our galaxy models (i.e. the simulated [Mg/Fe]–[Fe/H] tracks). However, this also results in a complicated selection function, meaning that we cannot use this sample to construct a representative metallicity distribution function (MDF)[9].

[8]The stellar [α/Fe]–[Fe/H] abundance pattern for the Hayden et al. 2015 inner thick disk sample closely resembles that of the Bensby et al. 2014 thick disk sample for [Mg/Fe]–[Fe/H] (shown in the top panel of Figure 2.3). The primary difference is that the [α/Fe] calculated for the stars in the Hayden et al. 2015 sample is slightly lower (by $\sim$ 0.04 dex) than the [Mg/Fe] measured for the stars in the Bensby et al. 2014 sample at a corresponding [Fe/H], particularly at lower metallicities.

[9]Note that we use the terms metallicity distribution function, MDF, and [Fe/H] distribution function interchangeably in this chapter

Instead, we compare our simulations to [Fe/H] distribution function of the geometrically-defined thick disk (1kpc $<$ |z| $<$ 2kpc) from Hayden et al. (2015). Rather than use solar-neighborhood stars (defined here as stars with Galactocentric radii of 7kpc $<$ R $<$ 9kpc), we choose to compare our results to the MDF of the inner most thick disk stars (the stellar bin with 3kpc $<$ R $<$ 5kpc and 1kpc $<$ |z| $<$ 2kpc). This is done for the following reasons:

1. **Contamination of the solar-cylinder by stars born ex-situ:** The dynamical evolution of a galaxy can have important effects on the stellar abundance patterns we see today. For instance, Roškar et al. (2008) suggests that due to the radial-migration of stars resulting from interactions with transient spiral arms (Sellwood & Binney 2002), about 55% of the present-day solar-cylinder stars were born more than 2 kpc away from their current location and that this fraction of contaminants increases with increasing Galactic radius.

   Loebman et al. (2016) argues that the changing skewness of the MDF as a function of radius, seen in Hayden et al. (2015), can be completely explained by radial-migration effects in the context of inside-out Galaxy formation. Remarkably, their simulation also suggests that none of the high-[α/Fe] stars at larger radii were formed in-situ. Instead, the near-uniform MDF of the high-[α/Fe] stars in the geometric thick-disk, observed in Hayden et al. (2015), is due to the entirety of high-[α/Fe] stars forming at small Galactic radii (around 3-4kpc) in a short period of time with a fraction of these stars subsequently radially-migrating to larger radii. Consequently, the inner disk should have the greatest proportion of

high-[α/Fe] stars that formed in-situ and the Hayden et al. (2015) MDF for stars with 3kpc < R < 5kpc and 1kpc < |z| < 2kpc should be the most comparable to our simulations.

2. **Capturing the old, low-metallicity tail:** The low-metallicity tail of the MDF has historically played an important role in constraining the chemical evolution of Milky Way (e.g., the G-dwarf problem, see Pagel 2009). The low-metallicity tail generally corresponds to the oldest stars, formed out of near-pristine/barely enriched gas. Given that galaxies are believed to form inside-out (e.g., Larson 1976; Fall & Efstathiou 1980; Matteucci & Francois 1989; Samland & Gerhard 2003; Dutton et al. 2011; Frankel et al. 2019; Vincenzo & Kobayashi 2020; Bird et al. 2021, and references therein), these old stars are likely to have formed in the inner disk of the Galaxy and are more likely to be properly captured in this region.

3. **Dominance of the high-[α/Fe] stellar population:** Beyond the more theoretical considerations listed above, Figure 4 in Hayden et al. (2015) indicates that the low-[α/Fe] track mostly disappears in the inner disk, particularly for $|z| > 0.5$kpc. As discussed in Freudenburg et al. (2017), the stars within the inner most bin of Hayden et al. (2015) (3kpc < R < 5kpc) have stellar abundance patterns that resemble the expected [α/Fe] – [Fe/H] tracks produced by one-zone chemical evolution models. This reinforces our choice to validate our Milky Way model against the Hayden et al. (2015) MDF for the geometric thick disk at the inner most Galactocentric radii.

The Hayden et al. (2015) MDF for 3kpc $<$ R $<$ 5kpc and 1kpc $<$ |z| $<$ 2kpc is plotted in the bottom panel of Figure 2.3 as the dashed slate gray line[10].

[10]The data to reproduce this MDF were kindly provided by Dr. Michael Hayden.

Figure 2.3 *(next page)*: *Top panel (a)*: The [Mg/Fe] and [Fe/H] abundance ratios, shown as light gray circles, for the subsample of 156 kinematically-selected Milky-Way thick disk stars from Bensby et al. 2014 to which we compare our simulated galaxy [Mg/Fe]–[Fe/H] tracks. The light gray cross in the upper-right corner depicts representative mean error bars for these measurements. Two dashed lines corresponding to [Mg/Fe]= 0 and [Fe/H]= 0 have been added as visual guides. *Bottom panel (b)*: The [Fe/H] distribution function constructed by Hayden et al. 2015 for their geometrically-selected (1kpc $<$ |z| $<$ 2kpc) thick disk Milky-Way stars at 3kpc $<$ R $<$ 5kpc is shown as a slate gray dashed line. For ease of comparison to our simulated galaxy MDFs, the histogram shown here has been normalized to the peak of the distribution (i.e., by the maximum number of stars in a Δ[Fe/H] bin). Additional details about both data sets are provided in the text of Section 2.3.2.

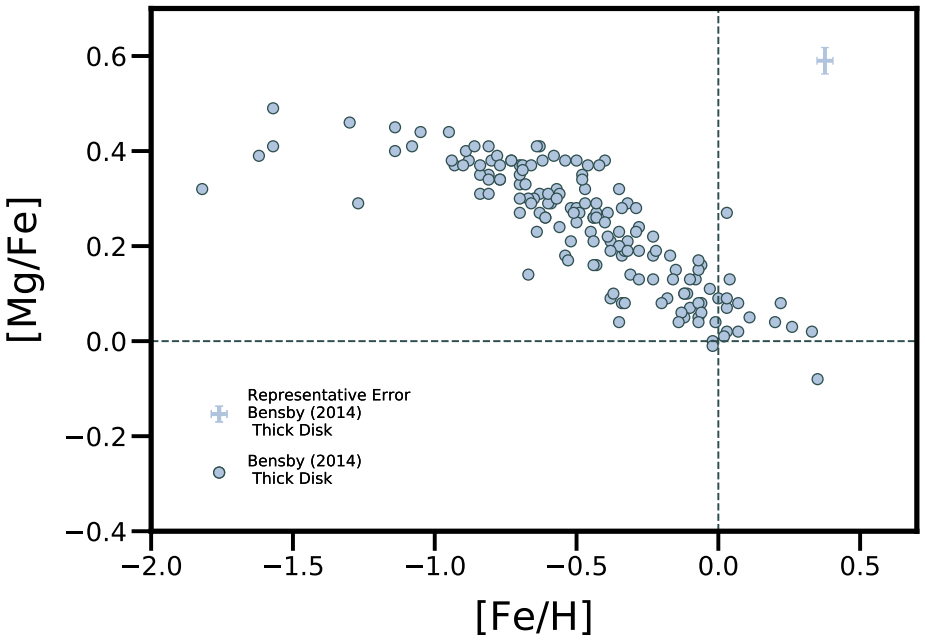

(a) [Mg/Fe]–[Fe/H]

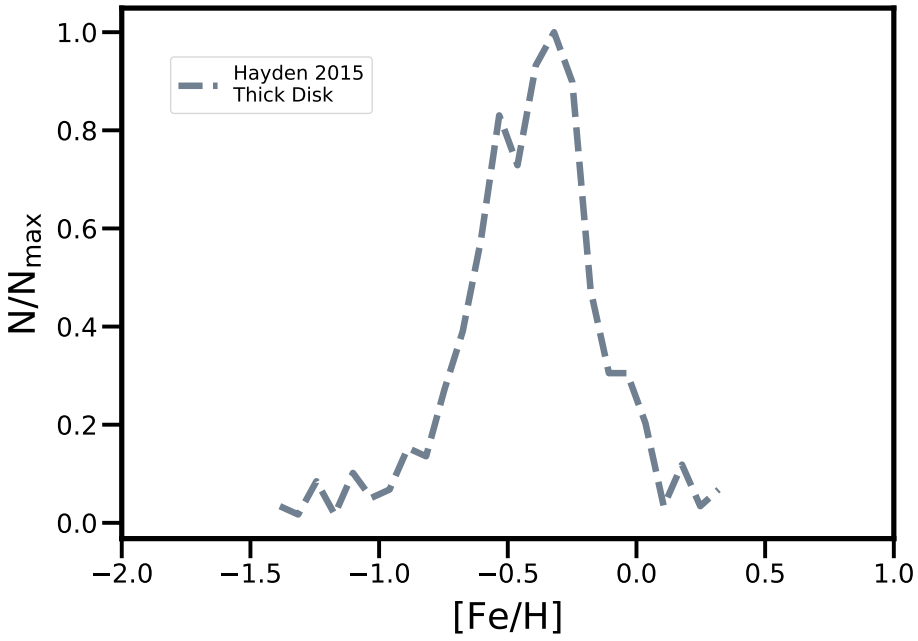

(b) Metallicity Distribution Function

Figure 2.3: The observed Milky-Way thick disk [Mg/Fe]–[Fe/H] stellar abundance ratios (top panel) and metallicity distribution function (bottom panel). See the previous page for the full caption text.

2.4 Results

The low-mass stars in our Galaxy are long-lived and preserve a record of the abundance of the gas from which they were formed. Therefore, in order to explain the observed abundance patterns of stars in the Milky Way and hope to draw inferences regarding the formation and evolution of our Galaxy, it is crucial to understand what physical processes drive the chemical evolution of the gas.

Starting with the simplest model for galaxy evolution, a closed box, we demonstrate in Section 2.4.1 the crucial role played by the star-formation efficiency ($\epsilon_{\rm SF}$) and the stellar and SNIa gas returns in determining the chemical evolution of a galaxy. In Section 2.4.2.1, we use this framework to understand the basic stellar abundance features and properties expected from closed box galaxy evolution before increasing the complexity of our model by including inflows (Section 2.4.2.2) and outflows (Section 2.4.2.3). We find that extending the $\epsilon_{\rm SF}$ and the gas returns to their more generalized forms (i.e. the gas removal efficiency, $\epsilon_{\rm rm}$, and the effective gas returns) allows us to explain why adding inflows and outflows changes the gas abundance as a function of time and how this is reflected in the stellar [Mg/Fe] and [Fe/H] abundances that we observe today.

In Section 2.4.3, we explore how other important galaxy ingredients (and the parameters that characterize them) affect the gas removal efficiency and effective gas returns and thus the chemical evolution as well as how they shape important features in the [Mg/Fe]–[Fe/H] tracks and stellar metallicity distribution function. Finally, in Section 2.4.4 we validate our chemical evolution model by presenting two simulations

that produce a reasonable match to the observed Milky Way stellar [Mg/Fe]–[Fe/H] abundances and metallicity distribution function from Section 2.3.2. Our "best-fit" Milky Way simulations are shown in Figure 2.4.4 and the corresponding simulation parameter values are provided in Table 2.4.4.

2.4.1 A simple framework for gauging the impact of a physical process on the gas chemical evolution

The most general form of our gas enrichment equations is presented in Section 2.2.7. However, in order to build the reader's intuition, we begin by contextualizing them in the case of the simplest galactic chemical evolution scenario: a closed box model (see Section 2.4.2.1). In subsequent sections, we expand our framework to include inflows and outflows.

In the absence of inflows and outflows, we can describe the chemical evolution of our model galaxy using simplified forms of the equations from Section 2.2.7. Equation 2.16 for the gas reservoir mass at the end of time-step i, becomes

$$G[i] = G[i-1] + R[i] - S[i] \tag{2.29}$$

and the gas reservoir mass of a given element (see Equation 2.19) reduces to:

$$
\begin{aligned}
G_{\mathrm{elem}}[i] &= G_{\mathrm{elem}}[i-1] + R_{\mathrm{elem}}[i] - Z_{\mathrm{elem}} \times S[i] \\
&= \left(G_{\mathrm{elem}}[i-1] + R_{\mathrm{elem}}[i]\right)\left(1 - \frac{S[i]}{G[i-1] + R[i]}\right) \\
&= \left(G_{\mathrm{elem}}[i-1] + R_{\mathrm{elem}}[i]\right)\left(1 - \epsilon_{\mathrm{SF}}[i]\right)
\end{aligned} \tag{2.30}
$$

where $\epsilon_{\mathrm{SF}}[i] = \dfrac{S[i]}{G[i-1] + R[i]}$.

From Equation 2.30, it is clear that in order for a physical process or parameter to affect G_{elem}, it must either change the mass of that element in the gas returns, R_{elem}, or it must impact the galaxy's star formation efficiency, ϵ_{SF}. The larger the element return mass, the faster the element gas mass will increase. Similarly, the smaller the element mass already present in the gas, the larger the impact of a fixed amount of element return gas.

For a closed box model, the star-formation efficiency can be thought of as the fraction of the gas reservoir that is being removed each time-step, since in the absence of outflows, the gas removal efficiency defined in Section 2.2.7.4 reduces to $\epsilon_{\mathrm{SF}}[i]$. The larger the star-formation efficiency, the less gas remains in the reservoir, and thus, the larger the impact of the element gas return on the current G_{elem}. As $\epsilon_{\mathrm{SF}}[i-1] \rightarrow 1$, $G_{\mathrm{elem}}[i-1] \rightarrow 0$ and consequently, the element gas mass available to form stars approaches $R_{\mathrm{elem}}[i]$. **In a way, the** $(1 - \epsilon_{\mathrm{SF}}[i])$ **term can be thought of as a measure of how much memory the reservoir gas retains of its previous chemical enrichment history.** The smaller the $(1 - \epsilon_{\mathrm{SF}}[i])$ term, the less memory or inertia the system has and the more it will be impacted by the current gas returns (as

opposed to the integrated enrichment from previous gas returns).

Since stellar abundances reflect the element mass fractions of the gas from which they were formed and do not encode anything about the absolute element gas masses, it would behoove us to also look at the time-evolution of element ratios. The ratio of the gas mass of two elements, elem1 and elem2 is:

$$\begin{aligned}\frac{G_{\rm elem1}[i]}{G_{\rm elem2}[i]} &= \frac{\left(G_{\rm elem1}[i-1] + R_{\rm elem1}[i]\right)\left(1-\epsilon_{\rm SF}[i]\right)}{\left(G_{\rm elem2}[i-1] + R_{\rm elem2}[i]\right)\left(1-\epsilon_{\rm SF}[i]\right)} \\ &= \frac{G_{\rm elem1}[i-1] + R_{\rm elem1}[i]}{G_{\rm elem2}[i-1] + R_{\rm elem2}[i]}\end{aligned} \tag{2.31}$$

Though the instantaneous star-formation efficiency term cancels out when looking at the ratio of elements, the impact of $\epsilon_{\rm SF}[i]$ on $\frac{G_{\rm elem1}[i]}{G_{\rm elem2}[i]}$ over time implicitly remains due to its effect on the gas mass and thus on the $G_{\rm elem1}[i-1]$ and $G_{\rm elem2}[i-1]$ terms.

As discussed earlier, the (1-$\epsilon_{\rm SF}[i]$) term is a measure of how reactive or resistant the gas reservoir abundances are to change. In the case of extremely high star-formation efficiency, where nearly all the remaining gas reservoir mass is turned into stars, then $(1-\epsilon_{\rm SF}[i-1]) \rightarrow 0$, $G_{\rm elem1}[i-1] \rightarrow 0$ and $G_{\rm elem2}[i-1] \rightarrow 0$ such that the gas reservoir abundance ratio approaches the abundance ratio of the gas returns: $\frac{G_{\rm elem1}[i]}{G_{\rm elem2}[i]} \rightarrow \frac{R_{\rm elem1}[i]}{R_{\rm elem2}[i]}$. Thus, the higher the star-formation efficiency, the more reactive the system is, and the more quickly or effectively the gas reservoir element ratios approach the gas return element ratios.

For our three particular elements of interest, Mg, Fe, and H, their gas mass as a function of time-step can be written as:

$$G_{\rm Mg}[i] = \left(G_{\rm Mg}[i-1] + R_{\rm Mg}[i]\right)\left(1 - \epsilon_{\rm SF}[i]\right)$$

$$G_{\rm Fe}[i] = \left(G_{\rm Fe}[i-1] + R_{\rm Fe}[i]\right)\left(1 - \epsilon_{\rm SF}[i]\right)$$

$$G_{\rm H}[i] = \left(G_{\rm H}[i-1] + R_{\rm H}[i]\right)\left(1 - \epsilon_{\rm SF}[i]\right)$$

As discussed in Section 2.2.7 and is evident in the plots of the yields in Figure **??**, SNIa produce significant amounts of Fe but negligible amounts of Mg and H. Therefore, $R_{\rm Mg}$ and $R_{\rm H}$ can be considered to have purely stellar origins, such that $R_{\rm Mg} = R^*_{\rm Mg}$ and $R_{\rm H} = R^*_{\rm H}$, while $R_{\rm Fe}$ will be a combination of returns from stars and SNIa ($R_{\rm Fe} = R^*_{\rm Fe} + R^{\rm SNIa}_{\rm Fe}$). Accordingly, the element gas mass equations become:

$$G_{\rm Mg}[i] = \left(G_{\rm Mg}[i-1] + R^*_{\rm Mg}[i]\right)\left(1 - \epsilon_{\rm SF}[i]\right) \tag{2.32}$$

$$G_{\rm Fe}[i] = \left(G_{\rm Fe}[i-1] + \left(R^*_{\rm Fe}[i] + R^{\rm SNIa}_{\rm Fe}[i]\right)\right)\left(1 - \epsilon_{\rm SF}[i]\right) \tag{2.33}$$

$$G_{\rm H}[i] = \left(G_{\rm H}[i-1] + R^*_{\rm H}[i]\right)\left(1 - \epsilon_{\rm SF}[i]\right) \tag{2.34}$$

and the element ratios evolve as

$$\frac{G_{\rm Mg}[i]}{G_{\rm Fe}[i]} = \frac{G_{\rm Mg}[i-1] + R^*_{\rm Mg}[i]}{G_{\rm Fe}[i-1] + R^*_{\rm Fe}[i] + R^{\rm SNIa}_{\rm Fe}[i]} \tag{2.35}$$

$$\frac{G_{\rm Fe}[i]}{G_{\rm H}[i]} = \frac{G_{\rm Fe}[i-1] + R^*_{\rm Fe}[i] + R^{\rm SNIa}_{\rm Fe}[i]}{G_{\rm H}[i-1] + R^*_{\rm H}[i]} \tag{2.36}$$

2.4.1.1 The Abundance Evolution of the Gas Returns

Broadly speaking, the stellar returns per stellar mass formed, $R^{*}_{\rm gen}(t-{\rm t_{gen}})/{\rm M_{\odot}}$, for a generation of stars formed at time $\rm t_{gen}$, are determined by 1) the IMF, which sets the fraction of the generation that will produce CCSN vs AGB stars, vs. low mass stars, 2) the CCSN and AGB yield tables and 3) the lifetime of stars as a function of mass. Similarly, the SNIa returns per stellar mass formed, $R^{\rm SNIa}_{\rm gen}(t-{\rm t_{gen}})/{\rm M_{\odot}}$, for a generation of stars formed at time $\rm t_{gen}$, are set by 1) the SNIa yield table and 2) the SNIa delay-time distribution. Thus, the returns, $R(t)$, will be a convolution of these stellar and SNIa generation returns with the star formation history (which sets the mass and age of each generation).

As discussed in Section 2.2.4, the minimum delay-time, $\rm t_{DTD}$, prior to the onset of SNIa is set primarily by the lifetimes of the most massive stars that produce CO WD remnants. This upper mass limit has a theoretical range of around $5.5\,{\rm M_{\odot}} \lesssim {\rm M_i} \lesssim 8\,{\rm M_{\odot}}$, corresponding to stellar lifetimes (and thus a minimum SNIa delay time) of $\sim 40-100$ Myr. For this work, we assume a fiducial $\rm t_{DTD} = 100$ Myr. In contrast, the most massive stars that result in CCSN can explode much sooner after the formation of the stellar generation, on timescales of ~ 10 Myr. Thus, prior to the onset of SNIa from the first stellar generation (so while the galaxy is less than 100 Myrs old), the gas returns will have a purely stellar origin [11] such that

$$\frac{G_{\rm Mg}}{G_{\rm Fe}}(t<100{\rm Myr}) = \frac{{\rm R^{*}_{Mg}}}{{\rm R^{*}_{Fe}}}({\rm t}) \tag{2.37}$$

[11] Note that in this work, we categorize gas returns that are not from SNIa (i.e., unenriched stellar winds, enriched AGB and super-AGB winds, and enriched CCSN ejecta) as having a "stellar origin".

The return ratio is primarily set by the stellar IMF-weighted yields, particularly the CCSN yield tables. The exact shape of [Mg/Fe] for the returns at very early times will reflect minute details of the yield tables, like the fact that the CCSN yields for the most massive stars produce returns with higher [Mg/Fe] than those with lower progenitor masses. Over all, however, the [Mg/Fe] of the returns will be close to constant, appearing as a plateau (whose normalization is set primarily by the CCSN IMF-weighted yields). Then, after the onset of the first SNIa, the contribution of the $R_{\rm Fe}^{\rm SNIa}[i]$ term becomes non-zero.

$$\frac{G_{\rm Mg}[i]}{G_{\rm Fe}[i]} = \frac{R^*_{\rm Mg}[i]}{R^*_{\rm Fe}[i] + R^{\rm SNIa}_{\rm Fe}[i]} \tag{2.38}$$

The power-law shape of the SNIa DTD means that the most SNIa (per solar mass formed) go off promptly as soon as $t > {\rm t_{DTD}}$ (aka as soon as possible). This causes a sudden and significant increase in $R_{\rm Fe}^{\rm SNIa}[i]$ that results in a sharp decline from the plateau in the return [Mg/Fe] that looks a lot like a "knee".

As time progresses, the $R^*_{\rm Mg}[i]$ and $R^*_{\rm Fe}[i]$ components continue to be dominated by recent star formation while $R_{\rm Fe}[i]$ has a growing contribution from older stellar generations. In this regime, [Mg/Fe] decreases steadily and the slope of this leg depends on the exact IMF-weighted stellar yields, the SNIa DTD (and yields), and the shape of the star formation history. Eventually, the gas return mass starts to outpace the mass of gas being formed into stars, marking a transition where star formation stops being significant. Before this point, $R^*_{\rm Mg}[i] = R^{\rm CCSN}_{\rm Mg}[i] + R^{\rm AGB}_{\rm Mg}[i]$, with $R^{\rm CCSN}_{\rm Mg}$ providing a large proportion of (if not the majority of) the Mg stellar returns, $R^*_{\rm Mg}$. After this

point, the contribution from recent star formation to the yields becomes much smaller (and eventually negligible). Thus, as $R_{\rm Mg}$ drops due to the lack of a significant CCSN contribution while $R_{\rm Fe}$ continues to have a steady contribution from SNIa with long delay-times, $\frac{R_{\rm Mg}[i]}{R_{\rm Fe}[i]}$ declines precipitously. The returns eventually reach a new [Mg/Fe] plateau or equilibrium value set by the combination of lower mass IMF-weighted AGB yields and SNIa yields. Note that the equilibrium value reached, for instance, in the fiducial closed box simulation, is higher than the SNIa [Mg/Fe] yields of ~ -1.66. Thus, there must still be a non-negligible contribution from $R^{*}_{\rm Mg}$ to the gas returns even at late times.

The [Fe/H] abundance of the gas returns are shaped by the same processes. The early-time [Fe/H] abundances are dictated primarily by the CCSN IMF-weighted yields. The lower [Fe/H] before 20 Myrs are probably due to significant amounts of H being returned as winds from the highest mass stars. Then, a high [Fe/H] plateau value is set by the CCSN IMF-weighted yields, until the onset of SNIa. At this point, the high amounts of Fe returned by SNIa result in an increase in the [Fe/H] abundance of the returns. After the transition point when returns from recent star-formation stops being significant, the [Fe/H] increases more sharply (as even less H is returned by the stars and more long-delay SNIa keep exploding).

As a general note, we would like to point out that in our implementation of galactic chemical evolution modelling, the star formation history of the galaxy follows a linear-exponential distribution characterized by a star-formation timescale $\tau_{\rm SF}$ and is a predetermined input to the simulation (see Section 2.2.1). Thus, other than small effects

from using metallicity-dependent yield tables, the gas returns are independent of the inflows and outflows. This is in contrast to models that implement a star-formation rate prescription that resembles a Kennicutt-Schmidt law where $\mathrm{SFR}(t) = \epsilon_{\mathrm{SF}} \times \mathrm{M_{gas}(t)}$. In these "bathtub"-like models the inflows and outflows directly shape the star-formation history, and the star formation efficiency is usually assumed to be fixed. We highlight this difference in implementation since it strongly impacts aspects of our framework and interpretation, particularly once we go beyond the closed box model.

2.4.2 Modelling the Chemical Evolution of a Galaxy

2.4.2.1 The Closed Box Model

We have discussed what shapes the time-evolution of the gas return abundances and have built a framework for understanding how these gas returns, along with other physical processes can affect the gas reservoir abundances. In this section, we examine more concretely how these factors play together in the context of a simple chemical evolution model to produce the stellar abundance patterns we can observe today.

One of the simplest descriptions of galaxy evolution is to assume that the galaxy is a closed system, such that it experiences neither inflows nor outflows and its total mass is constant with time. When the galaxy is born, all of its mass is in the form of pristine gas ($\mathrm{M_{gas,0}} = \mathrm{M_{tot}}$). Eventually, some of the gas collapses to form stars and as those stars die off in the form of CCSN, AGB winds, and eventually SNIa, they return enriched gas to the reservoir. As the reservoir gas becomes more highly enriched, so too are the stars that subsequently form. This very basic model for galaxy chemical

evolution is known as the closed box model.

The parameters for our fiducial Closed Box simulation are listed in Table 2.3.1. The time evolution of the gas reservoir [Mg/Fe] and [Fe/H]abundance ratios are shown as red solid lines in Figure 2.2 (c) and (d) respectively, while the gas return abundance ratios appear as red dotted lines.

We notice that the evolution of the gas return abundances look exactly as we predicted in Section 2.4.1.1. However, the evolution of the gas reservoir abundances differs significantly from that of the gas returns. This is due to the $(1 - \epsilon_{\rm SF})$ term in Equation 2.30. Since a closed box simulation must commence with enough gas to fuel the entirety of its star formation history (which is predetermined and an input of our GCEM implementation), the large initial gas mass, $M_{\rm gas,0}$, results in a very low star-formation efficiency, particularly before a majority of the stars have formed and consumed a substantial fraction of the initial gas. This low $\epsilon_{\rm SF}$ means that the gas abundance at any point depends more strongly on its prior enrichment history and is less impacted by the current gas return abundance.

Therefore, as the [Mg/Fe] of the gas returns begins to decline at the onset of SNIa (panel (c) in Figure 2.2), the lower impact of the gas returns due to the low star-formation efficiency results in the gas reservoir [Mg/Fe] abundance ratio decreasing much more slowly than the gas return abundance ratio. As for the effect of a lower $\epsilon_{\rm SF}$ on [Fe/H], the decreased impact of the high [Fe/H] returns will mean that the gas reservoir enriches much more slowly and does not approach the gas returns until the star-formation efficiency peaks (around 2-3 Gyr, as seen in panel (d) of Figure 2.2).

The ϵ_{SF} then decreases again, causing the [Fe/H] of the gas reservoir to plateau at late times.

Consequently, stars are formed at a wide range of [Fe/H], with a significant number of stars formed when the gas has not been substantially enriched. Additionally, the late-time [Fe/H] plateau results in considerable stellar mass being formed when the gas [Fe/H] abundance is at or above solar. Thus, the [Fe/H] distribution function for a Closed Box model is very broad, with a heavy tail at low-metallicities and a peak at a super-solar [Fe/H]. As is evident in Figure 2.2 (b), the MDF generated by a closed box model does a very poor job of reproducing the observed Milky Way MDF, an issue historically known as the G-dwarf problem (van den Bergh 1962; Schmidt 1963).

The slow [Fe/H] enrichment also affects the stellar [Mg/Fe]-[Fe/H] track (shown in Figure 2.2 (a)) since it causes the onset of SNIa to occur when the gas reservoir [Fe/H] is still very low. As a result, the knee in the [Mg/Fe]-[Fe/H] track for the fiducial Closed Box simulation appears shifted far to the left and can even fail to appear if the plotted [Fe/H] range is not big enough. Additionally, the sluggish [Fe/H] enrichment causes the slope of the leg in the [Mg/Fe]-[Fe/H] track to appear much more gradual than the slope of the leg in [Mg/Fe] vs time (panel (c) of Figure 2.2). This is an important reminder that even though [Fe/H] is often thought of as a proxy for time, the enrichment is not linear and this can create strange artifacts in [Mg/Fe]–[Fe/H] that can be misleading.

2.4.2.2 Adding Inflows

The classic solution to the Milky Way G-dwarf problem is to gradually supply a galaxy with pristine inflowing gas (Larson 1972). This allows a galaxy to start

with less gas at birth and slowly build up its mass through inflows. As discussed in the context of a closed box, decreasing $M_{gas,0}$ increases the star-formation efficiency. The higher ϵ_{SF} allows the first generations of stars to more effectively enrich their surrounding gas. Subsequent stellar generations are formed out of more metal-rich gas, eliminating the low-metallicity tail of the MDF that plagued the Closed Box model. To better understand why this happens, we can reexamine our gas evolution equations from Section 2.2.7 in the presence of inflows. With the addition of inflows the gas mass evolution becomes

$$G[i] = G[i-1] + I[i] + R[i] - S[i] \tag{2.39}$$

and the gas chemical evolution equation (Equation 2.19)) reduces to:

$$\begin{aligned} G_{\rm elem}[i] &= G_{\rm elem}[i-1] + I_{\rm elem}[i] + R_{\rm elem}[i] - Z_{\rm elem} \times S[i] \\ &= (G_{\rm elem}[i-1] + I_{\rm elem}[i] + R_{\rm elem}[i]) \left(1 - \frac{S[i]}{G[i-1] + I_{\rm elem}[i] + R[i]}\right) \\ &= (G_{\rm elem}[i-1] + I_{\rm elem}[i] + R_{\rm elem}[i]) \left(1 - \epsilon_{\rm SF}[i]\right) \end{aligned} \tag{2.40}$$

where $\epsilon_{\rm SF}[i] = \dfrac{S[i]}{G[i-1] + I[i] + R[i]}$.

For pristine inflows, which is our default assumption, any metal (elements that are not hydrogen or helium) will have $I_{\rm elem}[i] = 0$. In this case, our gas element mass equations for Mg and Fe look exactly the same as for the closed box model (see Equations 2.32 and 2.33), while the equation for H (Equation 2.34) gains an additional inflow term:

$$G_{\rm Mg}[i] = \left(G_{\rm Mg}[i-1] + R^{*}_{\rm Mg}[i]\right)\left(1 - \epsilon_{\rm SF}[i]\right) \tag{2.41}$$

$$G_{\rm Fe}[i] = \left(G_{\rm Fe}[i-1] + \left(R^{*}_{\rm Fe}[i] + R^{\rm SNIa}_{\rm Fe}[i]\right)\right)\left(1 - \epsilon_{\rm SF}[i]\right) \tag{2.42}$$

$$G_{\rm H}[i] = \left(G_{\rm H}[i-1] + I_{\rm H}[i] + R^{*}_{\rm H}[i]\right)\left(1 - \epsilon_{\rm SF}[i]\right) \tag{2.43}$$

Thus, for $G_{\rm Mg}$ and $G_{\rm Fe}$, inflows only affect the gas abundance evolution though their impact on the star formation efficiency, $\epsilon_{\rm SF}$. However, for $G_{\rm H}$, the inflows directly contribute to the hydrogen gas mass evolution.

As a result, assuming pristine inflows, the element ratio equation for Mg to Fe looks the same as for a closed box.

$$\frac{G_{\rm Mg}[i]}{G_{\rm Fe}[i]} = \frac{G_{\rm Mg}[i-1] + R^{*}_{\rm Mg}[i]}{G_{\rm Fe}[i-1] + R^{*}_{\rm Fe}[i] + R^{\rm SNIa}_{\rm Fe}[i]} \tag{2.44}$$

The inflows implicitly appear in $G_{\rm Mg}[i-1]$ and $G_{\rm Fe}[i-1]$ via the $(1-\epsilon_{\rm SF})$ term. Like in the closed box case, a higher star formation efficiency will increase the impact of the gas returns and more effectively drive $\dfrac{G_{\rm Mg}[i]}{G_{\rm Fe}[i]}$, and thus the gas reservoir [Mg/Fe], to the gas return abundance ratio,

$$\frac{R_{\rm Mg}[i]}{R_{\rm Fe}[i]} = \frac{R^{*}_{\rm Mg}[i]}{R^{*}_{\rm Fe}[i] + R^{\rm SNIa}_{\rm Fe}[i]}. \tag{2.45}$$

The element ratio equation for Fe to H, in the presence of inflows, looks a bit different than its closed box counterpart:

$$\frac{G_{\rm Fe}[i]}{G_{\rm H}[i]} = \frac{G_{\rm Fe}[i-1] + R^{*}_{\rm Fe}[i] + R^{\rm SNIa}_{\rm Fe}[i]}{G_{\rm H}[i-1] + I_{\rm H}[i] + R^{*}_{\rm H}[i]} \tag{2.46}$$

In this case, rather than driving the gas reservoir abundance to the gas return abundance, $\frac{R_{\rm Fe}[i]}{R_{\rm H}[i]}$, a higher star formation efficiency instead drives the gas [Fe/H] abundance to $\frac{R_{\rm Fe}[i]}{I_{\rm H}[i] + R_{\rm H}[i]}$. This can be thought of as the effective Fe/H gas return ratio and is what we use to calculate the effective [Fe/H] gas return abundance ratio plotted as dotted lines in Figure 2.2 (d) as well as in all other [Fe/H] evolution figure subplots where we show simulations that include inflows.

Comparing the fiducial Closed Box and Inflows-Only simulations plotted in Figure 2.2 (shown in red and sky blue respectively), we see from panel (e) that providing the Galaxy with gas when it is actually needed to fuel star formation (as is the case for the Inflows-Only simulation) hugely increases the star formation efficiency at all times until $t_{\rm trans,SF}$. After this point, the Closed Box and Inflow-Only simulations have the same gas mass due to them having the same $f_{\rm gas,f}$ (see panel (f)) and since they also have identical SFHs, they will likewise have the same $\epsilon_{\rm SF}$.

This dramatic increase in $\epsilon_{\rm SF}$ means that for the Inflows-Only simulation, the gas reservoir abundance ratios for [Mg/Fe] and [Fe/H] will much more efficiently be driven to the gas return [Mg/Fe] abundance ratio and effective [Fe/H] gas return abundance ratio, respectively. This is very apparent in Figure 2.2 (c) and (d), where the Inflows-Only gas abundance very quickly approaches the gas return (or effective gas return) abundance ratio and continues to do so until $t_{\rm trans,SF}$. Since the [Mg/Fe] for the gas returns decreases after the onset of SNIa, this means that the gas reservoir [Mg/Fe]

abundance ratio for the Inflows-Only simulation will appreciably decline sooner than for the Closed Box model and will reach a lower [Mg/Fe] by the end of the simulation.

In the plot of the [Fe/H] vs time (panel (d) of Figure 2.2), we notice that for the Inflows-Only simulation, the gas approximately reaches the effective return abundance ratio around 0.3 Gyr (well before the peak of star formation), compared to it taking ≈ 5 Gyr for the Closed Box model (well after the peak of star formation). However, even though the Inflows-Only gas abundance ratio reaches approximately the effective [Fe/H] return abundance ratio very quickly, the continued influx of large amounts of hydrogen later in the simulation prevents the gas from reaching the same level of enrichment at later times as achieved by the fiducial Closed Box simulation. Thus, the [Fe/H] evolution for the Inflows-Only simulation appears to plateau much earlier than for the Closed Box model.

Due to the rapid [Fe/H] enrichment early in the simulation, the onset of SNIa at $t_{DTD} = 100$Myr will correspond to a higher $[Fe/H]_{gas}$. Therefore, the knee in the [Mg/Fe]-[Fe/H] track will appear shifted to the right (toward higher $[Fe/H]_{gas}$) when compared to the knee for the Closed Box simulation. This provides a much better fit to the knee in the observed Milky Way stellar abundance ratios. Additionally, since for the Inflows-Only simulation, $[Fe/H]_{gas}$ starts to plateau shortly after the onset of SNIa, the leg of the [Mg/Fe]–[Fe/H] track will appear to have a much steeper slope. This steeper leg also provides a much better match to the observed Milky Way stellar abundance patterns.

The rapid enrichment when the Galaxy is young, and before many stars have

had the chance to form, also eliminates the low-metallicity tail present in the Closed Box MDF and solves the G-dwarf problem. Additionally, the large amount of hydrogen added by the inflows at late times slows down the [Fe/H] enrichment at late times and suppresses the build-up of high-metallicity stars that caused the Closed Box MDF to peak at super-solar [Fe/H]. This results in a much more narrow MDF for the Inflows-Only fiducial simulation that peaks around solar [Fe/H], as shown in Figure 2.2 (b). Nonetheless, no variation of the key Inflows-Only parameters allows the simulations to peak at the sub-solar [Fe/H] value that would properly reproduce the observed Milky Way MDF, as demonstrated in Section 2.4.3 (specifically panels (a) and (b) of Figures 2.5, 2.6, 2.8, and 2.11). In order to do this, we must include outflows, which we discuss below in Section 2.4.2.3.

2.4.2.3 Including Ouflows

In Section 2.4.2.2, we found that the inclusion of pristine infalling gas can solve the G-dwarf problem, fix the slope of the post-knee leg of the [Mg/Fe] vs [Fe/H] distribution, and produces a much more reasonable narrow metallicity distribution function than the Closed Box model. However, inflows alone fail to reproduce the sub-solar peak of the mass-weighted Milky Way stellar [Fe/H] distribution function.

To address this issue, we include a prescription for gas outflows, as described in Section 2.2.5. Qualitatively, outflows drive metal-enriched gas out of the galaxy while inflows replace it with pristine gas. As with the Inflows-Only model, the lower initial gas mass allows the reservoir gas to rapidly enrich at early times, such that few stars are formed at very low [Fe/H], thus preventing the G-dwarf problem. Unlike the Inflows-

Only model, however, this efficient enrichment is soon curtailed as higher star-formation rates produce greater numbers of CCSN explosions that drive significant outflows of this newly enriched gas. As pristine infalling gas dilutes what is left of the metals, [Fe/H] starts to plateau and evolve much more slowly. This slower [Fe/H] enrichment, while significant amounts of stars are still forming, results in the majority of stars being formed at lower [Fe/H] and therefore produces an MDF that peaks at sub-solar values of [Fe/H].

A more detailed picture of how outflows impact the gas reservoir mass and abundance evolution can be gleaned from the equations introduced in Section 2.2.7. Note that in this section, we will compare our fiducial Inflows-Only and Inflows+Outflows simulations, which were both run with the same SFH, $M_{gas,0}$, and $f_{gas,f}$ (see Section 2.3.1 and Table 2.3.1). This is done primarily for illustrative purposes and the findings that we discuss are often much more general.

For pristine inflows and for outflows where $f_{SN} = 0$ (i.e., when none of the SN ejecta is removed in the outflow before it has a chance of being mixed back into the gas reservoir), Equations 2.19 and 2.22 become:

$$\begin{aligned} G_{Mg}[i] &= (G_{Mg}[i-1] + R^{*}_{Mg}[i]) \left(1 - \frac{O[i] + S[i]}{G[i-1] + I[i] + R[i]}\right) \\ &= (G_{Mg}[i-1] + R^{*}_{Mg}[i]) \left(1 - \epsilon_{SF}[i] - \psi_{out}[i]\right) \end{aligned} \tag{2.47}$$

$$
\begin{aligned}
G_{\mathrm{Fe}}[i] &= \left(G_{\mathrm{Fe}}[i-1] + \left(R^{*}_{\mathrm{Fe}}[i] + R^{\mathrm{SNIa}}_{\mathrm{Fe}}[i]\right)\right)\left(1 - \frac{O[i]+S[i]}{G[i-1]+I[i]+R[i]}\right) \\
&= \left(G_{\mathrm{Fe}}[i-1] + \left(R^{*}_{\mathrm{Fe}}[i] + R^{\mathrm{SNIa}}_{\mathrm{Fe}}[i]\right)\right)\left(1 - \epsilon_{\mathrm{SF}}[i] - \psi_{\mathrm{out}}[i]\right)
\end{aligned}
\tag{2.48}
$$

$$
\begin{aligned}
G_{\mathrm{H}}[i] &= \left(G_{\mathrm{H}}[i-1] + I_{\mathrm{H}}[i] + R^{*}_{\mathrm{H}}[i]\right)\left(1 - \frac{O[i]+S[i]}{G[i-1]+I[i]+R[i]}\right) \\
&= \left(G_{\mathrm{H}}[i-1] + I_{\mathrm{H}}[i] + R^{*}_{\mathrm{H}}[i]\right)\left(1 - \epsilon_{\mathrm{SF}}[i] - \psi_{\mathrm{out}}[i]\right)
\end{aligned}
\tag{2.49}
$$

The gas abundance ratios $\frac{G_{\mathrm{Mg}}[i]}{G_{\mathrm{Fe}}[i]}$ and $\frac{G_{\mathrm{Fe}}[i]}{G_{\mathrm{H}}[i]}$ simplify to the same expressions as in the Inflows-Only case (Equations 2.44 and 2.46 respectively). Like for the Inflows-Only model, the effective returns for Mg and Fe are equal to the actual gas returns (since $I_{\mathrm{Mg}} = I_{\mathrm{Fe}} = 0$), such that

$$
\frac{R_{\mathrm{Mg,eff}}[i]}{R_{\mathrm{Fe,eff}}[i]} = \frac{R_{\mathrm{Mg}}[i]}{R_{\mathrm{Fe}}[i]} = \frac{R_{\mathrm{Mg}^{*}}[i]}{R^{*}_{\mathrm{Fe}}[i] + R^{\mathrm{SNIa}}_{\mathrm{Fe}}[i]} \tag{2.50}
$$

Parallelly, the effective gas returns for H are not the same as the actual hydrogen returns ($R_{\mathrm{H,eff}}[i] \neq R_{\mathrm{H}}[i]$) since the inflows contribute significantly to the gas reservoir hydrogen mass. Thus, the effective Fe to H gas return ratio is

$$
\frac{R_{\mathrm{Fe,eff}}[i]}{R_{\mathrm{H,eff}}[i]} = \frac{R_{\mathrm{Fe}}[i]}{I_{\mathrm{H}}[i] + R_{\mathrm{H}}[i]}. \tag{2.51}
$$

In the case of Inflows+Outflows, the more generalized efficiency term that

appears implicitly in $G_{\rm Mg}[i-1]$, $G_{\rm Fe}[i-1]$, and $G_{\rm H}[i-1]$ is

$$(1-\{\epsilon_{\rm SF}+\psi_{\rm out}\}) = \left(1-\frac{O[i]+S[i]}{G[i-1]+I[i]+R[i]}\right)$$

As mentioned in Section 2.2.7.4, $\epsilon_{\rm rm} \equiv (\epsilon_{\rm SF}+\psi_{\rm out})$ can be thought of as a "gas removal efficiency" that quantifies how efficiently gas is removed from the reservoir by outflows or by being converted into stars. This gas removal efficiency term affects the gas abundance evolution in much the same way as $\epsilon_{\rm SF}$ in the Closed Box and Inflows-Only case, determining how responsive the system is to changes in the effective returns.

Given that the fiducial Inflows-Only and Inflows+Outflows simulations have the same star-formation history, $R[i]$ and $S[i]$ must be the same in both cases (excepting minor differences in $R[i]$ that may arise due to using metallicity-dependent yield tables). Thus, in order for both simulations to have the same $f_{\rm gas,f}$ (while also starting with the same initial gas mass), it is clear from Equation 2.16 that the simulation with outflows must have a greater inflow mass ($I[i]$) to compensate for the gas mass that is lost as outflows ($O[i]$).

Since the inflows are primarily composed of hydrogen, an increase in $I[i]$ results in a commensurate increase in $I_{\rm H}[i]$, which, per Equation 2.51, leads to a lower $\frac{R_{\rm Fe,eff}[i]}{R_{\rm H,eff}[i]}$. This can be seen in Figure 2.2 (d), where the purple dotted line depicting the effective [Fe/H] gas returns for the Inflows+Outflows fiducial simulation is always below that of the Inflows-Only simulation (light blue dotted line). The high gas removal efficiency ($\epsilon_{\rm rm}$), shown in Figure 2.2 (e), of both the Inflows-Only and Inflows+Outflows simulations quickly drives the gas reservoir abundances to the effective gas returns.

Therefore, since the effective [Fe/H] gas return abundance ratio is always lower in the Inflows+Outflows case, so too is the [Fe/H] gas reservoir abundance ratio. This is evident in Figure 2.2 (d), where the gas reservoir [Fe/H] abundance ratio for the Inflows-Only (light blue solid line) and Inflows+Outflows (purple solid line) simulations quickly approach their respective [Fe/H] effective gas return abundance ratios (dotted lines), resulting in a lower gas reservoir [Fe/H] for the Inflows+Outflows simulation.

This is reflected in the MDF shown Figure 2.2 (b). As in the case of the Inflows-Only model, the rapid initial [Fe/H] enrichment enabled by the low $M_{gas,0}$ (as compared to the Closed Box simulation) prevents an excess of stars from being formed at very low-metallicity. The lower $[Fe/H]_{ret,eff}$, that results from the increased influx of pristine gas (that is mostly composed of hydrogen) needed to compensate for the gas that is being removed from the galaxy as outflows, slows the enrichment of the reservoir gas and leads to the majority of stars being born at a lower [Fe/H] than for the Inflows-Only simulation. This slower enrichment of $[Fe/H]_{gas}$ at later times manifests as a narrow MDF whose peak and the high-metallicity edge are shifted to the left, as compared to the Inflows-Only simulation. Our choice of $\epsilon_{out} = 3$ for the fiducial Inflows+Outflows is relatively small so the shift of the peak of the MDF to lower [Fe/H] is not very dramatic. However, it is clear that stronger outflows result in a more sub-solar peak metallicity, which we investigate in more detail in Section 2.4.3.2.

The evolution of [Mg/Fe] as a function of time is very similar for both the Inflows-Only and Inflows+Outflows case, as seen in Figure 2.2 (c). As discussed for Equation 2.50, pristine inflows do not contribute to Mg or Fe, and thus $[Mg/Fe]_{ret,eff}$

= $[\mathrm{Mg/Fe}]_{\mathrm{ret}}$. Since the Inflows-Only and Inflows+Outflows simulations have the same star-formation history, the gas returns should be nearly identical, excepting small differences at late times due to passive returns reflecting slightly different enrichment histories (as discussed above and seen in panels (c) and (d) of Figure 2.2). However, we can see the impact of the gas removal efficiency in the subtle cross-over of $[\mathrm{Mg/Fe}]_{\mathrm{gas}}$ for the Inflows+Outflows (purple solid line) and Inflows-Only simulation (light-blue solid line), as plotted in Figure 2.2 (e). After the peak in ϵ_{rm}, we see that when ϵ_{rm} for the Inflows-Only simulation is higher than for the Inflows+Outflows simulation, the $[\mathrm{Mg/Fe}]_{\mathrm{gas}}$ for the Inflows-Only simulation is more efficiently driven down to the declining $[\mathrm{Mg/Fe}]_{\mathrm{ret}}$, resulting in a lower $[\mathrm{Mg/Fe}]_{\mathrm{gas}}$.

We can now combine the time-evolution of [Mg/Fe] and [Fe/H] (panels (c) and (d) respectively) to understand the [Mg/Fe]–[Fe/H] evolution in Figure 2.2 (a). Since the Inflows-Only and Inflows+Outflows simulations have the same SFH and initial gas mass, the early enrichment (when inflows are pretty minimal) is very similar. Therefore, the "knee" corresponds to the same [Fe/H] for both simulations. However, as the increasing star-formation drives substantial outflows in the Inflows+Outflows model, the additional inflows needed to compensate for the removed gas cause a more gradual $[\mathrm{Fe/H}]_{\mathrm{gas}}$ enrichment and lower final $[\mathrm{Fe/H}]_{\mathrm{gas}}$ at the end of the simulation. This smaller change in $[\mathrm{Fe/H}]_{\mathrm{gas}}$ between the onset of SNIa, which sets the knee, and the end of the simulation results in slightly steeper leg in the [Mg/Fe]–[Fe/H] track that is shifted toward the left.

2.4.2.4 Summary of our Closed Box, Inflows-Only and Inflows+Outflow Results

In Section 2.4.2.1, we find that the knee at low-[Fe/H] and gradual slope of the leg in the [Mg/Fe]–[Fe/H] track as well as the broad, strongly negatively-skewed MDF that are characteristic of the closed box model are a consequence of the low gas removal efficiency. The large initial gas mass needed to fuel the entirety of the star-formation history will result in a very low $\epsilon_{\rm rm}$, particularly at early times when the star-formation rate is also low. The resulting slow initial enrichment of the gas reservoir means that the onset of SNIa, which produces the knee, will correspond to a low $[{\rm Fe/H}]_{\rm gas}$ and that a considerable fraction of the stars will be born while $[{\rm Fe/H}]_{\rm gas}$ remains low, as reflected in the heavier low-metallicity tail of the MDF. Similarly, the low $\epsilon_{\rm rm}$ will also slow the decline in $[{\rm Mg/Fe}]_{\rm gas}$, leading to a more gentle slope of the [Mg/Fe]–[Fe/H] leg.

The inclusion of inflows, as explained in Section 2.4.2.2, remedies the excess production of low-metallicity stars known as the G-dwarf problem. The lower initial gas mass enabled by the addition of inflows greatly increases $\epsilon_{\rm rm}$ and thus the gas reservoir abundances quickly approach the effective gas return abundances. Thus, since $[{\rm Mg/Fe}]_{\rm ret}$ drops quickly after the onset of SNIa, so to will $[{\rm Mg/Fe}]_{\rm gas}$, producing a sharper leg slope in the [Mg/Fe]–[Fe/H]. Likewise, the rapid enrichment at early times shifts the knee to higher [Fe/H] and reduces the number of low-Z stars formed in the galaxy, thus suppressing the low-[Fe/H] tail of the MDF. The effective gas return of hydrogen is also boosted by the pristine inflows, essentially diluting the gas returns and lowering the $[{\rm Fe/H}]_{\rm ret,eff}$ abundance ratio. Therefore, after the initial rapid enrichment

at early times, the $[Fe/H]_{gas}$ evolves more slowly and is prevented from reaching as high of a $[Fe/H]_{gas,f}$. As a result, the MDF for a galaxy with significant inflows will appear much more symmetrical and narrow than for the closed box model. However, the MDF still peaks around a solar metallicity that would not be match to the abundance patterns observed for the Milky Way thick disk.

In Section 2.4.2.3, we establish that in the context of our model implementation, a galaxy that is driving outflows must also have higher inflows, otherwise the gas reservoir would deplete prematurely and the full star-formation history could not be produced. The increased hydrogen mass in the inflows decreases the effective gas return abundance ratio $[Fe/H]_{ret,eff}$, preventing the gas reservoir from enriching as much as in the inflows-only case. Since ϵ_{rm} is relatively high soon after the start of star-formation, the gas reservoir enriches rapidly at early times. Therefore, the knee in [Mg/Fe]–[Fe/H] is unaffected and few stars are formed at very low metallicity such that the low-[Fe/H] tail remains suppressed. However, once the $[Fe/H]_{gas}$ gets closer to $[Fe/H]_{ret,eff}$, the impact of the extra inflow hydrogen is felt, and so the MDF remains narrow but the peak and high-Z edge of the MDF are shifted to lower [Fe/H]. Thus, we find that as outflows remove enriched gas from the reservoir that is replaced by pristine inflows, the galaxy will produce the majority of it stars at lower [Fe/H] than in the inflow-only case, allowing the MDF to have a sub-solar peak.

2.4.3 Varying parameters: How and why individual galaxy ingredients shape the final stellar abundances

In this section, we study the more detailed roles played by individual ingredients in shaping a galaxy's chemical evolution. We go beyond simply the presence or absence of a physical process like inflows and outflows and instead change e.g., the strength, amount, or timing of galaxy ingredients by varying the parameters detailed in Section 2.3.1. We then examine how and why these paramater changes affect $\epsilon_{\rm rm}$ and $R_{\rm gas,eff}$ and result in alterations to the features in the stellar abundance pattern and distribution.

In investigating our 9 parameters, we find that two ($f_{\rm gas,f}$, $\rm M_{gas,0}$) primarily affect the gas removal efficiency, four ($\rm t_{DTD}$, $\rm Z_{in}$, $\epsilon_{\rm out}$, $f_{\rm SN}$) primarily affect the effective gas returns, and three ($\tau_{\rm in}$, the IMF, $\tau_{\rm SF}$) significantly impact both of these terms. Each of these cases and the relevant parameters are discussed below.

2.4.3.1 Parameters that primarily affect the gas removal efficiency, $\epsilon_{\rm rm}$

The gas removal efficiency, $\epsilon_{\rm rm}$, is defined as the fraction of gas removed from a galaxy's gas reservoir at a given time. In our chemical evolution model, the only processes that can remove gas from the gas reservoir are star formation and outflows. Therefore, for our purposes, $\epsilon_{\rm rm} = \dfrac{\rm SFR + Outflow\ Mass}{\rm Gas\ Mass} = \epsilon_{\rm SF} + \psi_{\rm out}$, where $\epsilon_{\rm SF}$ is the star formation efficiency and $\psi_{\rm out}$ is the outflow efficiency (see Section 2.2.7.3). In the case of a galaxy that evolves as a closed box or that only has inflows, the gas removal efficiency is equivalent to the star formation efficiency (which is defined as

$\epsilon_{\rm SF} \equiv \frac{\rm SFR}{\rm Gas\ Mass}$). As we explained in Section 2.4.1, the $(1 - \epsilon_{\rm rm})$ term is a measure of the gas reservoir's responsiveness to changes in the effective gas returns. The higher the gas removal efficiency, the more effectively and rapidly the gas reservoir abundance ratios are driven to the effective gas return abundance ratios.

Below, we consider how changing the final gas fraction, $f_{\rm gas,f}$, and the initial gas mass, $\rm M_{gas,0}$, of a galaxy affects the gas removal efficiency and why these changes in $\epsilon_{\rm rm}$ give rise to differences in the stellar MDF and [Mg/Fe]–[Fe/H] tracks. Unlike a traditional "bathtub" chemical evolution model that assumes a constant $\epsilon_{\rm SF}$ and a constant outflow mass loading factor, and thus a constant $\epsilon_{\rm rm}$ (see Section 2.2.7.3), our implementation results in a time-dependent $\epsilon_{\rm rm}$. Therefore, as we explore the impacts of galaxy ingredients (and their related parameters) on $\epsilon_{\rm rm}$, it is important to not only consider changes in the magnitude of $\epsilon_{\rm rm}$ but also when in the simulation they occur.

The final gas fraction ($f_{\rm gas,f}$)

Figure 2.4 shows the effect of changing the final gas fraction from our fiducial Closed Box simulation assumption of $f_{\rm gas,f} = 0.2$, incrementally decreasing $f_{\rm gas,f}$ by a factor of 2, down to a minimal value of $f_{\rm gas,f} = 0.05$. The fiducial Closed Box simulation with $f_{\rm gas,f} = 0.2$ is plotted in red, while the dark blue lines and sky blue lines assume $f_{\rm gas,f} = 0.1$ and $f_{\rm gas,f} = 0.05$, respectively, with all other parameters kept the same as for the fiducial simulation (see Table 2.3.1). As is evident from the dotted gas return lines in panels (c) and (d), the gas return evolution for our three simulations is nearly identical. This is expected since the gas returns are determined by a convolution of the star-formation history, SNIa rate, and IMF-weighted yields, which are all held fixed

across the three simulations. Therefore, any changes in the stellar [Mg/Fe]–[Fe/H] tracks and MDFs must stem from the impact of $f_{\rm gas,f}$ on the gas removal efficiency.

At early times, all three simulations have very low $\epsilon_{\rm rm}$, which, as discussed in Section 2.4.2.1, is a consequence of the closed box model having to start with at least enough gas mass to fuel the entirety of its star-formation history. Since $M_{\rm gas,0}$ is so high for all the simulations, differences in $\epsilon_{\rm rm}$ at this point are very small and have negligible effects on the early $[{\rm Mg/Fe}]_{\rm gas}$ and $[{\rm Fe/H}]_{\rm gas}$ evolution. However, as the star-formation rate increases and more of the gas reservoir is converted into stars, these differences become more apparent. A galaxy with a lower final gas fraction must, by definition, have a lower $M_{\rm gas}$ at late times (see panel (f)) which results in a correspondingly higher $\epsilon_{\rm rm}$ that is clearly seen in panel (e).

Since a higher $\epsilon_{\rm rm}$ more effectively drives the gas reservoir abundances to the gas return abundances, the $f_{\rm gas,f} = 0.05$ simulation will have late time gas reservoir abundance ratios that more closely match the gas return abundance ratios, as shown in panels (c) and (d). This more effective enrichment of the gas reservoir by the gas returns, results in $[{\rm Fe/H}]_{\rm gas}$ nearly reaching $[{\rm Fe/H}]_{\rm ret}$ before it starts to plateau when $\epsilon_{\rm rm}$ decreases again around $t=t_{\rm transSF}$. As compared to the fiducial Closed Box simulation, the $f_{\rm gas,f} = 0.05$ simulation will reach a significantly higher $[{\rm Fe/H}]_{\rm gas}$ at $t= T_{\rm gal}$ and produce a slightly shorter and steeper $[{\rm Fe/H}]_{\rm gas}$ plateau at late times. This manifests in [Mg/Fe]–[Fe/H] as a slightly more gradually-sloped leg that extends to higher [Fe/H]. Due to the faster $[{\rm Fe/H}]_{\rm gas}$ enrichment, more stars will be born at higher metallicity, which extends the right edge of the MDF and shifts the average stellar metallicity to

higher [Fe/H].

To verify that the role of an ingredient is consistent across galaxy evolution models, we also look at $f_{\mathrm{gas,f}}$ in the context an inflows-only model. As we see in Figure 2.5, varying $f_{\mathrm{gas,f}}$ has the same effect in the inflows-only model as in the closed box model. The lowest final gas fraction simulation ($f_{\mathrm{gas,f}} \approx 0.07$, shown in lime green) experiences a huge increase in ϵ_{rm} at late times as compared to the fiducial Inflows-Only simulation ($f_{\mathrm{gas,f}} = 0.2$, shown in light blue). As usual, the higher ϵ_{rm} at later times allows the gas reservoir to more rapidly and closely reach the effective gas returns, enabling $[\mathrm{Fe/H}]_{\mathrm{gas}}$ to reach a higher final value and producing a slightly shorter and steeper [Fe/H] plateau. Once again, this is reflected in the [Mg/Fe]–[Fe/H] track as the leg having a slightly more gentle slope and in the MDF as a shift in the right edge and the average stellar metallicity (and peak) to higher [Fe/H].

As we can see, the effect of varying a parameter is generally superimposed on top of the base model behavior. Therefore, we will study the other parameters in the context of the simplest model to which they are relevant.

Figure 2.4 *(next page)*: Chemical evolution of three Closed Box simulations when **varying the final gas fraction ($f_{\mathbf{gas,f}}$)** (or equivalently, the initial gas mass, $M_{gas,0}$, since for the closed box model the choice of $M_{gas,0}$ directly determines $f_{gas,f}$): (a) [Mg/Fe]–[Fe/H] (b) MDF, (c) [Mg/Fe] evolution, (d) [Fe/H] evolution, (e) ϵ_{rm} evolution, and (f) gas mass evolution. The red lines correspond to the fiducial Closed Box simulation with $f_{gas,f} = 0.2$ ($M_{gas,0} = 6.75 \times 10^{10} M_\odot$). The dark blue lines and sky blue lines assume $f_{gas,f} = 0.1$ ($M_{gas,0} = 6.00 \times 10^{10} M_\odot$) and $f_{gas,f} = 0.05$ ($M_{gas,0} = 5.70 \times 10^{10} M_\odot$), respectively, and all other parameters are the same as for the fiducial Closed Box simulation (see Table 2.3.1). The colored squares in panel (a) denote the average abundances of each simulation. The gray circles are the Bensby et al. 2014 abundance ratios for the kinematically-selected thick disk stars described in Section 2.3.2. Two gray dashed lines corresponding to [Mg/Fe]=0 and [Fe/H]=0 have been added as visual guides. The Milky-Way MDF for the geometrically-selected thick disk stars at 3kpc < R < 5kpc from Hayden et al. 2015 (detailed in Section 2.3.2) is shown as a comparison as a slate gray dashed line in panel (b). In panels (c) and (d), the solid lines indicate the gas reservoir abundance ratios while the dotted lines indicate the gas return abundance ratios. The gray dot-dashed lines show the onset of SNIa at $t = 100$ Myr. In panels (e) and (f), the gray dotted lines mark the peak of the star-formation history at $t = \tau_{SF} = 1$ Gyr.

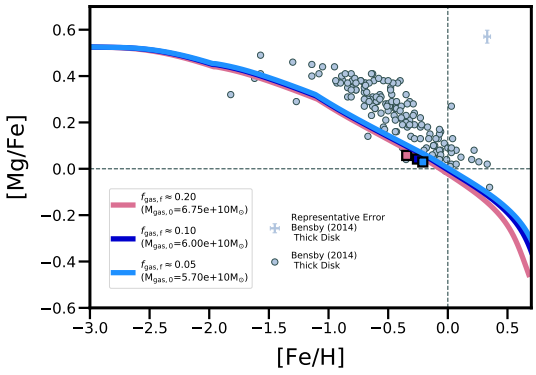

(a) [Mg/Fe]–[Fe/H]

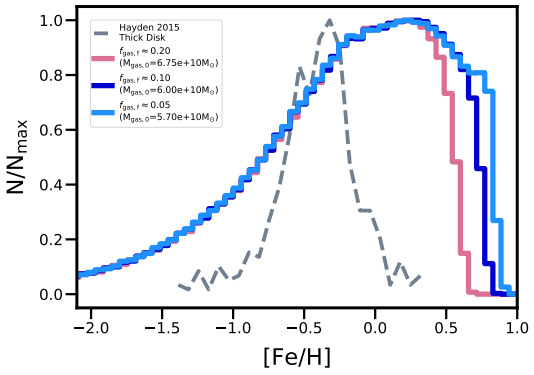

(b) Metallicity Distribution Function

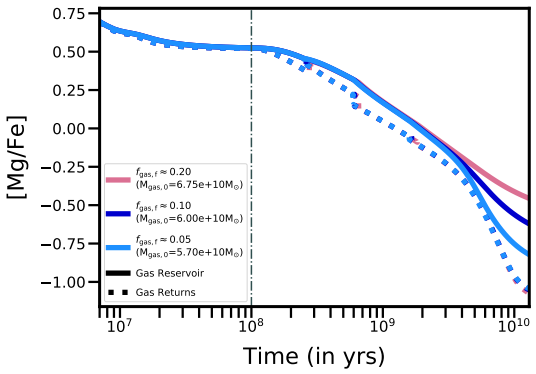

(c) [Mg/Fe] evolution

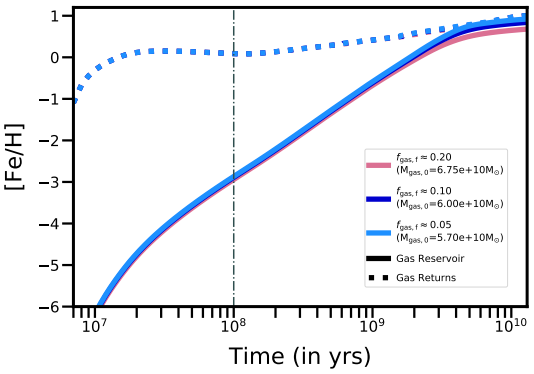

(d) [Fe/H] evolution

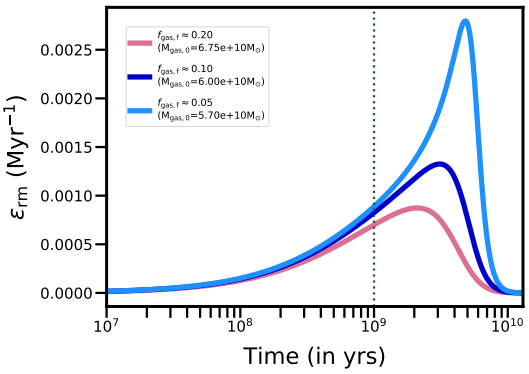

(e) Gas removal efficiency evolution

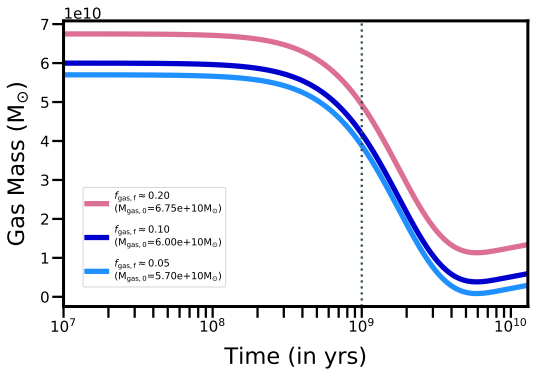

(f) Gas reservoir mass evolution

Figure 2.4: **Varying the final gas fraction ($f_{gas,f}$)** in the context of a closed box model, see the previous page for the full caption text.

Figure 2.5 *(next page)*: Chemical evolution of three Inflows-Only simulations when **varying the final gas fraction ($f_{\mathbf{gas,f}}$)**: (a) [Mg/Fe]–[Fe/H] (b) MDF, (c) [Mg/Fe] evolution, (d) [Fe/H] evolution, (e) $\epsilon_{\rm rm}$ evolution, and (f) gas mass evolution. The light blue lines correspond to the fiducial Inflows-Only simulation with $f_{\rm gas,f} = 0.2$. The dark blue and lime green lines assume $f_{\rm gas,f} = 0.1$ and $f_{\rm gas,f} = 0.07$, respectively, and all other parameters are the same as for the fiducial Inflows-Only simulation (see Table 2.3.1). The colored squares in panel (a) denote the average abundances of each simulation. The gray circles are the Bensby et al. 2014 abundance ratios for the kinematically-selected thick disk stars described in Section 2.3.2. Two gray dashed lines corresponding to [Mg/Fe]=0 and [Fe/H]=0 have been added as visual guides. The Milky-Way MDF for the geometrically-selected thick disk stars at 3kpc $<$ R $<$ 5kpc from Hayden et al. 2015 (detailed in Section 2.3.2) is shown as a comparison as a slate gray dashed line in panel (b). In panels (c) and (d), the solid lines indicate the gas reservoir abundance ratios while the dotted lines indicate the effective gas return abundance ratios. The gray dot-dashed lines show the onset of SNIa at $t = 100$ Myr. In panels (e) and (f), the gray dotted lines mark the peak of the star-formation history at $t = \tau_{\rm SF} = 1$ Gyr. The effect of changing $f_{\rm gas,f}$ in the context of an inflows-only model is the same as in the context of a closed box model (see Figure 2.4 and the text in 2.4.3.1).

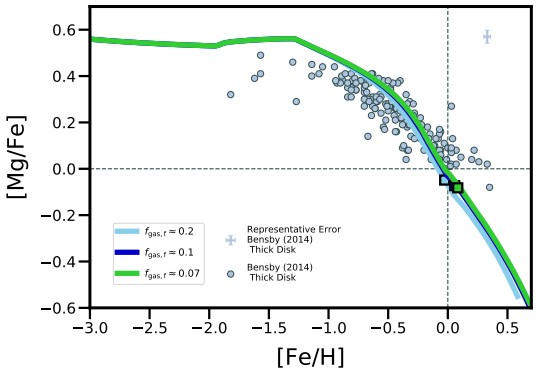

(a) [Mg/Fe]–[Fe/H]

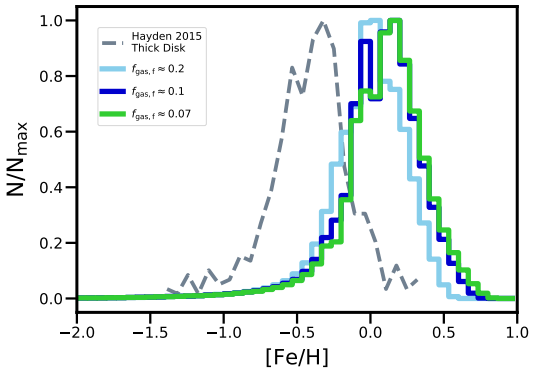

(b) Metallicity Distribution Function

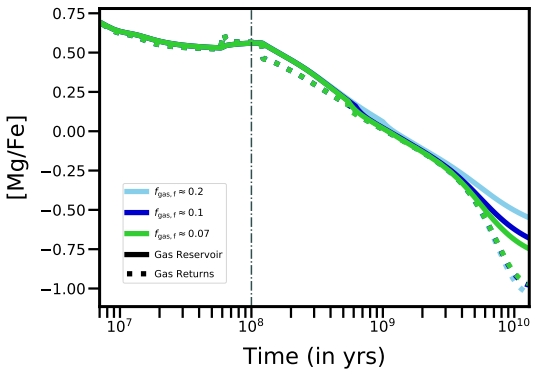

(c) [Mg/Fe] evolution

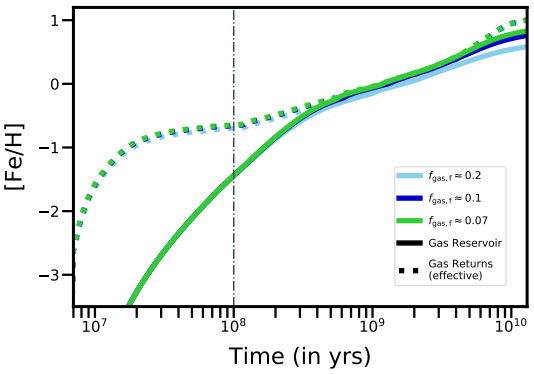

(d) [Fe/H] evolution

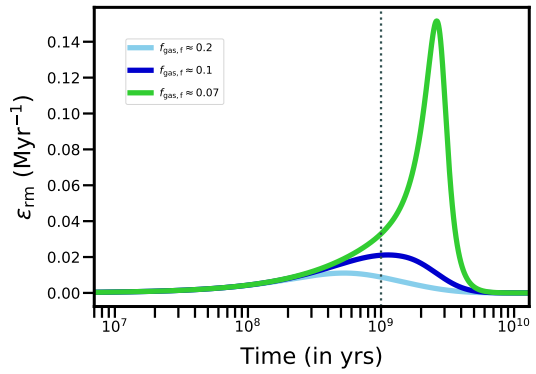

(e) Gas removal efficiency evolution

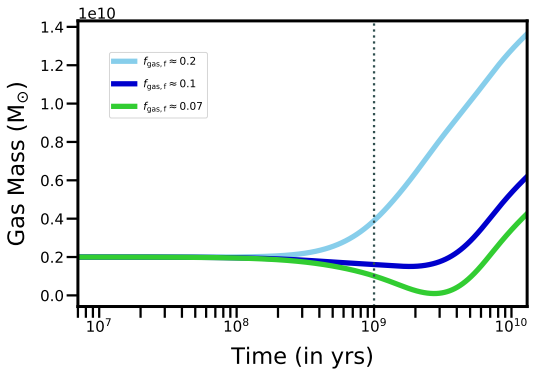

(f) Gas reservoir mass evolution

Figure 2.5: **Varying the final gas fraction ($f_{gas,f}$)** in the context of an inflows-only model, see the previous page for the full caption text.

The initial gas mass ($M_{gas,0}$)

As with the $f_{gas,f}$ simulations, $M_{gas,0}$ primarily affects the gas removal efficiency. In this scenario, we see the exact same principles in action as when we varied $f_{gas,f}$, the only difference being when in the simulation ϵ_{rm} is affected. Starting with a lower initial gas mass, as in the sky blue simulation in Figure 2.6 ($M_{gas,0} = 2 \times 10^7 M_\odot$), dramatically increases ϵ_{rm} at early times, as shown in panel (e), such that the gas reservoir abundance ratios are quickly driven to the gas return ratios. At late times, however, the ϵ_{rm} of our three simulations must be the same since they all have the same SFH and final gas fraction.

As seen in panel (c), the early boost to ϵ_{rm} means that $[Mg/Fe]_{gas}$ will be more responsive to the onset of SNIa and therefore, it will decline more rapidly and produce a sharper knee than for a simulation with a higher $M_{gas,0}$ (and consequently a lower ϵ_{rm} at early times, see e.g. the dark blue simulation with $M_{gas,0} = 2 \times 10^{10} M_\odot$). The early enrichment of $[Fe/H]_{gas}$ is similarly efficient, allowing $[Fe/H]_{gas}$ for the sky blue simulation to nearly match the gas returns ($[Fe/H]_{ret}$) well before the onset of SNIa. This means that the onset of SNIa will occur when the gas reservoir has been enriched to a higher metallicity, and therefore, the corresponding knee in [Mg/Fe]–[Fe/H] will be shifted to the right toward higher [Fe/H]. After this point, $[Fe/H]_{gas}$ gently increases, following $[Fe/H]_{ret}$ until ϵ_{rm} decreases again at late times. This forms a very long, gradual [Fe/H] plateau that is reflected in [Mg/Fe]–[Fe/H] as a quite steeply-sloped leg. The early [Fe/H] enhancement greatly reduces the mass of stars formed at low [Fe/H], and thus, the low metallicity tail of the MDF (as discussed when adding inflows in

Section 2.4.2.2). This results in a much more narrow MDF, as shown in panel (b).

Figure 2.6 *(next page)*: Chemical evolution of three Inflows-Only simulations when **varying the initial gas mass ($M_{gas,0}$)**: (a) [Mg/Fe]–[Fe/H] (b) MDF, (c) [Mg/Fe] evolution, (d) [Fe/H] evolution, (e) ϵ_{rm} evolution, and (f) gas mass evolution. The light blue lines correspond to the fiducial Inflows-Only simulation with $M_{gas,0} = 2 \times 10^9$ $M_\odot$. The dark blue and lime green lines assume $M_{gas,0} = 2 \times 10^{10}$ $M_\odot$ and $M_{gas,0} = 2 \times 10^7$ $M_\odot$, respectively, and all other parameters are the same as for the fiducial Inflows-Only simulation (see Table 2.3.1). The colored squares in panel (a) denote the average abundances of each simulation. The gray circles are the Bensby et al. 2014 abundance ratios for the kinematically-selected thick disk stars described in Section 2.3.2. Two gray dashed lines corresponding to [Mg/Fe]=0 and [Fe/H]=0 have been added as visual guides. The Milky-Way MDF for the geometrically-selected thick disk stars at 3kpc $<$ R $<$ 5kpc from Hayden et al. 2015 (detailed in Section 2.3.2) is shown as a comparison as a slate gray dashed line in panel (b). In panels (c) and (d), the solid lines indicate the gas reservoir abundance ratios while the dotted lines indicate the effective gas return abundance ratios. The gray dot-dashed lines show the onset of SNIa at $t = 100$ Myr. In panels (e) and (f), the gray dotted lines mark the peak of the star-formation history at $t = \tau_{SF} = 1$ Gyr.

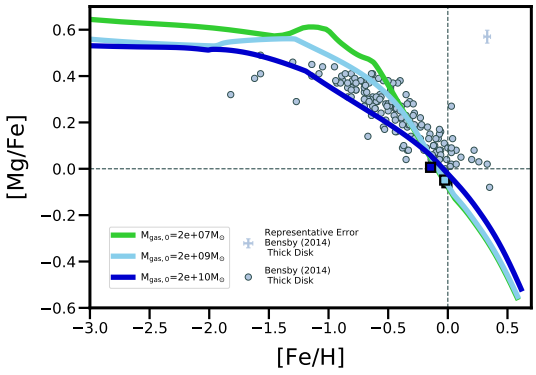

(a) [Mg/Fe]–[Fe/H]

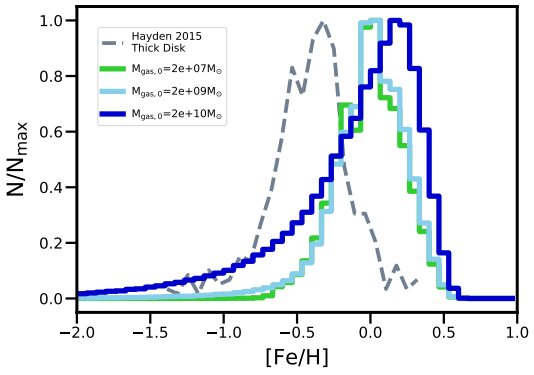

(b) Metallicity Distribution Function

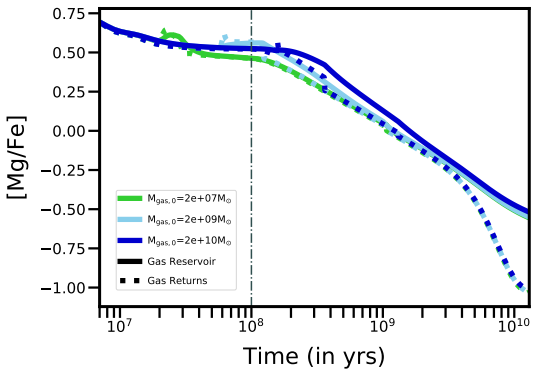

(c) [Mg/Fe] evolution

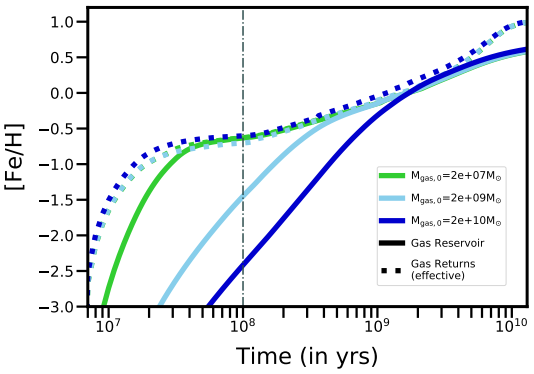

(d) [Fe/H] evolution

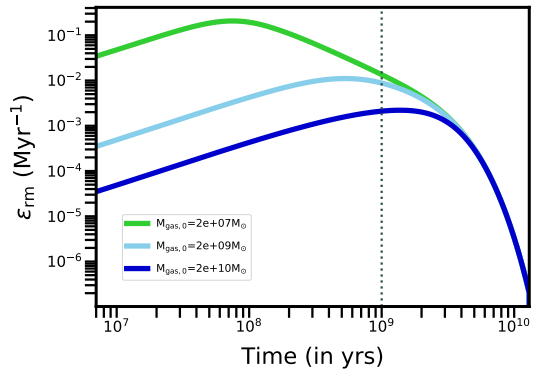

(e) Gas removal efficiency evolution

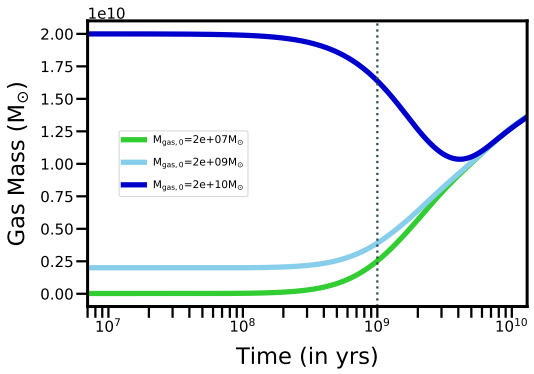

(f) Gas reservoir mass evolution

Figure 2.6: **Varying the initial gas mass ($M_{gas,0}$)**, see the previous page for the full caption text.

2.4.3.2 Parameters that primarily affect the effective gas returns

As stars evolve, they lose mass in the form of stellar winds or as stellar SN ejecta that can cool and become available for future star formation as part of what we call the gas reservoir. This returned gas may have the same metallicity and abundance patterns as the star (and the gas from which the star was born), thus producing no net yield, as is the case for passively evolving stars or high mass winds, or the gas may be enriched as for AGB winds and CCSN or SNIa ejecta. The gas returned at any given time is shaped by the star-formation history, the initial mass function, the SNIa delay time distribution, and the metallicity-dependent yields, as described in Section 2.2.7.

In our chemical evolution model, the gas return for an element, elem, in a given time-step, i, is therefore:

$$R_{\rm elem}[i] = R^{\rm pass}_{\rm elem}[i] + R^{\rm AGB}_{\rm elem}[i] + R^{\rm CCSN}_{\rm elem}[i] + R^{\rm SNIa}_{\rm elem}[i] \tag{2.52}$$

where $R^{\rm pass}_{\rm elem}$, $R^{\rm AGB}_{\rm elem}$, $R^{\rm CCSN}_{\rm elem}$, and $R^{\rm SNIa}_{\rm elem}$ are the mass of elem contributed by winds from passively evolving stars, AGB stellar winds, CCSN ejecta, and SNIa ejecta, respectively. For a single stellar population, the relative contribution from each component to $R_{\rm elem}$ will depend on the element in question as well as the age of the stellar population since these four components return gas on different timescales.

Since stars record the abundance ratios of the gas from which they were formed rather than information about the absolute abundances, we are primarily concerned with element ratios. Considering that SNIa return barely any Mg and no H, such that $R^{\rm SNIa}_{\rm Mg} = 0$ and $R^{\rm SNIa}_{\rm H} = 0$, we find that the gas return ratios for Mg to Fe and Fe to H,

respectively, are

$$\frac{R_{\rm Mg}[i]}{R_{\rm Fe}[i]} = \frac{R^{*}_{\rm Mg}[i]}{R^{*}_{\rm Fe}[i] + R^{\rm SNIa}_{\rm Fe}[i]} \tag{2.53}$$

and

$$\frac{R_{\rm Fe}[i]}{R_{\rm H}[i]} = \frac{R^{*}_{\rm Fe}[i] + R^{\rm SNIa}_{\rm Fe}[i]}{R^{*}_{\rm H}[i]}, \tag{2.54}$$

where we have grouped $R^{\rm pass}_{\rm elem}$, $R^{\rm AGB}_{\rm elem}$, $R^{\rm CCSN}_{\rm elem}$ under the umbrella of gas returns from stellar sources, such that $R^{*}_{\rm elem}[i] \equiv R^{\rm pass}_{\rm elem}[i] + R^{\rm AGB}_{\rm elem}[i] + R^{\rm CCSN}_{\rm elem}[i]$. We have discussed how these ratios generally evolve in Section 2.4.1.1.

However, as argued in Sections 2.4.2.2, these gas returns may be only part of the gas enrichment puzzle. We therefore define the more general "effective gas returns" to encompass all sources that contribute to the gas that is added back to the gas reservoir. Typically, these sources include the standard gas returns from evolving stars and SNIa as well as contributions from infalling gas, so that $R_{\rm elem,eff}[i] = R^{*}_{\rm elem}[i] + R^{\rm SNIa}_{\rm elem}[i] + I_{\rm elem}[i]$, where $I_{\rm elem}$ is the amount of element, elem from the galaxy inflows that is mixed into the gas reservoir during time-step i. Therefore, the effective gas return ratios can be written as:

$$\frac{R_{\rm Mg,eff}[i]}{R_{\rm Fe,eff}[i]} = \frac{R^{*}_{\rm Mg}[i] + I_{\rm Mg}[i]}{R^{*}_{\rm Fe}[i] + R^{\rm SNIa}_{\rm Fe}[i] + I_{\rm Fe}[i]} \tag{2.55}$$

and

$$\frac{R_{\rm Fe,eff}[i]}{R_{\rm H,eff}[i]} = \frac{R^{*}_{\rm Fe}[i] + R^{\rm SNIa}_{\rm Fe}[i] + I_{\rm Fe}[i]}{R^{*}_{\rm H}[i] + I_{\rm H}[i]} \tag{2.56}$$

where $I_{\rm Mg}[i] = 0$ and $I_{\rm Fe}[i] = 0$ in the case of pristine inflows. Including the contribution to the effective gas returns from inflows is especially important when considering the

gas reservoir [Fe/H] evolution, as we shall see when examining the impact of changing Z_{in} and ϵ_{out}.

In this section, we examine four parameters that influence the galactic chemical evolution primarily by changing the effective gas returns. We find that the minimum SNIa delay time, t_{DTD}, alters the gas return ratios by changing $R^{SNIa}_{elem}[i]$, while the inflow metallicity, Z_{in}, and the outflow parameter, ϵ_{out}, affect the effective gas returns by changing the inflow term. Finally, we consider an additional source that can contribute to $R_{elem,eff}$ by exploring the impact of a non-zero f_{SN}.

The minimum delay-time, t_{DTD}, of the SNIa DTD

Figure 2.7 shows the effect of varying the minimum delay-time of the SNIa DTD by a factor of 2, as compared to the default t_{DTD} = 100 Myr of the fiducial Closed Box simulation (plotted in red). The dark blue and sky blue simulations have a minimum delay times of t_{DTD} = 50 Myr and t_{DTD} = 200 Myr respectively. The t_{DTD} controls when, after the birth of a stellar generation, SNIa start to explode. Therefore, the SNIa that would have exploded between 100 Myr and 200 Myrs after the formation of each stellar generation in the fiducial simulation never occur in the case of the sky blue simulation with t_{DTD} = 200 Myr. A simulation with a longer t_{DTD} will have fewer SNIa shortly after star-formation and thus, fewer SNIa explosions overall. As we can see in panels (e) and (f), this has no noticeable effect on the overall gas mass of each simulation and therefore all three simulations have the same gas removal efficiency evolution.

However, this change in the number of short delay-time SNIa has a considerable

effect on the iron in the gas returns and thus on the [Mg/Fe] and [Fe/H] evolution (as seen in panels (c) and (d)). Most noticeably, the delayed onset of SNIa production for the longer t_{DTD} simulation allows the gas reservoir to become more enriched and reach higher [Fe/H] before the SNIa Fe returns cause $[Mg/Fe]_{ret}$ to decline. Therefore, the "knee" in the [Mg/Fe]–[Fe/H] track will correspond to a higher [Fe/H] and be pushed to the right in panel (a). The lower number of SNIa will also slow the [Fe/H] enrichment causing more stars to be born at lower [Fe/H] which results in a heavier low-metallicity tail in the MDF and shifting its peak to lower [Fe/H] (as seen in panel (b)).

Figure 2.7 *(next page)*: Chemical evolution of three Closed Box simulations when **varying the minimum SNIa delay-time (t_{dtd})**: (a) [Mg/Fe]–[Fe/H] (b) MDF, (c) [Mg/Fe] evolution, (d) [Fe/H] evolution, (e) ϵ_{rm} evolution, and (f) gas mass evolution. The red lines correspond to the fiducial Closed Box simulation with $t_{DTD} = 100$ Myr while the dark blue lines and sky blue lines vary t_{DTD} by a factor of 2 such that $t_{DTD} = 50$ Myr and $t_{DTD} = 200$ Myr, respectively, with all other parameters are kept the same as for the fiducial Closed Box simulation (see Table 2.3.1). The colored squares in panel (a) denote the average abundances of each simulation. The gray circles are the Bensby et al. 2014 abundance ratios for the kinematically-selected thick disk stars described in Section 2.3.2. Two gray dashed lines corresponding to [Mg/Fe]=0 and [Fe/H]=0 have been added as visual guides. The Milky-Way MDF for the geometrically-selected thick disk stars at 3kpc $<$ R $<$ 5kpc from Hayden et al. 2015 (detailed in Section 2.3.2) is shown as a comparison as a slate gray dashed line in panel (b). In panels (c) and (d), the solid lines indicate the gas reservoir abundance ratios while the dotted lines indicate the gas return abundance ratios. For each simulation, a thin dot-dashed line (in a matching color) shows the corresponding onset of SNIa. In panels (e) and (f), the gray dotted lines mark the peak of the star-formation history at $t = \tau_{SF} = 1$ Gyr.

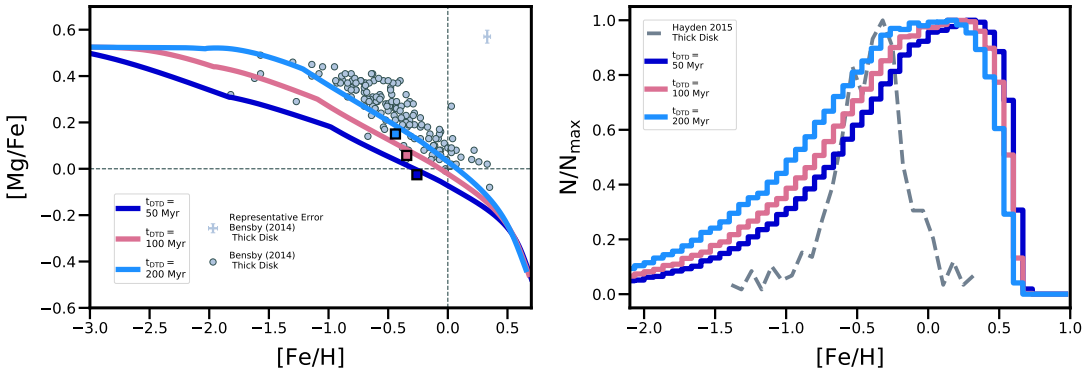

(a) [Mg/Fe]–[Fe/H]

(b) Metallicity Distribution Function

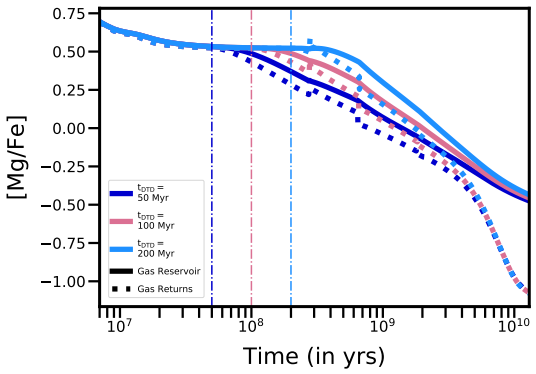

(c) [Mg/Fe] evolution

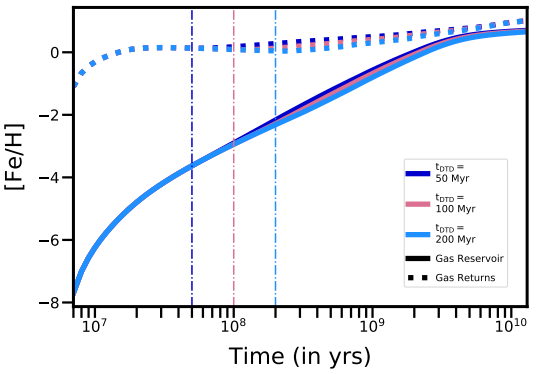

(d) [Fe/H] evolution

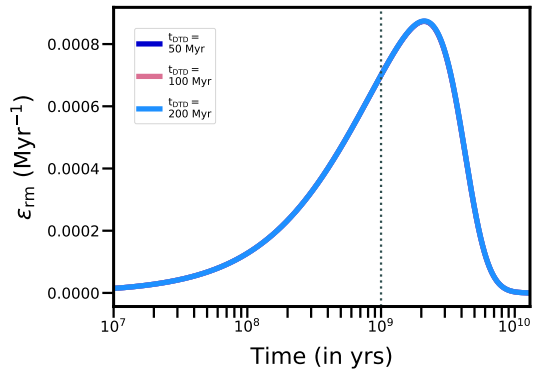

(e) Gas removal efficiency evolution

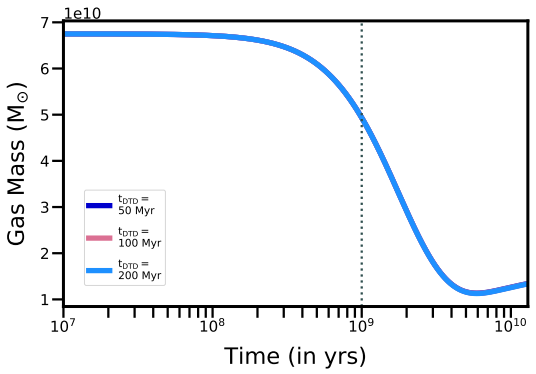

(f) Gas reservoir mass evolution

Figure 2.7: **Varying the SNIa minimum delay-time (t_{DTD})**, see the previous page for the full caption text.

The inflow metallicity, Z_{in}

Figure 2.8 shows the effect of changing the inflow metallicity, Z_{in}. The greater the inflow metallicity, the greater the Fe mass included in the infalling gas and therefore the less H is present in the inflows. This leads to the effective gas returns, which are plotted as dotted lines in panel (d), having a higher [Fe/H] for higher Z_{in}. As compared to the light-blue fiducial Inflows-Only simulation, the early $[Fe/H]_{gas}$ enrichment of the higher-Z_{in} simulations is accelerated and the inflows at later times do not dilute the gas reservoir abundance as much. Thus, more stars form at high metallicity, shifting the peak and the average [Fe/H] of the MDF to the right (to higher [Fe/H]) and suppressing the low-metallicity tail thus making the MDF more narrow (as seen in panel (b)). The faster $[Fe/H]_{gas}$ enrichment at early times also means that the onset of SNIa will correspond to a higher [Fe/H], so that the "knee" is shifted to the right, toward higher [Fe/H], in [Mg/Fe]–[Fe/H] (panel (a)).

Furthermore, the enriched inflows also bring in Mg (as well as Fe) in ratios that correspond to the IMF-weighted CCSN yields for the closest metallicity yield table (see Section 2.2.6). Thus, the higher Z_{in} inflows will bring in significant amounts of Mg and Fe in proportions that are either equal to or exceed the gas reservoir ratios. This serves to slow down the post-"knee" decline in [Mg/Fe], as seen in panel (c), and results in a higher average stellar [Mg/Fe]. Note that the average [Mg/Fe] and [Fe/H] of each simulation is shown as a square in panel (a).

Figure 2.8 *(next page)*: Chemical evolution of four Inflows-Only simulations when **varying the inflow metallicity (Z_{in})**: (a) [Mg/Fe]–[Fe/H] (b) MDF, (c) [Mg/Fe] evolution, (d) [Fe/H] evolution, (e) ϵ_{rm} evolution, and (f) gas mass evolution. The light blue lines correspond to the fiducial Inflows-Only simulation with $Z_{in} = 10^{-10}$. The lime green lines, dark blue lines, and sky blue lines assume $Z_{in} = 0.001$, $Z_{in} = 0.005$ and $Z_{in} = 0.01$, respectively, and all other parameters are the same as for the fiducial Inflows-Only simulation (see Table 2.3.1). The colored squares in panel (a) denote the average abundances of each simulation. The gray circles are the Bensby et al. 2014 abundance ratios for the kinematically-selected thick disk stars described in Section 2.3.2. Two gray dashed lines corresponding to [Mg/Fe]=0 and [Fe/H]=0 have been added as visual guides. The Milky-Way MDF for the geometrically-selected thick disk stars at 3kpc < R < 5kpc from Hayden et al. 2015 (detailed in Section 2.3.2) is shown as a comparison as a slate gray dashed line in panel (b). In panels (c) and (d), the solid lines indicate the gas reservoir abundance ratios while the dotted lines indicate the effective gas return abundance ratios. The gray dot-dashed lines show the onset of SNIa at $t = 100$ Myr. In panels (e) and (f), the gray dotted lines mark the peak of the star-formation history at $t = \tau_{SF} = 1$ Gyr.

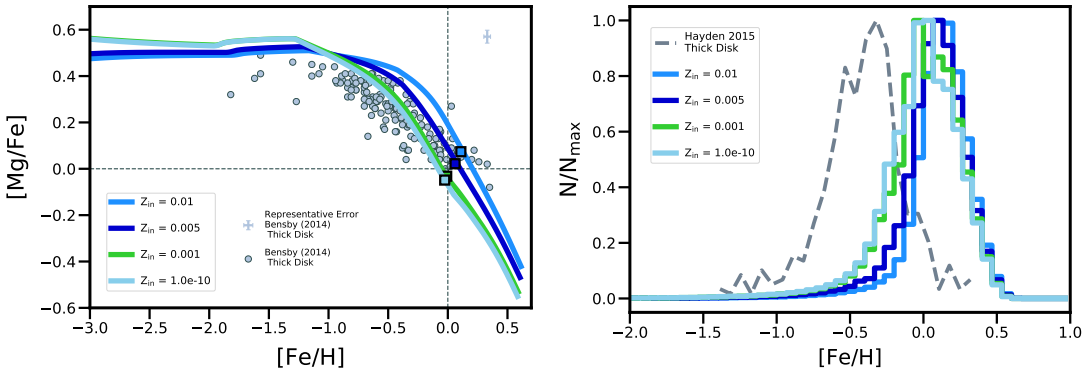

(a) [Mg/Fe]–[Fe/H]

(b) Metallicity Distribution Function

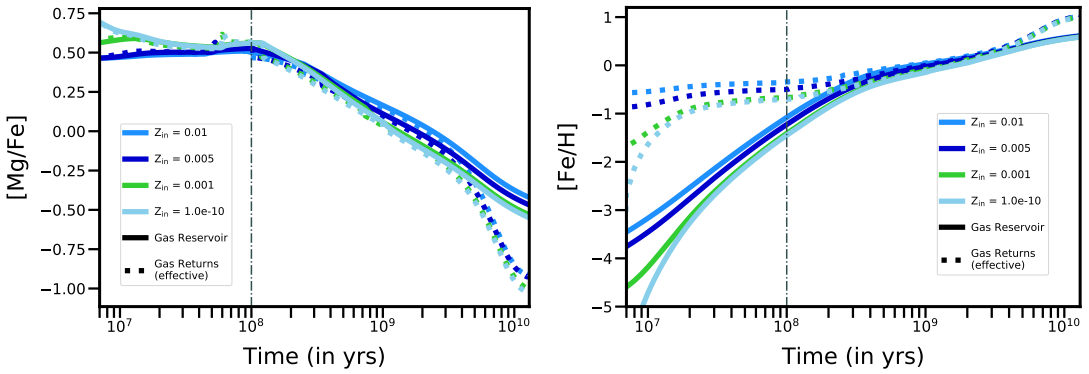

(c) [Mg/Fe] evolution

(d) [Fe/H] evolution

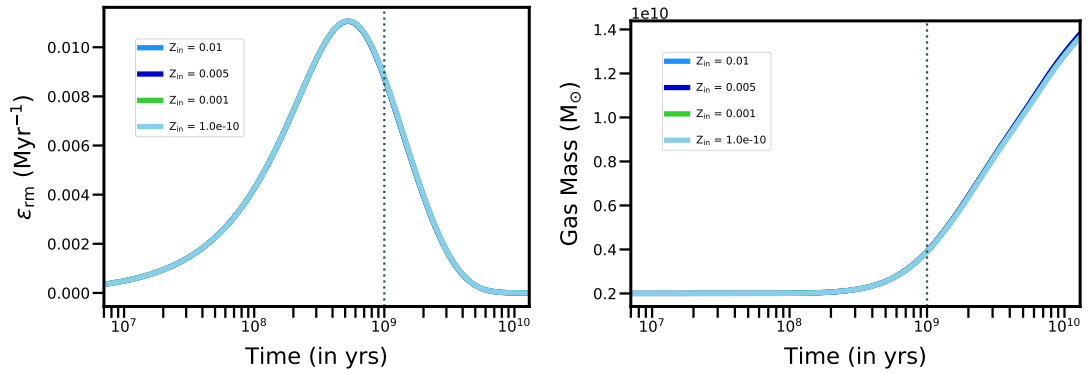

(e) Gas removal efficiency evolution

(f) Gas reservoir mass evolution

Figure 2.8: **Varying the inflow metallicity (Z_{in})**, see the previous page for the full caption text.

The outflow parameter, $\epsilon_{\rm out}$

The effect of increasingly strong outflows on a galaxy's chemical evolution is shown in Figure 2.9. The three Inflows+Outflows simulations shown have varying amounts of outflows, as controlled by our $\epsilon_{\rm out}$ outflow parameter. The light-blue simulation has $\epsilon_{\rm out} = 0$ and is equivalent to the fiducial Inflows-Only simulations, our fiducial Inflows+Outflows simulation has $\epsilon_{\rm out} = 3$ and is shown in purple, while the pink simulation has the strongest outflows with $\epsilon_{\rm out} = 10$.

Similarly to when we varied $\rm Z_{in}$ above, the changes in panel (a) and (b) are driven by the influence of $\epsilon_{\rm out}$ on the effective gas returns. The larger the outflow parameter the higher the inflow mass needed to replace the gas removed in outflows. The higher inflow mass increases the $I_{\rm H}$ term in the effective gas return ratio, $\frac{R_{\rm Fe}[i]}{R_{\rm H}[i]}$, resulting in the lower effective [Fe/H] for the gas returns that is shown by the dotted lines in panel (d). This suppresses the enhancement of the gas reservoir [Fe/H], causing it to plateau. Thus, as $\epsilon_{\rm out}$ increases, the slower enrichment results in a lower final $\rm [Fe/H]_{gas}$, causing the leg to move leftward in panel (a) (to lower [Fe/H]). This is also reflected in the overall leftward shift of the MDF toward lower [Fe/H], as seen in panel (b). Note that generally, a flatter [Fe/H] plateau in panel (d) results in a steeper slope to the leg of the [Mg/Fe]–[Fe/H] track (and a sharper looking knee).

Figure 2.9 *(next page)*: Chemical evolution of three Inflows+Outflows simulations when **varying the outflow parameter ($\epsilon_{\mathbf{out}}$)**: (a) [Mg/Fe]–[Fe/H] (b) MDF, (c) [Mg/Fe] evolution, (d) [Fe/H] evolution, (e) $\epsilon_{\rm rm}$ evolution, and (f) gas mass evolution. The light blue lines correspond to the fiducial Inflows-Only simulation with $\epsilon_{\rm out} = 0$ and the purple lines correspond to the fiducial Inflow+Outflows simulation with $\epsilon_{\rm out} = 3$. The pink lines assume a much bigger outflow parameter of $\epsilon_{\rm out} = 10$ and all other parameters are the same as for the fiducial Inflows+Outflows simulation (see Table 2.3.1). The colored squares in panel (a) denote the average abundances of each simulation. The gray circles are the Bensby et al. 2014 abundance ratios for the kinematically-selected thick disk stars described in Section 2.3.2. Two gray dashed lines corresponding to [Mg/Fe]=0 and [Fe/H]=0 have been added as visual guides. The Milky-Way MDF for the geometrically-selected thick disk stars at 3kpc $<$ R $<$ 5kpc from Hayden et al. 2015 (detailed in Section 2.3.2) is shown as a comparison as a slate gray dashed line in panel (b). In panels (c) and (d), the solid lines indicate the gas reservoir abundance ratios while the dotted lines indicate the effective gas return abundance ratios. The gray dot-dashed lines show the onset of SNIa at $t = 100$ Myr. In panels (e) and (f), the gray dotted lines mark the peak of the star-formation history at $t = \tau_{\rm SF} = 1$ Gyr.

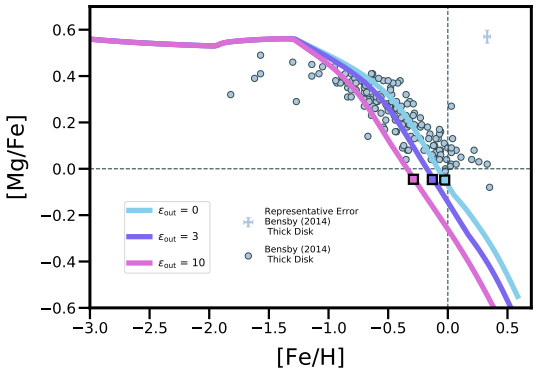

(a) [Mg/Fe]–[Fe/H]

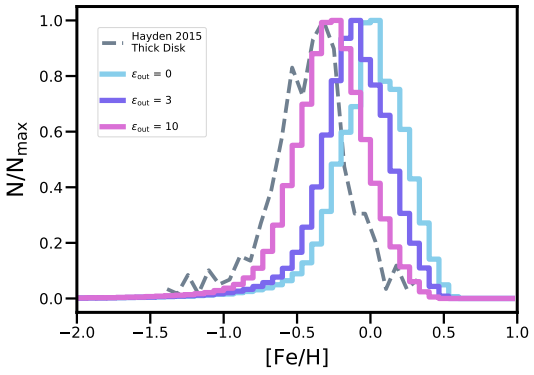

(b) Metallicity Distribution Function

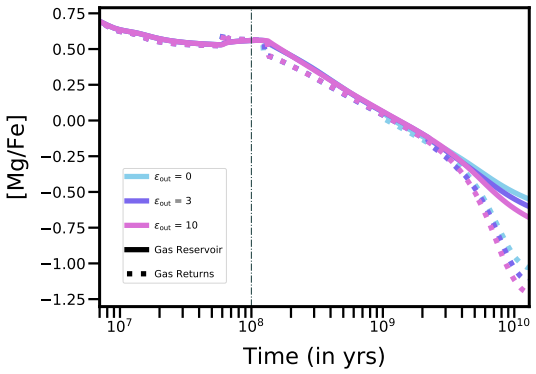

(c) [Mg/Fe] evolution

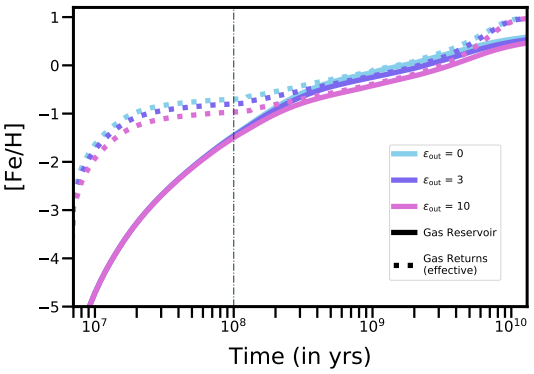

(d) [Fe/H] evolution

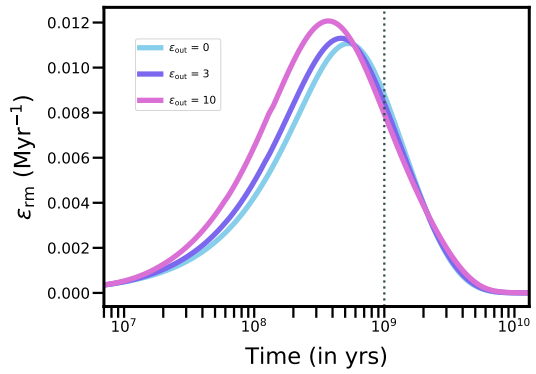

(e) Gas removal efficiency evolution

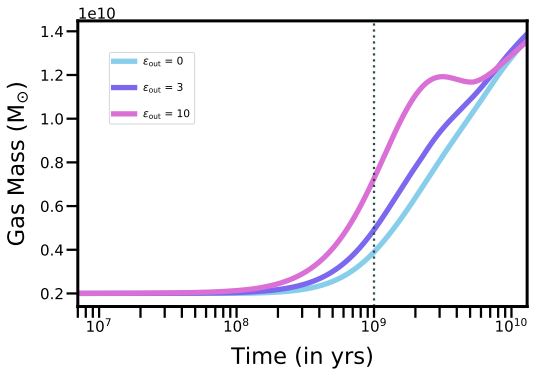

(f) Gas reservoir mass evolution

Figure 2.9: **Varying the outflow parameter ($\epsilon_{\mathbf{out}}$)**, see the previous page for the full caption text.

The fraction of the supernova ejecta removed in outflows, $f_{\rm SN}$

As discussed in Section 2.2.5, when $f_{\rm SN} = 0$, as is the case for the purple fiducial Inflows+Outflows simulation in Figure 2.10, the outflows are just ISM gas from the reservoir. The dark blue and pink simulations show the effect of increasing the fraction of SN ejecta removed in outflows, to $f_{\rm SN} = 0.25$ and $f_{\rm SN} = 0.5$ respectively. The higher $f_{\rm SN}$, the more SN ejecta is removed from the galaxy in the form of metal enriched outflow before it can enrich the gas reservoir. Removing a fraction of the CCSN and SNIa gas returns changes the effective gas return abundance ratios as follows:

$$\frac{R_{\rm Mg,eff}[i]}{R_{\rm Fe,eff}[i]} = \frac{R^{*}_{\rm Mg}[i] - f_{\rm SN}\left(R^{\rm CCSN}_{\rm Mg}[i] + R^{\rm SNIa}_{\rm Mg}[i]\right) + I_{\rm Mg}[i]}{R^{*}_{\rm Fe}[i] + R^{\rm SNIa}_{\rm Fe}[i] - f_{\rm SN}\left(R^{\rm CCSN}_{\rm Fe}[i] + R^{\rm SNIa}_{\rm Fe}[i]\right) + I_{\rm Fe}[i]} \tag{2.57}$$

$$\frac{R_{\rm Fe,eff}[i]}{R_{\rm H,eff}[i]} = \frac{R^{*}_{\rm Fe}[i] + R^{\rm SNIa}_{\rm Fe}[i] - f_{\rm SN}\left(R^{\rm CCSN}_{\rm Fe}[i] + R^{\rm SNIa}_{\rm Fe}[i]\right) + I_{\rm Fe}[i]}{R^{*}_{\rm H}[i] - f_{\rm SN}R^{\rm CCSN}_{\rm H}[i] + I_{\rm H}[i]} \tag{2.58}$$

Unlike the varying $\epsilon_{\rm out}$ case above, the inflow history is the same for all three simulations. Therefore the effective gas return abundance ratio, $\frac{R_{\rm Fe,eff}[i]}{R_{\rm H,eff}[i]}$, is not primarily affected by differences in H from $I_{\rm H}[i]$, but rather by differences in Fe due to the added $-f_{\rm SN}\left(R^{\rm CCSN}_{\rm Mg}[i] + R^{\rm SNIa}_{\rm Mg}[i]\right)$ term. The higher $f_{\rm SN}$, the more SN ejecta is removed from the galaxy before it can enrich the gas reservoir. Therefore, less Fe from both SNIa and CCSN ever reaches the gas reservoir, decreasing the [Fe/H] of the gas returns, as shown in panel (d). The lower Fe gas return slows the [Fe/H] enrichment and results in a lower final [Fe/H] of the gas reservoir. This shifts the right edge of the MDF and the peak of

the MDF to the left to lower [Fe/H] while also shifting the [Mg/Fe]–[Fe/H] leg inward, to lower [Fe/H].

Perhaps surprisingly, the [Mg/Fe] of the gas returns is also affected by $f_{\rm SN}$. If there were no enrichment from AGB stars, the gas return [Mg/Fe] would actually be the same for all of these simulations because the same fraction of CCSN ejecta is removed as SNIa ejecta (which would keep the ratios of Mg to Fe the same). However, the larger the fraction of SN ejecta removed in outflows, the smaller the contribution of CCSN and SNIa to the overall galaxy enrichment and the larger the relative importance of AGB stars. The larger AGB stars produce winds with [Mg/Fe] that is enhanced compared to solar winds, and this can help slow down the decline in the gas reservoir [Mg/Fe] now that the amount of Fe returned to the gas from SNIa has decreased. This leads to a higher average [Mg/Fe] for higher $f_{\rm SN}$ simulations, unlike for our $\epsilon_{\rm out}$ simulations.

Figure 2.10 *(next page)*: Chemical evolution of three Inflows+Outflows simulations when **varying the fraction of the SN ejecta removed in outflows ($f_{\rm SN}$)**: (a) [Mg/Fe]–[Fe/H] (b) MDF, (c) [Mg/Fe] evolution, (d) [Fe/H] evolution, (e) $\epsilon_{\rm rm}$ evolution, and (f) gas mass evolution. The purple lines correspond to the fiducial Inflow+Outflows simulation with $f_{\rm SN} = 0$. The navy blue and pink lines assume increasingly larger fractions of the SN ejecta ($f_{\rm SN} = 0.25$ and $f_{\rm SN} = 0.5$, respectively) are removed in the outflows before ever being mixed into the gas reservoir. All other parameters are the same as for the fiducial Inflows+Outflows simulation (see Table 2.3.1). The colored squares in panel (a) denote the average abundances of each simulation. The gray circles are the Bensby et al. 2014 abundance ratios for the kinematically-selected thick disk stars described in Section 2.3.2. Two gray dashed lines corresponding to [Mg/Fe]=0 and [Fe/H]=0 have been added as visual guides. The Milky-Way MDF for the geometrically-selected thick disk stars at 3kpc $<$ R $<$ 5kpc from Hayden et al. 2015 (detailed in Section 2.3.2) is shown as a comparison as a slate gray dashed line in panel (b). In panels (c) and (d), the solid lines indicate the gas reservoir abundance ratios while the dotted lines indicate the effective gas return abundance ratios. The gray dot-dashed lines show the onset of SNIa at $t = 100$ Myr. In panels (e) and (f), the gray dotted lines mark the peak of the star-formation history at $t = \tau_{\rm SF} = 1$ Gyr.

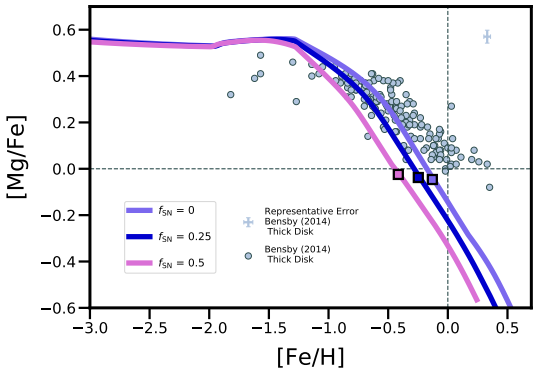

(a) [Mg/Fe]–[Fe/H]

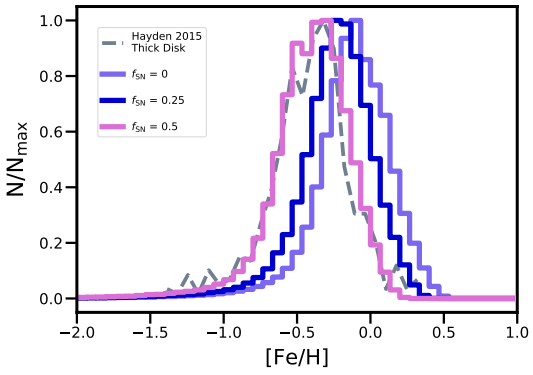

(b) Metallicity Distribution Function

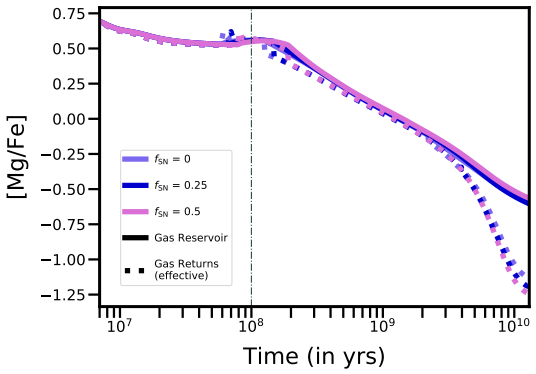

(c) [Mg/Fe] evolution

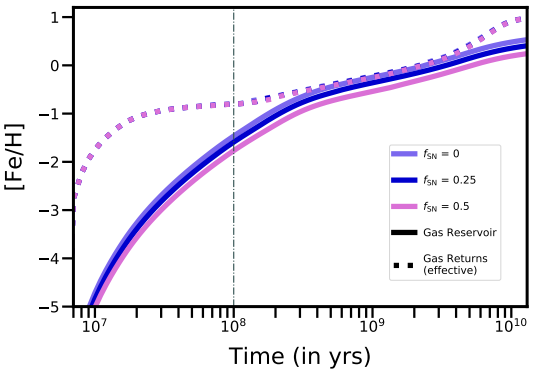

(d) [Fe/H] evolution

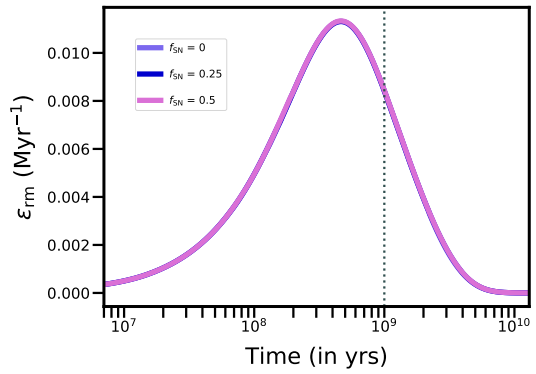

(e) Gas removal efficiency evolution

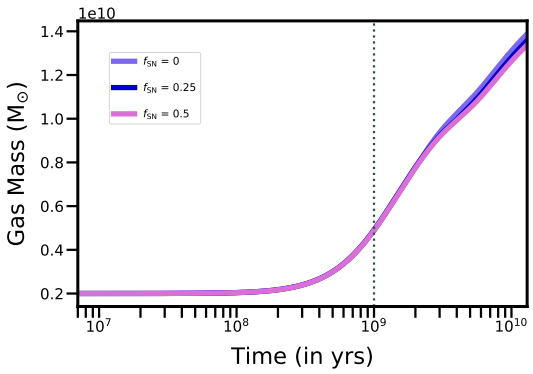

(f) Gas reservoir mass evolution

Figure 2.10: **Varying the fraction of the SN ejecta removed in outflows (f_{SN})**, see the previous page for the full caption text.

2.4.3.3 Parameters that significantly affect both the gas removal efficiency and the effective gas returns

The inflow timescale, $\tau_{\rm in}$

Figure 2.11 shows the effect of changing the inflow timescale, $\tau_{\rm in}$. All three simulations have the same star-formation timescale of $\tau_{\rm SF} = 1$ Gyr. For the fiducial Inflows-Only model, shown in light blue, the inflow timescale of $\tau_{\rm in} = 0.9$ Gyr is very close to the star-formation timescale, mimicking a scenario in which the inflowing gas directly fuels star-formation. In this case, the gas entering the galaxy as inflows is quickly converted into stars such that, as seen in panel (f), the gas mass does not build up significantly until late times when the star-formation rate is quite low. This results in a considerable increase in $\epsilon_{\rm rm}$ (shown in panel (e)) until around $\rm t_{transSF}$. The very short inflow timescale of $\tau_{\rm in} = 0.1$ Gyr for the dark blue simulation, closely resembles the closed box model, as discussed below, since the majority of the inflows enter the galaxy very early on. This build-up of gas greatly suppresses the gas removal efficiency. Finally, the lime green simulation represents an intermediate case with $\tau_{\rm in} = 0.5$ Gyr.

Since these models assume pristine inflows and $\tau_{\rm in}$ does not affect the IMF-weighted yields or the star-formation history, the $\rm [Mg/Fe]_{ret}$ of the gas returns will be the same for all three simulations, as shown in panel (c). Therefore, the differences in the gas reservoir [Mg/Fe] evolution must be the result of changes in $\epsilon_{\rm rm}$. As we have explained before, the higher $\epsilon_{\rm rm}$, the more quickly the gas reservoir abundance ratios approach the gas returns abundance ratios. Therefore, when the onset of SNIa causes $\rm [Mg/Fe]_{ret}$ to rapidly decline, the $\rm [Mg/Fe]_{gas}$ of the fiducial ($\tau_{\rm in} = 0.9$ Gyr) simulation quickly

decreases and $[\mathrm{Mg/Fe}]_{\mathrm{gas}}$ soon approaches $[\mathrm{Mg/Fe}]_{\mathrm{ret}}$. In comparison, the $\tau_{\mathrm{in}} = 0.1$ Gyr simulation has a much lower ϵ_{rm} that causes the gas reservoir abundances to not be as responsive to the gas returns. Thus, $[\mathrm{Mg/Fe}]_{\mathrm{gas}}$ declines much more slowly, producing a more gently sloped leg in both the [Mg/Fe] evolution and in the [Mg/Fe]–[Fe/H] track (panel (a)). The intermediate $\tau_{\mathrm{in}} = 0.5$ Gyr simulation initially has an elevated ϵ_{rm}, leading to a faster initial decline in $[\mathrm{Mg/Fe}]_{\mathrm{gas}}$ that resembles the early behavior of the fiducial simulation ($\tau_{\mathrm{in}} = 0.9$ Gyr). But after about 0.2 Gyr, the gas removal efficiency drops again, causing $[\mathrm{Mg/Fe}]_{\mathrm{gas}}$ to decrease more slowly again as with the later-time behavior of the $\tau_{\mathrm{in}} = 0.1$ Gyr closed-box-like simulation.

The [Fe/H] evolution, however, is more strongly shaped by the change to the effective gas returns due to the large hydrogen gas component of the inflows, as seen in panel (d). We can clearly see this for the closed-box-like ($\tau_{\mathrm{in}} = 0.1$ Gyr) simulation, where the short τ_{in} leads to a large influx of hydrogen gas that greatly decreases $[\mathrm{Fe/H}]_{\mathrm{ret}}$ at early times. As usual, the slower enrichment of [Fe/H] at early times (due to the lower [Fe/H] of the effective gas returns) leads to a heavier low-metallicity tail in the MDF. At later times, the effective gas returns increase dramatically due to the very low inflow rate (around $2.5 - 3 \times \tau_{\mathrm{in}}$). At this point, [Fe/H] starts to increase more quickly, before plateauing again at later times. It eventually reaches a final [Fe/H] that exceeds that of the fiducial ($\tau_{\mathrm{in}} = 0.9$ Gyr) simulation. The increase in metallicity around the peak of star formation and the late-time plateau results in a significant number of stars being formed at high metallicities, producing in the characteristic high-metallicity peak with a much more abrupt right edge that resembles that of the fiducial Closed-Box

simulation (shown in red in Figure 2.2).

In contrast, the Inflows-Only fiducial simulation ($\tau_{\rm in} = 0.9$ Gyr) has a much more narrow MDF (as previously explained in Section 2.4.2.2) and the post-"knee" leg slope is much steeper. Additionally, due to the earlier enrichment, the knee of the fiducial model corresponds to a higher [Fe/H] and is moved rightward in panel (a). The intermediate $\tau_{\rm in} = 0.5$ Gyr simulation initially looks very similar to the Inflows-Only fiducial simulation but the drop in $\epsilon_{\rm rm}$ around when the inflows mass peaks causes the later-time features to resemble that of the closed-box-like $\tau_{\rm in} = 0.1$ Gyr simulation. Thus, as shown in panel (b), the low-metallicity tail is suppressed like that of the fiducial ($\tau_{\rm in} = 0.9$ Gyr) simulation but the MDF is also much broader with a final $[{\rm Fe/H}]_{\rm gas}$ that is very close to that of the closed-box-like simulation. Note that the intermediate nature of the $\tau_{\rm in} = 0.5$ Gyr simulation makes the [Mg/Fe]–[Fe/H] track look quite odd. Initially, it matches that of the Inflows-Only fiducial model. At later times, it changes to much more closely resembling that of the closed-box-like $\tau_{\rm in} = 0.1$ Gyr simulation and the transition from the early behavior to the late-time behavior causes a very sharp knee and a strong inflexion point in between.

Figure 2.11 *(next page)*: Chemical evolution of three Inflows-Only simulations when **varying the inflow timescale ($\tau_{\rm in}$)**: (a) [Mg/Fe]–[Fe/H] (b) MDF, (c) [Mg/Fe] evolution, (d) [Fe/H] evolution, (e) $\epsilon_{\rm rm}$ evolution, and (f) gas mass evolution. The light blue lines correspond to the fiducial Inflows-Only simulation with $\tau_{\rm in} = 0.9$ Gyr. The dark blue and lime green lines assume $\tau_{\rm in} = 0.1$ Gyr and $\tau_{\rm in} = 0.5$ Gyr, respectively, and all other parameters are the same as for the fiducial Inflows-Only simulation (see Table 2.3.1). The colored squares in panel (a) denote the average abundances of each simulation. The gray circles are the Bensby et al. 2014 abundance ratios for the kinematically-selected thick disk stars described in Section 2.3.2. Two gray dashed lines corresponding to [Mg/Fe]=0 and [Fe/H]=0 have been added as visual guides. The Milky-Way MDF for the geometrically-selected thick disk stars at 3kpc $<$ R $<$ 5kpc from Hayden et al. 2015 (detailed in Section 2.3.2) is shown as a comparison as a slate gray dashed line in panel (b). In panels (c) and (d), the solid lines indicate the gas reservoir abundance ratios while the dotted lines indicate the effective gas return abundance ratios. The gray dot-dashed lines show the onset of SNIa at $t = 100$ Myr. In panels (e) and (f), the gray dotted lines mark the peak of the star-formation history at $t = \tau_{\rm SF} = 1$ Gyr.

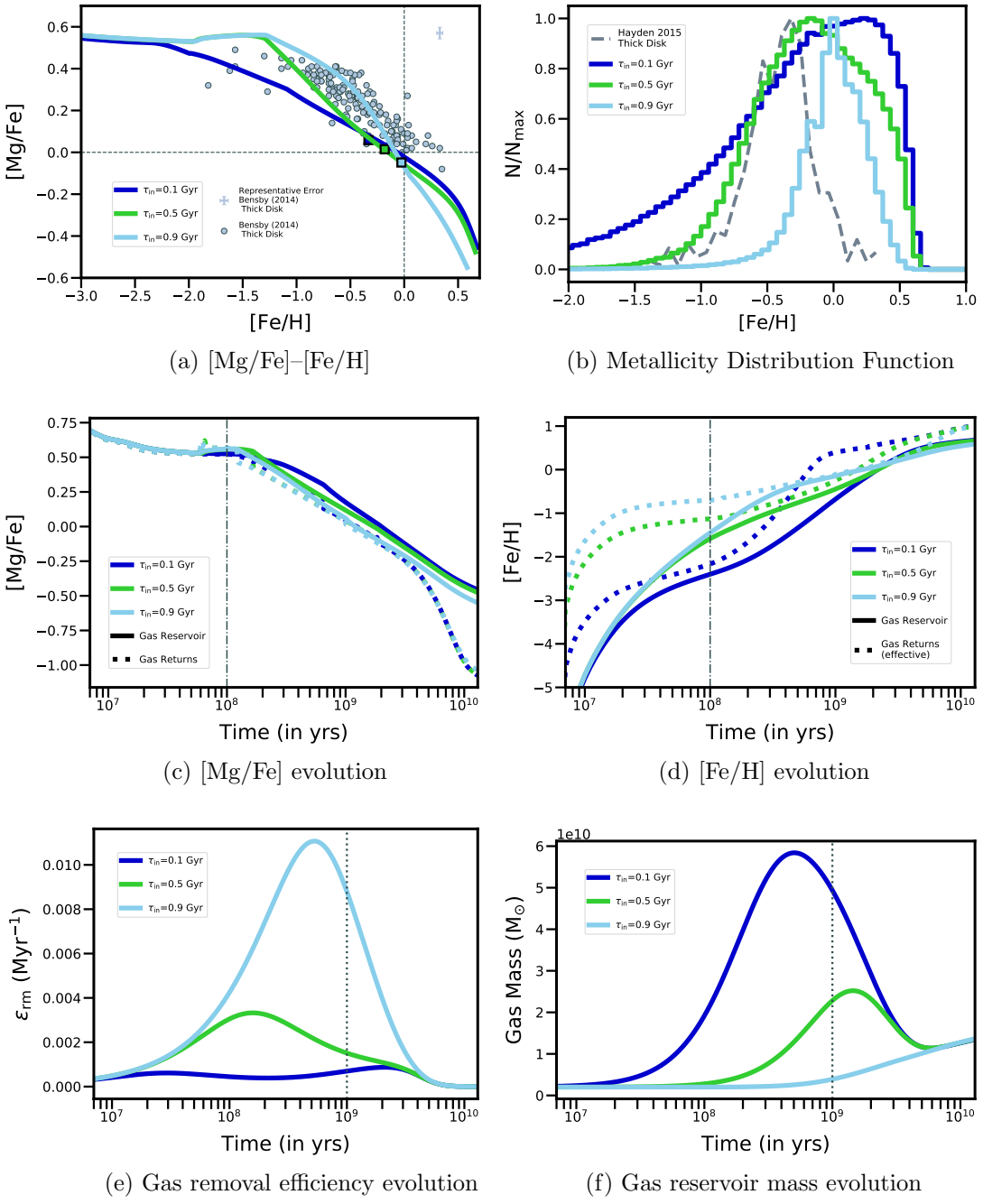

(a) [Mg/Fe]–[Fe/H]

(b) Metallicity Distribution Function

(c) [Mg/Fe] evolution

(d) [Fe/H] evolution

(e) Gas removal efficiency evolution

(f) Gas reservoir mass evolution

Figure 2.11: **Varying the inflow timescale ($\tau_{\mathbf{in}}$)**, see the previous page for the full caption text.

The Initial Mass Function

Figure 2.12 shows the effects of changing the initial mass function, comparing the fiducial Closed Box model with a standard Kroupa IMF in red, to a Salpeter IMF in dark blue, a Kroupa-like IMF with a less top-heavy high-mass slope ($\alpha = 2.6$) in green, and a Kroupa-like IMF with a more top-heavy high-mass slope ($\alpha = 1.8$) in sky blue. Varying the IMF affects the returns by changing the fraction of stellar generation mass that goes into CCSN progenitors vs AGB progenitors vs low-mass stars that will slowly and passively evolve.

The $\alpha = 1.8$ IMF simulation produces more high mass stars that explode as CCSN (and more high mass AGB stars). Therefore, while stellar returns will still have roughly the same ratio of [Mg/Fe], which is set by the yields, the more top-heavy IMF simulation will produce a higher mass of stellar returns from these short-lived massive stars. So long as star-formation is still significant ($t < \mathrm{t_{transSF}}$), $R^{*}_{\mathrm{Mg}}[i]$ and $R^{*}_{\mathrm{Fe}}[i]$ are both proportionally higher as compared to $R^{\mathrm{SNIa}}_{\mathrm{Fe}}[i]$ for the top-heavy IMF than for the fiducial standard Kroupa IMF simulation, producing a higher gas return $\dfrac{R_{\mathrm{Mg}}[i]}{R_{\mathrm{Fe}}[i]}$ ratio. Note that in reality, a more top-heavy IMF simulations would likely result in a smaller fraction of the stellar mass being converted into stars that would produce C+O white dwarfs. Since C+O white dwarfs are the main progenitors of SNIa, a more top-heavy IMF should produce fewer SNIa. However, due to our implementation of an observationally-derived SNIa DTD, this is not taken into account but it would increase $\dfrac{R_{\mathrm{Mg}}[i]}{R_{\mathrm{Fe}}[i]}$ even further. This higher proportion of stellar returns to SNIa returns means that the decline in the gas return [Mg/Fe] will be slower for a more top-heavy IMF,

producing a more shallow leg slope, as seen in panels (c) and (a).

The higher proportion of high-mass stars that are formed by a more top-heavy IMF has the additional consequence of having the stellar mass die off more quickly. Therefore, to produce the same $M_{*,f}$, more stars must have been born initially and thus, the star-formation rate must have been higher. Since the gas mass evolution is very similar for all four simulations (panel (f)), the increased star-formation rate results in a higher gas removal efficiency, as shown in panel (e). The higher $\epsilon_{\rm rm}$ decreases the inertia of the gas reservoir, making it less capable of resisting changes in the return [Mg/Fe]. However, the returns are already decreasing much more slowly for the top-heavy IMF so this does not have a very noticeable impact on the evolution of [Mg/Fe].

On the other hand, this higher $\epsilon_{\rm rm}$, does have a significant effect on the [Fe/H] evolution. The [Fe/H] gas returns are quite similar across the four simulations. Due to the considerably higher $\epsilon_{\rm rm}$ of the top-heavy IMF simulation, its $[{\rm Fe/H}]_{\rm gas}$ is rapidly driven to the super-solar gas returns and, as we can see in panel (d), by $t \approx 2.5-3$ Gyr, $[{\rm Fe/H}]_{\rm gas} \approx [{\rm Fe/H}]_{\rm ret}$. The decline in $\epsilon_{\rm rm}$ shortly thereafter results in $[{\rm Fe/H}]_{\rm gas}$ plateauing, causing the remaining star-formation to happen at very high (and significantly super-solar) [Fe/H]. This is reflected in the MDF shown in panel (b) as a lighter low-metallicity tail, since fewer stars are born at low [Fe/H], and a pile-up of stars formed at very high metallicity, resulting in a very super-solar peak and right-edge to the MDF. Since the other three simulations are less top-heavy, their $\epsilon_{\rm rm}$ is lower at all times and their $[{\rm Fe/H}]_{\rm gas}$ never get as close to the gas return [Fe/H]. Thus, the enrichment happens more gradually, with a shorter plateau and a less extreme pile-up at high-metallicity

and a heavier low-metallicity tail. The faster enrichment of the more top-heavy IMF simulation also results in the "knee" in the [Mg/Fe]–[Fe/H] track corresponding to a higher [Fe/H] and thus being shifted to the right in panel (a).

Figure 2.12 *(next page)*: Chemical evolution of three Closed Box simulations when **varying the initial mass function**: (a) [Mg/Fe]–[Fe/H] (b) MDF, (c) [Mg/Fe] evolution, (d) [Fe/H] evolution, (e) $\epsilon_{\rm rm}$ evolution, and (f) gas mass evolution. The red lines correspond to the fiducial Closed Box simulation which uses a standard Kroupa IMF with a high mass slope, $\alpha = 2.3$. The sky blue lines and green lines respectively assume a top-heavy ($\alpha = 1.8$) and top-light ($\alpha = 2.6$) Kroupa-like IMF, while the dark blue lines use a Salpeter IMF. All other parameters are the same as for the fiducial Closed Box simulation (see Table 2.3.1). The colored squares in panel (a) denote the average abundances of each simulation. The gray circles are the Bensby et al. 2014 abundance ratios for the kinematically-selected thick disk stars described in Section 2.3.2. Two gray dashed lines corresponding to [Mg/Fe]=0 and [Fe/H]=0 have been added as visual guides. The Milky-Way MDF for the geometrically-selected thick disk stars at 3kpc $<$ R $<$ 5kpc from Hayden et al. 2015 (detailed in Section 2.3.2) is shown as a comparison as a slate gray dashed line in panel (b). In panels (c) and (d), the solid lines indicate the gas reservoir abundance ratios while the dotted lines indicate the gas return abundance ratios. The gray dot-dashed lines show the onset of SNIa at $t = 100$ Myr. In panels (e) and (f), the gray dotted lines mark the peak of the star-formation history at $t = \tau_{\rm SF} = 1$ Gyr.

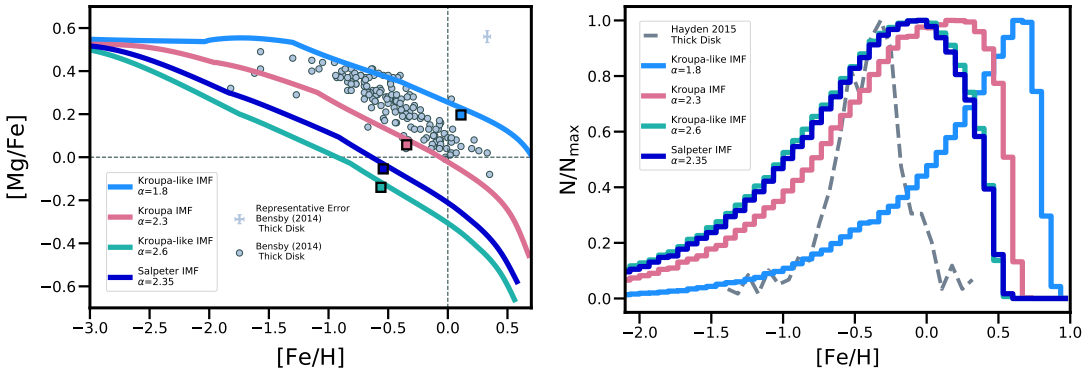

(a) [Mg/Fe]–[Fe/H]

(b) Metallicity Distribution Function

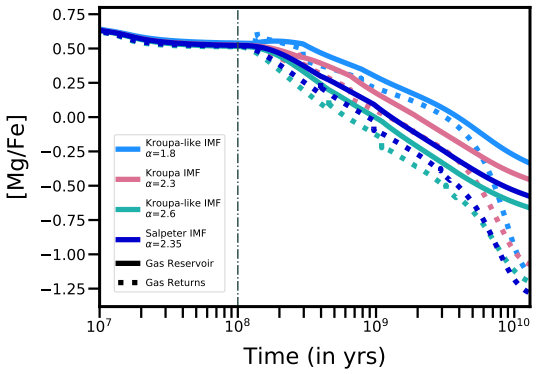

(c) [Mg/Fe] evolution

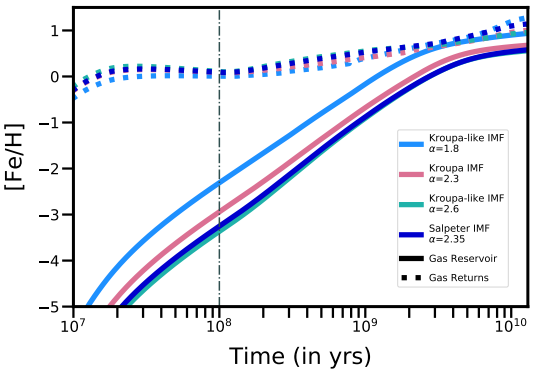

(d) [Fe/H] evolution

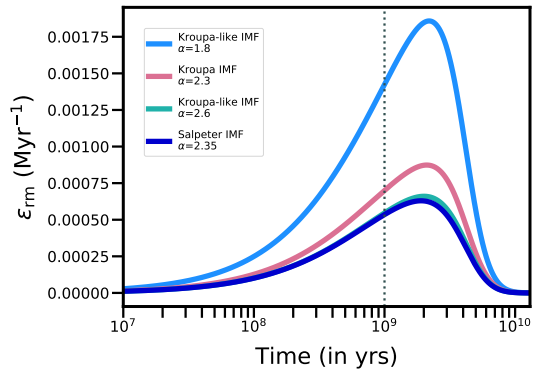

(e) Gas removal efficiency evolution

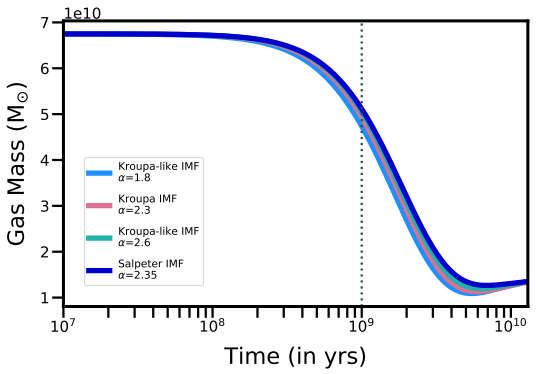

(f) Gas reservoir mass evolution

Figure 2.12: **Varying the initial mass function**, see the previous page for the full caption text.

The star-formation timescale, $\tau_{\rm SF}$

Figure 2.13 shows three closed box simulations where the star-formation timescale has been varied by a factor of 2 from the default $\tau_{\rm SF} = 1$ Gyr of the fiducial Closed Box simulation that is plotted as the red lines. The sky blue simulation has the shortest star-formation timescale of $\tau_{\rm SF} = 0.5$ Gyr while the dark blue simulation has the longest with $\tau_{\rm SF} = 2$ Gyr. Changing the star-formation timescale affects both the gas removal efficiency, as is clear in panel (e), and the gas returns, which are shown in panels (c) and (d) as dotted lines.

In the case of a shorter $\tau_{\rm SF}$, the bulk of the stars form earlier in the simulation and in a shorter period of time. Therefore, to produce the same $M_{*,f}$, the shorter $\tau_{\rm SF}$ simulation must have a higher SFR around the peak of star-formation. As a result, while star-formation is important (prior to $t_{\rm transSF}$), the shorter $\tau_{\rm SF}$ simulation will have a significantly higher $\epsilon_{\rm rm}$ that will also peak earlier than for the fiducial Closed Box simulation.

In addition, this also impacts the gas return abundance ratios. Since the bulk of the stars form earlier in the simulation, more SNIa will have had time to explode in the short $\tau_{\rm SF}$ simulation than in the fiducial simulation. Thus, after the onset of SNIa, the $[{\rm Fe/H}]_{\rm ret}$ for the three simulations start to diverge, as seen in panel (d), due to the increased Fe gas mass returned from SNIa for shorter-$\tau_{\rm SF}$ simulations. Similarly, the increased contribution of Fe from the higher number of SNIa will also cause $[{\rm Mg/Fe}]_{\rm ret}$ to decline more rapidly after $t_{\rm DTD}$ for a shorter-$\tau_{\rm SF}$ simulation. This effect is clearly evident in panel (c) where the [Mg/Fe] of the gas returns for the sky blue simulation

($\tau_{\rm SF}$ = 0.5 Gyr) decreases much faster after the knee than for the fiducial or $\tau_{\rm SF}$ = 2 Gyr simulations.

For the $[{\rm Mg/Fe}]_{\rm gas}$ evolution, the faster decline of the [Mg/Fe] of the gas returns and the higher $\epsilon_{\rm rm}$ work in tandem to produce a very steep post-knee slope that is also reflected in the steeper slope of the leg in the [Mg/Fe]–[Fe/H] track (panel (a)). In the case of the $[{\rm Fe/H}]_{\rm gas}$ evolution, the early gas reservoir abundance ratios are a result of the impact of $\tau_{\rm SF}$ on $\epsilon_{\rm rm}$. The gas returns at this point are nearly identical since the difference in SNIa production is not yet relevant. Instead, the significantly higher $[{\rm Fe/H}]_{\rm gas}$ of the sky blue simulation is due to the higher $\epsilon_{\rm rm}$ that allows the gas returns to more effectively enrich the gas reservoir at early times. At later times, as discussed above, $[{\rm Fe/H}]_{\rm ret}$ for the short-$\tau_{\rm SF}$ simulation increases due to the higher number of SNIa explosions but these returns have little effect on $[{\rm Fe/H}]_{\rm gas}$ due to the precipitous drop in $\epsilon_{\rm rm}$ caused by the declining SFR. Thus, $[{\rm Fe/H}]_{\rm gas}$ plateaus significantly earlier and is flatter than for the other two simulations that have higher $\epsilon_{\rm rm}$ at late times.

As a result of the more rapid early enrichment of the short-$\tau_{\rm SF}$ simulation, the knee is shifted to the right, to higher [Fe/H] in the [Mg/Fe]–[Fe/H] track shown in panel (a). As mentioned above, the sharper decline in [Mg/Fe] produces a steeper leg slope. Though we have previously deduced the changes in the shape of the MDF from the differences in the behavior of the $[{\rm Fe/H}]_{\rm gas}$ evolution, this will give us an incomplete picture in the case of varying $\tau_{\rm SF}$. For all other parameters that we have discussed, the star-formation histories are the same for the simulations being compared (or proportional to one another in the case of the IMF). However, changing $\tau_{\rm SF}$ also

changes the mass of stars formed from the gas at different $[Fe/H]_{gas}$, which changes the weighting for the MDF between the simulations that we examine here. Therefore, while we would normally expect the longer and flatter late time $[Fe/H]_{gas}$ plateau of the sky blue simulation to produce a more narrow MDF with a less heavy low-metallicity tail, this does not take into consideration that for a shorter τ_{SF}, the bulk of the stars are born earlier, when $[Fe/H]_{gas}$ is lower. Instead, as seen in panel (b), this results in a heavier low-metallicity tail and thus a broader MDF with a peak at lower-[Fe/H] and a lower average stellar [Fe/H]. Similarly, we might expect the faster decline in [Mg/Fe] to produce a lower average stellar [Mg/Fe] but the earlier star-formation means that the majority of stars are born before many SNIa have had a chance to explode, thus resulting in a higher average [Mg/Fe], as plotted in panel (a).

Figure 2.13 *(next page)*: Chemical evolution of three Closed Box simulations when **Varying the star-formation timescale ($\tau_{\rm SF}$)**: (a) [Mg/Fe]–[Fe/H] (b) MDF, (c) [Mg/Fe] evolution, (d) [Fe/H] evolution, (e) $\epsilon_{\rm rm}$ evolution, and (f) gas mass evolution. The red lines correspond to the fiducial Closed Box simulation with $\tau_{\rm SF} = 1$ Gyr. The dark blue lines and sky blue lines assume $\tau_{\rm SF} = 2$ Gyr and $\tau_{\rm SF} = 0.5$ Gyr, respectively, and all other parameters are the same as for the fiducial Closed Box simulation (see Table 2.3.1). The colored squares in panel (a) denote the average abundances of each simulation. The gray circles are the Bensby et al. 2014 abundance ratios for the kinematically-selected thick disk stars described in Section 2.3.2. Two gray dashed lines corresponding to [Mg/Fe]=0 and [Fe/H]=0 have been added as visual guides. The Milky-Way MDF for the geometrically-selected thick disk stars at 3kpc $<$ R $<$ 5kpc from Hayden et al. 2015 (detailed in Section 2.3.2) is shown as a comparison as a slate gray dashed line in panel (b). In panels (c) and (d), the solid lines indicate the gas reservoir abundance ratios while the dotted lines indicate the gas return abundance ratios. The gray dot-dashed lines show the onset of SNIa at $t = 100$ Myr. In panels (e) and (f), each dotted line in the matching simulation color marks the peak of the star-formation history at the corresponding $t = \tau_{\rm SF}$.

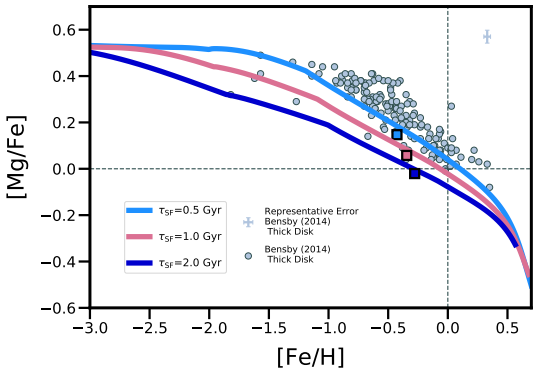

(a) [Mg/Fe]–[Fe/H]

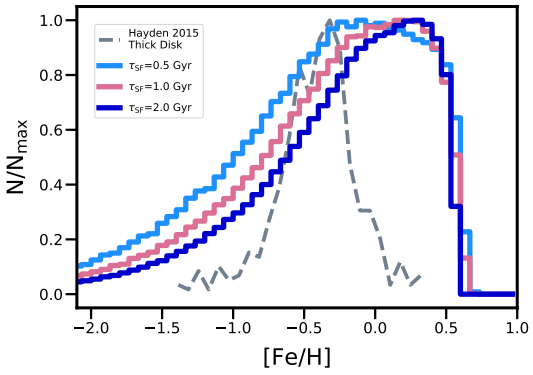

(b) Metallicity Distribution Function

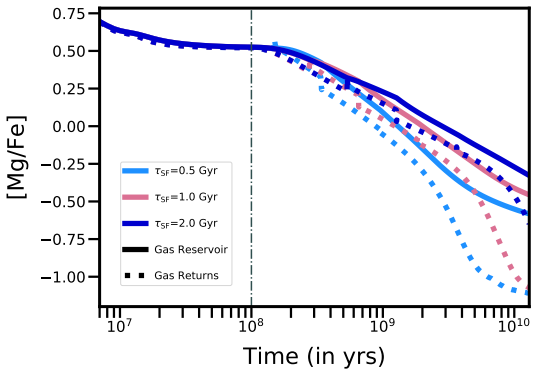

(c) [Mg/Fe] evolution

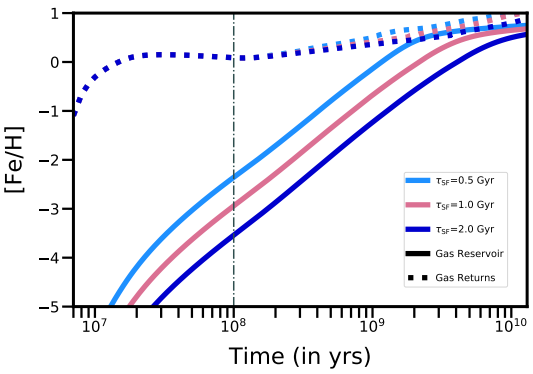

(d) [Fe/H] evolution

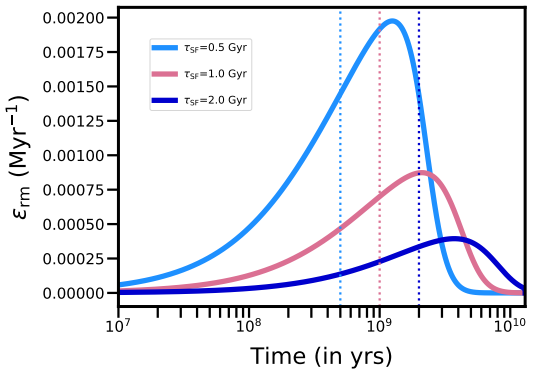

(e) Gas removal efficiency evolution

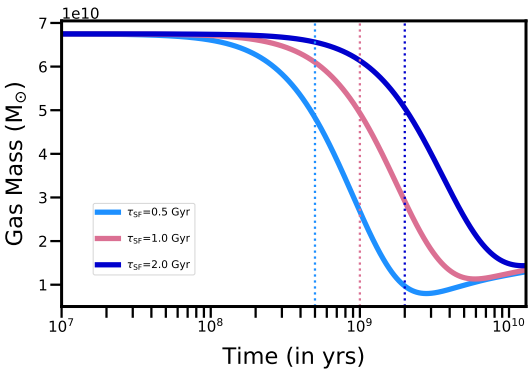

(f) Gas reservoir mass evolution

Figure 2.13: **Varying the star-formation timescale (τ_{SF})**, see the previous page for the full caption text.

2.4.4 Validating our chemical evolution model: The Milky Way Best-Fit

In Figure 2.14 and Table 2.4.4, we present a few simulations that reasonably reproduce the data described in Section 2.3.2. The simulation shown in light green represents an acceptable intermediate between the mass-weighted Milky-Way MDF derived by Bovy et al. (2012) and the Hayden et al. (2015) Milky Way mid disk MDF. The simulation shown in steel blue is a reasonable match to the Hayden et al. (2015) thick-disk MDF. There is a tension that arises between matching the Hayden et al. (2015) Milky Way thick-disk MDF and the slope of the [Mg/Fe]–[Fe/H] leg of the Bensby et al. (2014) stellar abundances. The Milky Way thick-disk MDF is very narrow and it peaks at a fairly low [Fe/H]$= -0.32$. Reproducing both sets of observations is rather difficult to achieve given the effects of the parameters we discussed above:

- Certain parameters that shift the MDF and keep the breadth ($\epsilon_{\rm out}$, $f_{\rm SN}$, and final gas fraction) would seem to be ideal for reproducing the MDF. However for $\epsilon_{\rm out}$, a higher outflow rate requires larger inflows to replace the gas that is removed and so the effective gas return abundance ratio for [Fe/H] is lower. As discussed in Section 2.4.3.2, this makes the slope of the leg steeper and moves it to the left, toward lower [Fe/H]. Moving the leg too far to the left means that the [Mg/Fe]–[Fe/H] Bensby thick disk data is no longer well matched. That is, the stellar abundance track should pass close to the origin, which is impossible when the leg is pushed toward lower [Fe/H]. For $f_{\rm SN}$, a very similar issue arises because the smaller stellar gas returns from SNIa and CCSN ejecta lower the effective gas

returns. Increasing the final gas fraction, as for $\epsilon_{\rm out}$, requires additional inflows so that [Fe/H] for the gas reservoir is consistently lower (starting shortly after the onset of SNIa) and a lower final [Fe/H] is reached at the end of the simulation. This, once again, has the effect of shifting the MDF to lower [Fe/H] as desired but it also shifts the leg of the [Mg/Fe]–[Fe/H] track to the left.

- Both increasing the $M_{\rm gas,0}$ and making the IMF more top heavy would make the [Mg/Fe]–[Fe/H] slope more gentle. However, a higher $M_{\rm gas,0}$ will also increase the low-Z tail of the MDF and serve to broaden it (see Section 2.4.3.1), which is incompatible with the distinctive narrowness of the observed MDF. The higher gas removal efficiency that accompanies a more top heavy IMF would also result in higher [Fe/H] enrichment of the gas reservoir, resulting in an MDF that peaks at higher [Fe/H] and thus is also incompatible with the observed MDF.

- Changes to $Z_{\rm in}$ and $\tau_{\rm in}$ do not have the desired effects on either the MDF or on the [Mg/Fe]–[Fe/H] track.

The two potentially promising parameters are $\tau_{\rm SF}$ and $t_{\rm DTD}$, which both shift the knee but do not strongly affect the late time chemical evolution of the gas reservoir. Thus, simulations varying $\tau_{\rm SF}$ and $t_{\rm DTD}$ change the slope of the leg in [Mg/Fe]–[Fe/H] without moving the leg inward (similar endpoints). We can shift the MDF to lower [Fe/H] through a combination of decreasing $\tau_{\rm SF}$ or increasing $t_{\rm DTD}$ so that lower (or less metal enhanced) outflows are required.

In the end, we find that reproducing the combination of narrowness and low-Z peak of the Milky Way thick disk MDF requires a higher final gas fraction of $f_{\rm gas,f} = 0.4$.

Though this is higher than our fiducial value of $f_{\rm gas,f} = 0.2$, constraining the gas content of the Milky Way and its component parts is very challenging and the estimates remain uncertain. Given the recent estimation of $M_{\rm gas}/M_* \approx 0.4$ for the solar neighborhood from McKee et al. (2015), this parameter value seems within the realm of possibility. While the minimum delay-time of SNIa is kept at its fiducial value of $\rm t_{DTD} = 100$ Myr, we find that we require a short star-formation timescale of $\tau_{\rm SF} = 0.4$ Gyr so that stars form early while $[\rm Fe/H]_{gas}$ is still low. We note that this timescale parameter is not easily comparable to the gas depletion timescale of more standard chemical evolution models, as discussed in more detail in Section 2.5.

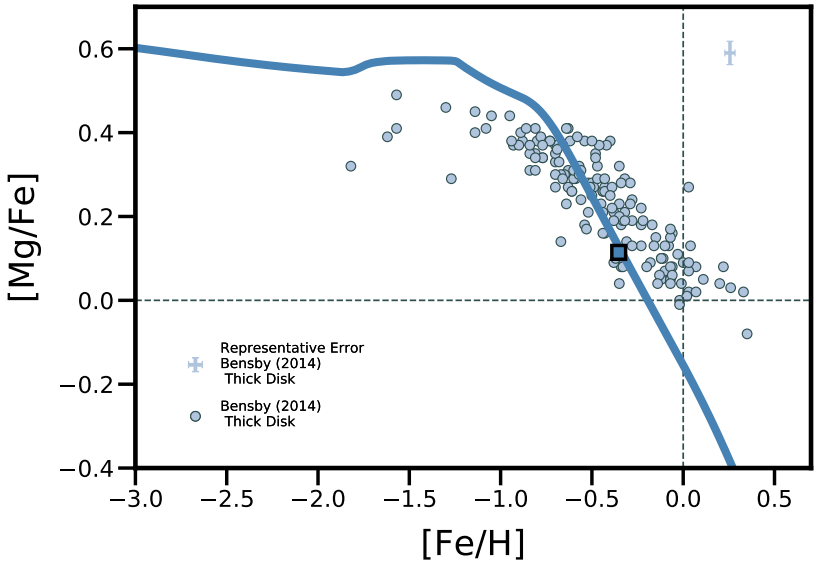

(a) [Mg/Fe]-[Fe/H]

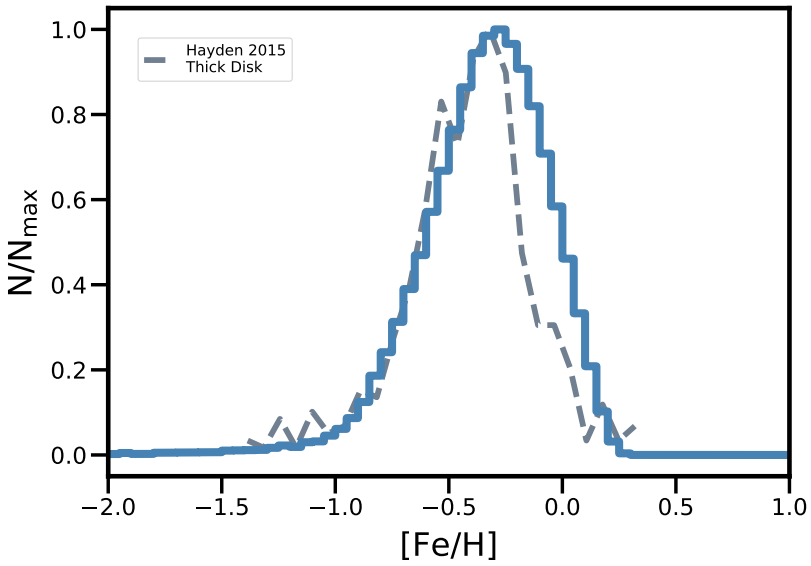

(b) Metallicity Distribution Function

Figure 2.14: *Top panel (a)*: Comparison of the [Mg/Fe]–[Fe/H] track produced by our best-fitting validation simulation (steel blue line) to the stellar abundance ratios (gray circles) of the kinematically-selected Bensby et al. 2014 Milky-Way thick disk stars described in Section 2.3.2. *Bottom panel (b)*: Comparison of the mass-weighted [Fe/H] distribution function (steel blue histogram) for the stars remaining at the end of our best-fitting validation simulation (at t = T_{gal} = 13 Gyr) to the observationally-derived Hayden et al. 2015 Milky-Way thick disk MDF at 3kpc < R < 5kpc (shown as the slate gray dashed line). Both sets of comparison data are described in Section 2.3.2. Within the constraints of our simple Galactic chemical evolution model, it is a significant challenge to simultaneously reproduce the observed [Mg/Fe]–[Fe/H] stellar abundance ratios (particularly the slope of the leg) and the remarkably narrow and quite sub-solar peak of the Milky-Way thick disk [Fe/H] distribution function.

Table 2.4: Parameter values for the Milky Way thick disk best-fit simulation

Parameter Name	**Parameter Value**
IMF α	Kroupa: 2.3 (high-mass slope) 1.3 (low-mass slope)
$\mathbf{M_{star,f}}$	$4.3 \times 10^{10} M_\odot$
$\mathbf{M_{*,f}}$	$5.4 \times 10^{10} M_\odot$
$\mathbf{M_{gas,0}}$	$2 \times 10^{9} M_\odot$
$\mathbf{t_{DTD}}$	100 Myr
$\boldsymbol{f}_{\mathbf{gas,f}}$	0.4
$\boldsymbol{\tau}_{\mathbf{SF}}$	0.4 Gyr
$\boldsymbol{\tau}_{\mathbf{in}}$	0.36 Gyr
$\mathbf{Z_{in}}$	10^{-10}
$\boldsymbol{\epsilon}_{\mathbf{out}}$	1.5
$\boldsymbol{f}_{\mathbf{SN}}$	0

2.5 Discussion and Conclusions

In Sections 2.3 and 2.4.1, we developed a framework for predicting and interpreting the influence of a physical process or ingredient in a galactic chemical evolution model on the final stellar abundance patterns. Here, we review how the chemical evolution of the (cold) gas in a galaxy is determined by the interplay of the effective gas returns, $R_{\rm eff}$, and the gas removal efficiency, $\epsilon_{\rm rm}$:

The convolution of the star formation history, IMF and yield tables sets the gas return abundance ratios and their expected time-evolution, as described in Section 2.4.1.1. As stars evolve and die they return gas to the reservoir that can be incorporated into future star-formation. These gas returns can be unenriched, as is the case for winds from passively evolving stars or they may be highly enriched due to byproducts of stellar nucleosynthesis in CCSN ejecta, AGB winds and eventually SNIa ejecta. However, these gas returns from stellar evolution are not the only contributions to the gas that get reincorporated into the reservoir and can change its composition. To take into account additional contributions like the hydrogen mass from inflows, we introduce the more general term "effective gas returns", as discussed in Section 2.4.3.2.

Aside from accounting for the gas that gets added to the gas reservoir, we must also consider the effect of removing gas from the reservoir. As summarized in Section 2.4.3.1, the gas removal efficiency is simply the fraction of the gas reservoir that is removed every time-step through, for instance, star-formation and galactic outflows. The gas removal efficiency controls how rapidly and closely the gas reservoir abundance ratios, such as $[{\rm Mg/Fe}]_{\rm gas}$ and $[{\rm Fe/H}]_{\rm gas}$, are driven to the abundance ratios of the

effective gas returns, $[\mathrm{Mg/Fe}]_{\mathrm{ret,eff}}$ and $[\mathrm{Fe/H}]_{\mathrm{ret,eff}}$. The larger the gas removal efficiency, the sooner the gas reservoir abundance ratios will approach the effective gas return ratios and the less the previous enrichment history will matter to the instantaneous gas reservoir abundances.

The effect on the chemical evolution of adding or changing a galaxy ingredient can be understood by examining its impact on the effective gas returns and the gas removal efficiency. In Section 2.4.2, we used this framework to understand the general stellar abundance properties of a galaxy and why they come about. We found that the basic features in the stellar [Mg/Fe]–[Fe/H] track, which we call the plateau, knee, and leg, arise from the abundance evolution of the gas returns (see Section 2.4.1.1). Finer details such as the location and sharpness of the knee and the steepness of the leg are influenced by the gas removal efficiency.

We discussed the key ways in which the effective gas returns and the gas removal efficiency evolve in the context of a closed box model and how they result in the characteristic broad MDF with a heavy low-metallicity tail and a super-solar peak as well as the rounded, gradual knee and gently sloped leg of the [Mg/Fe]–[Fe/H] track. We then examined how adding new galaxy ingredients such as inflows and outflows affects ϵ_{rm} and $\mathrm{R_{eff}}$ and produces a sharper knee that is shifted to higher [Fe/H] and a more steeply-sloped leg in the [Mg/Fe]–[Fe/H] track as well as a more narrow MDF with a peak that is shifted to lower [Fe/H].

In Section 2.4.3, we determined the detailed impact of nine key model parameters ($f_{\mathrm{gas,f}}$, $\mathrm{M_{gas,0}}$, $\mathrm{t_{DTD}}$, $\mathrm{Z_{in}}$, ϵ_{out}, f_{SN}, τ_{in}, the high-mass slope, α, of the IMF, and τ_{SF})

on $\epsilon_{\rm rm}$ and $R_{\rm eff}$ and the resulting changes to the features in the [Mg/Fe]–[Fe/H] track and to the shape of the MDF. Figure 2.15 depicts a summary of our findings for the [Mg/Fe]-[Fe/H] track. In purple, we detail which model parameters can shift the knee position and how they need to be adjusted to move the knee to higher [Fe/H]. Likewise, in green, we indicate the model parameters that affect the leg, with the arrows denoting how they need to be modified to steepen the slope and shift the leg inwards. We specify parenthetically if the feature changes are due to the parameter's influence on $\epsilon_{\rm rm}$, $R_{\rm eff}$, or both.

Similarly, we provide a schematic of the MDF in Figure 2.16, labeling the low-metallicity tail, the high-metallicity edge, the breadth, and the peak of the distribution. In Table 2.5, we document how a parameter must be adjusted to increase the low-Z tail, move the high-Z edge to the right, shift the peak to the left, and broaden (increase the breadth of) the distribution. We use the symbol $\Uparrow$ ($\Downarrow$) to denote that the parameter must be increased (decreased), followed by "small" if the overall impact is limited. If a feature is not significantly affected by a parameter such that it remains approximately the same regardless of the parameter value, we use the symbol $\approx$. If, on the other hand, the feature is impacted by the parameter in unpredictable ways (as is the case for how $\tau_{\rm in}$ shifts the MDF peak), the symbol $\emptyset$ is used.

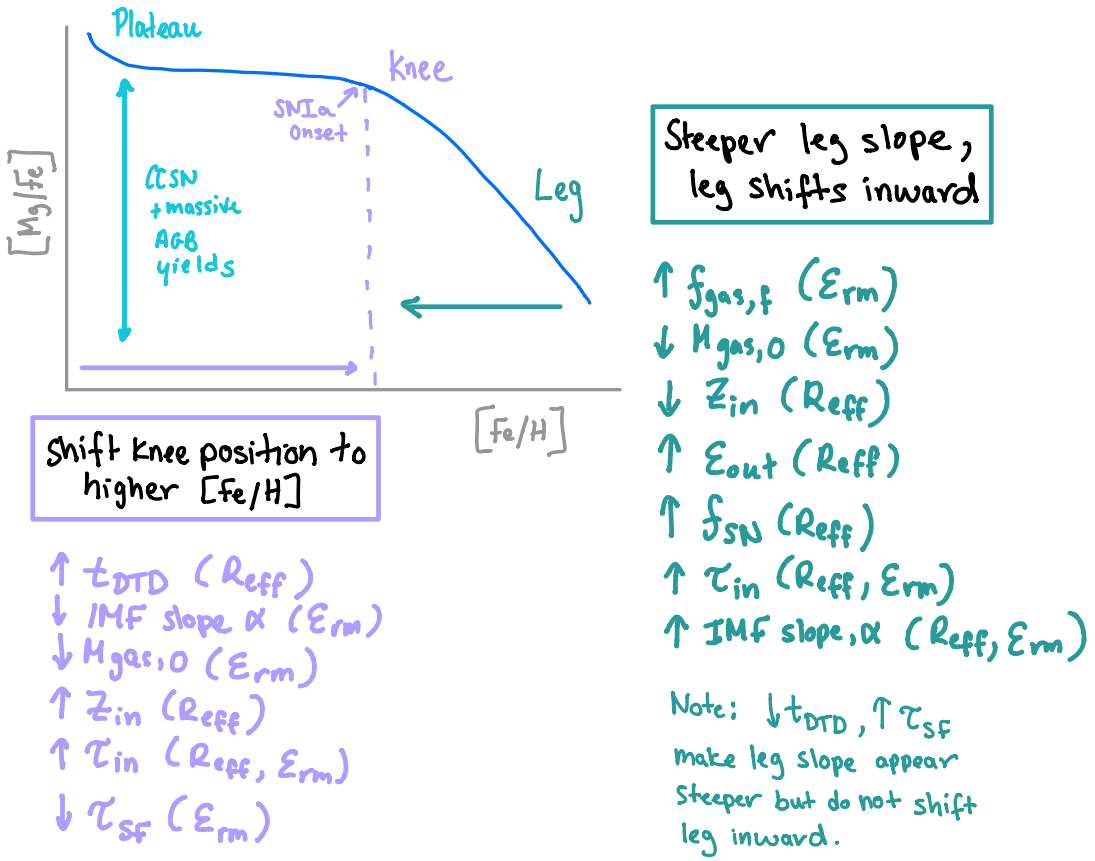

Figure 2.15: A schematic showing the plateau, knee, and leg of the [Mg/Fe]–[Fe/H] track and how changing our simulation parameters influences these characteristic features.

This framework of using $\epsilon_{\rm rm}$ and $R_{\rm eff}$ to interpret the role of a galaxy ingredient works for a wide variety of galaxy models. However, the way in which a physical process impacts $\epsilon_{\rm rm}$ and $R_{\rm eff}$ will depend on the particular prescription implemented in the model. We therefore compare our model implementation to the classic "gas-regulator" model and discuss some important distinctions and consequences.

The principal difference between these classic models and ours is in the implementation of the star-formation rate. In our model, we elect to provide the SFH of the galaxy as a simulation input, where the SFH has a functional form that is well-

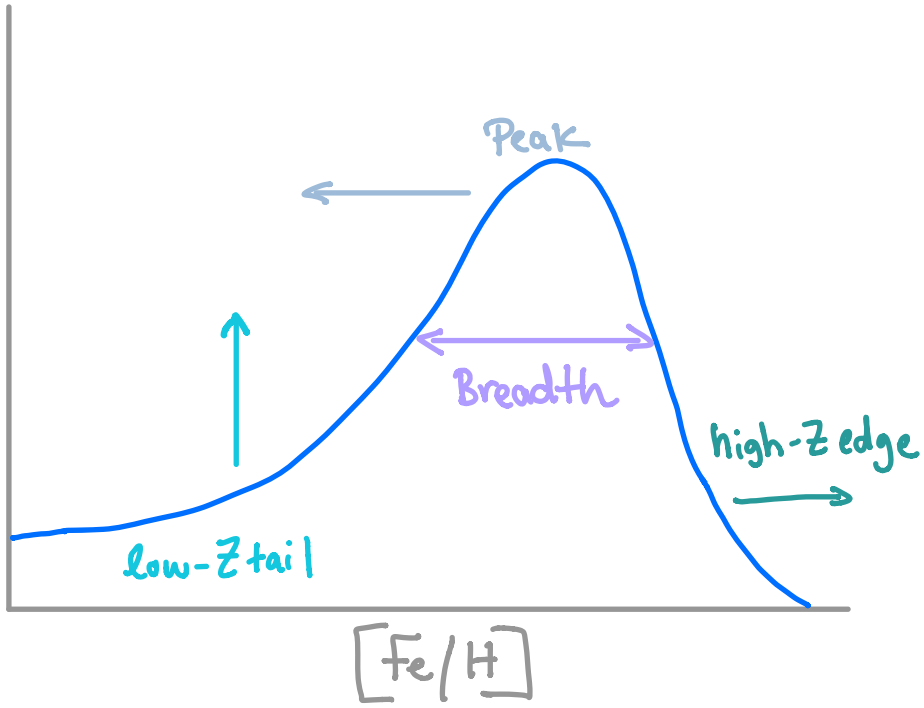

Figure 2.16: A schematic showing the characteristic features of the metallicity distribution function: the high-Z edge (i.e. the maximum stellar [Fe/H]), the peak (i.e. the mode of the distribution), the breadth, and the weight of the low-Z tail (heavy/light). Table 2.5 summarizes how the 9 parameters explored in Section 2.4.3 must be changed in order to make the low-Z tail heavier (i.e., have a higher proportion of stars born at low metallicities), push the high-Z edge to higher [Fe/H], shift the peak to lower [Fe/H], and broaden the MDF.

Table 2.5: How parameters affect features of the MDF

	low-Z tail $\Uparrow$	**high-Z edge** $\Rightarrow$	**peak** $\Leftarrow$	**breadth** $\Uparrow$
$\boldsymbol{f_{\mathrm{gas,f}}}$	$\Uparrow$	$\Downarrow$	$\Uparrow$	$\approx$
$\mathbf{M_{gas,0}}$	$\Uparrow$	$\Uparrow$	$\Downarrow$, small	$\Uparrow$
$\mathbf{t_{DTD}}$	$\Uparrow$	$\Downarrow$, small	$\Uparrow$	$\Uparrow$
$\mathbf{Z_{in}}$	$\Downarrow$	$\Uparrow$, small	$\Downarrow$	$\Downarrow$
$\boldsymbol{\epsilon_{\mathrm{out}}}$	$\Uparrow$	$\Downarrow$	$\Uparrow$	$\approx$
$\boldsymbol{f_{\mathrm{SN}}}$	$\Uparrow$	$\Downarrow$	$\Uparrow$	$\approx$
$\boldsymbol{\tau_{\mathrm{in}}}$	$\Downarrow$	$\Downarrow$	$\emptyset$	$\Downarrow$
IMF $\boldsymbol{\alpha}$	$\Uparrow$	$\Downarrow$	$\Uparrow$	$\Uparrow$
$\boldsymbol{\tau_{\mathrm{SF}}}$	$\Downarrow$	$\Downarrow$, small	$\Downarrow$	$\Downarrow$

Note. — This table summarizes how the 9 parameters explored in Section 2.4.3 must be changed in order to make the low-Z tail heavier (i.e., have a higher proportion of stars born at low metallicities; denoted as $\Uparrow$), push the high-Z edge to higher [Fe/H] ($\Rightarrow$), shift the peak to lower [Fe/H] ($\Leftarrow$), and broaden the MDF ($\Uparrow$). The symbols $\Uparrow$ and $\Downarrow$ depict whether increasing or decreasing the parameter will have the desired effect on the corresponding MDF feature. These arrow symbols are followed by "small" if the overall impact of the parameter on this feature is limited. If the feature is largely unaffected by the parameter, this is shown using the $\approx$ symbol. Finally, we use the $\emptyset$ symbol if the feature is affected by the parameter in unpredictable ways.

motivated by cosmological simulations and that reproduces the observed final stellar mass and final gas fraction of the Milky Way (see Section 2.2.1).

For our fiducial Inflows-Only and Inflows+Outflows, we choose to mimic a scenario where the accretion of gas triggers additional star formation by making the inflow timescale slightly shorter than the star-formation timescale. Thus, inflows shortly precede star formation. However, we do not enforce a causal relationship or physical link, and so this is not predictive (and more of an inverse modeling approach). On the other hand, this has the advantage of being a very flexible approach since the SFH can easily be modified to reflect different galaxy evolution assumptions. For example, in Chapter 3, we truncate the SFHs of elliptical galaxies to represent the star-formation quenching that must have occurred. This allows us to remain agnostic to which particular process caused the quenching while still gaining valuable insight into the evolution of these elliptical galaxies.

The "gas-regulator" model (Lilly et al. 2013), also known as the "bathtub model" (Krumholz & Dekel 2012), "reservoir" model (Bouché et al. 2010) or "equilibrium model" (Davé et al. 2012), takes more of a predictive or forward modeling approach, causally relating the gas mass, outflow rate, and star-formation rate of a galaxy through physically-motivated laws or prescriptions as well as connecting the evolution of the galaxy's gas accretion rate to the cosmological baryonic accretion rate and the growth of its dark matter halo as predicted by cosmological simulations. These models adopt a star-formation rate that resembles a Kennicutt-Schmidt (KS) law, with the SFR depending on the gas reservoir mass as $\mathrm{SFR}(t) = \epsilon_{\mathrm{SF}} \times \mathrm{M_{gas}(t)}$, with the

star-formation efficiency generally assumed to be constant (or changing very slowly) throughout the simulation. Additionally, episodes of star-formation can drive galactic winds or outflows where the outflow mass is assumed to be proportional to the instantaneous star-formation rate, such that $\mathrm{M_{out}}(t) = \eta \times \mathrm{SFR}$, where η is known as the mass-loading factor.

The gas-regulator model is predicated on the idea that galaxies mainly evolve in a quasi-steady state regime where the galaxy's gas reservoir mass remains approximately constant with time (as in Bouché et al. 2010; Davé et al. 2012) or changes much more slowly than the timescale, τ_{gas}, on which gas is consumed to form stars (e.g., Lilly et al. 2013). As gas and dark matter flows into a galaxy's dark matter halo, some fraction of the baryons will be accreted onto the galaxy, increasing the galaxy's gas reservoir mass, which in turn increases the SFR. This higher star-formation rate requires that a larger mass of gas be consumed to form stars, thus reducing the gas reservoir mass back toward its equilibrium value. Moreover, it also drives galactic winds that also remove gas from the reservoir, further aiding the return to equilibrium. In this way, the relationship between the star-formation, outflows, and gas mass serves to establish a mostly self-regulating system where, in the simplest case of a constant ϵ_{SF} and η, the SFR is approximately the inflow rate and the gas reservoir mass will remain approximately constant.

Lilly et al. (2013) stipulate that to be in this regime, the galaxy must have a gas consumption timescale (τ_{gas}) that is short compared to the timescale on which the star-formation efficiency, mass loading factor, and inflow rate evolve. A short τ_{gas} by

definition implies a large $\epsilon_{\rm SF}$, and since the gas removal efficiency for a gas-regulator model is simply $\epsilon_{\rm rm} = \epsilon_{\rm SF}(1+\eta)$ (see Section 2.2.7.3), a galaxy in the equilibrium regime will have a high gas removal efficiency. As we have extensively discussed, when the gas removal efficiency is high, the gas reservoir abundances reflect the current effective return abundances rather than the prior enrichment history. For the instantaneous recycling approximation that is assumed in classic regulator models, the gas returns only depend on the yields of the most recent star-formation and thus do not depend on the prior star-formation history. Consequently, for a galaxy evolving in conditions that are well approximated by a gas-regulator model, the gas reservoir abundances will depend predominantly on instantaneous galaxy properties like the current SFR (mediated by $\epsilon_{\rm SF}$ and η) and inflow rate, with these properties likely also depending on the galaxy's stellar mass. As we can see, the important conclusions of the gas-regulator models can also easily be understood in the context of our framework.

However, these conclusions are dependent on the instantaneous recycling approximation, which is unrealistic and cannot properly capture the evolution of galaxy abundance ratios. It is not only a terrible representation of the Fe enrichment of a galaxy due to the long delay-times associated with SNIa, but also fails to accurately capture the [α/H] metallicity evolution over time-spans $\gtrsim$ 1 Gyr due to the contributions of intermediate- and lower-mass stars, as discussed in Pipino et al. (2014). Therefore, we also compare our models to a more standard simple Galactic chemical evolution model that more accurately accounts for stellar lifetimes.

A recent such model is presented in Andrews et al. (2017), which uses the same

star-formation prescription and outflow prescription as the classic gas-regulator model. However their treatment allows for inflows that are not necessarily tied to cosmological simulations. They also assume a constant star-formation efficiency and mass loading factor, which are unlikely to be realistic over the full lifetime of the galaxy (e.g., Lilly et al. 2013; Bouché et al. 2010). Additionally, this causes the gas removal efficiency to be constant throughout the simulation, so differences in the evolution of [Mg/Fe] and [Fe/H] will primarily be due to the time-dependent behavior of the gas removal efficiency.

Unlike in the equilibrium regime of the gas regulator model, properly accounting for stellar lifetimes will cause the gas returns to strongly depend on the full SFH which is not known until the full simulation has been run. As such, this makes it much more difficult to predict, a priori, the resulting changes to the [Mg/Fe]–[Fe/H] track and MDF features, in contrast to our model where we provide the SFH as an input. The shape of the SFHs in more standard chemical evolution models are determined by the initial gas mass, inflows and outflows and therefore do not typically resemble the treatment in our model. For this reason, the star-formation timescales reported for these models cannot be directly compared to our results. Our star-formation timescales tend to be significantly shorter than theirs because we do not have an initial burst of star-formation.

We have presented a framework for understanding the impact of important physical processes on the chemical evolution of a galaxy. This framework is applicable to understanding other more classic models, although obviously the prescriptions will

make differences in how the gas removal efficiency and effective gas returns are affected. Our decision to use the SFH as an input to the simulation reflects more of an inverse modeling approach that is more agnostic to the causal relationships between different galaxy ingredients. This flexibility enables us to make choices for the SFH and inflow rate that can be more applicable to specific galaxy evolution scenarios and to incorporate additional external information. For instance, in recent years, we have been able to determine SFHs of local galaxies, and this model is better suited to studying their chemical evolution, as it can incorporate their measured SFH as an input. Therefore, this model is more versatile than classic chemical evolution models: it simultaneously allows us to explore non-standard assumptions (for instance, allowing us to decouple the SFR from the gas mass) and to more accurately model the chemical evolution of specific galaxies by directly incorporating additional constraints such as an observationally-derived SFH. We present another example of this model's versatility in Chapter 3 where we apply our model to study of low-redshift elliptical galaxies.

Chapter 3

The Chemical Evolution of Elliptical Galaxies

3.1 Introduction

In Chapter 2, we detailed our one-zone galactic chemical evolution code and validated it by reproducing the elemental abundance patterns of the Milky Way thick disk. The flexible framework we presented, however, applies to a wide range of galaxy evolution scenarios. Rather than using it to understand the evolution of a single galaxy like the Milky Way, our model can instead be employed (with some modifications described in Section 3.3) to investigate the formation and evolution of an entire population of galaxies that are very different from our own. One such population is elliptical galaxies[12] which, unlike star-forming galaxies like our Galaxy, have very red colors and are

[12]Elliptical galaxies are often also referred to as early-type galaxies, passive galaxies, and quiescent galaxies. Though they can have subtle distinctions in the literature, they are interchangeable for the

observed to be dispersion supported, gas-poor, and to primarily have old stellar populations and lack recent star-formation. In this chapter, we use our model to study the chemical evolution of elliptical galaxies in the nearby Universe across a wide range of stellar masses. However, in contrast to the work done in Chapter 2 for which we had a wealth of Milky Way star-by-star abundance measurements to constrain our models, for the investigation in this chapter of elliptical galaxy abundance patterns it is only possible to consider their integrated average abundances or population-wide averages. This is due to the fact that beyond the Local Group, star-by-star abundance measurements are either extremely challenging or impossible. Therefore, with only a few exceptions, the properties of the unresolved stellar populations of elliptical galaxies can solely be investigated by means of the integrated-light of these galaxies.

The observed α-enhancement with respect to iron[13] at the centers of massive elliptical galaxies has been well-established in the literature for the past 30 years. Worthey et al. (1992) was the first to convincingly show that [Mg/Fe] took on a wide range of super-solar values within the population of elliptical galaxies. Numerous other papers (e.g., Jørgensen 1999; Trager et al. 2000; Thomas et al. 2005; Schiavon 2007; Johansson et al. 2012) have since confirmed this, finding that the α-enhancement measured in elliptical galaxies increases with increasing galaxy velocity dispersion (and stellar mass). Worthey et al. proposed three mechanisms in their 1992 paper that could explain this galaxy mass-dependent α-enhancement: 1) shorter star formation timescales for more

purposes of this work.

[13]Whenever we use the terms α-enhancement or α-enhanced, we mean that the ratio of the α element abundance (most often Mg) to that of iron (Fe) is higher than what is observed in the Sun.

massive elliptical galaxies, 2) a variable initial mass function (IMF) with a flatter slope at the high-mass end for the more massive galaxies, and 3) galactic winds that would preferentially remove more Fe (but not Mg) from more massive ellipticals.

Historically, this first interpretation of [Mg/Fe] of as an indicator of the galactic star-formation timescale has been favored, whereby more massive elliptical galaxies convert their gas into stars much more rapidly than lower mass ellipticals (e.g., Trager et al. 2000; Pipino & Matteucci 2004; Thomas et al. 2005). This decrease in the star-formation timescale with increasing galaxy mass (sometimes referred to as "chemoarcheological downsizing", see Fontanot et al. 2009) has generally been attributed to the role of radio-mode feedback from active galactic nuclei (AGN) in shutting off the star formation in more massive galaxy halos (e.g., Di Matteo et al. 2005; De Lucia et al. 2006). Indeed, chemical evolution modeling of elliptical galaxies using cosmological semi-analytical models (SAMs) (e.g., Pipino et al. 2009) and hydrodynamical models (e.g., Segers et al. 2016) has been successful in, at least qualitatively, reproducing the observed α-enhancement trend with galaxy mass (cf. Arrigoni et al. 2010; Gargiulo et al. 2015; Fontanot et al. 2017, who also include AGN feedback but fail to reproduce the [α/Fe]-σ relation).

However, these same models fail to reproduce another important galaxy scaling relation — that the metallicity of galaxies is observed to increase with increasing galaxy mass. This is known as the mass-metallicity relation (MZR) and is observed both for the gas-phase metallicity (e.g., Tremonti et al. 2004) as well as for the stellar metallicity (e.g., Gallazzi et al. 2005; Kirby et al. 2013) across a range of galaxy masses that span

many orders of magnitude (for a review, see Maiolino & Mannucci 2019). Specifically, Thomas et al. (2005) and Gallazzi et al. (2006) found that the [Z/H] or $\log(Z/Z_{\odot})$ measured for elliptical galaxies also increases with galaxy mass and this has since been found to also hold true for [Fe/H] (e.g., Conroy et al. 2014).

The inability of chemical evolution models to self-consistently reproduce the observed positive correlation between α-enhancement and elliptical galaxy mass simultaneously with the mass-metallicity relation has been noted since 2009 by Pipino et al. and Calura & Menci and even in the most sophisticated state-of-the-art simulations this issue has yet to be satisfactorily resolved (see discussion in e.g., De Lucia et al. 2017; Yan et al. 2019). As a result of this on-going tension between the simulated and observed elliptical galaxy scaling relations, the idea that the slope of the IMF must vary with elliptical galaxy mass has gained renewed attention in the past few years. Numerous recent papers (e.g., Gargiulo et al. 2015; Fontanot et al. 2017; Barber et al. 2018; Yan et al. 2019) have advocated that a non-universal IMF that becomes more top heavy with increasing galaxy mass (such as the one proposed by the IGIMF theory Weidner & Kroupa 2005; Weidner et al. 2011, 2013) is needed to reproduce the observed abundance patterns of elliptical galaxies.

The aim of this work is to explore additional possible explanations of the observed elliptical galaxy abundance patterns and attempt to simultaneously reproduce the higher α-enhancement with increasing galaxy mass and the stellar MZR (as represented by the positive correlation between the measured $\langle$[Mg/Fe]$\rangle$ and $\langle$[Fe/H]$\rangle$ of ellipticals in the $\langle$[Mg/Fe]$\rangle$–$\langle$[Fe/H]$\rangle$ plane) without resorting to a non-universal IMF.

This chapter is organized as follows: We discuss the elliptical galaxy average abundance measurements (Conroy et al. 2014) that we use to constrain our simulations in Section 3.2. In Section 3.3 we describe our improved custom galactic chemical evolution code, focusing particularly on how the code from Chapter 2 has been updated and altered to better model elliptical galaxies. We explore the role of different parameters on the mass-weighted $\langle$[Mg/Fe]$\rangle$ and $\langle$[Fe/H]$\rangle$ of modeled elliptical galaxies and present "close-correspondence" models in Section 3.4. In Section 3.5, we summarize our results and discuss our alternative explanation of the observed $\langle$[α/Fe]$\rangle$ and $\langle$[Fe/H]$\rangle$ trends and its implications for elliptical galaxy evolution. Our main conclusions are summarized in Section 3.6.

3.2 Data

Traditionally, the abundance measurements of elliptical galaxies have been determined by analyzing specific stellar absorption line features (such as Hβ, Mgb, Fe5270, Fe5335) in the optical (4000Å$< \lambda <$ 6400Å) spectra of individual galaxies using the Lick/IDS index system (Burstein et al. 1984; Worthey 1994; Worthey & Ottaviani 1997). While the development of the Lick index system enabled a a tremendous leap in the quantitative study of the stellar population properties of elliptical galaxies (particularly in determining their elemental abundance patterns and breaking the age-metallicity degeneracy) this system also has some significant complications (see Schiavon 2010; Conroy 2013).

One important issue for the Lick index system is that other spectral features

can contaminate the nearby pseudo-continuum regions, making it very challenging to accurately determine the continuum associated with a Lick index absorption feature. This can greatly impact the derived abundance measurements (e.g., Prochaska et al. 2005). In addition, the number of elements whose abundances can be determined using Lick indices is limited. As a result, many important papers on the abundance patterns of elliptical galaxies (Trager et al. 2000; Thomas et al. 2005; Thomas et al. 2010) only report measurements of Mg (used as a tracer of α), Fe, H, and occasionally C, N, and Ca. Robust measurements of other α-element abundances derived using Lick indices such as those of oxygen and silicon remain rare (though see Schiavon 2007; Worthey et al. 2014). The oxygen abundance in particular can be extremely difficult to measure properly using Lick indices since atomic oxygen transitions cannot be seen in moderate resolution spectra and unfortunately, the impact of non-solar abundance ratios on the Lick indices of TiO (the only oxygen-containing molecule that has transitions in the optical) have not been well characterized (Conroy 2013).

The relatively recent development of SPS models that simultaneously fit the full optical to near infrared (NIR) spectrum and that allow for non-solar element abundance patterns (e.g., Walcher et al. 2009; Conroy & van Dokkum 2012a) has enabled more reliable abundance measurements for a wider array of elements (e.g., Conroy & van Dokkum 2012b). In particular, by applying these new full spectrum fitting techniques to high signal-to-noise (S/N) stacked elliptical galaxy spectra, Conroy et al. (2014) have been able to more robustly confirm the positive correlation between [α/Fe] and [Fe/H] with increasing galactic velocity dispersion and measure precise elemental abundances

that are well suited for chemical evolution modeling.

For this work we therefore adopt the chemical abundances derived by Conroy et al. (2014) using the full spectrum fitting of stacked SDSS spectra of elliptical galaxies. These galaxies were selected from the SDSS Main Galaxy Survey (Strauss et al. 2002) to be passive galaxies, according to the methodology described in Peek & Graves (2010). The individual galaxy spectra had signal-to-noise (S/N) ratios of $\sim 20\text{Å}^{-1}$, which is insufficient to accurately determine detailed abundance measurements. Hundreds of spectra within the redshift range of $0.025 < z < 0.06$ were therefore stacked into seven bins according to their stellar velocity dispersion, with mean values corresponding to $\sigma = 88,\ 112,\ 138,\ 167,\ 203,\ 246,$ and 300 km s^{-1}. This produced seven spectra with high S/N of around 500Å^{-1} to 1800Å^{-1}. These data were fit with a Monte-Carlo Markov Chain formalism as described by Conroy & van Dokkum (2012b), using the stellar population synthesis (SPS) model developed by Conroy & van Dokkum (2012a). The resulting 14 elemental abundances, as well as their corresponding average galactic stellar masses, are listed in Table 1 of Conroy et al. (2014). Since these elemental abundances are derived using stacked integrated-light spectra, they represent average values for the elliptical galaxies within each velocity dispersion bin. We therefore use angled brackets around these elemental abundances to highlight the averaged nature of these measurements.

In this chapter, we are primarily focused on $\langle$[Mg/Fe]$\rangle$ and $\langle$[Fe/H]$\rangle$ although we also examine how our "close-correspondence" models reproduce $\langle$[O/Fe]$\rangle$ and $\langle$[Si/Fe]$\rangle$ at the end of Section 3.4. Figure 3.1 shows the $\langle$[Mg/Fe]$\rangle$ and $\langle$[Fe/H]$\rangle$ average abun-

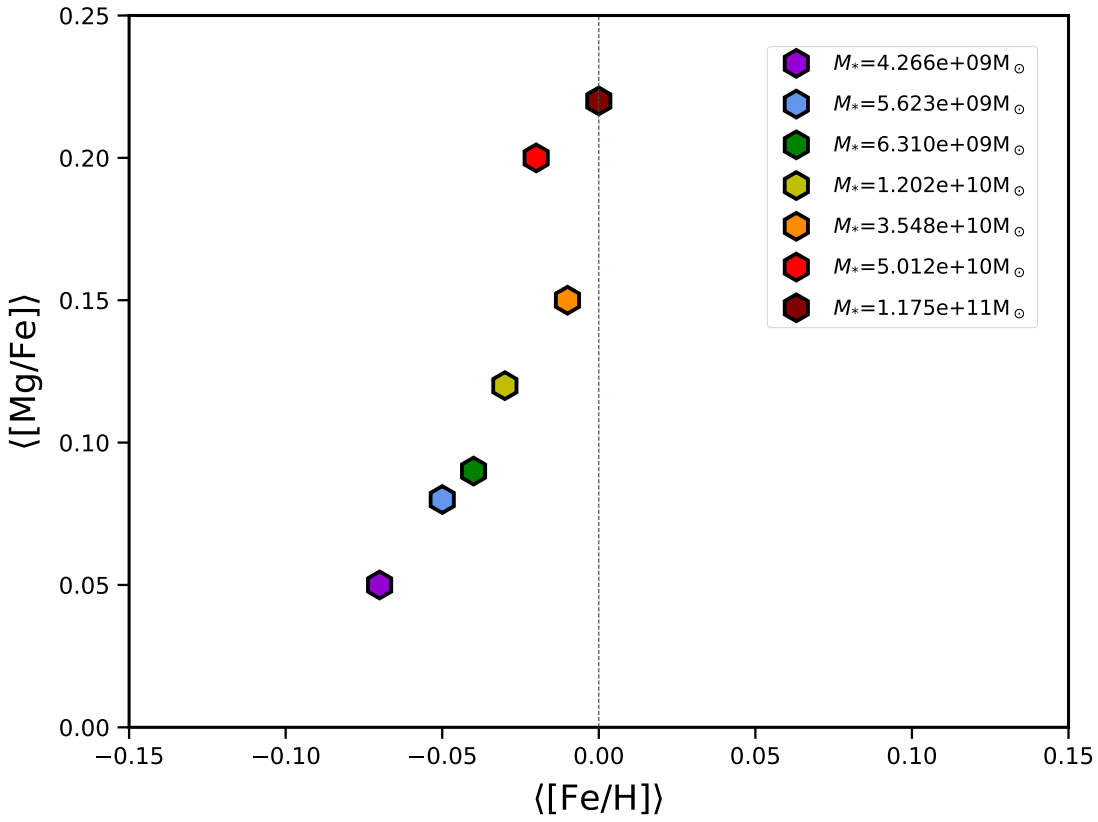

Figure 3.1: The observed ⟨[Mg/Fe]⟩ and ⟨[Fe/H]⟩ average abundance ratios for the seven stacked elliptical galaxy integrated-light spectra from Conroy et al. (2014). The purple, blue, green, yellow, orange, red, and maroon hexagons correspond to elliptical galaxy velocity dispersion bins of $\sigma = 88,\ 112,\ 138,\ 167,\ 203,\ 246$, and 300 km s^{-1}, respectively. The legend shows the equivalent galaxy stellar masses. A dashed line corresponding to ⟨[Fe/H]⟩ = 0 has been added as a visual guide. For more details on these data and how the abundances were measured, see the accompanying text in Section 3.2.

dance ratios for each of the $\sigma = 88,\ 112,\ 138,\ 167,\ 203,\ 246$, and 300 km s^{-1} stacked elliptical galaxy spectra as purple, blue, green, yellow, orange, red, and maroon hexagons, respectively. In this and all other figures in this chapter, hexagons with the same color-coding are used to denote the observed average abundances.

3.3 Model Description

For the work in this chapter, we use the chemical evolution code described in Chapter 2 with a few modifications or updates that we detail below. Most notably, we adopt truncated star-formation and inflow histories and implement net rather than absolute yields with the option of extrapolating the default CCSN yields to higher stellar masses. These modifications to our chemical evolution model were made to allow easier comparison with literature results or to better represent the evolution of elliptical galaxies.

The simulations in this chapter are run for 13 Gyr to match the age of the universe at z=0.06 which is the upper-limit on the redshift of the SDSS elliptical galaxies analyzed in Conroy et al. (2014). Unless specified otherwise, we assume that the masses of stars range from $0.1M_{\odot} \leq M \leq 100M_{\odot}$ and are formed according to a standard Kroupa initial mass function (IMF) (see previous chapter, Section 2.2.2). We adopt a truncated linear-exponential star-formation history (SFH) and inflow history which we elaborate on below in Sections 3.3.1 and 3.3.2, respectively, and the outflow prescription is identical to the one described in Section 2.2.5 of the previous chapter. As stars evolve to their final life-stages, they enrich the ISM according to the nucleosynthetic yields that we describe in Section 3.3.3, with stellar lifetimes determined from the MIST models[14] and assuming a initial-final mass relation (IFMR) for passively evolving stars from Renzini & Ciotti (1993) (see Section 2.2.3 in Chapter 2 for more details). As always,

[14] http://waps.cfa.harvard.edu/MIST/ (Dotter 2016; Choi et al. 2016; Paxton et al. 2011, 2013, 2015, 2018)

the number of Type Ia supernovae (SNIa) produced by a stellar generation, as a function of time, is set by the Maoz & Mannucci (2012) delay-time distribution (DTD), with a default minimum delay-time of $t_{DTD} = 100$ Myr.

The average chemical abundance ratios (e.g., $\langle$[Mg/Fe]$\rangle$ and $\langle$[Fe/H]$\rangle$) for the simulations in this work are determined by taking the weighted mean of the abundance ratio for each stellar generation where the weights are the final stellar mass of each generation (at the end of the simulation). This produces a mass-weighted average abundance as opposed to the light-weighted average abundance that is measured from an integrated-light spectrum of a galaxy. Therefore, our simulation averages will not perfectly capture the expected observed abundance ratio. For example, in the case of lower mass ellipticals with more recent star formation, the integrated light of the galaxy may be more disproportionately dominated by these young stellar populations, skewing the observed abundances as compared to our model abundance ratios. However, our simulated abundances should be a good approximation of the observed abundances of more massive ellipticals which have short star-formation timescales and stopped forming stars long ago and thus mostly comprise old stellar populations.

3.3.1 Star-Formation History

As in Chapter 2, we implement a linear-exponential star-formation history (SFH) with a characteristic star-formation timescale, τ_{SF}. Our choice of a smooth functional form rather than a bursty one is predicated on the fact that the measurements to which we compare our simulations are derived from stacked galaxy spectra (see Section 3.2) that reflect an average and therefore smoothed SFH. However, in order

to better replicate the lack of recent star formation and old ages observed in the red elliptical galaxies that comprise the Conroy et al. (2014) sample, we cut short the SFHs at a truncation time $T_{trunc} = F_{trunc} \times \tau_{SF}$.

We assume a default truncation factor of $F_{trunc} = 2.5$ and we explore the effect of changing F_{trunc} on the simulated average galaxy abundance ratios in Section 3.4 with the plotted results presented in panel (b) of Figure 3.3. As such, unless explicitly stated otherwise, the SFHs of simulated elliptical galaxies presented in this work are modeled as:

$$\Psi(t) = \begin{cases} \Psi_0 t e^{\left(-t/\tau_{SF}\right)} & \text{for } t \leq 2.5 \times \tau_{SF} \\ 0 & \text{for } t > 2.5 \times \tau_{SF} \end{cases} \tag{3.1}$$

where Ψ_0 is the normalization factor chosen such that the sum of the stellar mass and remnant mass at the end of the simulation, $T_{gal} = 13$ Gyr, is the corresponding average stellar galaxy mass presented in Table 1 of Conroy et al. (2014).

3.3.2 The Inflow History

As in Chapter 2, the galaxy is assumed to have an initial reservoir of cold gas of mass $M_{gas,0}$. The additional cold gas needed to sustain star-formation is provided according to the inflow history, which is represented by a linear-exponential functional form with a characteristic inflow timescale. The inflow timescale is assumed to be shorter than the star-formation timescale ($\tau_{in} < \tau_{SF}$) to reflect the fact that the star-formation is fueled by the inflow of external cold gas. The inflow history is truncated

at the same time as the SFH, $\mathrm{T_{trunc}} = \mathrm{F_{trunc}} \times \tau_{\mathrm{SF}}$, as would be expected if an active galactic nucleus (AGN) were quenching the star-formation by blowing out or heating up the galaxy's cold gas supply and thus also preventing the future infall of fresh cold gas.

$$\mathrm{M_{in}(t)} = \begin{cases} I_0 t e^{\left(-t/\tau_{\mathrm{in}}\right)} & \text{for } t \leq 2.5 \times \tau_{\mathrm{SF}} \\ 0 & \text{for } t > 2.5 \times \tau_{\mathrm{SF}} \end{cases} \tag{3.2}$$

The inflow normalization, I_0, is determined as in Section 2.2.6, except that rather than normalizing the inflow history to produce a given gas fraction at the end of simulation ($f_{\mathrm{gas,f}}$), we instead specify the gas fraction at the time of truncation, $f_{\mathrm{gas,trunc}} \equiv f_{\mathrm{gas}}(t = \mathrm{T_{trunc}})$. Since the elliptical galaxies in the Conroy et al. (2014) sample are generally "red and dead" with no present-day indicators of cold gas or recent star-formation, we choose a nearly zero default value for the gas fraction at truncation of $f_{\mathrm{gas,trunc}} = 0.007$, which would be expected if star-formation ceased due to the complete consumption of the cold gas reservoir. However, it is important to note that in the scenario described above where an AGN expels or heats up the cold gas reservoir, present-day observed cold gas fractions would not be indicative of the cold gas fraction at truncation.

The default inflow metallicity is nearly pristine with $\mathrm{Z_{in}} = 10^{-10}$ and we refer the reader to Section 2.2.6 in Chapter 2 for details on how we determine the inflow element mass fractions.

3.3.3 Nucleosynthetic Yields

For the work presented in this chapter, we adopt the nucleosynthetic yields by Kobayashi et al. (2006) for core-collapse supernovae (CCSNe), Karakas (2010), Fishlock et al. (2014), and Doherty et al. (2014a,b) for asymptotic giant branch stars (AGBs) and super-AGBs, and the W70 models from Nomoto et al. (1997) for Type Ia SNe (SNIa), as detailed in Section 2.2.3 of the previous chapter. However, while the simulations in Chapter 2 employed absolute yields (also known as gross yields or total yields), we chose instead to implement net yields for CCSNe and AGB stars when modeling the chemical evolution of elliptical galaxies. The absolute yield of element i produced by an AGB star (CCSN) is simply the mass of the element, $M_{\rm lost}(i)$, present in the integrated stellar winds (total stellar ejecta) and is a strictly positive quantity. In contrast, the net yield of element i, $M_{\rm net}(i)$, is the difference between the absolute yield and the mass of the element that would initially have been present in that mass of stellar material, with a positive value indicating an overall production of this element and a negative value signifying that the element is destroyed in these stars.

A challenge to implementing net yields in this chemical evolution code is that while the AGB yield tables include net yields and initial element mass fractions (or production factors), the Kobayashi et al. (2006) CCSN yield tables do not. In order to convert the provided absolute yields to net yields, we must therefore make an assumption about the initial composition of the progenitor model. For the sake of consistency and simplicity, we assume that the initial composition of the stars in the Z=0.001, Z=0.004, and Z=0.02 Kobayashi et al. (2006) yield tables are the same as for the equivalent

metallicity tables in Doherty et al. (2014a,b)[15], which we calculate from the provided production factor. For the Z=0 case, we assume a hydrogen mass fraction of X=0.25 and a helium mass fraction of Y=0.75, with all other elements set to zero. Not all the elements included in the Kobayashi et al. (2006) yield tables are also in the Doherty et al. (2014a,b), which the code handles by setting the missing initial mass fractions to zero, likely leading to an overproduction of these elements in our CCSN net yields. This is not, however, an issue for any of the elements (H, O, Mg, Si, and Fe) that we examine in this chapter. Additionally, in order to ensure mass conservation, we track an additional "Other" element since the Doherty et al. (2014a,b) tables include an s-process proxy element denoted "g" that we cannot have correspond to a specific element in our CCSN yield tables. This also enables the flexibility to track any number of elements with our code, allowing faster simulations by having fewer tracked elements with all non-tracked elements instead contributing to the "Other" element.

Since nucleosynthetic yield tables are only generated for a single initial stellar composition at each metallicity, we assume that the stellar yields depend only on the initial mass and total metallicity of the progenitor star. However, particularly given that we do not interpolate our stellar yield tables to a more finely sampled metallicity grid, instead using the same tabulated yields for relatively large stellar metallicity ranges, this means that using absolute yields can introduce unintended metallicity effects[16]. This issue is avoided when using net yields and while we find that the difference in the

[15]Note that in the Doherty et al. (2014a,b) yield tables, all the models for a given metallicity have the same initial stellar composition, regardless of their initial stellar mass.

[16]For instance, a slower [Fe/H] enrichment (due, e.g., to a higher initial gas mass) would unexpectedly lead to a higher overall production of metals in the simulation despite identical star-formation histories and the use of metallicity-independent yields.

average abundance ratios when using net yields vs absolute yields is rather small, we find net yields to be preferable due to their more predictable nature.

An additional benefit of using net yields is that they allow us to more easily and reasonably extrapolate our CCSN yields to stellar masses beyond those covered by the Kobayashi et al. (2006) yield tables. Many of the commonly used CCSN nucleosynthetic tables, particularly those covering non-solar stellar metallicities, do not calculate yields for stars more massive than $\sim 35 - 40$ $M_\odot$ (e.g., Woosley & Weaver 1995; Chieffi & Limongi 2004; Kobayashi et al. 2006). However, the stellar masses for which a massive star explodes as a CCSN rather than collapsing to a black hole, either directly or as a result of fallback, remains very uncertain (see e.g., Brown & Woosley 2013; Farrell et al. 2020, and references therein) and is highly dependent on factors like the star's rotation and mass-loss rate.

While all very massive stars may not explode as CCSNe, it is likely that at least some do. According to Sukhbold et al. (2016), some solar-metallicity stars above 60 $M_\odot$ are able to explode as CCSNe due to the large amount of mass striped off their cores as winds. Similarly, Hirschi (2017) notes that rotation can enable sufficient mass-loss for this to also occur at lower metallicities. For the Sukhbold et al. (2016) models, the nucleosynthetic contributions of these stars is expected to be similar to those of $12 - 39 M_\odot$ stars but with an increase in helium burning products due to their massive winds lost prior to explosion.

Therefore, in order to allow stars more massive than $40 M_\odot$ to produce CCSNe and contribute to the nucleosynthesis in our simulations, we extend the Kobayashi et al.

(2006) CCSN yield tables to higher initial masses using a similar approach as the one described in Appendix B of Andrews et al. (2017). We assume that stars with initial masses $M_{\rm init} > 40{\rm M}_{\odot}$ return the same net yields as the Kobayashi et al. (2006) $M_{\rm init} = 40{\rm M}_{\odot}$ star of corresponding metallicity. We fit a linear relationship between the initial stellar mass and the pre-explosion and remnant masses in the Kobayashi et al. (2006) yield tables using sklearn.linear_model.LinearRegression (Pedregosa et al. 2011), which we use to extrapolate to the extended initial mass range. The total ejected mass and mass lost as stellar winds are simply $M_{\rm ejecta,tot} = M_{\rm preexp} - M_{\rm rem}$ and $M_{\rm wind,tot} = M_{\rm init} - M_{\rm preexp}$, respectively, and the absolute yields for each element i are easily calculated according to $M_{\rm ejecta}(i) = M_{\rm net}(i) + (M_{\rm ejecta,tot} \times X_0(i))$ where $X_0(i)$ is the initial mass fraction of element i.

In this way, we can vary the maximum stellar mass that explodes as a CCSN, $\rm M_{max}^{CCSN}$, where $\rm M_{max}^{CCSN}$ can take on any value between $13{\rm M}_{\odot}$ and the maximum stellar mass produced by the IMF, $\rm M_{max} = 100M_{\odot}$. As in the previous chapter, all stellar winds from massive stars ($M_{\rm init} \geq 13{\rm M}_{\odot}$) are assumed to provide no net contribution to the yields. This likely leads to a significant underestimate of the light-element production (particularly elements up to silicon) since stellar winds should enrich the ISM with H- and He- burning products (e.g., Sukhbold et al. 2016; Hirschi 2017).

3.4 Results

As previously mentioned in Section 3.1, recent papers have highlighted the difficulty of simultaneously reproducing the α-enhancement and mass-metallicity rela-

tion of elliptical galaxies. The positive correlation between the α-enhancement and the stellar mass (or velocity dispersion) of elliptical galaxies has historically been attributed to the star-formation timescale decreasing with increasing elliptical galaxy mass. The shorter the star-formation timescale, the earlier and more quickly the galaxy's stellar mass is formed and the less time there is for SNIa to explode and contaminate the gas with their iron-rich ejecta. Thus, if more massive elliptical galaxies have shorter $\tau_{\rm SF}$, the bulk of their stars will be born from gas that has been primarily been enriched by CCSN, resulting in a higher α-enhancement.

Table 3.1: Parameter values for the elliptical galaxy fiducial closed box simulations

	Elliptical Galaxy Velocity Dispersion Bin						
	$\boldsymbol{\sigma = 300}$ km s^{-1}	$\boldsymbol{\sigma = 246}$ km s^{-1}	$\boldsymbol{\sigma = 203}$ km s^{-1}	$\boldsymbol{\sigma = 167}$ km s^{-1}	$\boldsymbol{\sigma = 138}$ km s^{-1}	$\boldsymbol{\sigma = 112}$ km s^{-1}	$\boldsymbol{\sigma = 88}$ km s^{-1}
$\mathbf{M_{*,f}}$	1.175×10^{11}M$_\odot$	5.012×10^{10}M$_\odot$	3.548×10^{10}M$_\odot$	1.202×10^{10}M$_\odot$	6.310×10^{9}M$_\odot$	5.623×10^{9}M$_\odot$	4.266×10^{9}M$_\odot$
$\boldsymbol{\tau_{SF}}$	1.3208 Gyr	1.5316 Gyr	2.2548 Gyr	2.878 Gyr	3.7 Gyr	4.028 Gyr	5.1144 Gyr
$\mathbf{t_{DTD}}$	100 Myr	100 Myr	100 Myr	100 Myr	100 Myr	100 Myr	100 Myr
$\mathbf{F_{trunc}}$	2.5	2.5	2.5	2.5	2.5	2.5	2.5
$\mathbf{M_{gas,0}}$	1.35632×10^{11}M$_\odot$	5.7273×10^{10}M$_\odot$	3.9247×10^{10}M$_\odot$	1.3106×10^{10}M$_\odot$	6.685×10^{9}M$_\odot$	5.9031×10^{9}M$_\odot$	4.31144×10^{9}M$_\odot$
$\boldsymbol{f_{gas,trunc}}$	0.007	0.007	0.007	0.007	0.007	0.007	0.007
IMF	Kroupa: $\alpha_H = 2.3$	Kroupa: $\alpha_H = 2.3$	Kroupa: $\alpha_H = 2.3$	Kroupa: $\alpha_H = 2.3$	Kroupa: $\alpha_H = 2.3$	Kroupa: $\alpha_H = 2.3$	Kroupa: $\alpha_H = 2.3$
$\mathbf{M_{max}^{CCSN}}$	42.3M$_\odot$	42.3M$_\odot$	42.3M$_\odot$	42.3M$_\odot$	42.3M$_\odot$	42.3M$_\odot$	42.3M$_\odot$
Color	Maroon	Red	Orange	Yellow	Green	Blue	Purple
Figure	Fig. 3.2	Fig. 3.2 Fig. 3.4(a)	Fig. 3.2 Fig. 3.3(a),(b)	Fig. 3.2	Fig. 3.2 Fig. 3.5(a)	Fig. 3.2	Fig. 3.2

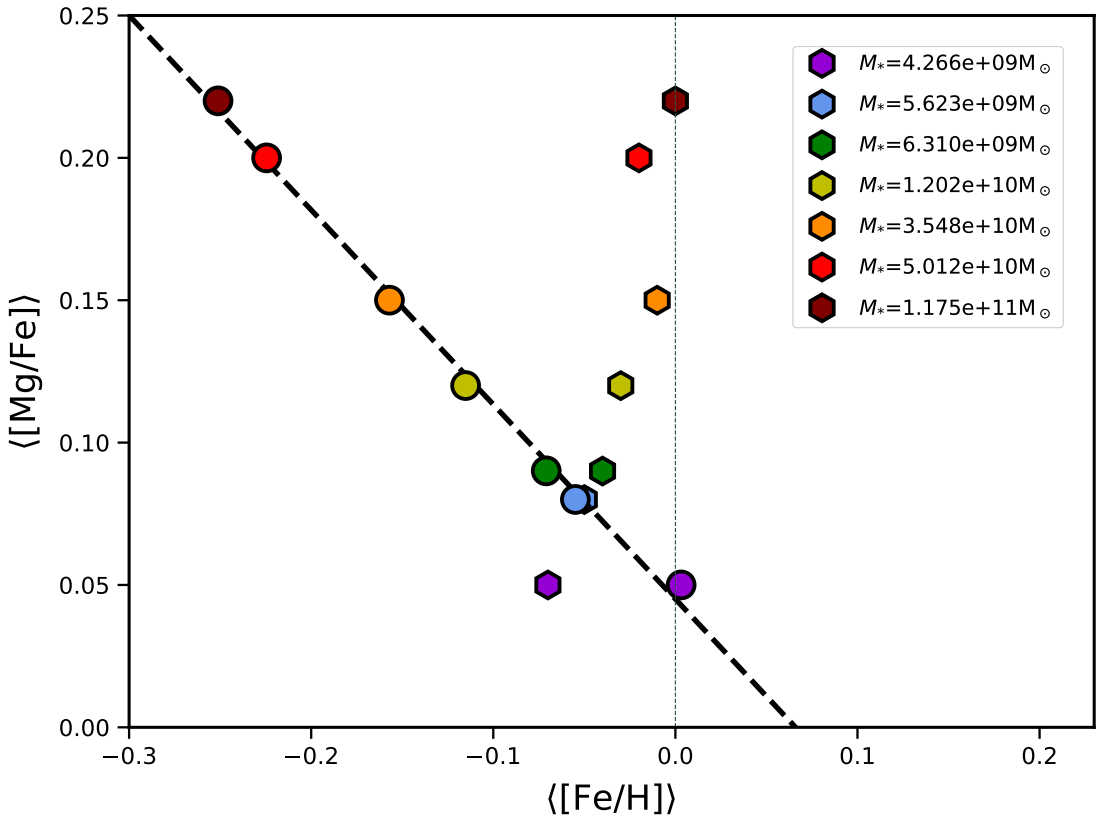

Figure 3.2: The average mass-weighted ⟨[Mg/Fe]⟩ and ⟨[Fe/H]⟩ of our seven fiducial closed box (no inflows or outflows) chemical evolution simulations (shown as circles) as compared to their corresponding observationally-derived abundance measurements from Conroy et al. (2014) (shown as hexagons). The same color-coding is used for the simulations as for the observations and is described in the caption for Figure 3.1. The star-formation timescales ($\tau_{\rm SF}$) of these fiducial closed box simulations have been tuned to reproduce the observed ⟨[Mg/Fe]⟩, resulting in shorter star-formation timescales for higher elliptical galaxy velocity dispersion (or stellar mass) bins. However, as discussed in the main text, for a closed box model a shorter $\tau_{\rm SF}$ results in a lower average metallicity. This produces an inverse relation between the galaxy mass and ⟨[Fe/H]⟩ that is contradictory to the observed mass-metallicity relation and the positive correlation between ⟨[Mg/Fe]⟩ and ⟨[Fe/H]⟩ that is seen in the Conroy et al. 2014 elliptical galaxy sample. The parameters for the fiducial closed box elliptical galaxy simulations are listed in Table 3.1. A linear fit to the simulated abundance ratios, which we refer to as the "closed box $\tau_{\rm SF}$-axis", is shown as the thick black dashed line. A thin grey dashed line at ⟨[Fe/H]⟩ = 0 has also been added as a visual guide.

Similarly, early and rapid star formation for massive ellipticals also implies that the gas out of which their stellar mass forms will not have time had to experience much enrichment overall. Since SNIa are the primary producer of Fe, these more massive elliptical galaxies would also be expected to have low average stellar metallicities or $\langle$[Fe/H]$\rangle$. However, the expected anti-correlation of the overall metallicity with galaxy stellar mass (or velocity dispersion) that results if the α-enhancement is simply due to a decreasing star-formation timescale, is in direct contradiction with the observed mass-metallicity relation, which shows that more massive galaxies have higher [Fe/H]. This tension is exemplified in the closed box simulations plotted in Figure 3.2. The parameters for these fiducial closed box simulations are listed in Table 3.1.

In this figure, the colored circles represent the average mass-weighted [Mg/Fe] and [Fe/H], denoted $\langle$[Mg/Fe]$\rangle$ and $\langle$[Fe/H]$\rangle$ respectively, of our seven fiducial closed box (no inflows or outflows) chemical evolution simulations. The star-formation timescales are tuned to reproduce the observed $\langle$[Mg/Fe]$\rangle$ (as is commonly done in the literature e.g, Matteucci 1994; Thomas et al. 2005) with best-fit values of $\tau_{\rm SF} \approx$ 1.32, 1.53, 2.25, 2.88, 3.70, 4.03, and 5.11 Gyr in order of decreasing galaxy stellar mass. As a comparison, we also plot as hexagons the observationally-derived abundance measurements from Conroy et al. (2014) (which are described in Section 3.2).

Each of these closed box simulations is run for 13 Gyr to match the approximate age of the Universe for the stacked SDSS galaxies observed by Conroy et al. (2014) at $0.025 < z < 0.06$. The final stellar mass of the simulation for each galaxy bin is listed in the legend and matches the one listed in Table 1 of Conroy et al. (2014). The initial

gas mass is chosen to fuel the full star-formation history with only a very small final gas fraction of $f_{\rm gas,trunc} = 0.007$ remaining at the time of star-formation truncation (see Section 3.3.2 for a discussion of our choice of $f_{\rm gas,trunc}$). The black dashed line, which we refer to as the "closed box $\tau_{\rm SF}$-axis", represents a linear fit to the $\langle$[Mg/Fe]$\rangle$-$\langle$[Fe/H]$\rangle$ relation of these $\tau_{\rm SF}$-varying fiducial closed box simulations.

We see that in requiring the simulations to replicate the observed $\langle$[Mg/Fe]$\rangle$, our models fail to reproduce the observed $\langle$[Fe/H]$\rangle$. Unlike the data, for which $\langle$[Fe/H]$\rangle$ varies by less than 0.1 dex and is positively correlated with galaxy mass, the closed box simulations predict an inverse correlation between galaxy mass and $\langle$[Fe/H]$\rangle$ and cover a much larger range of $\langle$[Fe/H]$\rangle$ (closer to 0.3 dex). Thus, it is apparent that the relationship between the average abundance ratios of elliptical galaxies and their stellar mass is not simply a result of the changing star-formation timescale.

Modifying other standard parameters of our closed box model, like the SNIa minimum delay time ($\rm t_{DTD}$) and the star-formation truncation factor ($\rm F_{trunc}$), have a similar impact as varying the star-formation timescale. All three of these parameters influence the relative timing of the onset of SNIa as compared to when the bulk of the stellar mass is formed: $\tau_{\rm SF}$ modifies the timescale on which stars are formed, $\rm t_{DTD}$ alters the minimum amount of time before SNIa start to explode, and $\rm F_{trunc}$ affects the fraction of the total stellar mass formed as a function of time. Since Fe is in both the denominator of $\langle$[Mg/Fe]$\rangle$ and the numerator of $\langle$[Fe/H]$\rangle$, parameters like these ones that primarily change the relative timing of the Fe production will impose an inverse relation (with similar slopes) between these average abundance ratios. This can be

seen in Figure 3.3 where we modify the fiducial $M_{star,f} = 3.548 \times 10^{10} M_{\odot}$ closed box simulation (shown as the orange circle in Figure 3.2), varying t_{DTD} for the top panel and F_{trunc} for the bottom panel.

Figure 3.3 *(next page)*: This figure shows the effects on the simulated elliptical galaxy abundance ratios of changing closed box parameters other than the star-formation timescale. In the top panel (a) we vary the SNIa minimum delay time from $t_{DTD} = 50$ Myr (lightest orange circle) to $t_{DTD} = 175$ Myr (darkest orange circle) in increments of 25 Myr and for the bottom panel (b) we increase the star-formation truncation factor from $F_{trunc} = 1.5$ (lightest orange circle) to $F_{trunc} = 6$ (darkest orange circle) in increments of 0.5. For each of these two sets of simulations, we modify the fiducial $M_{star,f} = 3.548 \times 10^{10} M_{\odot}$ closed box simulation (plotted as the orange circle in Figure 3.2) which assumes $t_{DTD} = 100$ Myr and $F_{trunc} = 2.5$ (the other default closed box parameter values are shown in Table 3.1). Varying the t_{DTD} and F_{trunc} parameters has a very similar impact on $\langle$[Mg/Fe]$\rangle$ and $\langle$[Fe/H]$\rangle$ as changing the τ_{SF} parameter, as can be seen from the over-plotted closed box τ_{SF}-axis (the thick dashed black line). As a visual reference, we include the observed abundance ratios measured by Conroy et al. 2014 (described in Section 3.2), which are shown as rainbow hexagons, and $\langle$[Fe/H]$\rangle = 0$, which appears as a thin grey dotted line.

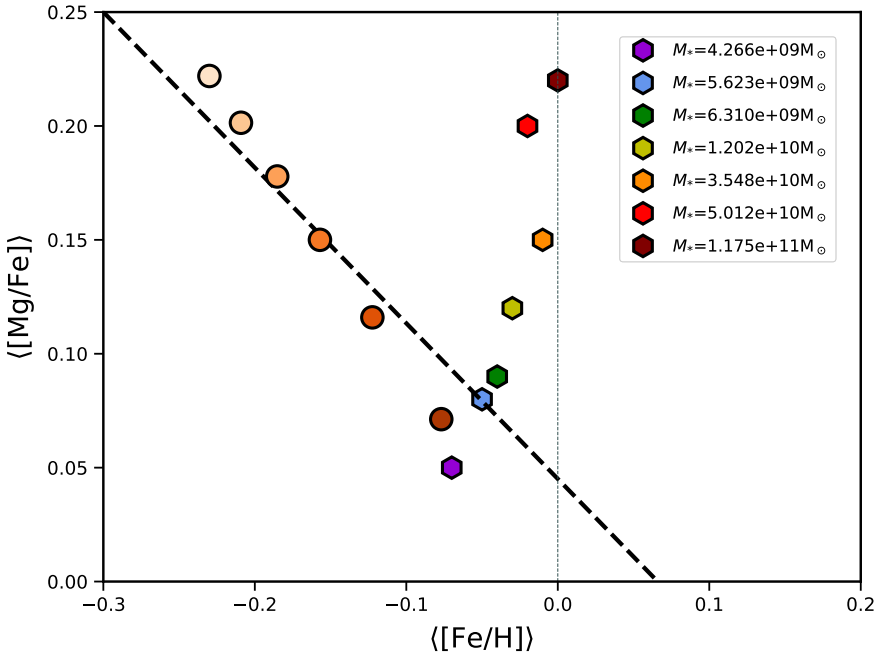

(a) Vary t_{DTD}

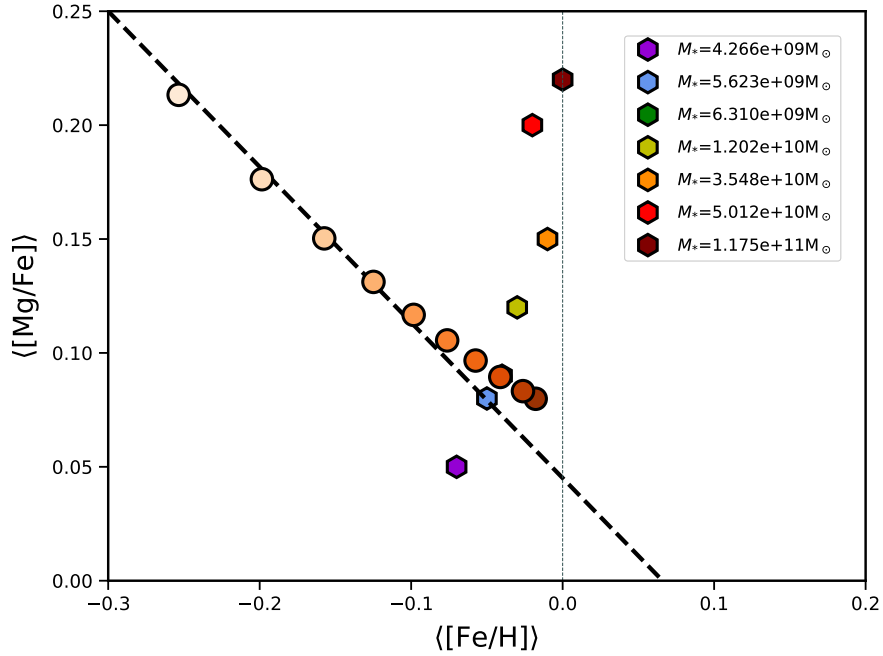

(b) Vary F_{trunc}

Figure 3.3: The effects on the simulated elliptical galaxy abundance ratios of changing closed box parameters other than the star-formation timescale. See the previous page for the full caption text.

It is therefore clear that, in order for a parameter to significantly shift the average abundance ratios off of the closed box τ_{SF}-axis, it must strongly impact the relative Mg or H abundances. One obvious way to affect the gas reservoir hydrogen abundance is by opening up the closed box model to include inflows and outflows. Simple prescriptions for the gas infall rate have been included in the chemical evolution modeling of elliptical galaxies since Tantalo et al. (1996) and Kodama & Arimoto (1997). While the infalling gas is commonly assumed to be pristine, with the inflow mass either proportional to the star-formation rate or to the galaxy's halo mass (e.g., Pipino & Matteucci 2004; Hirschmann et al. 2016, respectively), in our implementation, the inflow metallicity (defined as the mass fraction of metals in the inflows, Z_{in}) can take on any value between 0 and 1 and the inflow history is predetermined so as to produce the desired gas fraction at T_{trunc} (see Section 3.3.2 for more details).

In the closed box scenario, the gas needed to fuel the entirety of the star-formation history is present from the start of the simulation and consequently, the initial gas mass is required to be quite high (comparable to the stellar mass). In contrast, when inflows of external gas will later supplement a galaxy's original gas stores, it can begin with a much smaller initial gas reservoir mass. In this case, the enriched gas returns from early stellar generations will not be as heavily diluted by the initial pristine gas, allowing them to more effectively and rapidly raise the overall metallicity of the reservoir gas. As a result, subsequent stellar generations are born from comparatively higher metallicity gas, pushing the galaxy's final average stellar [Fe/H] to higher values of $\langle$[Fe/H]$\rangle$, as can be seen in panel (a) of Figure 3.4.

Table 3.2: Parameter values for the elliptical galaxy fiducial inflows ($\tau_{\rm in} = 0.1 \times \tau_{\rm SF}$) simulations

	Elliptical Galaxy Velocity Dispersion Bin						
	$\boldsymbol{\sigma = 300}$ km s^{-1}	$\boldsymbol{\sigma = 246}$ km s^{-1}	$\boldsymbol{\sigma = 203}$ km s^{-1}	$\boldsymbol{\sigma = 167}$ km s^{-1}	$\boldsymbol{\sigma = 138}$ km s^{-1}	$\boldsymbol{\sigma = 112}$ km s^{-1}	$\boldsymbol{\sigma = 88}$ km s^{-1}
$\mathbf{M_{*,f}}$	1.175×10^{11}M$_\odot$	5.012×10^{10}M$_\odot$	3.548×10^{10}M$_\odot$	1.202×10^{10}M$_\odot$	6.310×10^{9}M$_\odot$	5.623×10^{9}M$_\odot$	4.266×10^{9}M$_\odot$
$\boldsymbol{\tau_{\rm SF}}$	1.334 Gyr	1.5404 Gyr	2.274 Gyr	2.9 Gyr	3.7252 Gyr	4.052 Gyr	5.132 Gyr
$\mathbf{t_{DTD}}$	100 Myr	100 Myr	100 Myr	100 Myr	100 Myr	100 Myr	100 Myr
$\mathbf{F_{trunc}}$	2.5	2.5	2.5	2.5	2.5	2.5	2.5
$\mathbf{M_{gas,0}}$	1.368×10^{10}M$_\odot$	5.8×10^{9}M$_\odot$	4.13×10^{9}M$_\odot$	1.403×10^{9}M$_\odot$	7.38×10^{8}M$_\odot$	6.59×10^{8}M$_\odot$	5.23×10^{8}M$_\odot$
$\boldsymbol{\tau_{\rm in}}$	0.1334 Gyr	0.15404 Gyr	0.2274 Gyr	0.29 Gyr	0.37252 Gyr	0.4052 Gyr	0.5132 Gyr
$\boldsymbol{f_{\rm gas,trunc}}$	0.007	0.007	0.007	0.007	0.007	0.007	0.007
$\boldsymbol{\epsilon_{\rm out}}$	0	0	0	0	0	0	0
$\boldsymbol{f_{\rm SN}}$	0	0	0	0	0	0	0
$\mathbf{Z_{in}}$	10^{-10}	10^{-10}	10^{-10}	10^{-10}	10^{-10}	10^{-10}	10^{-10}
IMF	Kroupa: $\alpha_{\rm H} = 2.3$	Kroupa: $\alpha_{\rm H} = 2.3$	Kroupa: $\alpha_{\rm H} = 2.3$	Kroupa: $\alpha_{\rm H} = 2.3$	Kroupa: $\alpha_{\rm H} = 2.3$	Kroupa: $\alpha_{\rm H} = 2.3$	Kroupa: $\alpha_{\rm H} = 2.3$
$\mathbf{M_{max}^{CCSN}}$	42.3M$_\odot$	42.3M$_\odot$	42.3M$_\odot$	42.3M$_\odot$	42.3M$_\odot$	42.3M$_\odot$	42.3M$_\odot$
Color	Maroon	Red	Orange	Yellow	Green	Blue	Purple
Figure	Fig. 3.4	Fig. 3.4	Fig. 3.4	Fig. 3.4	Fig. 3.4 Fig. 3.5(a)	Fig. 3.4	Fig. 3.4

Table 3.3: Parameter values for the elliptical galaxy fiducial inflows ($\tau_{\rm in} = 0.9 \times \tau_{\rm SF}$) simulations

	Elliptical Galaxy Velocity Dispersion Bin						
	$\boldsymbol{\sigma = 300}$ km s^{-1}	$\boldsymbol{\sigma = 246}$ km s^{-1}	$\boldsymbol{\sigma = 203}$ km s^{-1}	$\boldsymbol{\sigma = 167}$ km s^{-1}	$\boldsymbol{\sigma = 138}$ km s^{-1}	$\boldsymbol{\sigma = 112}$ km s^{-1}	$\boldsymbol{\sigma = 88}$ km s^{-1}
$\mathbf{M_{*,f}}$	1.175×10^{11}M$_\odot$	5.012×10^{10}M$_\odot$	3.548×10^{10}M$_\odot$	1.202×10^{10}M$_\odot$	6.310×10^{9}M$_\odot$	5.623×10^{9}M$_\odot$	4.266×10^{9}M$_\odot$
$\boldsymbol{\tau_{\rm SF}}$	0.7108 Gyr	0.82 Gyr	1.196 Gyr	1.522 Gyr	1.958 Gyr	2.1368 Gyr	2.796 Gyr
$\mathbf{t_{DTD}}$	100 Myr	100 Myr	100 Myr	100 Myr	100 Myr	100 Myr	100 Myr
$\mathbf{F_{trunc}}$	2.5	2.5	2.5	2.5	2.5	2.5	2.5
$\mathbf{M_{gas,0}}$	1.368×10^{10}M$_\odot$	5.8×10^{9}M$_\odot$	4.13×10^{9}M$_\odot$	1.403×10^{9}M$_\odot$	7.38×10^{8}M$_\odot$	6.59×10^{8}M$_\odot$	5.052×10^{8}M$_\odot$
$\boldsymbol{\tau_{\rm in}}$	0.63972 Gyr	0.738 Gyr	1.0764 Gyr	1.3698 Gyr	1.7622 Gyr	1.9231 Gyr	2.5164 Gyr
$\boldsymbol{f_{\rm gas,trunc}}$	0.007	0.007	0.007	0.007	0.007	0.007	0.007
$\boldsymbol{\epsilon_{\rm out}}$	0	0	0	0	0	0	0
$\boldsymbol{f_{\rm SN}}$	0	0	0	0	0	0	0
$\mathbf{Z_{in}}$	10^{-10}	10^{-10}	10^{-10}	10^{-10}	10^{-10}	10^{-10}	10^{-10}
IMF	Kroupa: $\alpha_{\rm H} = 2.3$	Kroupa: $\alpha_{\rm H} = 2.3$	Kroupa: $\alpha_{\rm H} = 2.3$	Kroupa: $\alpha_{\rm H} = 2.3$	Kroupa: $\alpha_{\rm H} = 2.3$	Kroupa: $\alpha_{\rm H} = 2.3$	Kroupa: $\alpha_{\rm H} = 2.3$
$\mathbf{M_{max}^{CCSN}}$	42.3M$_\odot$	42.3M$_\odot$	42.3M$_\odot$	42.3M$_\odot$	42.3M$_\odot$	42.3M$_\odot$	42.3M$_\odot$
Color	Maroon	Red	Orange	Yellow	Green	Blue	Purple
Figure	Fig. 3.4	Fig. 3.4 Fig. 3.6	Fig. 3.4	Fig. 3.4	Fig. 3.4 Fig. 3.5	Fig. 3.4	Fig. 3.4 Fig. 3.5

Since infalling gas is primarily composed of hydrogen gas, the inflows also strongly influence the effective [Fe/H] of the gas returns, which we denote $[\mathrm{Fe/H}]_{\mathrm{ret,eff}}$. The higher the inflow rate, the more $[\mathrm{Fe/H}]_{\mathrm{ret,eff}}$ is depressed. The extent to which the change to the effective gas returns impacts the gas reservoir abundance ratios (and hence the observed stellar abundances) depends on the gas removal efficiency, ϵ_{rm}. The gas removal efficiency at a given time is simply the fraction of gas removed from the reservoir via star formation and outflows, such that $\epsilon_{\mathrm{rm}}(t) \equiv \frac{\mathrm{SFR + Outflow\ Mass}}{\mathrm{Gas\ Mass}} = \frac{\Psi(t) + \mathrm{M_{out}}(t)}{\mathrm{M_{gas}}(t)}$ (see Section 2.4.3.1 in the previous chapter for a more detailed summary). If outflows are not included in the galaxy chemical evolution model, as is the case for closed box or inflows-only simulations, the gas removal efficiency is simply the star-formation efficiency, $\epsilon_{\mathrm{SF}}(t) \equiv \frac{\mathrm{SFR}}{\mathrm{Gas\ Mass}} = \frac{\Psi(t)}{\mathrm{M_{gas}}(t)}$.

When the gas removal efficiency is high, the impact of the effective gas returns on the gas reservoir is greater, such that the gas reservoir abundance ratios more rapidly approach the effective gas return abundance ratios. Thus, when ϵ_{rm} is generally high throughout the SFH, the [Fe/H] of the gas reservoir (denoted $[\mathrm{Fe/H}]_{\mathrm{gas}}$) will quickly approach $[\mathrm{Fe/H}]_{\mathrm{ret,eff}}$, with further enrichment strongly dependent on the evolution of $[\mathrm{Fe/H}]_{\mathrm{ret,eff}}$. In this case, the growth of $[\mathrm{Fe/H}]_{\mathrm{gas}}$ is significantly suppressed when hydrogen from inflows lowers $[\mathrm{Fe/H}]_{\mathrm{ret,eff}}$. On the other hand, when ϵ_{rm} is quite low throughout the majority of the SFH, changes to the gas return abundance ratios will not affect the gas reservoir as much. $[\mathrm{Fe/H}]_{\mathrm{gas}}$ will initially increase much more slowly, not approaching $[\mathrm{Fe/H}]_{\mathrm{ret,eff}}$ until considerable later in the simulation. Therefore, in this regime, the reduction of $[\mathrm{Fe/H}]_{\mathrm{ret,eff}}$ due to inflows will not usually serve as the

principle limiting factor in the growth of $[Fe/H]_{gas}$.

The influence of these two ϵ_{rm} regimes (and the transition between them) can be seen in the changing slope of $\langle[Mg/Fe]\rangle$–$\langle[Fe/H]\rangle$ in Figure 3.4 when we vary the initial gas mass, $M_{gas,0}$ in panel (a), and the inflow timescale, τ_{in} in panel (b). For the simulations with low $M_{gas,0}$ (the lighter red diamonds in panel (a)), the gas removal efficiency remains relatively high at all times while the large amount of additional gas that must be supplied by inflows to fuel the entirety of the SFH serves to suppress $[Fe/H]_{ret,eff}$. As discussed above, in this ϵ_{rm} regime, the [Fe/H] of the gas reservoir is strongly influenced by the gas returns such that the substantial decrease in $[Fe/H]_{ret,eff}$ from these massive inflows acts to restrict the growth of $[Fe/H]_{gas}$. The smaller the initial gas mass, the higher the inflow mass, the more $[Fe/H]_{ret,eff}$ is suppressed and limits the $[Fe/H]_{gas}$ enrichment and thus the steeper the $\langle[Mg/Fe]\rangle$-$\langle[Fe/H]\rangle$ slope.

On the other hand, for the simulations with high $M_{gas,0}$ (the darker red diamonds) that are nearest the closed box value, the slope as $M_{gas,0}$ is decreased remains relatively shallow: The large amount of starting reservoir gas ensures that ϵ_{rm} remains low until the rapid rise around T_{trunc} when most of the gas has been converted into stars. As previously pointed out, this means that $[Fe/H]_{gas}$ is relatively resistant to any reduction in $[Fe/H]_{ret,eff}$ caused by additional inflows. Moreover, since $M_{gas,0}$ is still a large fraction of the closed box value, the missing gas needed to fuel star-formation that is accreted as inflows throughout the star-forming period is comparatively small. Therefore, $[Fe/H]_{ret,eff}$ for these simulations will not be significantly decreased by inflowing hydrogen and thus will not substantially limit the [Fe/H] enrichment of the gas

reservoir, even when $\epsilon_{\rm rm}$ is high around $T_{\rm trunc}$.

Changing the inflow timescale for our $M_{\rm star,f} = 5.012 \times 10^{10} M_\odot$ galaxy has a very similar effect as varying the initial gas mass, as evidenced by panel (b) of Figure 3.4. When $\tau_{\rm in}$ is a small fraction of $\tau_{\rm SF}$, as for the palest red diamond simulations, the infalling gas is accreted early and over a short period of time such that the mass of the gas reservoir increases rapidly and soon resembles that of the closed box or high $M_{\rm gas,0}$ simulations. As with those scenarios, the large gas reservoir mass will keep $\epsilon_{\rm rm}$ quite low throughout most of the star-formation history. However, unlike the case when $M_{\rm gas,0}$ is high, the large amount of inflows at early times will cause a correspondingly significant reduction in $[{\rm Fe/H}]_{\rm ret,eff}$. Therefore, the gas reservoir [Fe/H] enrichment for these shorter $\tau_{\rm in}$ simulations will be restricted by $[{\rm Fe/H}]_{\rm ret,eff}$, resulting in an initially steeper slope than is seen in panel (a) for the $M_{\rm gas,0}$ low-$\epsilon_{\rm rm}$ regime.

As $\tau_{\rm in}$ increases to approach the star-formation timescale, the inflow gas is added to the galaxy's gas reservoir closer to when it is actually needed for star formation. This results in a higher gas removal efficiency and a more evenly-distributed reduction in $[{\rm Fe/H}]_{\rm ret,eff}$ throughout the entirety of the star-formation period. This closely resembles what occurs for the low $M_{\rm gas,0}$ (high-$\epsilon_{\rm rm}$ regime) simulations and leads to a similar steepening of the $\langle[{\rm Mg/Fe}]\rangle$-$\langle[{\rm Fe/H}]\rangle$ slope for these longer-$\tau_{\rm in}$ simulations (plotted as darker red diamonds in panel (b)).

So, while increasing the relative contribution of the gas from inflows or the timescale of the inflows will initially increase the average stellar [Fe/H] by allowing early rapid growth of $[{\rm Fe/H}]_{\rm gas}$, this faster enrichment as a result of the higher $\epsilon_{\rm rm}$ will

eventually be significantly countered by the strong suppression of $[\mathrm{Fe/H}]_{\mathrm{ret,eff}}$ due to the increase in hydrogen gas mass from inflows. In addition, both $\mathrm{M_{gas,0}}$ and τ_{in} have natural limits beyond which they cannot physically be changed: A galaxy cannot have a negative gas reservoir mass nor can it form stars out of gas that has not yet been accreted. Therefore, the initial gas mass must be at least zero ($\mathrm{M_{gas,0}} \geq 0\ \mathrm{M_{\odot}}$) and the inflow timescale must be shorter than the star-formation timescale ($\tau_{\mathrm{in}} < \tau_{\mathrm{SF}}$). As the two parameters approach these bounds, they also become progressively less effective at enhancing $[\mathrm{Fe/H}]_{\mathrm{gas}}$ (and thus the stellar $\langle[\mathrm{Fe/H}]\rangle$), and the $\langle[\mathrm{Mg/Fe}]\rangle$-$\langle[\mathrm{Fe/H}]\rangle$ slope steepens dramatically.

Therefore, the combination of diminishing returns and firm physical parameter limits means that there is only so far these parameters can shift the closed box τ_{SF}-axis. By including inflows and modifying τ_{SF} along with τ_{in} and/or $\mathrm{M_{gas,0}}$, it is possible to reproduce the average abundance ratios of the galaxies that lie between the dashed closed box τ_{SF}-axis line and approximately the dot-dashed inflows τ_{SF}-axis line (for which $\tau_{\mathrm{in}} = 0.9 \times \tau_{\mathrm{SF}}$) shown in Figure 3.4. However, it is clear from panel (c) that no combination of these parameters will ever be able to simultaneously reproduce the observed stellar α-enhancement and metallicities of our two most massive and the least massive elliptical galaxy bins.

Figure 3.4 *(next page)*: This figure shows the important role that inflows play in shifting the average abundance ratios off of the closed box $\tau_{\rm SF}$-axis by changing the hydrogen abundance of the gas reservoir. We see that while including inflows in our simulations can appreciably move the abundance ratios off of the closed box $\tau_{\rm SF}$-axis (shown in each panel as the thick black dashed line), inflows cannot help invert the negative $\langle$[Mg/Fe]$\rangle$–$\langle$[Fe/H]$\rangle$ slope predicted by our fiducial closed box models.

Panel (a) shows the impact of changing the initial gas mass, $M_{\rm gas,0}$, on the $\langle$[Mg/Fe]$\rangle$ and $\langle$[Fe/H]$\rangle$ abundance ratios of the $M_{\rm star,f} = 5.012{\times}10^{10} M_{\odot}$ elliptical galaxy mass bin (whose corresponding observed abundance ratios are plotted as the bright red hexagon). The fiducial closed box simulation for this galaxy mass bin (shown as the red circle like in Figure 3.2) has an initial reservoir gas mass $M^{\rm CB}_{\rm gas,0} = 5.7273 \times 10^{10} M_{\odot}$, and a star-formation timescale, $\tau_{\rm SF} = 1.5316$ Gyr. The red diamonds represent inflow-only simulations for which $M_{\rm gas,0}$ is an incrementally smaller fraction of the closed box initial gas mass (denoted $M^{\rm CB}_{\rm gas,0}$), so that from the darkest red diamond to the lightest red diamond, $M_{\rm gas,0}/M^{\rm CB}_{\rm gas,0} = 0.8, 0.6, 0.4, 0.3, 0.2, 0.1, 0.01$. For these inflow simulations, $\tau_{\rm SF} = 1.5316$ Gyr and all other parameters besides $M_{\rm gas,0}$ are the same as the $\sigma = 246$ km s^{-1} fiducial ($\tau_{\rm in} = 0.9 \times \tau_{\rm SF}$) inflow simulation, as listed in Table 3.3.

Panel (b) shows the impact of increasing the inflow timescale, from $\tau_{\rm in} = 0.1 \times \tau_{\rm SF}$ to $\tau_{\rm in} = 0.9 \times \tau_{\rm SF}$ for the $M_{\rm star,f} = 5.012 \times 10^{10} M_{\odot}$ elliptical galaxy mass bin. From darkest to lightest, the red diamonds correspond to simulations where $\tau_{\rm in}/\tau_{\rm SF} = 0.1, 0.2, 0.3, 0.4, 0.5, 0.6, 0.7, 0.8, 0.9, 0.99$, respectively. All other parameters are the same as the $\sigma = 246$ km s^{-1} fiducial ($\tau_{\rm in} = 0.9 \times \tau_{\rm SF}$) inflow simulation, as listed in Table 3.3. In both panels (a) and (b), the influence of the gas removal efficiency ($\epsilon_{\rm rm}$) can be seen in the changing slope of changing slope of $\langle$[Mg/Fe]$\rangle$–$\langle$[Fe/H]$\rangle$ as the simulations transition from the low $\epsilon_{\rm rm}$ regime (darker red diamonds) to the high $\epsilon_{\rm rm}$ regime (lighter red diamonds).

In panel (c) we show the $\tau_{\rm SF}$-axis shifts when inflows are included in our chemical evolution modeling. For the simulations shown as triangles, the inflow timescales are a smaller fraction of the star-formation timescale ($\tau_{\rm in} = 0.1 \times \tau_{\rm SF}$) while the simulations shown as squares assume that inflow and star-formation timescales are similar ($\tau_{\rm in} = 0.9 \times \tau_{\rm SF}$). As with the fiducial closed box simulations, the star-formation timescales ($\tau_{\rm SF}$) of these fiducial ($\tau_{\rm in} = 0.1 \times \tau_{\rm SF}$) and ($\tau_{\rm in} = 0.9 \times \tau_{\rm SF}$) inflow simulations have been tuned to reproduce the observed $\langle$[Mg/Fe]$\rangle$ and their parameters are listed in Table 3.2 and Table 3.3, respectively. As always, the rainbow color-coding is as described in the caption of Figure 3.2. The black dot-dashed line represents a linear fit to the fiducial ($\tau_{\rm in} = 0.9 \times \tau_{\rm SF}$) inflow simulations, which we will refer to as the inflows $\tau_{\rm SF}$-axis.

As a visual reference, we also include in each panel the observed abundance ratios measured by Conroy et al. 2014 (described in Section 3.2), which are shown as rainbow hexagons, and $\langle$[Fe/H]$\rangle = 0$, which appears as a thin grey dotted line.

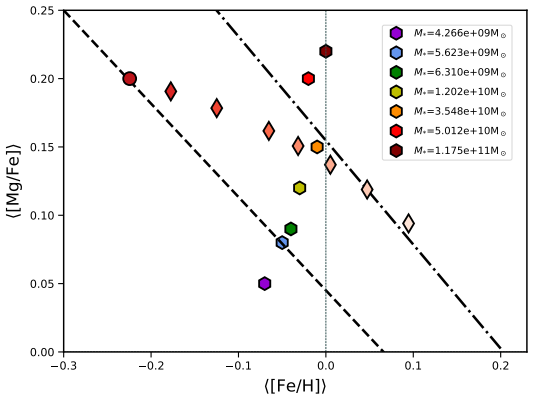

(a) Vary $M_{gas,0}$

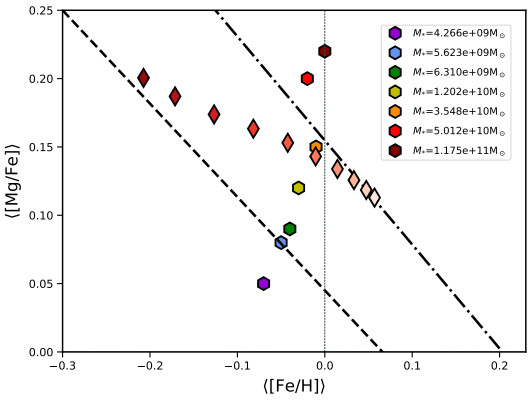

(b) Vary τ_{in}

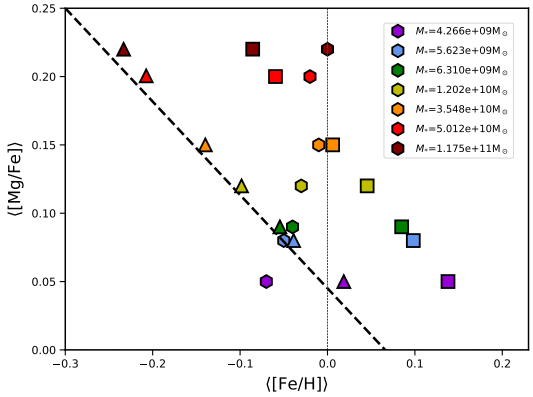

(c) The inflow τ_{SF}-axis when $\tau_{in} = 0.1\tau_{SF}$ and $\tau_{in} = 0.9\tau_{SF}$

Figure 3.4: An exploration of how inflows shift the τ_{SF}-axis and the effects of varying τ_{in} and $M_{gas,0}$ on the simulated elliptical galaxy abundance ratios. See the previous page for the full caption text.

To reproduce the observed $\langle$[Fe/H]$\rangle$ of the lowest-mass elliptical galaxy bin ($M_{star,f} = 4.266 \times 10^9 M_\odot$), the $[Fe/H]_{gas}$ enrichment must be even more strongly suppressed than what can be achieved by our fiducial closed box simulations. One way of further impeding the growth of $[Fe/H]_{gas}$ is to allow the galaxy to have a more substantial fraction of gas remaining when star-formation is truncated (i.e., $f_{gas,trunc} > 0.007$). When compared to our fiducial models, for which $f_{gas,trunc} = 0.007$, increasing $f_{gas,trunc}$ lowers ϵ_{rm} throughout the simulation by increasing the overall gas inflow mass (or the initial gas mass in the case of a closed box). This has a particularly significant impact in preventing rapid enrichment around T_{trunc}, when ϵ_{rm} would spike for our fiducial models. The $[Fe/H]_{gas}$ enhancement is further impeded, in the case of the inflows-only models, by the supplemental infalling gas which lowers $[Fe/H]_{ret,eff}$ even more.

In panel (a) of Figure 3.5, we see that a larger $f_{gas,trunc}$ is very effective at suppressing the [Fe/H] enrichment of the gas and as a consequence, the slope remains quite flat as we increase $f_{gas,trunc}$. This is exactly what we would expect given our earlier examination of the low ϵ_{rm} regime in the case of varying $M_{gas,0}$ and τ_{in}. Matching the observed $\langle$[Fe/H]$\rangle$ of the least massive galaxy bin (while simultaneously reproducing the observed $\langle$[Mg/Fe]$\rangle$) with our standard inflows-only model ($\tau_{in} = 0.9 \times \tau_{SF}$) would require $f_{gas,trunc}$ =blah. Whether such a high gas fraction at truncation is reasonable for our observed elliptical galaxy sample is difficult to determine. As mentioned in Section 3.3.2, while elliptical galaxies are observed to have very low present-day gas fractions, this is not necessarily true of the gas fraction immediately preceding star-formation termination. However, the degree to which $f_{gas,trunc}$ can plausibly be increased for

these galaxies remains unclear since $f_{\rm gas,trunc}$ cannot be directly observed while any theoretical constraints would depend on the specific mechanism that terminated the star formation.

An alternative method of increasing the inflow gas mass throughout the star-forming period is to allow CCSN and SNIa to drive galactic outflows (our outflow prescription is described in Section 2.2.5). The more gas is removed from the galaxy as outflows, the greater the inflow mass needed to replace it[17]. As the outflow parameter, $\epsilon_{\rm out}$, is increased in panel (b) of Figure 3.5, the amount of inflows needed to ensure that there is enough gas to fuel the SFH and produce the desired $f_{\rm gas,trunc}$ also increases, causing $[{\rm Fe/H}]_{\rm ret,eff}$ to be further reduced throughout the galaxy's star-forming period. The growth of $[{\rm Fe/H}]_{\rm gas}$ is strongly limited by this lower $[{\rm Fe/H}]_{\rm ret,eff}$, and consequently, stars are born at a lower $[{\rm Fe/H}]_{\rm gas}$ resulting in progressively decreasing $\langle[{\rm Fe/H}]\rangle$. If rather than increasing the outflow mass we instead change the fraction of supernova ejecta ($f_{\rm SN}$) swept up in the outflows, as in panel (c) of Figure 3.5, the effective [Fe/H] of the gas returns and thus the gas reservoir enrichment and stellar $\langle[{\rm Fe/H}]\rangle$ are similarly affected. However, in this case, the diminished $[{\rm Fe/H}]_{\rm ret,eff}$ is caused not by the increase of hydrogen in the gas returns due to higher inflows but rather by the reduced Fe mass that is returned to the gas reservoir as larger fractions of the SNe by-products are ejected in the outflows.

[17]Perhaps counter-intuitively, even though $\rm M_{out}(t)$ factors directly into the calculation of $\epsilon_{\rm rm}(t)$, the overall impact of outflows on $\epsilon_{\rm rm}$ is rather small. Instead, outflows primarily affect $[{\rm Fe/H}]_{\rm gas}$ by reducing $[{\rm Fe/H}]_{\rm ret,eff}$ due to the greater inflow mass that is required. This is discussed at length in Chapter 2, Section 2.4.3.2.

Figure 3.5 *(next page)*: In this figure we show the effects on the simulated elliptical galaxy abundance ratios of increasing the gas fraction at star-formation truncation ($f_{\rm gas,trunc}$), the outflow parameter ($\epsilon_{\rm out}$), and the fraction of SN ejecta that is removed in the outflow ($f_{\rm SN}$). All three of these parameters can significantly decrease $\langle$[Fe/H]$\rangle$ without having much of an effect on $\langle$[Mg/Fe]$\rangle$.

In panel (a), we increase $f_{\rm gas,trunc}$ for each of our fiducial simulations of the $\sigma = 138$ km s^{-1} ($M_{*,f} = 6.31 \times 10^9 M_\odot$) galaxy. The lightest green circle corresponds to the green fiducial closed box simulation that appears in Figure 3.2, which has $f_{\rm gas,trunc} = 0.007$. Then, by appropriately increasing $M_{\rm gas,0}$, the gas fraction at star-formation truncation becomes $f_{\rm gas,trunc} = 0.1, 0.2,$ and 0.3 and the depth of the marker color increases as $f_{\rm gas,trunc}$ increases. Similarly, the lightest green triangle corresponds to the green fiducial ($\tau_{\rm in} = 0.1 \times \tau_{\rm SF}$) inflow simulation that appears in Figure 3.4(c), which also uses $f_{\rm gas,trunc} = 0.007$. Again, the gas fraction at star-formation truncation is increased to $f_{\rm gas,trunc} = 0.1, 0.2,$ and 0.3 and the corresponding marker color becomes darker as $f_{\rm gas,trunc}$ increases. Finally, the lightest green square corresponds to the green fiducial ($\tau_{\rm in} = 0.9 \times \tau_{\rm SF}$) inflow simulation that appears in Figure 3.4(c), which also assumes $f_{\rm gas,trunc} = 0.007$. This time, the gas fraction at star-formation truncation is increased to $f_{\rm gas,trunc} = 0.1, 0.2, 0.3,$ and 0.4 and again, the corresponding marker color becomes darker as $f_{\rm gas,trunc}$ increases.

In panel (b), we include outflows in our simulations and explore how the abundance ratios are changed when the efficiency of the outflows is increased from $\epsilon_{\rm out} = 0$ (lightest square) to $\epsilon_{\rm out} = 7$ (darkest square) in increments of $\Delta\epsilon_{\rm out} = 1$. The lightest green square corresponds to the fiducial ($\tau_{\rm in} = 0.9\tau_{\rm SF}$) inflow simulation of the $\sigma = 138$ km s^{-1} ($M_{*,f} = 6.31 \times 10^9 M_\odot$) galaxy and all of the simulations shown as green squares in this panel assume, other than for $\epsilon_{\rm out}$, the same parameters as this one (listed in Table 3.3). Similarly, the lightest purple square corresponds to the fiducial ($\tau_{\rm in} = 0.9\tau_{\rm SF}$) inflow simulation of the $\sigma = 88$ km s^{-1} ($M_{*,f} = 4.266 \times 10^9 M_\odot$) galaxy and all of the simulations shown as purple squares in this panel assume, other than for $\epsilon_{\rm out}$, the same parameters as this one (listed in Table 3.3).

In panel (c), we include outflows in our simulations but this explore how the abundance ratios are changed when more of the SN ejecta is removed in galactic winds before they have a chance of being returned to the gas reservoir. For both sets of simulations, we assume $\epsilon_{\rm out} = 1$ and increase the removed SN fraction from $f_{\rm SN} = 0$ (lightest square) to $f_{\rm SN} = 0.5$ (darkest square) in increments of $\Delta f_{\rm SN} = 0.1$. The green squares have the same parameters as the fiducial ($\tau_{\rm in} = 0.9\tau_{\rm SF}$) inflow simulation of the $\sigma = 138$ km s^{-1} ($M_{*,f} = 6.31 \times 10^9 M_\odot$) galaxy listed in Table 3.3 except for $\epsilon_{\rm out}$ and $f_{\rm SN}$. Similarly, the purple squares correspond have the same parameters as the fiducial ($\tau_{\rm in} = 0.9\tau_{\rm SF}$) inflow simulation of the $\sigma = 88$ km s^{-1} ($M_{*,f} = 4.266 \times 10^9 M_\odot$) galaxy listed in Table 3.3 except for $\epsilon_{\rm out}$ and $f_{\rm SN}$.

As a visual reference, we include in all panels the observed abundance ratios measured by Conroy et al. 2014 (described in Section 3.2), which are shown as rainbow hexagons, and $\langle$[Fe/H]$\rangle = 0$, which appears as a thin grey dashed line. The thicker black dashed and dot-dashed lines represent the closed box $\tau_{\rm SF}$-axis and the inflow ($\tau_{\rm in} = 0.9 \times \tau_{\rm SF}$) $\tau_{\rm SF}$-axis, respectively.

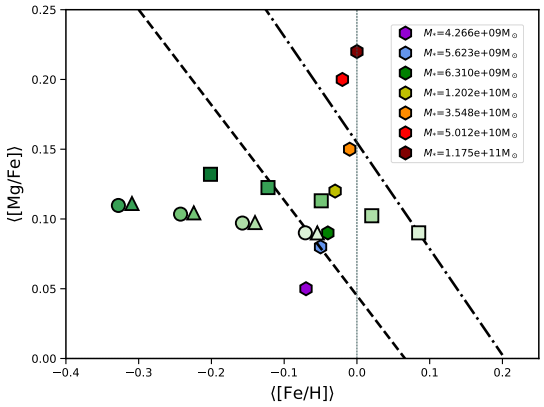

(a) Vary $f_{\rm gas,f}$

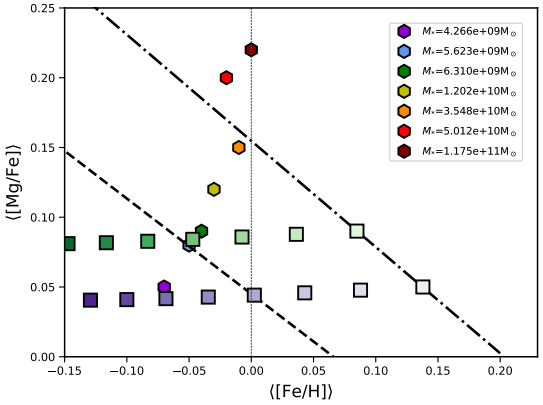

(b) Vary $\epsilon_{\rm out}$

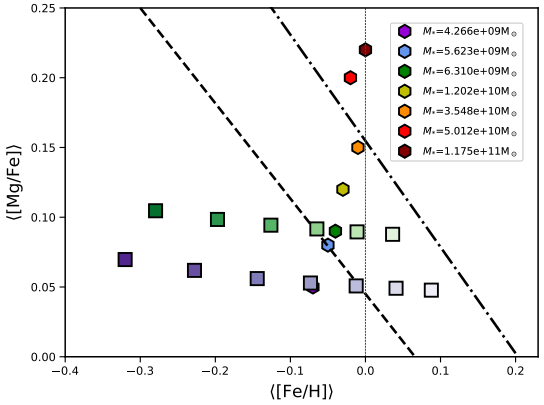

(c) Vary $f_{\rm SN}$

Figure 3.5: The effects on the simulated elliptical galaxy abundance ratios of increasing the gas fraction at star-formation truncation ($f_{\rm gas,trunc}$), the outflow parameter ($\epsilon_{\rm out}$), and the fraction of SN ejecta that is removed in the outflow ($f_{\rm SN}$). See the previous page for the full caption text.

While the three parameters examined in Figure 3.5 can all be used to help reproduce the observed $\langle$[Fe/H]$\rangle$ of the lower mass ellipticals, they cannot be used to increase the simulated $\langle$[Fe/H]$\rangle$ which is what is needed for our simulations to match those of the most massive elliptical galaxies. We therefore must consider additional model that can help shift the inflows $\tau_{\rm SF}$-axis to higher $\langle$[Fe/H]$\rangle$. One such parameter is the inflow metallicity, $\rm Z_{in}$. The greater the metallicity of the gas inflows, the smaller the mass of hydrogen that is accreted by the galaxy. The effective gas returns will therefore comprise less hydrogen, resulting in a higher $\rm [Fe/H]_{ret,eff}$ than in our fiducial models. Thus, regardless of the precise elemental composition of the infalling metals, the stellar $\langle$[Fe/H]$\rangle$ will rise (and be shifted to the right in Figure 3.6) as the metallicity of the inflows increases. It is likely, though, that higher metallicity inflows contain increasing amounts of Fe that will only further augment $\rm [Fe/H]_{ret,eff}$ and thus $\langle$[Fe/H]$\rangle$. The change in the stellar $\langle$[Mg/Fe]$\rangle$, however, will strongly depend not only on the total metallicity of the infalling gas but also on its α-enhancement.

This is demonstrated in Figure 3.6 where we show the effect of increasing $\rm Z_{in}$ from $\rm Z_{in} = 10^{-10}$ to $\rm Z_{in} = 0.004$ (or $\rm Z_{in} \approx 7.1 \times 10^{-9}$ $\rm Z_{\odot}$ to $\rm Z_{in} \approx 0.28$ $\rm Z_{\odot}$ assuming the solar metallicity value, $Z_{\odot} = 0.0141$, from Lodders et al. 2009) for two different assumptions for calculating the element ratios of the inflowing gas. As expected, the stellar $\langle$[Fe/H]$\rangle$ increases with inflow metallicity in both scenarios. For the set of simulations shown as thin diamonds, we assume that all elements heavier than He are in the same ratios as the IMF-weighted Z=0.001 Kobayashi et al. (2006) CCSN yields. The simulations shown as regular diamonds are very similar but instead use the CCSN

IMF-weighted yields for the Kobayashi et al. (2006) table with the metallicity closest to Z_{in} (see Section 3.3.2). Since both of these sets of simulations suppose that the infalling gas has not been contaminated by SNIa ejecta, their inflows are very α-enhanced and lead to progressively higher $\langle$[Mg/Fe]$\rangle$. At least for the two element-ratio assumptions tested here, the observed $\langle$[Mg/Fe]$\rangle$ and $\langle$[Fe/H]$\rangle$ of the two most massive galaxy bins can be simultaneously reproduced if we allow sufficiently enriched inflow metallicities.

Reducing the proportion of hydrogen present in the inflows is not the only way to push an elliptical galaxy's stellar $\langle$[Fe/H]$\rangle$ beyond the limits of the standard-inflows axis. For example, $[Fe/H]_{ret,eff}$ can instead be raised by changing the IMF-weighted yields such that more Fe is returned per solar mass formed to the galaxy's gas reservoir. The most commonly-used and straightforward method of altering the IMF-weighted yields is simply to modify the IMF to be more top-heavy than the standard Kroupa IMF that is observed for the Milky Way. As is evident in panel (a) of Figure 3.7, the inverse relation between $\langle$[Mg/Fe]$\rangle$ and $\langle$[Fe/H]$\rangle$ that plagued so many of the parameters we previously examined can be avoided if we instead change the slope of the IMF.

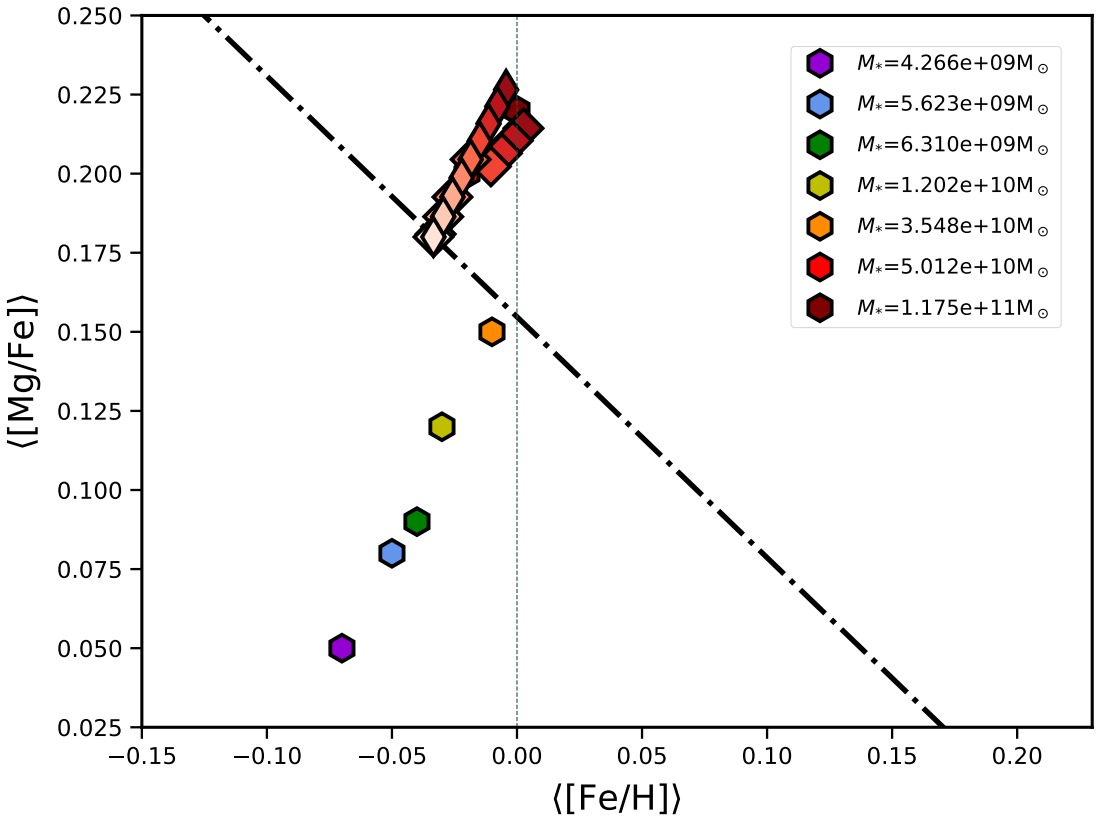

Figure 3.6: In this figure we show the effect of changing the inflow metallicity on the $\langle$[Mg/Fe]$\rangle$ and $\langle$[Fe/H]$\rangle$ abundance ratios of the $M_{star,f} = 5.012 \times 10^{10} M_{\odot}$ elliptical galaxy mass bin (whose corresponding observed abundance ratios are plotted as the bright red hexagon). The two sets of simulations shown in this figure (thin and thick diamonds) increase the initial mass from $Z_{in} = 10^{-10}$ to $Z_{in} = 0.004$ using two different assumptions for calculating the element ratios of the inflowing gas. From the lightest red markers to the darkest red markers, the inflow metallicities are as follows: $Z_{in} = 10^{-10}, 0.0005, 0.001, 0.0015, 0.002, 0.0025, 0.003, 0.0035, 0.004$. For the set of simulations shown as thin diamonds, we assume that all elements heavier than He are in the same ratios as the IMF-weighted Z=0.001 Kobayashi et al. (2006) CCSN yields. The simulations shown as thick diamonds are very similar but instead use the CCSN IMF-weighted yields for the Kobayashi et al. (2006) table with the metallicity closest to Z_{in} (see Section 3.3.2). All the parameters apart from Z_{in} are the same as the $\sigma = 246$ km s^{-1} fiducial ($\tau_{in} = 0.9 \times \tau_{SF}$) inflow simulation and are listed in Table 3.3. As a visual reference, we include the observed abundance ratios measured by Conroy et al. 2014 (described in Section 3.2), which are shown as rainbow hexagons, and $\langle$[Fe/H]$\rangle = 0$, which appears as a thin grey dotted line.

Figure 3.7 *(next page)*: This figure shows the considerable effect that the high-mass slope of the IMF ($\alpha_{\rm H}$) and the maximum stellar mass that explodes as a CCSN ($M_{\rm max}^{\rm CCSN}$) have on the average abundance ratios of our simulated elliptical galaxies. In panel (a), we vary the high-mass slope of the IMF, going from a top-light IMF slope of $\alpha_{\rm H} = 2.45$ (the lightest grey square) to a top-heavy IMF with a high-mass slope of $\alpha_{\rm H} = 2.20$ (the darkest grey square) in increments of $\Delta\alpha_{\rm H} = 0.05$. The simulation corresponding to the grey square nearest to the orange hexagon used a standard Kroupa IMF. For these simulations, we assume a star-formation timescale of $\tau_{\rm SF} = 1.1$ Gyr and all other parameters besides $\alpha_{\rm H}$ are the same as for the $\sigma = 203$ km s^{-1} fiducial ($\tau_{\rm in} = 0.9 \times \tau_{\rm SF}$) inflow simulation, as listed in Table 3.3. In panel (b), we change the maximum stellar mass that explodes as a CCSN from $M_{\rm max}^{\rm CCSN} = 31.7 M_{\odot}$ (lightest grey square) to $M_{\rm max}^{\rm CCSN} = 54.1 M_{\odot}$ (darkest grey square). These simulations assume a star-formation timescale of $\tau_{\rm SF} = 0.96$ Gyr and $M_{\rm max}^{\rm CCSN} = 31.7, 34.9, 37.4, 39.8, 42.3, 46, 49.7, 54.1 M_{\odot}$ (the depth of the marker color in panel (b) increases as $M_{\rm max}^{\rm CCSN}$ increases). All other parameters are the same as for the $\sigma = 203$ km s^{-1} fiducial ($\tau_{\rm in} = 0.9 \times \tau_{\rm SF}$) inflow simulation, as listed in Table 3.3. As a visual reference, we include in both panels the observed abundance ratios measured by Conroy et al. 2014 (described in Section 3.2), which are shown as rainbow hexagons, and $\langle$[Fe/H]$\rangle = 0$, which appears as a thin grey dotted line. The black dashed and dot-dashed lines are the closed box $\tau_{\rm SF}$-axis and the inflow ($\tau_{\rm in} = 0.9 \times \tau_{\rm SF}$) $\tau_{\rm SF}$-axis, respectively.

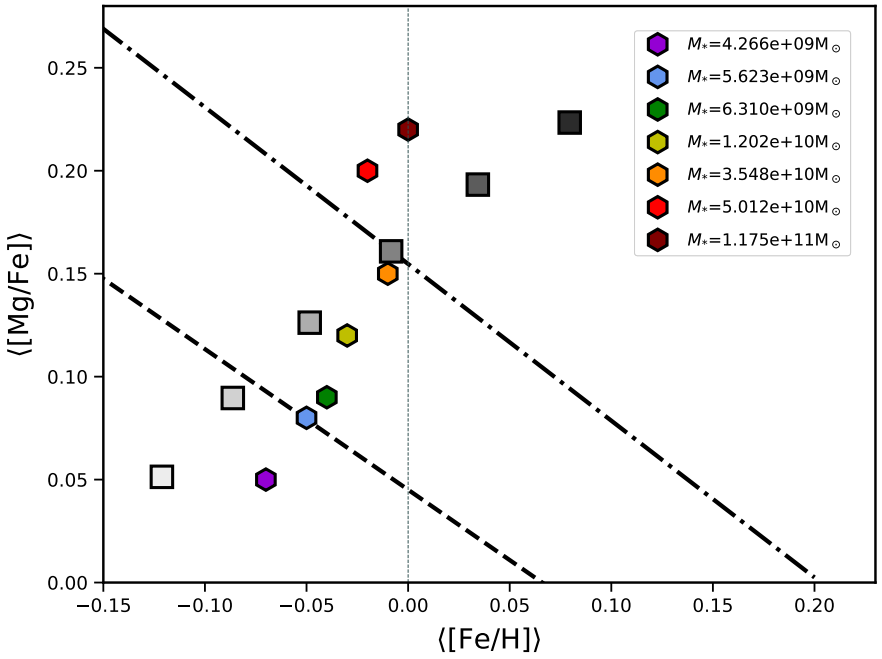

(a) Varying the high-mass slope ($\alpha_{\rm H}$) of the IMF

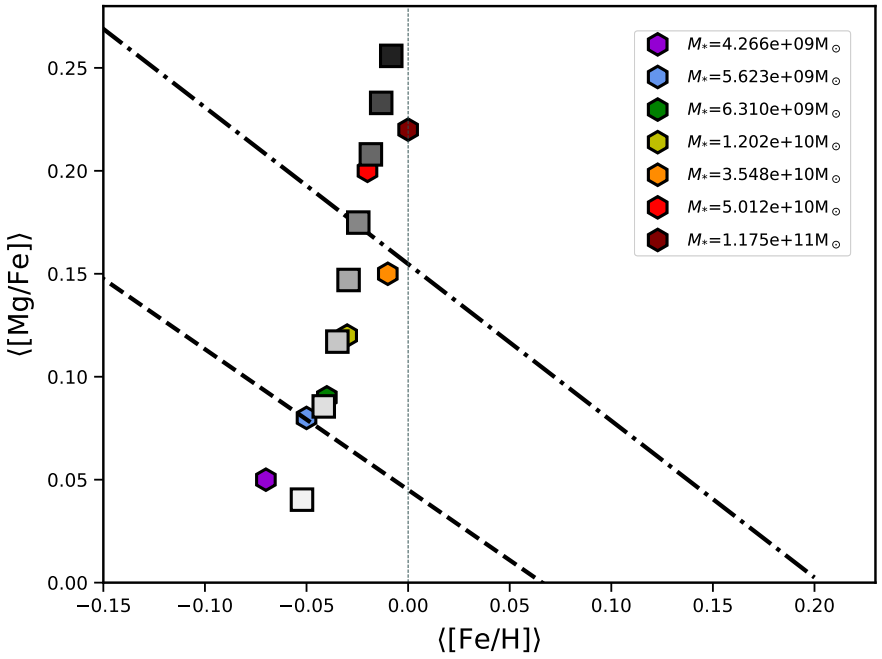

(b) Varying the maximum stellar mass that explodes as a CCSN, $\mathrm{M}_{\rm max}^{\rm CCSN}$

Figure 3.7: This figure shows the considerable effect that the high-mass slope of the IMF ($\alpha_{\rm H}$) and the maximum stellar mass that explodes as a CCSN ($\mathrm{M}_{\rm max}^{\rm CCSN}$) have on the average abundance ratios of our simulated elliptical galaxies. See the previous page for the full caption text.

A galaxy with a more top-heavy IMF generates a larger proportion of higher-mass, shorter-lived stars. This leads to a greater fraction of its stellar mass having died off at any given time. Consequently, the total stellar mass formed by the galaxy with a more top-heavy IMF must be greater in order to produce the same final stellar+remnant mass, $M_{*,f}$. The resulting higher star formation rate gives rise to an increased ϵ_{rm} that causes the galaxy's gas reservoir to enrich more rapidly. The larger stellar mass formed also means that a greater amount of gas is released from dying stars. Therefore, the hydrogen-heavy inflows, which remain essentially the same for both galaxies, comprise a smaller proportion of the effective gas returns. Additionally, the greater number of massive stars produced by a more top-heavy IMF gives rise to stellar returns with a higher [Fe/H] as well as a higher [Mg/Fe].

The combination of a comparatively smaller contribution from inflows and the higher [Fe/H] of the stellar returns results in a significant increase to $[Fe/H]_{ret,eff}$, while the greater returns from massive stars with highly α-enriched ejecta raises $[Mg/Fe]_{ret,eff}$. The impact of these greatly enhanced gas returns on the average stellar abundance ratios is only further amplified by the higher ϵ_{rm}, leading to the galaxy with the more top-heavy IMF having both a substantially higher stellar $\langle$[Mg/Fe]$\rangle$ and $\langle$[Fe/H]$\rangle$. This produces the positive relation between $\langle$[Mg/Fe]$\rangle$ and $\langle$[Fe/H]$\rangle$ that is seen as the IMF slope is varied in panel (a) of Figure 3.7.

The IMF, however, is not the only factor that impacts the IMF-weighted yields. The standard practice of treating the stellar returns (including the theoretically-calculated nucleosynthetic yield tables) as well-established and unvarying inputs to

chemical evolution models easily obfuscates the many uncertainties associated with our understanding of stellar evolution and its nucleosynthetic by-products as well as the multitude of choices and assumptions that must be made to compensate for our incomplete knowledge. Reasonable modifications to some of these assumptions can greatly impact the IMF-weighted yields. One such example is the poorly-constrained maximum stellar mass, M_{max}^{CCSN}, that explodes as a CCSN rather than collapsing to a black hole. We explore the effect of varying this maximum stellar mass from $M_{max}^{CCSN} = 32M_{\odot}$ (lightest grey square) to $M_{max}^{CCSN} = 55M_{\odot}$ (darkest grey square) in panel (b) of Figure 3.7.

Increasing M_{max}^{CCSN} converts stars that would otherwise be returning a large fraction of their stellar mass as unenriched stellar winds primarily consisting of H into producers of highly enriched CCSN ejecta. This simultaneously reduces H while increasing Fe, which raises $[Fe/H]_{ret,eff}$ and consequently the stellar $\langle[Fe/H]\rangle$ of the galaxy. Furthermore, not only is the amount of ejecta released by these most massive CCSN progenitor stars large but it is also the most α-enhanced, with the highest [Mg/Fe] of any other contributor to the gas returns. Thus, despite their rarity, these stars will not only increase the stellar $\langle[Fe/H]\rangle$ but also significantly raise $\langle[Mg/Fe]\rangle$. As demonstrated in panel (b) of Figure 3.7, even a small change in M_{max}^{CCSN} can strongly impact the average stellar abundance ratios in a way that resembles varying the IMF (shown in panel (a)). In this case, we have only examined how modifying our assumption for M_{max}^{CCSN} impacts the IMF-weighted yields, but we comment on the effect of other uncertainties in the nucleosynthetic yields in Section 3.5.

Figure 3.8 *(next page)*: In this figure, we present the average α-enhancement (calculated for three different α-elements; Mg, O, and Si) and the stellar metallicity (represented by $\langle$[Fe/H]$\rangle$) for two sets of close-correspondence models. Each set of models consist of seven simulations representing the Conroy et al. 2014 elliptical galaxy velocity dispersion bins described in Section 3.2 and the simulation parameters were tuned to simultaneously reproduce the observed $\langle$[Mg/Fe]$\rangle$ and $\langle$[Fe/H]$\rangle$ measured by Conroy et al. 2014 for their respective galaxy mass bins.

For the first set of close-correspondence models we used the fiducial ($\tau_{\rm in} = 0.9 \times \tau_{\rm SF}$) inflow simulations as a starting point, modifying only the star-formation timescale (and consequently the inflow timescale since $\tau_{\rm in} = 0.9 \times \tau_{\rm SF}$), the outflow parameter ($\epsilon_{\rm out}$), and, in the case of the two most massive galaxy bins, the inflow metallicity ($Z_{\rm in}$) was also increased. The exact parameter values for this first set of simulations can be found in Table 3.4 (labeled Set 1) and in the left-hand panels of this figure, we show the average mass-weighted stellar $\langle$[Fe/H]$\rangle$ and $\langle$[α/Fe]$\rangle$ of these seven simulations for the three previously-mentioned α-elements: $\langle$[Mg/Fe]$\rangle$ (top left panel), $\langle$[O/Fe]$\rangle$ (middle left panel), and $\langle$[Si/Fe]$\rangle$ (bottom left panel).

The second set of close-correspondence models were generated using a higher value for the maximum stellar mass that explodes as a CCSN ($M_{\rm max}^{\rm CCSN} = 54.1 M_{\odot}$ instead of the default $M_{\rm max}^{\rm CCSN} = 42.3 M_{\odot}$). We did this to underscore how important of an impact the IMF-weighted yields have on the parameter values needed to reproduce the observed average abundance ratios. Besides making this change to $M_{\rm max}^{\rm CCSN}$, for this set of simulations we only modified $\tau_{\rm SF}$ and $\epsilon_{\rm out}$ and all other parameters were kept at the values used for the fiducial ($\tau_{\rm in} = 0.9 \times \tau_{\rm SF}$) inflow simulation values. As can be seen by comparing the parameter values listed in Table 3.4 for the two sets of close-correspondence models, when $M_{\rm max}^{\rm CCSN}$ is increased, longer star-formation timescales and larger outflow parameters are needed to reproduce the observed $\langle$[Mg/Fe]$\rangle$ and $\langle$[Fe/H]$\rangle$.

For comparison, we include in all the panels of this figure the observed abundance ratios measured by Conroy et al. 2014 (described in Section 3.2), which are shown as rainbow hexagons. The simulation abundance ratios are shown as squares and are color-coded in the same way as the observed abundances. As a visual reference we show $\langle$[Fe/H]$\rangle = 0$ as a thin grey dashed line and in the two bottom panels, we also add a thin grey horizontal dashed line which corresponds to $\langle$[Mg/Fe]$\rangle = 0$. The black dashed and dot-dashed lines are the closed box $\tau_{\rm SF}$-axis and the inflow ($\tau_{\rm in} = 0.9 \times \tau_{\rm SF}$) $\tau_{\rm SF}$-axis, respectively.

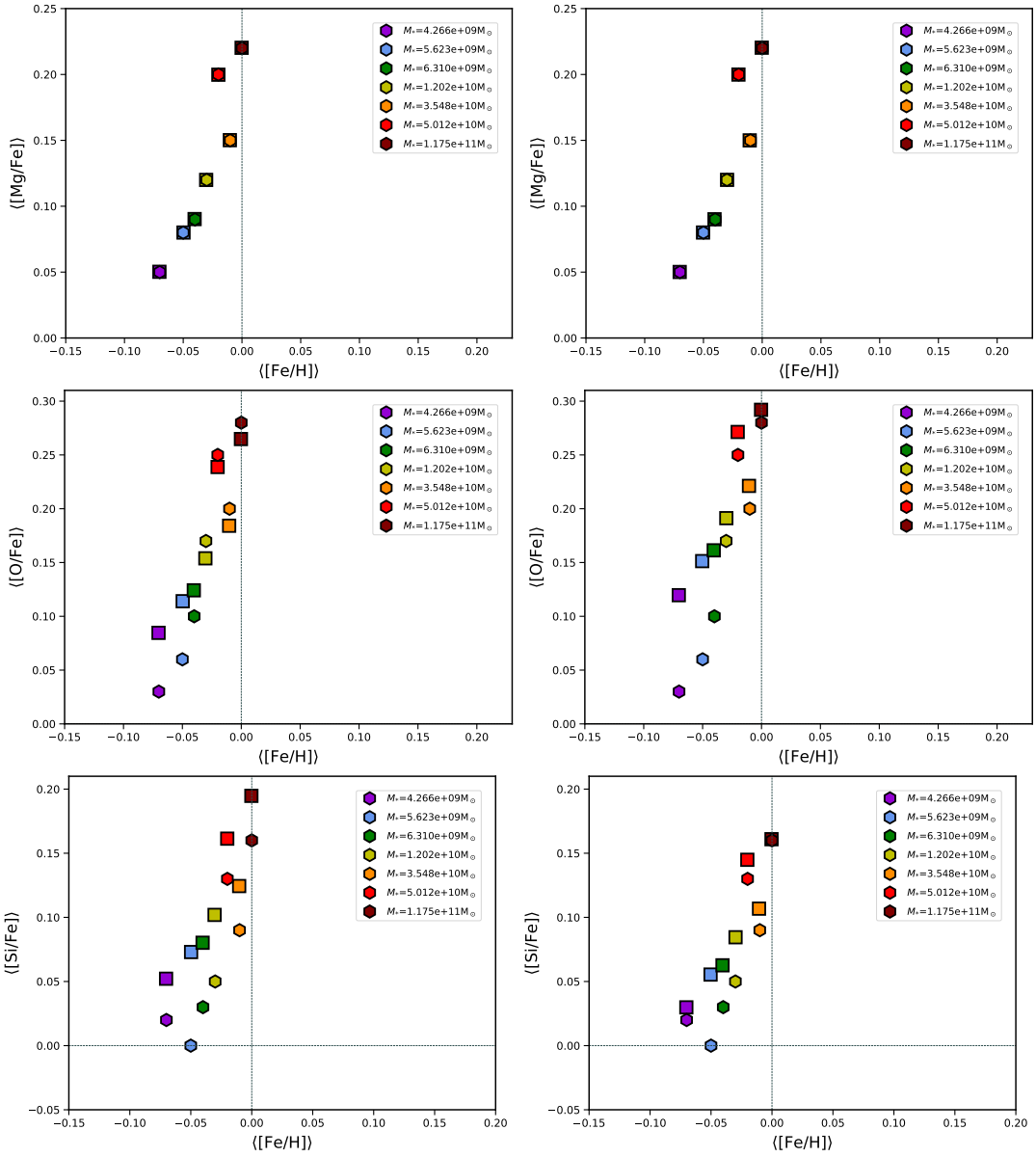

Figure 3.8: Comparing the average α-enhancement (calculated for three different α-elements; Mg, O, and Si) and the stellar metallicity (represented by $\langle$[Fe/H]$\rangle$) for two sets of close-correspondence models. See the previous page for the full caption text.

Table 3.4: Parameter values for the close-correspondence simulations

For both sets of close-correspondence models: $\boldsymbol{\tau_{in}} = 0.9 \times \tau_{SF}$, $\mathbf{t_{DTD}} = 100$ Myr, $\mathbf{F_{trunc}} = 2.5$, $\boldsymbol{f_{gas,trunc}} = 0.007$, $\boldsymbol{f_{SN}} = 0$, **IMF** $\boldsymbol{\alpha_H} = 2.3$

		Elliptical Galaxy Velocity Dispersion Bin[1]						
		$\boldsymbol{\sigma = 300}$[a] km s^{-1}	$\boldsymbol{\sigma = 246}$ km s^{-1}	$\boldsymbol{\sigma = 203}$ km s^{-1}	$\boldsymbol{\sigma = 167}$ km s^{-1}	$\boldsymbol{\sigma = 138}$ km s^{-1}	$\boldsymbol{\sigma = 112}$ km s^{-1}	$\boldsymbol{\sigma = 88}$ km s^{-1}
Close-Correspondence Models (Set 1) $\mathbf{M_{max}^{CCSN} = 42.3 M_\odot}$	$\boldsymbol{\tau_{SF}}$	0.92 Gyr	0.954 Gyr	1.188 Gyr	1.48 Gyr	1.866 Gyr	2.024 Gyr	2.59 Gyr
	$\boldsymbol{\epsilon_{out}}$	0	0	0.31	1.55	2.65	3.2	4.75
	$\mathbf{Z_{in}}$	4.25×10^{-3}	1.65×10^{-3}	10^{-10}	10^{-10}	10^{-10}	10^{-10}	10^{-10}
	$\mathbf{M_{gas,0}}$	$1.368 \times 10^{10} M_\odot$	$5.8 \times 10^{9} M_\odot$	$4.13 \times 10^{9} M_\odot$	$1.403 \times 10^{9} M_\odot$	$7.38 \times 10^{8} M_\odot$	$6.59 \times 10^{8} M_\odot$	$5.052 \times 10^{8} M_\odot$
Close-Correspondence Models (Set 2) $\mathbf{M_{max}^{CCSN} = 54.1 M_\odot}$	$\boldsymbol{\tau_{SF}}$	1.272 Gyr	1.48 Gyr	2.248 Gyr	2.912 Gyr	3.82Gyr	4.18 Gyr	5.2 Gyr
	$\boldsymbol{\epsilon_{out}}$	0.665	1.54	2.65	3.95	5.163	5.77	7.55
	$\mathbf{Z_{in}}$	10^{-10}	10^{-10}	10^{-10}	10^{-10}	10^{-10}	10^{-10}	10^{-10}
	$\mathbf{M_{gas,0}}$	$1.368 \times 10^{10} M_\odot$	$5.8 \times 10^{9} M_\odot$	$4.13 \times 10^{9} M_\odot$	$1.403 \times 10^{9} M_\odot$	$7.38 \times 10^{8} M_\odot$	$6.59 \times 10^{8} M_\odot$	$3.5 \times 10^{8} M_\odot$

[1]The values of $M_{*,f}$ corresponding to each velocity dispersion bin are from Conroy et al. 2014 (their Table 1) and are shown in Tables 3.1, 3.2, and 3.3 above.

Having explored a variety of physical processes and the manners in which they affect the final average stellar abundance ratios, it is now apparent which ones can be combined to replicate the observed positive correlation between the α-enhancement and metallicity of elliptical galaxies. In Figure 3.8 we present a set of "close-correspondence" simulations, based off of the fiducial ($\tau_{\rm in} = 0.9 \times \tau_{\rm SF}$) inflow simulations that, as can be seen in the top left panel, closely match the observed $\langle$[Mg/Fe]$\rangle$ and $\langle$[Fe/H]$\rangle$ of the seven elliptical galaxy mass bins. For this set of models, whose parameters values are listed in Table 3.4, we only change the star-formation timescale (and consequently the inflow timescale since $\tau_{\rm in} = 0.9 \times \tau_{\rm SF}$), the outflow parameter ($\epsilon_{\rm out}$), and, in the case of the two most massive galaxy bins, the inflow metallicity ($Z_{\rm in}$) is also increased. We also generate a second set of close-correspondence models where we use a higher value for the maximum stellar mass that explodes as a CCSN ($M_{\rm max}^{\rm CCSN} = 54.1 M_{\odot}$ instead of the default $M_{\rm max}^{\rm CCSN} = 42.3 M_{\odot}$). As a result of this higher $M_{\rm max}^{\rm CCSN}$, enriched inflows are no longer needed for the most massive galaxies and instead, even the most massive galaxies have outflows.

The average abundance ratios for both sets of "close-correspondence" models are shown in Figure 3.8 and the parameters used to run these simulations are listed in Table 3.4. $\langle$[α/Fe]$\rangle$–$\langle$[Fe/H]$\rangle$ is shown for three different α-elements, Mg, O, and Si, is shown in the top panels, middle panels, and bottom panels of Figure 3.8, respectively. Since the simulations were tuned to jointly reproduce the measured $\langle$[Fe/H]$\rangle$ and $\langle$[Mg/Fe]$\rangle$ of the SDSS elliptical galaxy stacked-spectra, the near-perfect match to the observed abundance ratios in the top panels (where $\langle$[Mg/Fe]$\rangle$ is plotted) is expected.

However, it is reassuring that the observed $\langle$[O/Fe]$\rangle$ and $\langle$[Si/Fe]$\rangle$ are also well replicated by our models.

Therefore, both of these sets of close-correspondence models demonstrate that the average stellar abundance patterns of elliptical galaxies can be explained without appealing to a galaxy-mass-dependent IMF. While the specific parameter values needed to reproduce each galaxy mass bin are inter-dependent, the general trends are still evident:

1. The more massive the elliptical galaxy, the shorter the star-formation timescales, $\tau_{\rm SF}$.

2. The lower the galaxy mass, the greater the amounts of outflows ($\epsilon_{\rm out}$), outflow enrichment ($f_{\rm SN}$), or gas fraction at star-formation truncation ($f_{\rm gas,trunc}$) that must be produced.

3. Replicating the stellar abundance ratios of the two most massive elliptical galaxy bins requires either enriched inflows or higher IMF-weighted yields.

3.5 Discussion

In this chapter we have explored possible explanations of the observed abundance patterns of elliptical galaxies using our flexible one-zone galactic chemical evolution code. The positive correlation between the observed stellar $\langle$[Mg/Fe]$\rangle$ and elliptical galaxy mass has been well-established in the literature for the past 30 years. This has generally been interpreted as evidence that the more massive the elliptical, the more rapidly the galaxy formed its stars. However, the foundational work by e.g., Pipino & Matteucci (2004); Thomas et al. (2005) modeling the chemical evolution of these galaxies found that the considerable α-enhancement of the most massive elliptical galaxies would require that these galaxies form their stars on timescales of $\sim$ few hundred Myr, which is so short as to possibly be unphysical (e.g., Johansson et al. 2012). More recent studies (e.g., De Lucia et al. 2006; Pipino et al. 2009; Calura & Menci 2011; Taylor & Kobayashi 2015; Segers et al. 2016) have found that the need for unrealistically short $\tau_{\rm SF}$ is alleviated by the inclusion of feedback from active galactic nuclei (AGN) which prevents late-time gas cooling (Kormendy & Ho 2013) or by otherwise truncating the galaxy's star-formation history (e.g., Segers et al. 2016; De Lucia et al. 2017; Weinberg et al. 2017). Indeed, using our chemical evolution code, for which star formation is normally truncated at $\rm T_{trunc} = 2.5 \times \tau_{SF}$ (Section 3.3.1), even the α-enhancement of the most massive ellipticals can be replicated with much more reasonable timescales of $\tau_{\rm SF} \sim 1$ Gyr (see Table 3.4).

To date, however, simultaneously reproducing the $\langle$[Mg/Fe]$\rangle$ and $\langle$[Fe/H]$\rangle$ trend with elliptical galaxy mass (or velocity dispersion) has remained a serious challenge

for simpler GCEM, cosmological semi-analytical models and more complex cosmological hydrodynamical simulations alike (e.g., Okamoto et al. 2017; De Lucia et al. 2017; Barber et al. 2018; Yan et al. 2019, and references therein): The shorter star-formation timescales that enable models to match the observed $\langle$[Mg/Fe]$\rangle$ of the most massive ellipticals result in the galaxy not having much time to enrich overall. Consequently, chemical evolution models that successfully reproduce the observed elliptical $\langle$[Mg/Fe]$\rangle$-galaxy mass trend predict an incorrect negative slope for the galaxy mass-metallicity (or mass-$\langle$[Fe/H]$\rangle$) relation and by extension, for the $\langle$[Mg/Fe]$\rangle$ – $\langle$[Fe/H]$\rangle$ relation (as seen in Figure 3.2 and discussed in the related text).

In response to this conundrum, recent papers (e.g., Gargiulo et al. 2015; Fontanot et al. 2017; Barber et al. 2018; De Masi et al. 2018; Yan et al. 2019) have claimed that a non-universal IMF, whereby more massive ellipticals have a more top-heavy IMF, is necessary to invert the $\langle$[Mg/Fe]$\rangle$ – $\langle$[Fe/H]$\rangle$ relation. However, we have presented two sets of close-correspondence models that simultaneously reproduce the observed $\langle$[Mg/Fe]$\rangle$ and $\langle$[Fe/H]$\rangle$ but do not require a top-heavy IMF or galaxy-mass dependent IMF variation. Instead, we find that the observed metallicities and α-enhancements (not only of Mg but also of O and Si) of elliptical galaxies can be explained if their star-formation timescales ($\tau_{\rm SF}$) and the efficiency with which SNe drive galactic outflows ($\epsilon_{\rm out}$) are both inversely proportional to galaxy mass (see Figure 3.8 and Table 3.4).

For our first set of simulations, the most massive galaxies do not require outflows and instead need enriched inflows to reproduce the approximately solar values

of $\langle$[Fe/H]$\rangle$ that are observed. Inflows that have been enriched with SN ejecta can significantly increase $\langle$[Mg/Fe]$\rangle$ (see Figure 3.6). This increases the normalization of the $\tau_{\rm SF}$-axis (defined as the predicted inverse-relation between $\langle$[Mg/Fe]$\rangle$ and $\langle$[Fe/H]$\rangle$ produced by varying $\tau_{\rm SF}$) so that a given $\langle$[Mg/Fe]$\rangle$ corresponds to a higher $\langle$[Fe/H]$\rangle$. While inflows are classically assumed to be pristine or very low-metallicity gas from the IGM, there is mounting evidence that galaxies also accrete higher metallicity gas.

Cosmological simulations repeatedly find that gas previously ejected as outflows is reaccreted onto/recycled back into galaxies on reasonably short timescales, especially in more massive galaxies (Oppenheimer et al. 2010; Ford et al. 2014; Brook et al. 2014; Christensen et al. 2016; Anglés-Alcázar et al. 2017). Galaxies can also accrete externally-enriched gas from nearby galaxies (e.g., Anglés-Alcázar et al. 2017) that has been removed through tidal or ram pressure stripping or launched in large-scale outflow. Furthermore, gas-rich mergers may also supply galaxies with externally-processed non-pristine gas.

As the inflows in our models represent the combined gas accretion from all of these sources, they are probably at least moderately metal-enriched. Indeed, observations of inflows, although rare, suggest that star-forming galaxies at redshifts $z \sim 0.35 - 1.4$ are accreting gas with metallicities $\rm Z_{in} \gtrsim 0.04 - 0.1\ Z_{\odot}$ (Martin et al. 2012; Rubin et al. 2012). Moreover, the cold dense gas in the CGM of galaxies, traced by Lyman-limit systems (LLS), which may be reaccreted, has been found to be relatively enriched. At low redshifts, Prochaska et al. (2017b) found median metallicities of $\sim 0.3\ Z_{\odot}$ while Lehner et al. (2013) and Wotta et al. (2016) found metallicities for their

sample of LLS that were bimodally distributed with peaks at $\sim 0.04\ Z_{\odot}$ and $\sim 0.5\ Z_{\odot}$ (also see Wotta et al. 2019; Lehner et al. 2019). However, for LLS at $z > 2$, Lehner et al. (2016) found that the enrichment was much lower ($\sim 0.01\ Z_{\odot}$).

It therefore remains to be seen if the inflow-enrichment can reach the metallicities of $Z_{in} \approx 0.3\ Z_{\odot}$ and $Z_{in} \approx 0.12\ Z_{\odot}$ needed for the close-correspondence models of our two most massive ellipticals, particularly at relatively high redshifts when the majority of the stars in these galaxies were formed. It is interesting to note though that high-resolution simulations of individual galaxies find that while inflows of low-mass galaxies are primarily pristine, massive galaxies accrete gas that is more highly enriched (Brook et al. 2014; Ma et al. 2016). This is, at least qualitatively, what we find for our first set of close-correspondence simulations.

A complicating factor is that since outflows are observed to be ubiquitous for a wide range of elliptical galaxy masses, and are seen at high redshift in the possible progenitors of massive elliptical (see review by Veilleux et al. 2020, and references therein), it seems likely that the ellipticals in the highest mass bin of our sample from Conroy et al. (2014) should have experienced outflows. However, as shown in Figure 3.5, outflows decrease $\langle$[Fe/H]$\rangle$ and our fiducial ($\tau_{in} = 0.9 \times \tau_{SF}$) inflows already under-produce $\langle$[Fe/H]$\rangle$ for these most massive ellipticals. Shifting the normalization of the τ_{SF}-axis so that our models could match the observed $\langle$[Fe/H]$\rangle$ despite these outflows could be difficult to achieve with the accretion of enriched gas alone (see Figure 3.6).

Fortunately, there are other ways of increasing the normalization. The stellar IMF-weighted yields and their implementation in our model play a crucial role in setting

the normalization of the $\tau_{\rm SF}$-axis. As can be seen in panel (a) of Figure 3.7, changing the IMF-weighted yields by modifying the slope of IMF itself has a significant impact on the simulated abundance ratios. Making the IMF more top-heavy, as for the simulations represented by the two darkest grey squares, enhances both $\langle$[Mg/Fe]$\rangle$ and $\langle$[Fe/H]$\rangle$, thus increasing the normalization of the $\tau_{\rm SF}$-axis. But the extent to which the slope of the IMF varies in galaxies is debated and direct observational constraints on the slope of the high-mass end of the IMF in ellipticals remain limited. Rather, evidence has mostly been for a bottom-heavy IMF at the center of elliptical galaxies (e.g., Cappellari et al. 2012; Conroy & van Dokkum 2012b; Martín-Navarro et al. 2015; Smith 2020) which would lower $\langle$[Fe/H]$\rangle$ and $\langle$[Mg/Fe]$\rangle$ and thus the normalization of the $\tau_{\rm SF}$-axis. This would making it even more difficult to reproduce the average stellar abundances of the most massive ellipticals.

However, a modified IMF is not the only way in which the default IMF-weighted yields implemented in our code could differ from the true values in elliptical galaxies. There are many aspects of late-stage stellar evolution that are widely acknowledged as being poorly constrained. These include mass loss rates, stellar rotation and even the exact mechanism which causes these stars to explode, and they greatly affect the final fates of massive stars (see Section 3.3.3 above as well as review by Nomoto et al. 2013). Thus, the maximum stellar mass that explodes as a CCSN, $\rm M_{max}^{CCSN}$, rather than collapsing directly to a black hole, and the nucleosynthetic contribution of stars with $M_{\rm init} \geq 40{\rm M}_{\odot}$ in general remain very uncertain. We choose a default value of $\rm M_{max}^{CCSN} = 42.3{\rm M}_{\odot}$ that is very close to the largest initial stellar mass of $40{\rm M}_{\odot}$ covered

by our CCSN yield tables (Kobayashi et al. 2006). However, it is likely that at least a subset of these massive stars have lost enough of their hydrogen envelopes to be able to explode. This is supported by the fact that a number of the most massive stellar models at solar metallicity in Sukhbold et al. (2016) ($M_{init \geq 60 M_\odot}$) are still able to produce CCSN.

From panel (b) of Figure 3.7 we can see that a relatively small increase in M_{max}^{CCSN} leads to a very significant increase in $\langle$[Mg/Fe]$\rangle$ and the normalization of the τ_{SF}-axis. Therefore, for our second set of close-correspondence models, we increased the normalization of the τ_{SF}-axis by using a higher value for the maximum stellar mass that explodes as a CCSN ($M_{max}^{CCSN} = 54.1 M_\odot$ instead of the default $M_{max}^{CCSN} = 42.3 M_\odot$). Since a higher M_{max}^{CCSN} results in a higher $\langle$[Mg/Fe]$\rangle$, these simulations do not need as short a star-formation timescale to match the observed α-enhancement. Consequently, the galaxy has longer to enrich its gas reservoir, leading to higher $\langle$[Fe/H]$\rangle$ and an increased τ_{SF}-axis normalization. In this case, the increase in M_{max}^{CCSN} shifts the τ_{SF}-axis so much that the $\langle$[Fe/H]$\rangle$ becomes super-solar at the $\langle$[Mg/Fe]$\rangle$ observed for the most massive ellipticals.

Thus, metal-enriched inflows are no longer needed to increase the $\langle$[Fe/H]$\rangle$ of the most massive ellipticals. Instead, we find that for this set of close correspondence models, all the elliptical galaxy bins, even the most massive ones, require outflows to shift the simulated $\langle$[Fe/H]$\rangle$ back to their observed values. The values of ϵ_{out} that are now needed for the lower mass galaxies also increase, becoming $1.6 - 2.5$ times higher than for the original set of close-correspondence models. In addition, the star-formation

timescales for the lower mass galaxies are about twice as long as those found by the first set of close-correspondence models

3.5.1 The feasibility of mass-dependent outflows

The increase in the measured $\langle$[Fe/H]$\rangle$ with increasing elliptical galaxy mass found by Conroy et al. (2014) and shown in Figure 3.1, is a reflection of the well-known galaxy mass-metallicity relation (M-Z; MZR). This correlation between stellar mass (or its proxy, luminosity) and the overall metallicity of the galaxy has been recognized since at least McClure & van den Bergh (1968) for both the stellar abundances (e.g., Faber 1973) and the gas-phase abundances (Lequeux et al. 1979). More recently, Tremonti et al. (2004) confirmed the existence of this relation in a much larger sample of $\sim$ 53000 local star-forming galaxies from SDSS, finding an increase in the gas phase oxygen abundance (12 + log(O/H)) as a function of stellar mass. Furthermore, the gas metallicities and stellar masses of star-forming galaxies remain tightly correlated up to at least $z \sim 3.5$ (e.g., Maiolino et al. 2008; Troncoso et al. 2014; Sanders et al. 2020).

It has long been suggested that galactic outflows are key drivers of this correlation and that the MZR is a reflection of galaxies' mass-dependent ability to retain metal-enriched gas. Larson (1974), expanding on the ideas of Mathews & Baker (1971) and van den Bergh (1972), proposed that the observed elliptical galaxy mass-metallicity relation could be explained if more of the metal-enriched recycled gas was lost by lower mass elliptical galaxies than by more massive ones. This was achieved in their galaxy evolution model by having short-lived SNe heat the surrounding ISM, allowing the gas to escape only once the energy imparted by these SNe exceeded the escape velocity of

the galaxy.

This idea that galaxies with smaller potential wells can more easily lose their gas and metals via galactic winds has been incorporated into many semi-analytical and hydrodynamical cosmological galaxy formation models by relating the galaxy's mass loading factor (defined as the ratio of the outflow mass rate to the star formation rate: $\eta \equiv \frac{\dot{M}_{\rm out}}{\dot{M}_*}$) to its maximum circular velocity, $V_{\rm circ}$, by either assuming energy-driven outflows ($\eta \propto {V_{\rm circ}}^{-2}$; e.g., Kauffmann et al. 1993; Somerville et al. 2008; Vogelsberger et al. 2014) or momentum-driven outflows ($\eta \propto {V_{\rm circ}}^{-1}$; e.g., Oppenheimer et al. 2010; Anglés-Alcázar et al. 2014)[18]. Moreover, even in simulations that model galactic winds self-consistently and do not explicitly relate the effectiveness of outflows to $V_{\rm circ}$, (e.g., Muratov et al. 2015; Christensen et al. 2016; Anglés-Alcázar et al. 2017; Mitchell et al. 2020) an inverse relation between η and $V_{\rm circ}$ (or the galaxy's mass) emerges nonetheless. Therefore, the fact that — in order to invert the $\tau_{\rm SF}$-axis and properly reproduce the observed $\langle$[Fe/H]$\rangle$–galaxy mass relation — our close-correspondence simulations find that SNe more effectively sweep up and remove ISM gas (as parametrized in our model by increasing $\epsilon_{\rm out}$) from lower mass ellipticals is well motivated from a theoretical perspective and in line with what is found by more sophisticated modeling.

Although outflows are commonly seen across a wide range of galaxy masses and redshifts (e.g., Martin 2005; Weiner et al. 2009; Chen et al. 2010; Rubin et al. 2010; Martin et al. 2012; Rubin et al. 2014; Chisholm et al. 2015; McQuinn et al. 2019; as well as the recent review by Veilleux et al. 2020 and references therein), observationally

[18] For a derivation of these scaling relations see Murray et al. (2005).

confirming this correlation between the galaxy mass (or V_{circ}) and the efficiency with which SNe drive gas outflows remains challenging. In particular, constraining this relation requires accurate galaxy outflow masses which are extremely difficult to measure: the diffuse and multi-phase nature of outflows means that only those in local galaxies can be observed using emission lines. Instead, absorption lines are often used but converting them into mass outflow rates generally requires many assumptions regarding the outflow geometry, opacity, metallicity, and ionization state (for a more detailed discussion of outflow mass measurements, see Chisholm et al. 2016; Veilleux et al. 2020). Despite these difficulties, in their recent work, Chisholm et al. (2017) were able to robustly measure the outflow masses of seven local star-forming galaxies and derive an inverse scaling relation between the outflow mass loading factor and galaxy stellar mass of $\eta \propto M_*^{-0.4}$.

To compare our models, which parametrize the outflow efficiency as ϵ_{out} (defined as the ratio of the outflow mass rate to the SN ejecta mass rate $\epsilon_{out} \equiv \frac{\dot{M}_{out}}{\dot{M}_{SN,ej}}$, see Equation 2.5), to these observations and predictions from other simulations, we also calculate the traditional mass loading factor η for our second set of close-correspondence simulations. We find that these simulations have average mass loading factors ranging from $\eta \approx 0.06 - 0.7$. This is much lower than Chisholm et al. (2017) but more similar to the $\eta \approx 0.2 - 0.9$ found by Martin et al. (2012) for galaxies at $z \sim 1$. However, since the elliptical galaxies that we model likely had very different evolutionary histories from the star-forming galaxies studied by Chisholm et al. (2017) or Martin et al. (2012), these observed mass loading factors may not be representative of the ones actually experi-

enced by our ellipticals over their star-forming histories. Moreover, it is also important to consider that the value of $\epsilon_{\rm out}$ (and thus of the corresponding η) needed to reproduce the $\langle$[Fe/H]$\rangle$ measured for the Conroy et al. (2014) stacked elliptical galaxies depends sensitively on the IMF-weighted yield (as discussed above) as well as on other poorly constrained parameters like $\rm M_{gas,0}$.

Furthermore, as demonstrated in Figure 3.5, the impact of $\epsilon_{\rm out}$ on $\langle$[Fe/H]$\rangle$ is degenerate with that of the $f_{\rm gas,trunc}$ and $f_{\rm SN}$ parameters. For instance, rather than having the outflow metallicity ($Z_{\rm out}$) match the metallicity of the ISM ($Z_{\rm ISM}$) as in our standard close-correspondence simulations, we could instead assume that a non-zero mass-fraction of the SN ejecta is mixed into the outflowing gas such that $\frac{Z_{\rm out}}{Z_{\rm ISM}} > 1$ (and increases as $f_{\rm SN}$ increases). As a result, smaller values of $\epsilon_{\rm out}$ would be needed to reproduce the observed $\langle$[Fe/H]$\rangle$. Indeed, Chisholm et al. (2018) measure the outflow metallicities for seven local star-forming galaxies whose stellar masses range from $\log(M_*) = 6.9 - 10.7$ and find that all but one have significantly enriched outflow metallicities as compared to their ISM metallicities, with $\frac{Z_{\rm out}}{Z_{\rm ISM}} \approx 12 - 46$ for their lowest mass galaxies and a median $\frac{Z_{\rm out}}{Z_{\rm ISM}} = 2.6$ for their higher mass galaxies. In the context of our model, this suggests that the fraction of SN ejecta removed ($f_{\rm SN}$) in outflows is very likely non-zero for the less massive elliptical galaxies in our comparison sample and that $f_{\rm SN}$ should be anti-correlated with galaxy stellar mass. Consequently, the degree to which galaxy outflows are enriched with metal-rich SN ejecta (parametrized by $f_{\rm SN}$) and its dependence on galaxy mass probably also plays an important role in shaping the elliptical galaxy mass-dependence of the observed $\langle$[Fe/H]$\rangle$.

The combined impact of the mass loading factor and the outflow metallicity (which in our code are most closely represented by $\epsilon_{\rm out}$ and $f_{\rm SN}$, respectively) is often jointly considered in the form of the metal loading factor, ζ, which is defined as the product of the mass loading factor and the outflow to ISM metallicity ratio ($\zeta \equiv \frac{Z_{\rm out}}{Z_{\rm ISM}} \times \eta = \frac{Z_{\rm out}}{Z_{\rm ISM}} \times \frac{\dot{M}_{\rm out}}{\dot{M}_*}$; Peeples & Shankar 2011). While observational constraints are not yet strong enough to distinguish which of these parameters is driving the change in ISM metallicity (note that it may well be both), our simulations suggest that their combined impact is greater on less massive ellipticals (i.e., the metal-loading factor is inversely related to the galaxy mass). This indeed seems to be born out observationally (Chisholm et al. 2018; Sanders et al. 2021; Tortora et al. 2021) and in other models (e.g., Mac Low & Ferrara 1999; Peeples & Shankar 2011; Muratov et al. 2015, 2017; Pandya et al. 2021).

3.6 Summary and Conclusions

In this chapter we have presented close-correspondence models (generated using our flexible one-zone galactic chemical evolution code) that reproduce the observed $\langle$[Mg/Fe]$\rangle$ and $\langle$[Fe/H]$\rangle$ measured for the seven elliptical galaxy mass bins from Conroy et al. (2014). While many recent papers (e.g., Gargiulo et al. 2015; Fontanot et al. 2017; Barber et al. 2018; Yan et al. 2019) have argued that a galaxy-mass dependent IMF is needed to simultaneously replicate the elliptical α-enhancement and mass-metallicity relation, our close-correspondence models only use a standard Kroupa IMF. Our models therefore serve as an alternative explanation of the average stellar abundance patterns

seen in elliptical galaxies.

- We find that our models require shorter star-formation timescales ($\tau_{\rm SF}$) for increasingly massive elliptical galaxies. This timescale is what sets the observed α-enhancement and its mass dependence is what produces the trend we see.

- If only the star-formation timescale is varied, our models produce an anti-correlation between the average stellar metallicity (represented by $\langle$[Fe/H]$\rangle$) and the galaxy mass which is contrary to the mass-metallicity relation observed in ellipticals. We refer to this predicted inverse-relation between $\langle$[Mg/Fe]$\rangle$ and $\langle$[Fe/H]$\rangle$ as $\tau_{\rm SF}$ is changed as the "$\tau_{\rm SF}$-axis".

- However, an outflow efficiency (controlled by $\epsilon_{\rm out}$ in our model) that decreases with elliptical galaxy mass will invert this predicted trend (the $\tau_{\rm SF}$-axis), allowing our models to reproduce the observed stellar abundance patterns of elliptical galaxies.

- The precise parameter values required to reproduce the observed abundances are inter-dependent. The value of a given parameters will depend not only on the choices made for other degenerate parameters, but also on the overall normalization (i.e. y-intercept) of the $\tau_{\rm SF}$-axis. For example, the greater the normalization, the larger the combination of outflow efficiency ($\epsilon_{\rm out}$), outflow enrichment ($f_{\rm SN}$), and gas fraction at star-formation truncation ($f_{\rm gas,trunc}$) that is needed to match the observed $\langle$[Fe/H]$\rangle$ for all the elliptical galaxy mass bins.

- Pristine (or very low-metallicity) inflows from the IGM are not the only type of gas accreted by galaxies. Metal-enriched gas from recycled galactic outflows or gas

that has been externally-processed in nearby galaxies will also contribute to the chemical enrichment of the gas reservoir. We find that allowing the inflowing gas to have a non-zero metallicity increases the normalization of the $\tau_{\rm SF}$-axis and can help explain the high metallicities observed in massive ellipticals. We note that though our chemical evolution code supports the use of a time-dependent inflow metallicity (and elemental composition), we have not yet explored how this would affect the stellar abundance patterns and leave it for future work.

- The IMF-weighted yields also play an important role in setting the normalization of the $\tau_{\rm SF}$-axis. However, due to our imperfect understanding of the IMF, stellar evolution and stellar nucleosynthesis, the IMF-weighted yields in our model may not fully capture the real IMF-weighted yields of elliptical galaxy stellar populations.

- Though a more top-heavy IMF can enhance the IMF-weighted yields and thus increase the normalization of the $\tau_{\rm SF}$-axis, so can making relatively small changes to the maximum stellar mass that explodes as CCSN. Raising $M_{\rm max}^{\rm CCSN}$ from 42.3 $M_{\odot}$ to 55 $M_{\odot}$, which is still well within the theoretical and observational uncertainties, will increase the [Mg/Fe] of the stellar gas returns, resulting in longer star-formation timescale for all elliptical galaxy bins. The most massive ellipticals will therefore have more time to enrich and — even with some amount of outflows (which remove metals from the gas reservoir and suppress its metallicity enrichment) — can still produce realistic stellar $\langle$[Fe/H]$\rangle$ in our simulations.

- Different reasonable decisions when implementing incomplete or missing theoreti-

cal yield tables will also affect the IMF-weighted yields of our models. In Section 3.3.3 we describe the challenges in accounting for the nucleosynthetic yields of stars in the mass range between $\sim 8-12 M_{\odot}$ for which theoretical yield tables at a range of metallicities do not currently exist. To not introduce poorly-characterized errors in our IMF-weighted yields (as would happen if we interpolated between the highest-mass super-AGB yield tables and the lowest-mass CCSN yields tables), we make the imperfect choice to have stars in this mass range evolve passively. This decision, while reasonable, means that the IMF-weighted yields in our model are likely underestimated. Therefore, the $\tau_{\rm SF}$-axis presented in this work could have a significantly higher normalization just by including the yields from these intermediate-mass stars.

- Despite these uncertainties, particularly in the normalization of the $\tau_{\rm SF}$-axis, that prevent us from determining exact parameter values for our close-correspondence models, the trends we find of shorter star-formation timescales and less effective outflows (smaller $\epsilon_{\rm out}$) for more massive elliptical galaxies are robust.

- To help improve the chemical evolution modeling of these elliptical galaxies and better distinguish between mostly degenerate options, we need better-constrained stellar nucleosynthetic yields and more complete theoretical yield tables. This is particularly important at the high-mass end where we need to know which stellar masses explode as CCSN, and in the region between $\sim 8-13 M_{\odot}$ for which yield tables do not really exist, especially at lower metallicities.

- In the future, we can use chemical evolution modeling of elliptical galaxies to

constrain new theoretical yield tables.

Chapter 4

The detection of intergalactic Hα emission from the Slug Nebula at $z \sim 2.3$

4.1 Introduction

In the standard paradigm of galaxy formation and evolution, galaxies are thought to be fueled by accreting material from their surrounding circumgalactic medium (CGM). However, the properties of this accreting material, such as the density, temperature, angular momentum and morphology, remain uncertain. Some cosmological simulations suggest that most of this material accretes in the form of relatively cold ($T \sim 10^4$ K) intergalactic filaments. This has even been found to be the case for the most massive galaxies at high redshift, for which a stable hot corona should be in place

(Dekel et al. 2009). On the other hand, theoretical arguments and higher resolution simulations have highlighted that such streams may not be able to survive instabilities (Nelson et al. 2013; Mandelker et al. 2016). Alternatively, such material could result from the cooling of the hot corona (Voit et al. 2015). In order to distinguish between these two scenarios, direct imaging of the CGM and intergalactic gas is essential.

Unfortunately, the expected emission of both the cold component (due to the recombination radiation of gas ionized by the cosmic ultraviolet background) and hot component (due to X-ray bremsstrahlung) of the CGM around a typical galaxy at $z > 2$ is well below current detection limits (e.g. Cantalupo et al. 2005; Gallego et al. 2018). Local ultraviolet (UV) radiation fields, such as in the vicinity of a bright active galactic nucleus (AGN), may be used to increase the detectability of Ly α emission. Indeed, in recent years, several enormous Ly α nebulae (ELANe) have been discovered at $z > 2$ around bright radio-quiet quasars. ELANe are characterized by their extended Ly α emission that traces the CGM, and even intergalactic medium (IGM), out to several hundred kpc from their quasars. These detections were made using custom-made narrow-band (NB) filters on the W.M. Keck I telescope (Cantalupo et al. 2014; Hennawi et al. 2015; Cai et al. 2017) or by performing integral field spectroscopy using the Keck Cosmic Web Imager (KCWI) (Cai et al. 2018) or the Multi Unit Spectroscopic Explorer (MUSE) on the Very Large Telescope of the European Southern Observatory (Borisova et al. 2016; Arrigoni Battaia et al. 2018; see Cantalupo 2017 for a review).

The largest and brightest of such Ly α emitting structures, nicknamed the 'Slug Nebula', was discovered by Cantalupo et al. (2014). The 'Slug' was found near

the radio-quiet quasar UM287 using a custom NB filter on the Low Resolution Imaging Spectrometer (LRIS) instrument mounted on the Keck I telescope. With a total projected size of at least 480 physical kpc, this nebula extends well beyond the virial radius of the halo of a typical bright quasar host with a mass of $\sim 10^{12.5} M_{\odot}$ (see da Ângela et al. 2008; Trainor & Steidel 2012). The UM287 Nebula (also referred to as the Slug Nebula, Slug, or Nebula throughout this paper), therefore, represents the best system available to date in which to jointly study the circumgalactic and intergalactic medium in emission.

The filamentary and asymmetric morphology of the Slug Nebula is similar to the predictions of recent cosmological simulations. However, the very high surface brightness (SB) of the Ly α emission (above 10^{-17} erg s^{-1} cm^{-2} arcsec^{-2}) extending over hundreds of kpc presents a serious challenge to our current theoretical understanding of baryonic structure formation in the massive halos associated with quasars. As discussed in Cantalupo et al. (2014), there are at least two possible scenarios for the origin of the extended Ly α emission: (i) fluorescent Ly α emission following hydrogen recombinations of the gas ionized by the quasar, and (ii) Ly α 'photon-pumping' or 'scattering' of the quasar broad-line region emission.

In the first case, the observed Ly α SB can only be explained if the recombining gas is 'cold' ($T < 10^5$ K) and has very large densities ($> 1 - 10$ cm^{-3}) that are much higher than the typical gas densities expected at such large distances from a galaxy. However, because recombination emission scales with the density squared, a small volume filling factor or a large gas clumping factor ($C > 1000$) below the scale of

a few kpc could explain the Ly α emission as well as the much lower volume-averaged densities. Therefore, this interpretation of the data would require dense photoionized 'clumps' of gas within the CGM but these clumps must have sizes that are well below the current resolution limits of cosmological simulations (see e.g., Cantalupo et al. 2014, Arrigoni Battaia et al. 2015a for further discussion).

The second case, as discussed in Cantalupo et al. (2014), would require very large column densities of neutral gas above 10^{20} cm^{-2} (i.e., corresponding to damped Ly α systems, abbreviated as DLAs) to be present on scales of hundreds of kpc around the quasar. This material would then have to be illuminated by the Ly α emission of the quasar's broad-line region without being photoionized by the quasar itself. Although optically thick gas is routinely observed in the proximity of quasars (Prochaska et al. 2013), such large column densities of neutral material over these distance scales are not typically observed either in absorption studies or in cosmological simulations. However, recent deep observations have found that some DLAs are also associated with Ly α nebulae, although these nebulae have much smaller physical scales and luminosities than the Slug (Fumagalli et al. 2017).

Either scenario therefore requires very high densities and Ly α observations alone are not able to distinguish whether the gas is mostly neutral and diffuse or ionized and clumpy. In order to break this degeneracy, a non-resonant line such as He II[1640] or H α is needed. In particular, a detection or limit on H α emission would put the most stringent constraint on the recombination or 'scattering' origin of the Ly α emission because these two transitions arise in the same atom. Another advantage of searching for

H α emission is that the presence of He II[1640] emission could require favourable conditions in terms of the ionization spectrum and ionization parameter (see e.g., Arrigoni Battaia et al. 2015a; Cantalupo et al., in preparation).

To our knowledge, there have been no reported detections prior to our study of H α emission from intergalactic gas associated with Ly α nebulae around radio-quiet quasars.[19] Similarly, no He II[1640] emission has been found in long-slit spectroscopic observations of ELANe around radio-quiet quasars (Arrigoni Battaia et al. 2015a), although deep integral-field spectroscopic observations are now revealing He II emission at fainter levels than expected (Cantalupo et al., in preparation). In contrast with ELANe, a few detections of He II[1640] in radio-quiet Ly α blobs (LABs, see Cantalupo 2017 for a review) have been reported (e.g., Prescott et al. 2015a), though the majority of LABs show no sign of He II[1640] emission (Arrigoni Battaia et al. 2015b).

Although the terms LAB and ELAN are often used interchangeably, it is important to note some distinctions. ELANe are bright ($L_{\mathrm{Ly}\alpha} \sim 10^{44}$ erg s^{-1}) Ly α nebulae around $z > 2$ quasars with extents > 100 kpc (e.g. Cantalupo et al. 2014; Hennawi et al. 2015; Arrigoni Battaia et al. 2018). Though comparable in size and brightness to ELANe, LABs were historically distinguished by their apparent lack of association with an AGN or bright continuum source at the time of their discovery (e.g., Steidel et al. 2000; Matsuda et al. 2004; Dey et al. 2005; Prescott et al. 2009; Yang et al. 2009; Arrigoni Battaia et al. 2015b). However, follow-up observations of LABs often uncovered evidence of the presence of obscured AGN or massively star-forming galaxies

[19] Detection of H α emission from galaxies embedded in some Ly α nebulae at z$\sim$2.3 have been reported by, for example Yang et al. (2014)

(e.g., Chapman et al. 2001; Geach et al. 2009; Overzier et al. 2013; Prescott et al. 2015b; Hine et al. 2016). Therefore, the term LABs has started being used by some authors to refer to large Ly α nebulae with physical extents greater than $\sim$ 100 kpc.

Given this broader definition of LABs, ELANe could be considered a subtype of LABs. However, since LABs encompass a wide variety of systems, it would be a mistake to blindly apply any inferences about ELAN emission mechanisms to LABs as a whole. Similarly, though very extended Ly α nebulae have been found around high-redshift radio-loud galaxies with large radio jets, these more commonly exhibit extended He II[1640] emission and broader kinematics. This could suggest that different processes are at play between radio-quiet and radio-loud systems (see e.g. Villar-Martín 2007, Miley & De Breuck 2008, and Cantalupo 2017 for reviews).

Nevertheless, despite the different classifications and nomenclatures associated with highly extended Ly α emission discovered in the last decades, they are almost always associated with AGN or massively star-forming galaxies. This suggests that the presence of a strong ionizing field, and therefore emission produced by fluorescent recombination radiation, is likely a necessary requirement in all cases (see Cantalupo 2017 for discussion).

In this paper, we report the results of our search for extended H α emission from the Slug Nebula using long-slit NIR spectroscopy with the new MOSFIRE instrument on the W.M. Keck I telescope. We also perform high-resolution Ly α spectroscopy of a similar region in the Slug Nebula with the goal of both guiding our H α search in the velocity dimension and gaining a deeper understanding of the Ly α kinematics.

The paper is organized as follows: In Section 4.2.1, we describe the deep Keck I/LRIS observations taken of the brightest region of the Slug Nebula and in Section 4.2.2, discuss the data reduction process of these observations. Similarly, the two nights of deep near-infrared (NIR) spectroscopy, obtained using Keck I/MOSFIRE , and their reduction, are described in Sections 4.2.3 and 4.2.4, respectively. In Section 4.3.1 we explore the Ly α kinematics of the Slug and in Section 4.3.2 we measure the Ly α flux contained within the MOSFIRE N1 slit. Sections 4.3.3 and 4.3.4.1 discuss the measurement of the Slug Nebula's H α flux. We also extract the 1-D spectra of two compact sources in the vicinity of the Slug Nebula ($z \sim 2.287$) from the MOSFIRE N1 and N2 observations in Section 4.3.5, and calculate their N II and H α fluxes. In Section 4.4.1 we examine the implications of the Ly α kinematics for the Nebula's gas distribution. In Section 4.4.2, we compute the Ly α to H α flux ratio and compare it to predictions from case B recombination radiation. In Section 4.4.3, we constrain the origin of the compact source 'C' and 'D' emission (AGN versus star-formation versus QSO A fluorescence). Finally, in Section 4.5, we summarize our results.

4.2 Observations

4.2.1 LRIS spectroscopy

On UT 2015 September 09, we used the blue camera of the Low Resolution Imaging Spectrometer (LRIS; Oke et al. 1995) on the Keck I 10m telescope to observe the Ly α emission of the UM287 Nebula. The spectra were obtained with a 1 arcsec slit as part of a multi-object slit mask. The slit was oriented with a position angle (PA)

of 322 to match the PA of the MOSFIRE Night 2 (N2) mask (see Fig. 4.1). In order to cover the Ly α emission of the Slug, we used the D460 dichroic and the 1200 lines mm^{-1} grism blazed at 3400 Å, which covers ≈3300-4200Å. The measured full-width at half-max (FWHM) was found to be $\sim$ 1 arcsec. We acquired 9 $\times$ 1800 s science exposures, for a total exposure time of 4.5 h. In between each exposure, we dithered $\sim$ 1 arcsec along the slit. In addition to the science exposures, we took bias frames, arcs, as well as slitless and slitted twilight flats which were used in the data reduction process. All exposures were read out with 1 $\times$ 1 CCD binning.

4.2.2 LRIS calibrations and data reduction

The LRIS blue camera data were reduced using the publicly available LOWREDUX package, distributed within XIDL (Prochaska et al. 2017a) producing nine calibrated, unfluxed 2D spectra. This pipeline performs standard data reduction steps, including overscan and bias subtraction, flat fielding, and wavelength calibration.

The flat fielding procedure constructs a pixel flat used to correct for pixel sensitivity variation from the slitless twilight flats. In addition, the slitted twilight flats are utilized to correct for the non-uniform illumination of the slit. LOWREDUX determines a wavelength solution by fitting low order polynomials to the arc lamp spectra and is reported in air wavelengths for the 2D spectra.

We wrote custom python scripts using the ASTROPY (Astropy Collaboration et al. 2013), IPYTHON (Perez & Granger 2007), MATPLOTLIB (Hunter 2007), NUMPY (Walt et al. 2011), and SCIPY (Jones et al. 2001) packages, to coadd the individual reduced spectra since LOWREDUX does not combine 2D spectra. Due to the dither-

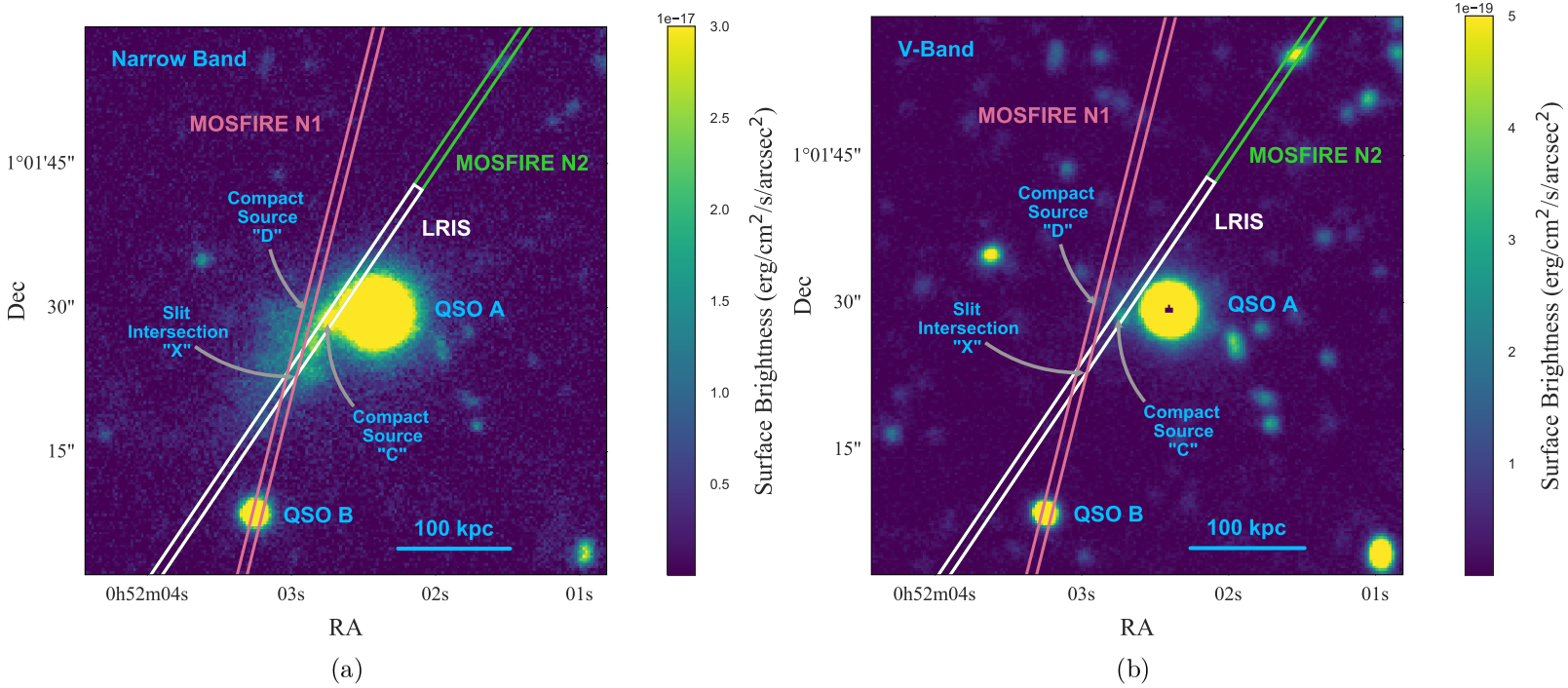

Figure 4.1: This figure depicts the 10 h NB image (left-hand panel) and deep continuum image (right-hand panel) of the region surrounding the UM287 Nebula, adapted from Figure 1 of Cantalupo et al. (2014). The NB data were taken on the Keck I telescope with the LRIS NB3985 filter, selected to cover Ly α emission at the redshift of QSO A. The continuum image was taken simultaneously with the LRIS V-band filter on the red camera. The MOSFIRE Night 1 (N1), MOSFIRE Night 2 (N2) and LRIS slit positions are overlaid in red, green, and white respectively. The green MOSFIRE N2 slit extends the full length of the image, overlapping with the white LRIS slit. QSOA, QSOB, compact source 'C', compact source 'D', and position 'X' (the intersection of the MOSFIRE N1 and LRIS slits), are also labeled.

ing along the slit between exposures, each image needed to be shifted, in the spatial direction, to a common frame (chosen to be that of the fifth exposure). To calculate the required shift, we fit Gaussians to the spatial profile of a star in a separate slit on the mask and determined the change in the centroid position. The applied shifts were rounded to the nearest integer pixel in order to avoid interpolation and complications in calculating the associated error. The uncertainty associated with integer shifts is at most 1/2 pixel, which corresponds to an error of 0.0675 arcsec, which is far less than the 1 arcsec seeing disk.

LRIS is known to experience significant telescope pointing position-dependent flexure, which shifts the location of a fixed wavelength on the detector. LOWREDUX uses the known wavelengths of skylines to measure, in an extracted 1D spectrum, the wavelength solution offset caused by the flexure. We therefore used LOWREDUX to extract a 1D spectrum of compact source 'C' (see Fig. 4.2), which is located in the same slit as the Slug Nebula, and calculate the flexure-induced spectral pixel shift for each exposure. This shift of $\sim 11-13$ unbinned pixels was then rounded to the nearest integer pixel and applied in the spectral direction of each of the 2D spectra. The rounding error of at most 1/2 pixels amounts to an uncertainty of ≈ 0.135Å or $\approx$10 km s^{-1}.

Once the exposures were corrected for flexure and dithering offsets, we ran each of them through the publicly distributed DCR package (Pych 2004, 2012) to detect and remove cosmic rays. We then coadded these nine cleaned images by summing the electron counts in each pixel and renormalizing by the total exposure time. In addition,

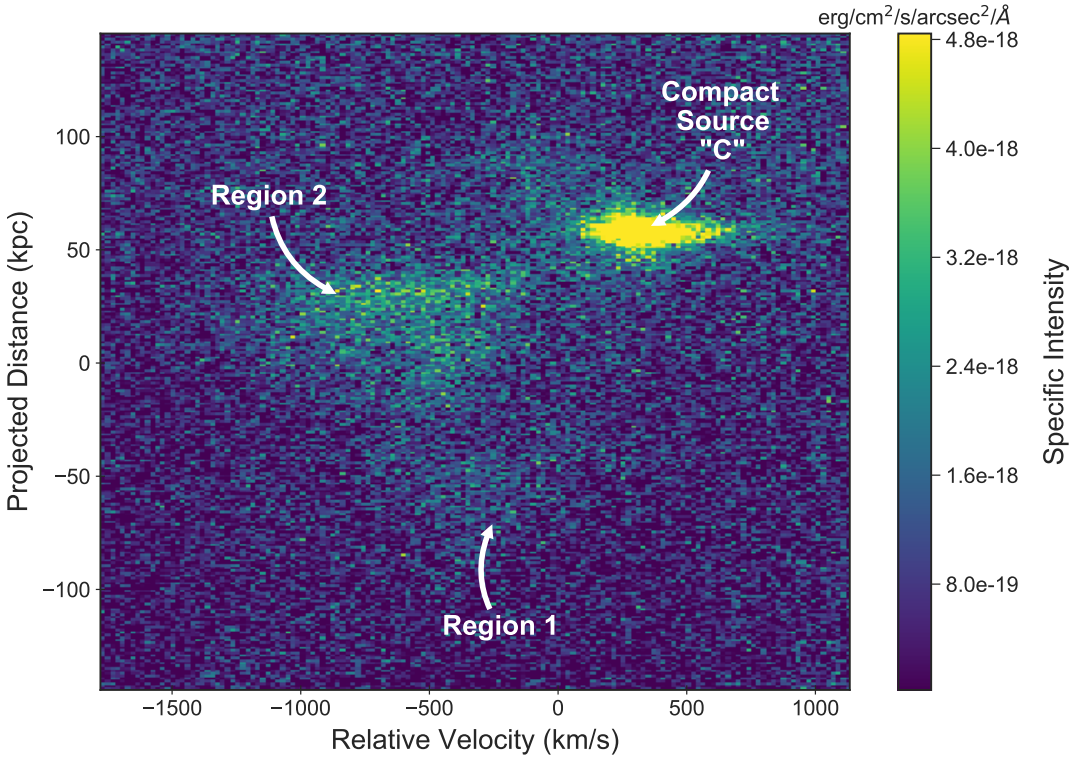

Figure 4.2: The unsmoothed 2D spectrum taken with Keck I/LRIS (the white slit in Fig. 4.1). The $v = 0$ km s^{-1} corresponds to the expected Ly α emission at a redshift of $z = 2.283$, the redshift of QSO A. The projected distance corresponding to 0 kpc indicates the location of the MOSFIRE N1 and LRIS slit intersection, referred to as position 'X' in Fig. 4.1. The bright Ly α emitter around $v \sim 300$ km s^{-1} and spatial position of ~ 60 kpc is compact source 'C' (see Fig. 4.1). The Slug Nebula has a physical extent along the slit of ~ 150 kpc. Its Ly α emission is blue-shifted with respect to that of compact source ($z = 2.287$) and the redshift of QSO A ($z = 2.283$).

the corresponding 2D wavelength fits file produced by LOWREDUX was converted from air wavelengths to vacuum wavelengths.

Lastly, we flux calibrated our coadded spectrum using the deep NB imaging of the UM287 field presented in Cantalupo et al. (2014). In order to do so, we applied the LRIS slit to the NB image, choosing only the pixels that contributed to the flux in our spectrum. Next, we trimmed off the outer edges of the slit, selecting the region of the spectrum that has flux from the Nebula and very good background subtraction. We then summed up the NB flux within this shortened slit, which was four binned pixels wide by 135 binned pixels long and covered 1.08 arcsec by 36.45 arcsec on the sky.

This total NB flux is compared to that of the 2D spectrum over the same wavelength range and spatial location. The equivalent flux of the 2D spectrum is calculated by first applying the filter transmission function to the spectral direction of the spectrum. We then integrate the flux, in $e^{-}s^{-1}$, over the shortened slit region and divide the total NB flux by the summed 2D spectrum flux to compute the conversion factor from $e^{-}s^{-1}$ to erg cm^{-2} s^{-1}. This conversion factor is then applied to each pixel of the LRIS spectrum to produce a fully flux-calibrated 2D spectrum.

In order to use an integer number of pixels, the width of the NB shortened slit corresponds to 1.08 arcsec which is slightly bigger than the LRIS slit width of 1 arcsec. Therefore, we expect the flux-calibration of the LRIS spectrum to be biased slightly high, by approximately 8 percent. To estimate the systematic error on our flux calibration, we calculated the flux of the compact source, marked as 'C' in Fig. 4.1 and Fig. 4.2. We find that the compact source flux in the NB and spectrum differ by 20

percent, which we will take to be our systematic uncertainty.

4.2.3 MOSFIRE spectroscopy

We observed the Slug Nebula on 2014 October 02 (Night 1 or N1) and 2014 October 03 (Night 2 or N2), using the MOSFIRE (McLean et al. 2010, 2012) instrument on the Keck I 10 m telescope. The spectra were taken using the K-band grating so as to cover the expected H α emission (λ6562.8) of the Nebula ($z \sim 2.283$), with a total wavelength coverage of $19540 - 24060$Å. We used a 1 arcsec slit width for both nights of observation, resulting in a spectral resolution of $R \sim 2500$ at λ =21545.67Å.

The two masks we designed had three slitlets; the middle slitlet was centered on a region of the UM287 Nebula predicted to have the highest H α emission, while the top and bottom slitlets were aligned on two stars from the Two Micron All Sky Survey (2MASS). All coordinates are shown in Table 4.1). These 2MASS stars were included to help locate the exact position of the UM 287 Nebula in case of a non-detection as well as to help track the drift of the mask across the detector (see Kriek et al. 2015).

Table 4.1: Coordinates for the MOSFIRE Mask Targets.
We also include here the coordinates of QSO A for completeness.

Target name	RA (J2000)	Dec (J2000)	Slitlet #
2MASS Star 1	$00^h51^m54^s.26$	$+01°03'21''.2$	1
QSO A	$00^h52^m02^s.40$	$+01°01'29''.3$	N/A
UM287 Nebula	$00^h52^m02^s.99$	$+01°01'23''.1$	2
QSO B (Night 1 only)	$00^h52^m03^s.26$	$+01°01'08''.6$	2
2MASS Star 2	$00^h52^m07^s.78$	$+00°59'06''.9$	3

For the first night, we used a slit at a PA of 342 We observed using an AB'BA'

dither pattern with offsets of $+51, -17, +17, -51$ arcsec respectively, and exposure times of 119.3 s for a total integration of 4.8 h. The median seeing during Night 1 was about 0.7 arcsec for both nights but there were intermittent cirrus clouds such that the conditions were not photometric. So as to cover a larger area of the Nebula, we used a different PA for Night 2 of 322 centered on the same patch of Nebula as for Night 1 (see Fig. 4.1). We observed using the same AB'BA' dither pattern and exposure times as for Night 1, for a total integration of 2.6 h. Both slit orientations are shown in Fig. 4.1.

4.2.4 MOSFIRE calibrations and data reduction

At the beginning of each night, we took neon and argon arcs through the masks as well as dome flats and thermal flats. Immediately prior to observing UM287, we took spectroscopic standards of HIP5164 with a 1 arcsec longslit on Night 1 and a 0.7 arcsec longsit on Night 2. These were used to flux calibrate our data as well as correct for telluric absorption. Since we only observed HIP5164 once in the evening, we cannot account for any changes to the telluric absorption throughout the night.

The UM287 data, as well as the standard HIP5164, were reduced using the publicly available MOSFIRE Data Reduction Pipeline (version 2016 August; DRP; Steidel et al. 2014). The DRP first flat fields the images and traces the slit edges. To correct for the dome's emission of K-band wavelength photons, the software subtracts the thermal flats from the dome flats before creating a normalized combined flat. Next, the code combines exposures and preforms the wavelength calibration, combining an interactive fitting of the night skylines with neon and argon arcs to correct for the faintness of the skylines at the reddest wavelengths. The sky background is then subtracted

and the images are rectified, producing a 2D spectrum for each slitlet along with their corresponding noise frames and integration time maps.

To prevent smearing out the emission due to the mask drift across the detector over the course of our observations (see for instance, Kriek et al. 2015), we reduced our Night 1 data in six batches of 24 exposures ($\sim$ 48 min) each (other than the last batch which only had 23 exposures). We then measured the mask drift between batches by tracking the centroids of the two 2MASS stars (see Table 4.1) also present in the MOSFIRE mask. We found shifts of $\pm 1-2$ pixels ($0.18-0.36$ arcsec) between batches which we corrected for before coadding the data. Due to the shortness of the Night 2 observations and the shifts of only about 1 pixel found in the Night 1 data over the course of $\approx$ 1h, we did not bother correcting for mask drift in the Night 2 data.

In order to flux calibrate our UM287 Nebula 2D spectrum, we used the spectrum of the A0 standard star HIP5164. The 1D spectrum of HIP5164 was derived from the 2D spectrum returned by the DRP, using a boxcar extraction that assumes a Gaussian spatial profile. We then calculated the sensitivity function by comparing this 1D spectrum to a template spectrum of Vega from Bohlin (2014) that has the NIR emission from the debris disk removed. That spectrum was then renormalized to have the same 2MASS magnitude as HIP5164. This sensitivity function, as well as a simple slit loss correction to account for the finite slit width, was applied to achieve the final flux calibrated UM287 Nebula 2D spectrum, shown in Fig. 4.3.

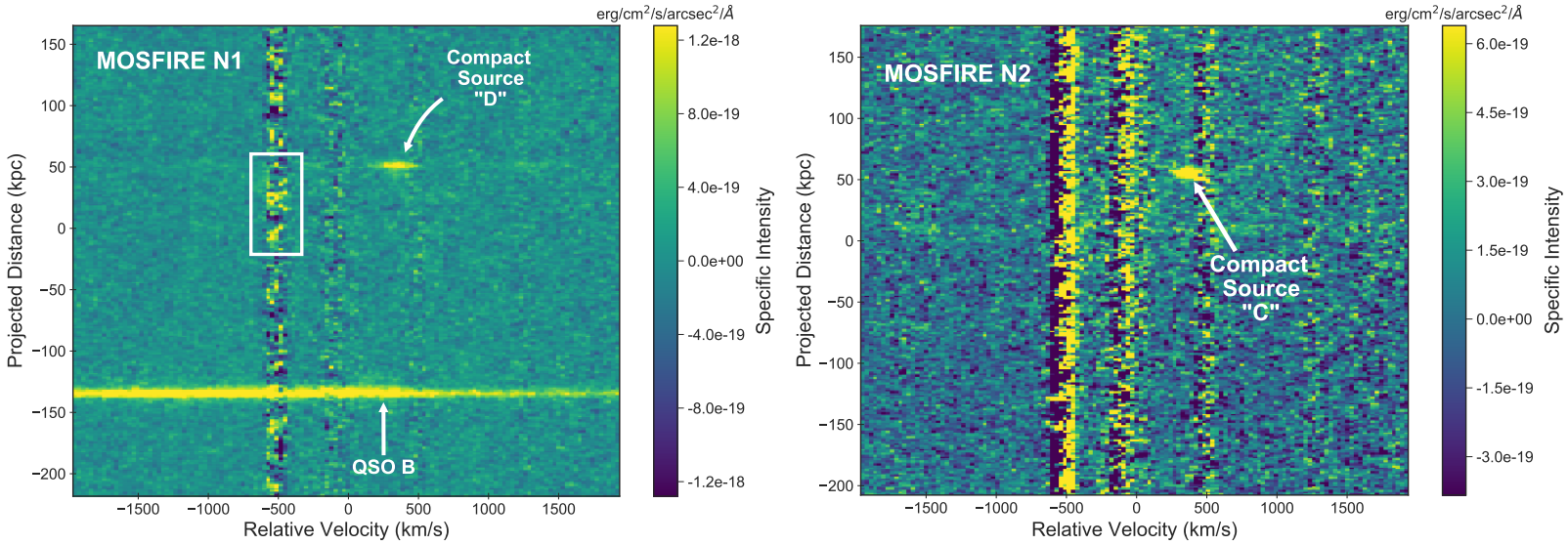

(a) (b)

Figure 4.3: The left-hand panel shows the unsmoothed 2D spectrum taken with Keck I/MOSFIRE (4.8 h) using the N1 slit orientation (the red slit in Fig. 4.1). The $v = 0$ km s^{-1} corresponds to the expected H α emission at a redshift of $z = 2.283$, the redshift of QSOA. The spatial offset of 0 kpc indicates the location of the MOSFIRE N1 and LRIS slit intersection, referred to as position 'X' in Fig. 4.1. The white rectangle indicates the region in which the H α flux of the Slug was measured (see Section 4.3.3.1 for a description of how the dimensions and location of the rectangle were chosen). Note that the flux measurement aperture overlaps with the continuum emission from compact source 'D'. This contaminant is masked out when we perform any analyses or measure fluxes. The bright continuum source around $\sim$ 150 kpc is QSO B. The H α and N II[6583] emission lines of compact source 'D' ($z = 2.287$) are visible at a spatial position of $\sim$ 50 kpc and spectral positions of $\sim$ 400 km s^{-1} and $\sim$ 1200 km s^{-1} respectively. The right-hand panel shows the unsmoothed 2D spectrum taken with Keck I/MOSFIRE (2.6 h) using the N2 slit orientation (the green slit in Fig. 4.1). The spectral and spatial axes match those of the N1 spectrum and their zero-points are defined in the same way as in the top panel. The emission line at $\sim$ 400 kms^{-1} and $\sim$ 50kpc is the H α line of compact source 'C' ($z = 2.287$).

4.3 Analysis and Results

The final 2D LRIS and MOSFIRE spectra are shown in Fig. 4.2 and Fig. 4.3. In this section, we first examine the kinematics of the Slug Nebula. In Section 4.3.1, we calculate the first and second moments of the LRIS Ly α spectrum to determine the kinematic structure and gas distribution of the Nebula. Next, we measure the Ly α (Section 4.3.2) and H α (Section 4.3.3) flux emitted by the brightest part of the Slug, using the LRIS NB image and MOSFIRE spectrum, respectively. In Section 4.3.4.1 we derive the Ly α to H α ratio, which will help us constrain the mechanism powering the Slug Nebula's Ly α emission. Finally, we compute the H α and corresponding N II[6583] line fluxes of compact sources 'C' and 'D' in Section 4.3.5.

4.3.1 The Ly α kinematics

The velocity centroid and velocity dispersion as a function of spatial position for the Ly α emission around the Slug Nebula is shown in the top left and top right-hand panels of Fig. 4.4, respectively. To calculate these kinematic tracers, we first selected an appropriate region around the Slug Nebula. We started by running CUBEXTRACTOR (Cantalupo, in preparation; see also Borisova et al. 2016 and Marino et al. 2018 for a short description) on the LRIS 2D spectrum with spatial and wavelength Gaussian smoothing of $\sigma = 2$ pixels and a signal-to-noise threshold of 3 per smoothed pixel. The resulting region is shown in the bottom-left panel of Fig. 4.4.

Next, we partitioned the spatial extent of Ly α emission into bins of five pixels (5.68 kpc). Note that these are not independent regions since the seeing in the spatial

direction was $\sim$ 10 pixels but this box size allows us to finely sample the kinematics of the transition region between the Slug Nebula and compact source 'C'. We then calculated the flux-weighted first and second moments of the Ly α velocity distribution for each spatial bin according to equations 4.1 and 4.2.

$$V_{\rm cent} = \frac{\sum vF(v)}{\sum F(v)}, \tag{4.1}$$

$$V_{\rm disp} = \sqrt{\frac{\sum (v - V_{\rm cent})^2 F(v)}{\sum F(v)}}. \tag{4.2}$$

The flux-weighted mean velocity, which we also refer to as the centroid velocity, is presented in the left-hand panel of Fig. 4.4 as a function of spatial distance from point 'X' (the intersection point of the Night 1 and Night 2 slits denoted in Fig. 4.1). The standard error on the velocity centroid, for each spatial bin, was determined using statistical bootstrapping and is shown as the black error bars. Since each spatial bin is about half the size of the atmospheric seeing, each of these bins are correlated. Therefore, the bootstrapped errors are likely an underestimate of the true errors.

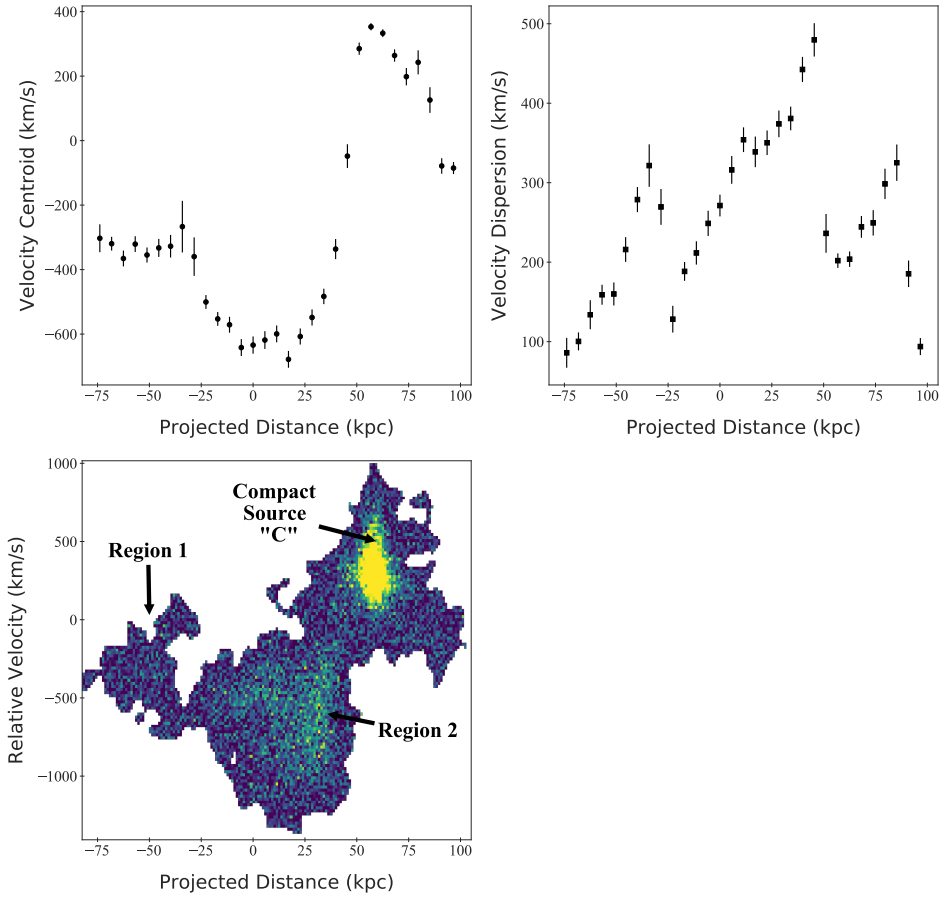

Figure 4.4: The Ly α kinematics of the region around the Slug Nebula. The flux-weighted first moment of the velocity distribution, also referred to as the velocity centroid, is plotted as a function of position along the slit in the top-left panel. The velocity centroid was calculated according to Equation 4.1, within spatial bins of five pixels. Similarly, the flux-weighted second moment of the velocity distribution about the-flux weighted mean, which we refer to as the velocity dispersion, was calculated according to Equation 4.2. The velocity dispersion in spatial bins of five pixels is shown as a function of projected distance along the slit in the top-right panel of this figure. In both top panels, the 1σ error bars were computed using standard bootstrapping techniques. The area of Ly α emission used to measure the velocity centroid and dispersion only includes pixels with a SNR ≥ 3, and is depicted in the bottom-left panel (the color bar matches that of Fig. 4.2). The $v = 0$ km s^{-1} corresponds to the expected Ly α emission at the redshift of QSO A ($z = 2.283$). The projected distance of 0 kpc indicates the location of the MOSFIRE N1 and LRIS slit intersection. Three distinct spatial regions, with different kinematic properties, are apparent in both the velocity centroid and velocity dispersion plots: the dimmer left-most region of the Nebula ('region 1'), the brighter region of the Nebula to the right ('region 2') and the compact source 'C' area in the right-most part of the figure.

As seen in the top-left panel of Fig. 4.4, the kinematics indicate that the Slug Nebula, the part of the spectrum between 35 kpc and -75 kpc, is comprised of two regions with distinct kinematics. 'Region 1', located at ~ -50 kpc, has a velocity centroid of -333 ± 12 km s^{-1}, while 'region 2', is at ~ 25 kpc and is centered at -555 ± 8 km s^{-1}. There is then a sharp transition around ~ 40 kpc marking the beginning of compact source 'C', which is centered at a velocity of 254 ± 8 km s^{-1}.

The top right-hand panel of Fig. 4.4 shows the flux-weighted velocity dispersion of the Ly α emission as a function of the projected distance from point 'X'. The corresponding error bars for the velocity dispersion were also computed using statistical bootstrapping. As with the velocity centroid, the velocity dispersion of the Slug Nebula displays the same demarcations between the two regions that comprise the Slug and compact source 'C'. Their representative velocity dispersions are 217 ± 7, 418 ± 6, and 453 ± 9 km s^{-1}, respectively.

4.3.2 The Ly α flux of the Slug Nebula

We used the NB image (see the top panel of Fig. 4.1) to calculate the Ly α flux of the Slug Nebula in the region defined within the MOSFIRE Night 1 slit, corresponding to where we measure the H α emission in Section 4.3.4.1. So that comparisons to the MOSFIRE data would be as accurate as possible, we chose the same spatial width and centroid as was used to compute the H α flux (see Section 4.3.4.1). Though we could not precisely select the same velocity range, comparing the NB and continuum images shows that there are no continuum sources that could be contaminating the Ly α measurement in our region of interest. In addition, the NB filter covers a much larger spectral window

than the velocity dispersion of the Nebula (see Fig. 4.4), ensuring that all of the Ly α velocities included in the spectrum are also included in the NB flux measurement.

Integrating over the region defined by the over-plotted MOSFIRE N1 slit within the aforementioned spatial window spanning ∼81.76 kpc, results in a total Ly α flux of $F_{\mathrm{Ly}\alpha} = 1.44 \pm 0.10 \times 10^{-16}$ erg cm^{-2} s^{-1} (equivalent to a surface brightness of $\mathrm{SB}_{\mathrm{Ly}\alpha} = 1.48 \pm 0.10 \times 10^{-17}$ erg cm^{-2} s^{-1} arcsec^{-2}).

4.3.3 The H α emission of the Slug Nebula

4.3.3.1 Determining the optimal aperture for H α detection and flux measurement

The large spatial scale (and possibly, the large velocity width) of the H α emission expected from the Slug Nebula necessarily requires spatial and spectral binning of our original data presented in Fig. 4.3. Moreover, we do not know a priori where the spatial and velocity center of such an aperture should be located.

In this section, we discuss how we obtained the optimal rectangular aperture for the detection of the Slug's H α emission. Because of the lower exposure time and higher systematic noise of the MOSFIRE Night 2 observations (see Fig. 4.3), we will limit our search for, and analysis of, extended emission to the MOSFIRE Night 1 observations here and in the remainder of the paper. However, we will make use of the MOSFIRE N2 observations for the spectral analysis of compact source 'C'.

As discussed in this section, we find that the optimal aperture has a spatial dimension of ∼81.76 kpc and is centered a distance of ∼19.68 kpc from the intersection

of the MOSFIRE N1 and N2 slits. The optimal spectral dimension has a width of 363 km s^{-1} centered at a velocity of -511 km s^{-1} with respect to the systemic velocity of H α at a redshift of $z = 2.283$ (the systemic redshift of the UM287 quasar obtained from CO observation; Decarli et al, in preparation).

Figure 4.5 *(next page)*: Though the spatial aperture size and centroid can be determined empirically from the NB Ly α image (see Fig. 4.1), radiative transfer effects can modify the kinematics of the Ly α such that it cannot be used to inform the expected wavelength of the H α emission. To determine the most likely velocity centroid, we calculated the flux as a function of velocity position within a narrow velocity window (six pixels/ 181 km s^{-1}), as shown in green in the top panel of this figure. The velocity that maximized the flux, -511 km s^{-1}, was chosen as the centroid position. Note that doubling the velocity window does not change the location of the peak (shown in blue). We used a flux curve-of-growth approach to determine the optimal spectral window size. The flux within the MOSFIRE aperture (centered at the velocity centroid of -511 km s^{-1}) is shown in the bottom panel as a function of velocity-aperture width. At a spectral width of 363 km s^{-1}, the H α flux starts to level off. We therefore choose this as the size of the velocity width of our aperture when calculating the Slug's H α flux. The flux within these aperture dimensions result in a SNR of $\sim 5.6\sigma$.

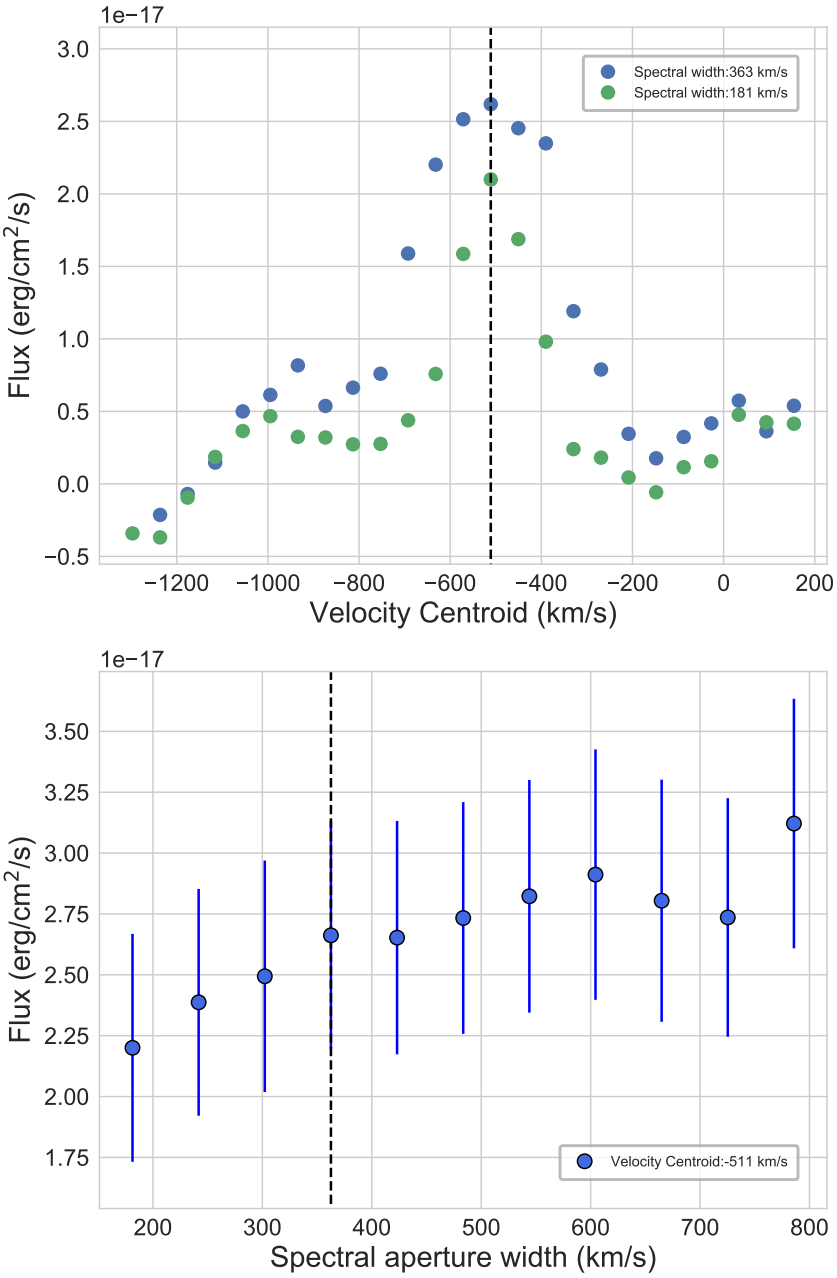

Figure 4.5: The top panel shows the flux as a function of velocity position within a narrow velocity window (six pixels/ 181 km s^{-1}). The bottom panel shows the flux within the MOSFIRE aperture (centered at the velocity centroid of −511 km s^{-1}) as a function of velocity-aperture width. See the previous page for the full caption text.

The spatial scale and center were chosen based on the intersection of the MOSFIRE N1 slit with the Ly α NB emission. The NB Ly α surface brightness was first rescaled to an expected H α surface brightness assuming a case B recombination ratio of $SB_{Ly\alpha}/SB_{H\alpha} = 8.1$. We then calculated a 3σ contour, assuming an estimated MOSFIRE H α surface brightness error of $1\sigma = 3.7 \times 10^{-19}$ erg cm^{-2} s^{-1}. The region within the intersections of the Night 1 slit and the 3σ contour was 9.71 arcsec long and centered a distance of 2.34 arcsec from the intersection of the N1 and N2 slits (point 'X'). Assuming a redshift of $z = 2.283$, this translates to a spatial aperture in which to calculate the H α flux of $\sim$81.76 kpc centered at a distance of $\sim$19.68 kpc from point 'X'.

We then determined the optimal spectral aperture width and central velocity. In the absence of radiative transfer effects influencing the velocity distribution of the Ly α emission, we would expect the H α emission to be centered close to the velocity centroid of the Ly α, found to be at -555 km s^{-1} in Section 4.3.1. However, possible asymmetries in the Ly α due to scattering effects could bias our determination of the precise H α central velocity.

In order to allow for this possibility, we chose a 'priorless' approach to determining the velocity centroid and width of the H α emission. Rather than select the velocity centroid based on its expected location, we took a curve-of-growth approach, finding the central velocity in a wide velocity window (shown in the top panel of Fig. 4.5), that maximized the H α flux. We first masked out the compact source continuum emission located at $\sim$50 kpc from the slit intersection 'X', then the H α flux was

measured assuming a narrow velocity window of 181 km s^{-1} (six pixels) so as to finely sample the velocity range. The H α flux peaks at a velocity centroid of -511 km s^{-1}, a result that is corroborated if we double the velocity width to 363 km s^{-1}, as shown in the top panel of Fig. 4.5. The curve-of-growth determined velocity centroid of -511 km s^{-1} is extremely close to the velocity centroid of the Ly α region 2 emission, which was measured to be -555 km s^{-1}.

Finally, we determined the spectral aperture width, which cannot simply be obtained from the breadth of the Ly α emission, since radiative effects can broaden the width of this resonant line. Instead, we varied the spectral aperture width from 181 to 784 km s^{-1} and selected the width at which the measured H α flux leveled off. As shown in the bottom panel of Fig. 4.5, the optimal velocity aperture has a width of 363 km s^{-1}.

Since this curve-of-growth approach to finding the velocity centroid and width of the flux aperture seeks to maximize the H α flux, one could be concerned that this approach would consistently bias our H α flux towards higher values. In order to quantify this effect, we used the same methodology described above to find the peak H α flux in several pure sky background regions. When we varied the velocity centroid and width of the flux apertures, we consistently found that the maximum H α peaks exceeded the mean flux value in that sky background region by up to about 5×10^{-18} erg cm^{-2} s^{-1}. Therefore, we conclude that this 'priorless' aperture selection would inflate the H α flux by $\leq 5 \times 10^{-18}$ erg cm^{-2} s^{-1}. We emphasize that our estimate is an upper limit, as it is unlikely that a statistical fluctuation would land near or on top of the detected H α

flux.

4.3.3.2 An empirical estimate of the sky noise

We determined an empirical noise estimate by calculating the standard deviation of the flux in 'pure-sky' regions. These regions were chosen so as to avoid the expected spatial location of Slug H α emission as well as the outer edges of the slit, which have a reduced total exposure time. We measured the flux in these background regions using the same-sized rectangular aperture and velocity centroid as when measuring the Slug Nebula flux (see Section 4.3.4.1). We found that these fluxes were dominated by a linearly varying, spatially dependent background gradient, which we modeled and removed prior to calculating the flux scatter for the pure-sky regions. We note that the removal of this background model does not affect our measurement of the Slug's H α flux since the estimated background was very close to zero at that spatial position.

The pure-sky fluxes, with the background gradient removed, are plotted in Fig. 4.6 as unfilled blue squares. The $\pm 1\sigma$ standard deviation of the sky fluxes (our empirical noise estimate) is shown as the transparent blue shaded region. The light blue unfilled circles show the flux at spatial locations close to the expected H α emission and were not included in the calculation of our noise estimate. The background gradient was not removed at the location of the light blue unfilled circles. The flux at the location of the Slug is represented by the larger filled blue square.

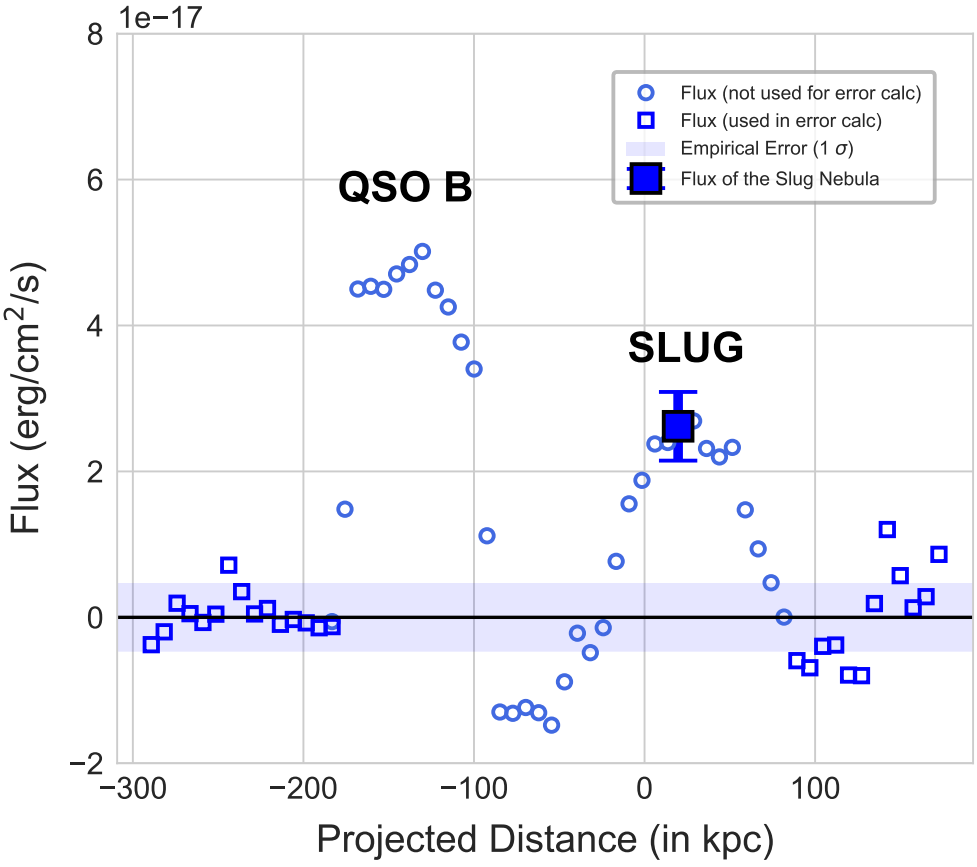

Figure 4.6: The H α flux computed within rectangular apertures of size 81.76 kpc by 363 km s^{-1}, measured as a function of spatial position along the MOSFIRE N1 slit. For all these flux calculations, the apertures were centered at a velocity of -511 km s^{-1}. The bigger filled blue square point marks the flux at the expected location of the Slug Nebula (see Fig. 4.3). The light blue points with much higher flux values (~ -75 to ~ 75 kpc) are associated with the QSOB emission. The small darker blue unfilled squares correspond to regions far enough away from the expected location of the Slug Nebula to be considered 'pure-sky'. The error on the measurement of the Slug Nebula flux was calculated using the standard deviation of the flux in these pure-sky apertures. We note here that the pure-sky regions have a background gradient removed but the rest of data do not, see Section 4.3.3.2 for details. The $\pm 1\sigma$ error is shown as the transparent blue region as well as the blue error bars associated with the Slug Nebula flux (large blue square). The flux at the location of the Slug Nebula corresponds to a $\sim 5.6\sigma$ detection.

4.3.4 Examining the robustness of the Slug Nebula H α detection

It is important to note that our chosen velocity centroid is coincident with the skyline at 20517Å. The presence of a bright, imperfectly subtracted skyline at the location of our H α detection might cause concern that the observed H α flux within our chosen aperture is due to variance in the skyline rather than emission from the Slug Nebula.

Fig. 4.3 shows no clear emission at the location of the chosen aperture. However, once the spectrum is smoothed using a median filter with a 41 kpc $\times$ 363 km s^{-1} kernel, the H α emission becomes apparent, as seen within the white rectangle in the top panel of Fig. 4.7. In addition, this sort of line-like emission appears nowhere else along the skyline or generally in the vicinity of the expected H α emission.

The idea that the emission within our aperture is uncharacteristic of the variance of the skyline is corroborated by the fact that the signal to noise also peaks at the same velocity centroid as the flux. The error used in the SNR was empirically calculated by taking the standard deviation of the flux in apertures along the skyline (see Section 4.3.3.2). Therefore, if the emission in our aperture was typical of the skyline, this would be reflected in the noise estimate. While the flux could be biased by the presence of a skyline, the signal-to-noise ratio should be much less susceptible to this effect. The velocity centroid corresponding to the peak SNR was unchanged whether we used our empirical noise estimate or a noise estimate calculated from the error array produced by the MOSFIRE DRP.

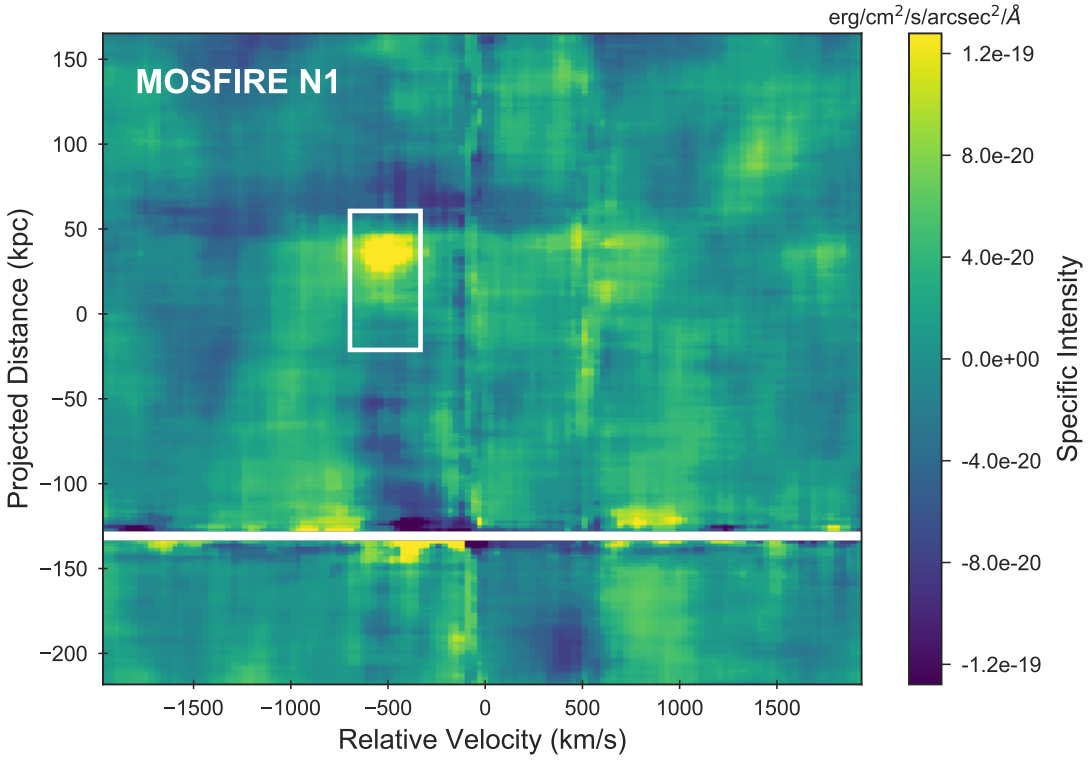

Figure 4.7: The smoothed MOSFIRE N1 2D spectrum produced using a median filter with a smoothing kernel of 41 kpc (27 pixels) in the spatial direction and 363 km s^{-1} (12 pixels) in the spectral direction. These dimensions correspond to half the size of the white rectangular aperture that was used to measure the H α flux. Prior to smoothing, the continuum and line emission from compact source 'D' as well as QSO B were masked out. Since the median-smoothing filter does not conserve flux, this figure is meant to be purely illustrative and was not used for any of the measurements in the analysis. Though the H α detection lies on top of a relatively bright skyline, we argue in Section 4.4.2.1 that the emission is produced by the Slug Nebula rather than high-variance pixels in the skyline residual.

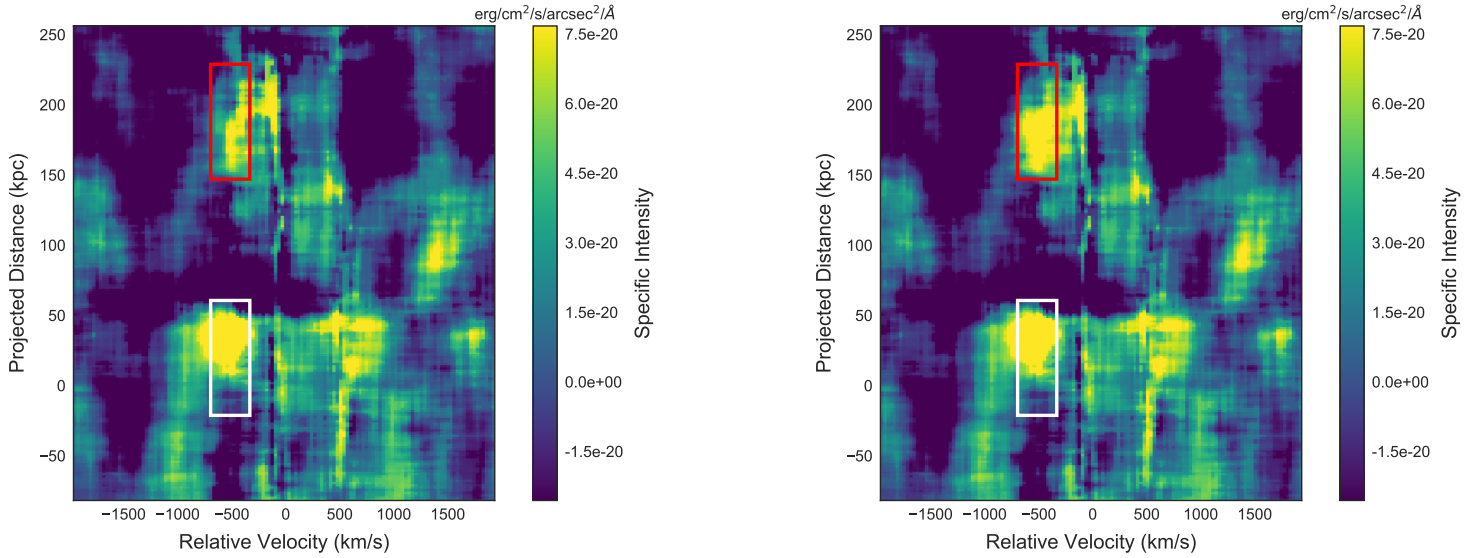

Figure 4.8: This figure presents a visual verification that our observed H α flux (in the white rectangle) resembles a reasonable model of the H α emission of the Slug. The injected fake sources represent two extremes of the possible H α velocity distributions: (a) the H α emission is assumed to have a broad velocity distribution that matches that of region 2 in the LRIS Ly α spectrum (left-hand panel) and (b) the H α line is assumed to have been emitted at a much more narrow range of velocities and the Ly α was broadened by radiative transfer effects (right-hand panel). The left-hand panel shows the median-smoothed image of the MOSFIRE N1 spectrum (using a kernel of 41 kpc $\times$ 363 km s^{-1}) with an injected fake source that was modeled by taking the Ly α flux from 'region 2' in the LRIS spectrum and rescaling it to match the H α flux. Thus, this H α emission model keeps the velocity distribution of the Ly α emission intact and is centered at a spatial position of 188 kpc and at a velocity of -718 km s^{-1}. We find that the brightest region of the injected source (expected location shown as the red rectangle) appears less significant than the observed emission (in the white rectangle). Similarly, in the right-hand panel we show the MOSFIRE N1 spectrum median-smoothed with the same kernel of 41 kpc $\times$ 363 km s^{-1} that was applied in Fig. 4.7. The injected fake source, centered at 188 kpc and a velocity centroid that matches the observed H α emission, was modeled as a 2D Gaussian. The fake emission had a standard deviation in the spatial direction of 18 kpc and of 181 km s^{-1} in the spectral direction and a total flux of 2.62×10^{-17} erg s^{-1} cm $^{-2}$ that matches the observed H α flux. This emission model (visible within the red rectangle) better resembles the observed H α emission (at the location of the white rectangle), suggesting that the H α emission of the Slug has different kinematics than the Ly α and is emitted at a narrower range of velocities.

As an additional test of the validity of the H α emission, we inserted two types of fake sources into the MOSFIRE N1 spectrum in order to verify that the observed emission line is consistent with what would be predicted from the Ly α. The first fake source was created by taking the integrated Ly α flux within region 2 of the LRIS slit and rescaling it to the total H α flux (2.62×10^{-17} erg cm^{-2} s^{-1}). It was then inserted into the MOSFIRE N1 spectrum with a velocity window and spatial extent matching that of region 2 (centered at -718 km s^{-1}) but centered at a spatial position away from the expected Slug emission. The results are shown in the left-hand panel of Fig. 4.8, with the red rectangle denoting the fake source and the white rectangle the actual observed emission at the location of the Slug.

Since the Ly α could be broadened by radiative transfer effects that would not affect the H α emission, the H α could be emitted with a much more concentrated velocity distribution. The second fake source, inserted into the MOSFIRE N1 spectrum at the observed H α velocity centroid (-511 km s^{-1}), was chosen to be a 2D Gaussian with $\sigma_{\rm vel} = 181$ km s^{-1} and $\sigma_{\rm spat} = 18$ kpc and a total flux equivalent to that of the detected H α flux.

As seen in the right-hand panel of Fig. 4.8, the observed H α emission (white rectangle) looks similar to the compact 2D Gaussian fake source (red rectangle). Though this exercise was purely for illustrative purposes, the fact that the observed emission looks similar to a reasonable expectation of the H α emission supports the idea that the observed H α emission is not simply due to the underlying skyline. In addition, the apparent compact size of the H α as compared with the expected size seen in Ly α

could suggest that the Ly α emission is broaden by radiative transfer effects.

4.3.4.1 The H α flux and the Ly α to H α ratio

We measured the H α flux of the observed portion of the Slug Nebula within the MOSFIRE N1 slit using the rectangular aperture obtained as discussed above. This aperture has a spatial dimension of 81.76 kpc and spectral dimension of 363 km s^{-1} and it is spatially centered at a distance of 19.68 kpc from the intersection of the Night 1 and Night 2 slits (point 'X' in Fig. 4.1). The velocity centroid of the aperture is -511 km s^{-1}. The region in which the H α flux was measured is over-plotted as a white rectangle in the top panel of Fig. 4.3 and both panels of Fig. 4.7.

We find an H α flux within our aperture of $F_{\mathrm{H}\alpha} = 2.62 \pm 0.47 \times 10^{-17}$ erg cm^{-2} s^{-1} (equivalent to a surface brightness of $\mathrm{SB}_{\mathrm{H}\alpha} = 2.70 \pm 0.48 \times 10^{-18}$ erg cm^{-2} s^{-1} arcsec^{-2}), where the error is calculated from the standard deviation of the fluxes in 'pure-sky' regions as described in Section 4.3.3.1. Considering the Ly α flux in the same spatial region obtained from the NB image (found to be $F_{\mathrm{Ly}\alpha} = 1.44 \pm 0.10 \times 10^{-16}$ erg cm^{-2} s^{-1} in Section 4.3.2), the Ly α to H α flux ratio in this region of the Slug is 5.5 ± 1.1. If, as discussed in Section 4.3.3.1, we take into account that the H α flux might be biased high by up to 5×10^{-18} erg cm^{-2} s^{-1}, the Ly α to H α flux ratio would instead be around 6.9. We will discuss the possible implications of this flux ratio with respect to the physical emission mechanism and Ly α escape fraction in Section 4.4.2.2.

4.3.5 The compact sources in the MOSFIRE data

Two line emitters were also observed in our MOSFIRE spectra. These sources were originally detected in the LRIS NB and V-band data and were dubbed compact source 'D' and compact source 'C', corresponding to the MOSFIRE N1 and MOSFIRE N2 slits, respectively. The sources are shown and labeled in Fig. 4.1 and their spectra are plotted in Fig. 4.9. Note that emitter 'C' is the same as source 'C' in Martin et al. (2015) and the compact source in our LRIS spectrum (see Fig. 4.2).

The bright H α emission line of sources 'C' and 'D' in our MOSFIRE spectra allow us to determine the redshifts of each compact source. We find that both sources are at the same redshift of $z \approx 2.287$, which is slightly redshifted with respect to that of QSO A. This corresponds to a velocity offset between the compact sources and QSO A of $\sim$355 km s^{-1} that could be explained by peculiar motions within the halo of QSO A.

In addition to computing the redshifts, we also produced a K-band 1D spectrum for each source using a simple boxcar extraction. These spectra were used to calculate the H α and corresponding N II[6583] line fluxes. For compact source 'D', we find an H α flux of $F_{\mathrm{H}\alpha} = 6.6 \pm 0.3 \times 10^{-17}$erg cm^{-2} s^{-1} and an N II flux of $F_{\mathrm{NII}} = 2.2 \pm 0.2 \times 10^{-17}$ erg cm^{-2} s^{-1}. For compact source 'C', we find an H α flux of $F_{\mathrm{H}\alpha} = 4.3 \pm 0.4 \times 10^{-17}$ erg cm^{-2} s^{-1} and a N II 3σ flux upper-limit of $F_{\mathrm{NII}} = 2.4 \times 10^{-18}$ erg cm^{-2} s^{-1}.

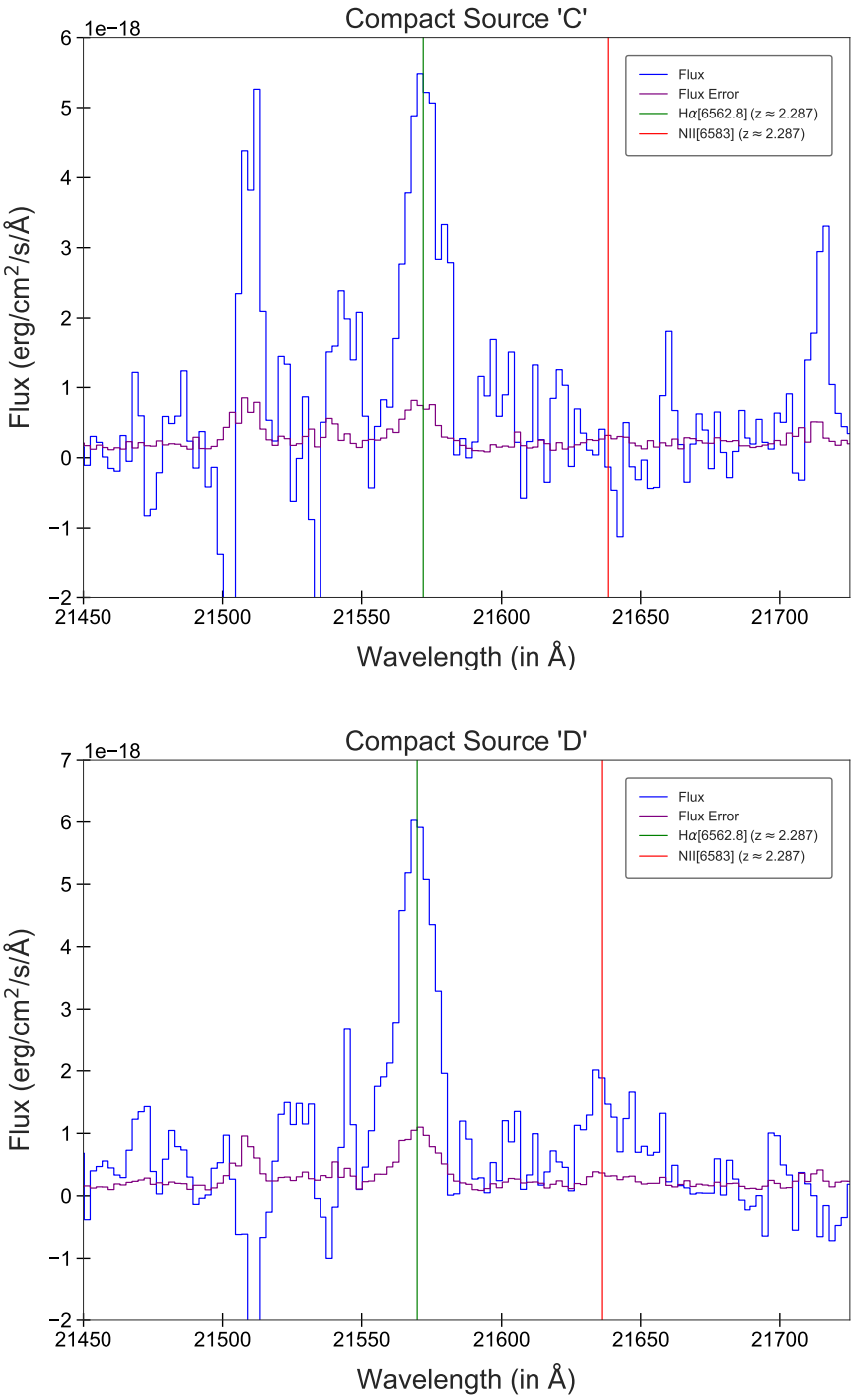

Figure 4.9: The 1D spectra of compact sources 'C' (top panel) and 'D' (bottom panel) derived from the 2D MOSFIRE N2 and N1 spectra, respectively, using a simple box extraction. The flux is shown in blue, the error array is plotted in purple, while the green and red vertical lines shows the expected wavelength of H α and N II[6583], respectively, given the redshift of $z = 2.287$ for each source.

4.4 Discussion

In this work, we presented deep spectroscopy of the Ly α and H α emission of the Slug Nebula. We use these data in the following sections to discuss the physical structure of the Slug Nebula's gas as well as the production mechanism of the Slug's Ly α emission and its implications. In Section 4.4.1, we use the kinematic indicators derived from the Keck I/LRIS spectroscopy (see Section 4.3.1) to address the question of how the Slug's gas is physically distributed.

In Section 4.4.2, the Slug's H α flux, measured in Section 4.3.4.1, is compared to its corresponding Ly α flux (Section 4.3.2) so as to determine the emission mechanism producing the Slug's observed Ly α. In particular, we distinguish between two scenarios for the production of the Ly α emission: (1) a purely *ex situ* production of Ly α in the broad-line region of QSO A that is then scattered and reemitted by neutral hydrogen in the Nebula and (2) a significant contribution of *in situ* fluorescent Ly α emission produced by case B recombination of the Slug's hydrogen gas.

Finally, we examine the origin of the H α emission of compact sources 'C' and 'D'. In Section 4.4.3, we use the ratio of their N II/H α flux to place these galaxies on a BPT diagram and determine whether these galaxies are star-forming or have a central AGN. In addition, we explore the possibility of a contribution of fluorescent emission due to QSO A.

4.4.1 The Ly α kinematics of the Slug Nebula

We can gain insight into the physical structure of the gas by examining the Ly α kinematics. In their work, Martin et al. (2015) claimed that the brightest region of the Slug Nebula is an extended rotating hydrogen disk contained within an $\approx 10^{13} M_{\odot}$ dark matter halo. However, the kinematics shown in Fig. 4.4 belie the idea that the Slug Nebula is a simple monolithic structure like a disk.

As discussed in Section 4.3.1, the velocity centroid as a function of spatial position (the upper-left panel of Fig. 4.4) reveals three clearly distinguishable regions with distinct velocity centroids. These same regions are clearly recognizable in the plot of velocity dispersion as a function of spatial position and are marked by very sharp transitions at ~ -35 and ~ 45 kpc.

The two left-most regions comprise the Slug Nebula. The dimmer 'region 1' is centered at ~ -50 kpc with a characteristic velocity centroid of -333 km s^{-1} while the brighter 'region 2' is located at $\sim$ 25 kpc with a velocity centroid of -555 km s^{-1}. The Ly α emission of the Slug is separated from that of compact source 'C' by a very narrow transition region ($\sim$10 kpc). We also see that the velocity dispersion has sharp transitions at the same locations as where we see sharp changes in the mean velocity, lending further credence to our interpretation that these are kinematically distinct regions.

Although it is difficult to disentangle velocity effects from distances along the line of sight, these sharp transitions suggest that the Slug Nebula could be composed of several structures. This is not unexpected from our theoretical understanding of cosmic

structure formation: the most massive filaments of the cosmic web are composed of both diffuse material and more massive halos containing denser gas. If the Ly α emission is produced by recombination radiation and therefore scales with the gas density squared, our observations would be most sensitive to detecting the densest clumps and structures within the filaments.

This interpretation of the Slug's physical structure is inconsistent with the giant disk argued for by Martin et al. (2015), despite the fact that Martin et al.'s pseudo-slit largely overlaps with our LRIS slit. We believe that the lower spatial and spectral resolution of the pseudo-slit observations may have smoothed out the sharp transitions that we resolve, making the distribution of velocity centroids resemble that of a giant disk.

Instead, our observation reveals a very abrupt cutoff, seen in Fig. 4.2, of the Ly α flux at a spatial position of $\sim$ 50kpc. It is currently unclear whether this sharp edge to the Ly α emission is due to an absence of cold gas or whether the Ly α emission is instead being absorbed along the line of sight. Intriguingly, the cutoff location is very close to compact source 'C'. However, compact source 'C' is located several hundred km s^{-1} on the red side of this feature and therefore we do not think that the compact source and its environment are the origin of a possible absorption feature. It is also interesting to note that the Ly α emission cutoff is adjacent to the brightest region of the nebular emission. Deeper integral field observations with Keck II/KCWI and MUSE of both Ly α and other emission lines (Cantalupo et al. in preparation) could be useful to disentangle whether this may be due to a lack of quasar illumination in a

particular direction (i.e., a 'shadow' of some absorber that is associated with the quasar) or suggestive of a possible alternative physical origin for this emission (e.g. shocks).

4.4.2 Constraining the emission mechanism of the Slug Nebula

Cantalupo et al. (2014) presents two possible mechanisms that could power the Ly α emission of the Slug Nebula. In the first case, Lyman continuum photons produced by the nearby QSO A ionize the gas of the Nebula, producing Ly α photons as the hydrogen atoms recombine. In the so-called 'case A', the gas is optically thin to ionizing radiation, while the opposite optically-thick situation is referred to as 'case B'. In the absence of dust, for reasonable nebular temperatures of $5 \times 10^3 - 2 \times 10^4$ K and electron densities $n_e < 10^4$ cm^{-3} the expected integrated Lyα/Hα ratio for case B recombination should range between 8.1 and 11.6 (Hummer & Storey 1987). In order to remain consistent with the broader literature, we use the conventional case B ratio of 8.7 set by Hu et al. (1998) (for further discussion, see Hayes 2015; Henry et al. 2015; Trainor et al. 2015).

Note that this ratio assumes spatially integrated measurements with apertures large enough to capture the full Ly α flux as the Ly α can scatter and spatially diffuse while H α cannot. If the spatial aperture does not encompass all the Ly α, the measured Ly α/H α may be considered to be a lower limit to the true value.

In the second case, the Ly α emission is produced as mostly neutral hydrogen gas absorbs Ly α and doppler-shifted Balmer continuum photons ('photon-pumping') from the broad-line region of QSO A and re-emits them as Ly α photons into our line of sight. In this scenario, we would expect little to no H α to be produced. Thus, we

would expect to only obtain an upper limit on H α, and therefore a lower limit on the Lyα/Hα ratio. If we were to observe a Lyα/Hα ratio of at least 12 or so, this scenario could then be distinguished from the recombination case.

4.4.2.1 Evidence for a detection of the Slug Nebula's H α emission

In order to differentiate between these two production mechanisms, it is important to ensure that our H α detection in the MOSFIRE N1 spectrum originated from the Slug Nebula. As mentioned in Section 4.3.4, despite of the presence of a bright, imperfectly subtracted skyline at the location of our H α detection there are several points that help support the idea that the measured H α flux is indeed emission from the Slug.

1. **There is significant H α emission**: The H α flux we measured corresponds to a 5.6σ detection if we use our empirical sky-noise estimator. If we instead use the error file from the MOSFIRE DRP to estimate the noise, the SNR doubles. In either case, the detection is significant despite being on top of a skyline. Though the H α flux we measure is not clearly visible in the unsmoothed 2D MOSFIRE spectrum shown in Fig. 4.3, once the spectrum is smoothed, as shown in Fig. 4.7, the emission line becomes evident.

2. **The H α emission is located where it is expected**: When determining the aperture in which to measure the H α flux, we determined the spatial centroid and width solely from the NB image. It is therefore notable that the only significant emission besides QSO A and compact source 'D' in the region is located

within these independently derived spatial constraints. In addition, it is striking that despite our priorless search for the velocity centroid of the H α emission, it coincides so well with the velocity centroid of the Ly α emission that we derived from the LRIS slit kinematics.

Note that while the LRIS slit does not match the orientation of the MOSFIRE N1 slit, they do have an overlap region at point 'X', where the velocity centroids of the Ly α and H α are very closely matched. In addition, the LRIS kinematics shown in Fig. 4.4 indicate a constant velocity centroid within each region. Since the MOSFIRE N1 slit goes squarely through region 2 of the Nebula, it is unlikely that the Ly α velocity centroid within a MOSFIRE N1-like slit would differ much from our observed LRIS kinematics.

3. **The H α emission looks like what we would expect from the Ly α**: In order to verify that our observed H α emission looked reasonably similar to what we would expect from the Slug Nebula, we visually compared it to two simple emission prediction models based on the LRIS Ly α emission and an assumption of case B recombination radiation.

   As described in Section 4.3.4 and shown in Fig. 4.8, we found that our observed H α detection is visually consistent with a compact 2D Gaussian emission model ($\sigma_{\rm vel}$ = 181 km s^{-1} and $\sigma_{\rm spat}$ = 18 kpc) with a total flux that is the same as our observed H α flux.

Thus, there is significant H α emission at a location consistent with that of the Ly α emission of the Slug Nebula and that it looks similar to what would be expected

assuming a relatively narrow H α velocity distribution produced by case B recombination radiation. These facts together indicate that our MOSFIRE H α flux is very likely a true detection of the Slug Nebula's H α emission. However, the only way to definitively confirm the H α detection at much higher significance level would require observations that are not affected by sky-lines, i.e. from space using the James Webb Space Telescope (JWST).

4.4.2.2 The fluorescent nature of the Slug Nebula's emission

The ratio of the Ly α flux, measured in Section 4.3.2, to the corresponding H α flux, calculated in Section 4.3.4.1, allows us to determine which mechanism is primarily responsible for powering the Slug Nebula's emission. We find a ratio of

$$\frac{\mathrm{F_{Ly\alpha}}}{\mathrm{F_{H\alpha}}} = 5.5 \pm 1.1. \tag{4.3}$$

Despite the large uncertainties and the limitations of our current observations, our measured value of $\mathrm{F_{Ly\alpha}/F_{H\alpha}}$ is clearly much lower than the ratio of $\mathrm{F_{Ly\alpha}/F_{H\alpha}} > 12$ expected if the Ly α emission of the Slug Nebula were primarily being produced via 'photon-pumping' or scattering of the quasar broad-line region. Rather, it is remarkably close to the 'standard' case B recombination ratio of 8.7. If, as discussed in Section 4.3.3.1 and Section 4.3.4.1, the H α flux is biased slightly high due to our aperture selection, the flux ratio could be as large as $\mathrm{F_{Ly\alpha}/F_{H\alpha}}$= 6.9±1.1, driving it even closer to the canonical 8.7 value. Observing Ly α to H α emission ratios that are so close to those expected for case B recombination implies that the gas in the Slug Nebula must be

mostly ionized, presumably by QSO A, optically thick to Ly α photons, and producing the fluorescent Ly α and corresponding H α emission *in situ* as the gas recombines. Of course, some small contribution due to 'photon-pumping' or scattering from the quasar broad-line region cannot be excluded.

In studies of Ly α emitting galaxies, it is customary to interpret this ratio in terms of the Ly α escape fraction ($f_{\rm esc}$). The Ly α escape fraction compares the ratio of observed $F_{\rm Ly\alpha}/F_{\rm H\alpha}$ (where $F_{H\alpha}$ is generally dust corrected) to the ideal case B recombination value of 8.7 (see i.e. equation 2 of Atek et al. 2009). If we convert our measurement of the $F_{\rm Ly\alpha}/F_{\rm H\alpha}$ ratio from equation (4.3) into a Ly α escape fraction, it would correspond to $f_{\rm esc} \sim 63$ percent. This value is in keeping with the escape fractions found for Ly α-selected galaxies at redshifts of $z \sim 2-3$, which range from a few percent to over 100 percent, but are typically $\sim$ 30 percent (e.g. Hayes et al. 2010; Steidel et al. 2011; Erb et al. 2014; Trainor et al. 2015; Matthee et al. 2016). The presence of dust is often used to explain escape fractions that are below 100 percent, since dust preferentially destroys Ly α as compared to H α. Hayes et al. (2010); Steidel et al. (2011), and to a lesser extent Matthee et al. (2016), all observe that $f_{\rm esc}$ is anti-correlated with dust attenuation.

However, it is important to remember that the Slug Nebula is not a Ly α galaxy. Rather, it is a very massive reservoir of cool gas that spans over 450 kpc, has no detected stellar continuum component, and as discussed in Section 4.4.1, has kinematics that are inconsistent with being a massive rotating disk. Therefore, as discussed in Cantalupo et al. (2014), the Slug Nebula is likely a filamentary structure in the IGM, and we do not

expect significant amounts of dust to be present on these intergalactic scales. Indeed, the non-detection of metal emission, from C IV[1549] (Arrigoni Battaia et al. 2015a) suggests that the metallicity of the Slug is not as high as in the ISM of high-redshift galaxies.

Another explanation for the $f_{\rm esc} < 100$ percent observed in Ly α emitting galaxies was proposed by Steidel et al. (2011). As they point out, it is not necessary to destroy Ly α photons to affect the Ly α flux measurement. Resonant scattering causes the Ly α photons to diffuse spatially outwards while leaving the non-resonant H α unaffected. Therefore, an aperture that encompasses all of the H α emission will likely be missing a significant amount of the Ly α, leading to measured escape fractions that are less than 100 percent.

This scattering of Ly α photons to larger spatial scales is probably the dominant effect contributing to why our measured Ly α flux is below what we would expect for case B recombination. We are measuring the Ly α flux corresponding to the MOSFIRE Night 1 slit by integrating the Ly α flux within a pseudo-slit region of the NB image. We are therefore likely missing a significant fraction of the Ly α photons produced in this bright region, particularly those that are scattered by more than the 1 arcsec slit width. This explanation is further supported by the fact that we see possible radiative transfer effects playing a role in producing a Ly α spectral width that is broadened compared to that of the H α. In this case, we would expect higher Ly α to H α ratios in the outer, fainter regions of the Slug Nebula that are currently not covered by our spectroscopic slit, which was centered on the brightest emission. Deep H α NB

or integral field spectroscopic observations would be needed to confirm this scenario.

As discussed in Borisova et al. (2016), another conceivable contribution to the lower than expected Ly α flux could be 'filter-loss' effects. These filter losses occur when a portion of the broad Ly α emission falls outside of the peak transmission of the NB filter. In our case, we can compare the measured transmission curve of the NB filter in the laboratory to the Ly α kinematics from our LRIS spectrum, assuming that these kinematics are similar to those that would have been observed using the MOSIFRE N2 slit. We find that the Ly α emission coincides well with the NB filter peak transmission and that any filter-losses would be too small to explain the lower than expected Ly α to H α ratio.

The recombination nature of the Slug Nebula's emission has important implications for the conditions of the gas on intergalactic and circumgalactic scales around quasars. As discussed in detail in Cantalupo et al. (2014) and Arrigoni Battaia et al. (2015a) (also see Cantalupo 2017 for a review), the large Ly α (and H α) SB of the Slug in the recombination case would imply very high gas densities ($n > 1$ cm^{-3}) that can only be explained by large clumping factors (C$\sim$1000), and therefore small volume filling factors, given the large intergalactic scales associated with the emission. In addition, there are indications that Ly α is being radiatively broadened due to radiative transfer effects, suggesting that the gas is highly ionized but not completely optically thin to the Ly α radiation produced by recombination. This would imply a neutral hydrogen column density significantly above 10^{14} cm^{-2} and will help future studies to further constrain the ionization parameter, total column densities, and volume densities

of the gas.

4.4.3 Elucidating the nature of compact sources 'C' and 'D'

In Section 4.3.5, we calculated the H α and N II[6583] fluxes for compact sources 'C' and 'D', which we can use to surmise the origin of the H α emission. Cantalupo et al. (in preparation) modeled the UV continuum emission of compact source 'C' using STARBURST 99 (Leitherer et al. 1999) and found that the galaxy was consistent with having little to no dust and a star formation rate (SFR) of $\approx 2-3$ $M_\odot$ yr^{-1}. We can convert this SFR into a predicted H α flux by using the classic conversion of SFR to H α luminosity from Kennicutt (1998). In this way, we calculate that a SFR = 3 $M_\odot$ yr^{-1} corresponds to an expected H α flux of $F_{\mathrm{H}\alpha,\mathrm{expected}} = 9.0 \times 10^{-18}$ erg cm^{-2} s^{-1}. Comparing this expected flux to the observed H α flux measured in Section 4.3.5, we find that the observed flux is 4.8 times higher than what would be predicted from star formation alone when using the Kennicutt (1998) relation.

We can perform a similar analysis on compact source 'D'. Since we do not have a UV spectrum of compact source 'D', we cannot do the full modeling of its UV continuum emission, as we did for compact source 'C'. Instead, we can attempt to rescale the SFR we computed for compact source 'C' to one for compact source 'D' by comparing their UV continuum fluxes as determined from the V-band photometry (see Fig. 4.1). We find that $F_{\mathrm{UV,C}}/F_{\mathrm{UV,D}} \approx 2.9$, suggesting a SFR for compact source 'D' of ~ 1 $M_\odot$ yr^{-1}. It is important to note, however, that this method implicitly assumes that compact source 'D', like 'C', has little to no dust extinction in the UV continuum. A SFR of 1 $M_\odot$ yr^{-1} corresponds to a predicted H α flux of $F_{\mathrm{H}\alpha,\mathrm{expected}} = 3.0 \times 10^{-18}$

erg cm^{-2} s^{-1} for compact source 'D', which, as in the case of compact source 'C', is a factor of $F_{\mathrm{H}\alpha,\mathrm{observed}}/F_{\mathrm{H}\alpha,\mathrm{expected}} = 22$ times lower than the observed H α flux.

Both of these comparisons rely on the classic Kennicutt (1998) value based on the typical conditions of star-formation in nearby, massive galaxies. However, interpreting the additional H α flux as evidence of a contribution of ionizing radiation from a source other than star-formation is not a secure conclusion for many low-mass and vigorously star-forming galaxies. A classic method of interpreting the ionization state of a galaxy is the N2-BPT diagram (Baldwin et al. 1981; Veilleux & Osterbrock 1987) which compares the ratio of N II/H α to O III/H β. When examining this relation for low-redshift systems, Brinchmann et al. (2008b,a) find a tail of star-forming systems with small N II/H α and high O III/Hβ, generally with high SFRs ($10^7 - 10^8$ yr^{-1}.) Such galaxies are common in surveys of star-forming systems at $z \sim 2$, yielding a N2-BPT diagram populated with extreme ratios of N II/H α (Maseda et al. 2013; Nakajima et al. 2013; Steidel et al. 2014; Shapley et al. 2015; Holden et al. 2016; Trainor et al. 2016; Strom et al. 2017). To produce these extreme ratios requires a much harder ionizing flux than typically produced by star-forming regions in, for example, the Milky Way. One method of producing such ratios would be the nearby QSO A, but the frequency of these galaxies outside of the neighborhoods of QSOs points to different conditions of star formation such as is discussed in, for instance, Kewley et al. (2013), Steidel et al. (2016), and Eldridge et al. (2017).

4.5 Conclusions

The recent discovery of ELANe (also referred to as giant Ly α nebulae) around quasars has opened up a new observational window into the study of intergalactic gas in emission on scales of several hundred kpc around massive galaxies at high redshift (see e.g., Cantalupo 2017 for a review). The Slug Nebula is one of the largest and most luminous among the ELANe discovered to date. Its very high Ly α surface brightness extends over 450 physical kpc around the bright quasar UM287 at z=2.283 (Cantalupo et al. 2014).

Depending on the Ly α emission mechanism, these high SB values would imply either a 'clumpy' and mostly ionized medium (in the case of recombination radiation) or large column densities of neutral gas (in the case of 'photon-pumping' or scattering radiation from the quasar broad-line emission region), as discussed in Cantalupo et al. (2014).

In order to clearly distinguish between these two scenarios, we searched for the non-resonant hydrogen H α emission from the brightest part of the Slug Nebula by means of deep Keck I/MOSFIRE long-slit spectroscopic observations. In addition, we obtained a deep, moderately high-resolution Ly α Keck I/LRIS spectrum in order to guide our H α emission search in the spectral direction and to study the detailed kinematics of the Slug.

1. Compared to previous lower-resolution and lower signal-to-noise Ly α spectral studies, our LRIS observation of Ly α emission revealed a more complex kinematic pattern than that of a simple, giant rotating disk (Martin et al. 2015). Instead,

as presented in Section 4.3.1 and discussed in Section 4.4.1, these kinematics seem more consistent with the presence of at least two structures that are clearly separated in velocity space.

2. We then independently analysed the H α spectrum obtained using Keck I/MOSFIRE. By optimizing the spectral aperture size and velocity centroid using a curve-of-growth approach, we found an H α detection of $F_{\mathrm{H}\alpha} = 2.62 \pm 0.47 \times 10^{-17}$ erg cm^{-2} s^{-1} with a significance of $\sim 5.6\sigma$, at a velocity of -511 km s^{-1} from the systemic redshift of the quasar UM287 ($z = 2.283$) (see Section 4.3.3 for more details). Such a detection is exactly at the spatial position obtained from the LRIS NB image and extremely close to the velocity expected from the Ly α kinematics derived from the LRIS spectrum. This reinforces the reliability of the detected emission.

3. The observed H α signal overlaps with residuals from a relatively bright NIR skyline, reducing the overall signal-to-noise ratio and hampering the possibility of a detailed kinematic analysis of this emission line. However, our curve-of-growth analysis in Section 4.3.3.1 suggests that the H α emission could be significantly more narrow (181 km s^{-1}) than its Ly α counterpart (418 km s^{-1}). This possible broadening of the Ly α emission as compared to the H α emission would naturally be produced by resonant scattering of Ly α photons if the Nebula were optically thick to the Ly α radiation, thus implying $\mathrm{N_{HI}} > 10^{14}$ cm^{-2}.

4. The most important result from our observations is the direct measurement of the Ly α to H α ratio in the region covered by our MOSFIRE N1 slit. We found the

ratio $F_{\mathrm{Ly}\alpha}/F_{\mathrm{H}\alpha}$ to be 5.5 ± 1.1 +1.4 (sys), see Section 4.3.3.1 for a discussion of the systematic error. Since photon-pumping or scattering emission from the quasar broad-line region contributes Ly α photons without producing any corresponding H α photons, we would expect these emission mechanisms to result in very high values of $F_{\mathrm{Ly}\alpha}/F_{\mathrm{H}\alpha}$ that would be well above the expected case B recombination (8.7 for total integrated emission or slightly lower for a slit observation like our own).

Therefore, the fact that the observed Ly α to H α is this close to the expected case B recombination value suggests that any contribution to the Ly α emission from these alternate emission mechanisms should be negligible and that the dominant source of Ly α emission for the Slug Nebula is recombination radiation. As derived in Cantalupo et al. (2014), H I column densities above $\mathrm{N_{HI}} \sim 10^{19}$ cm^{-2} are expected to have a significant Ly α flux contribution due to photon-pumping or scattering from the quasar broad-line region. Thus, our Ly α to H α flux ratio places an upper limit on the H I column density of $\mathrm{N_{HI}} < 10^{19}$ cm^{-2}.

Taken as a whole, the above conclusions imply that the Ly α emission from the Slug Nebula is powered by case B recombination with minimal contributions from the scattering of *ex situ* Ly α photons. Thus, the IGM and CGM around UM287 must be highly ionized, with an H I column density between 10^{14} and 10^{19} cm^{-2}. Considering the work of Cantalupo et al. (2014) and Arrigoni Battaia et al. (2015a), this suggests that the observed Slug Nebula emission requires the presence of high-density gas structures (clumps) with a small volume filling factor. Though the exact gas-density distribution

is not well constrained, these clumps could be the high-density tail of a very broad gas distribution (Cantalupo et al, in preparation).

Despite the technical challenges and limitations of extended, faint emission spectroscopy in the NIR, our results demonstrate the potential of H α intergalactic fluorescent observations at high-redshift. Future surveys from space-based observatories such as JWST that do not suffer from the presence of sky-lines would be necessary for a significant step forward in the H α study of the Slug Nebula and for other enormous Ly α nebulae at high redshift.

Chapter 5

Summary

In this dissertation, we combine both chemical evolution modeling and direct observations of gas around galaxies to study the fundamental astrophysical processes that drive the baryon cycle and shape the evolution of galaxies. This work is organized in three parts: In the first part of this work, we present our flexible galactic chemical evolution modeling code and validate it against abundance measurements of stars in the thick disk of the Milky Way. Next, we apply this chemical evolution code to characterize the physical processes that shaped the mass metallicity relation and α-enhancement trend observed in elliptical galaxies. Finally, we investigate the physical properties (i.e., structure, kinematics, emission mechanism) of a very bright enormous Lyman-α nebula, known as the Slug Nebula, that traces the CGM and possibly even the IGM of a massive galaxy halo at $z \sim 2.3$. We briefly summarize each project below.

In Chapter 2, we present our flexible one-zone galactic chemical evolution model. Our code incorporates simple but reasonable prescriptions and parametriza-

tions for a variety of galaxy ingredients. These include realistic stellar lifetimes, an observationally derived but modifiable initial mass function and Type Ia supernova (SNIa) delay-time distribution and modern metallicity-dependent nucleosynthetic yield tables to account for the gas enrichment from late-stage stellar evolution. Rather than having the star formation rate depend on the gas reservoir mass, a predetermined linear-exponential star-formation history and inflow history is precalculated based on the choice of star-formation timescale, inflow timescale and metallicity, initial gas reservoir mass, final gas fraction, and final stellar mass. In addition, gas outflows are assumed to be driven by both CCSN and SNIa and can be composed purely of entrained interstellar medium (ISM) or also include a fraction of the highly-enriched SN ejecta.

We then develop a general framework for understanding *why* different physical processes and their parametrization within a chemical evolution model impact the present-day stellar abundances in the way they do. In particular, we find that the effect of a model ingredient or parameter on the chemical evolution of a galaxy can be characterized with respect to its influence on two key terms that we call the "effective gas returns", $R_{\rm eff}$, and the "gas removal efficiency", $\epsilon_{\rm rm}$. In essence, the effective gas returns represent the sources of gas that replenish and enrich a galaxy's interstellar medium (ISM) while the gas removal efficiency characterizes how enriched ISM gas is depleted. The higher the gas removal efficiency, the more the ISM abundance ratios are changed by the effective gas returns and the more rapidly they are driven to the abundance ratios of the current effective gas returns.

Next, we establish the manner in which different galaxy ingredients affect $\epsilon_{\rm rm}$

and R_{eff} and thus change the characteristic features in the stellar abundance patterns we observe today. The impacts of the parameters we investigated are conveniently summarized in Figures 2.15 and 2.16 as well as in Table 2.5. Finally, we validate our chemical evolution code by generating simulated [Mg/Fe]–[Fe/H] tracks and MDFs that adequately reproduce the observed star-by-star abundance patterns and [Fe/H] distribution function of the Milky Way's thick disk. We also discuss the differences between our galactic chemical evolution model and more classic one-zone models that have the SFR depend on the gas mass.

In Chapter 3, we consider possible explanations of the abundance patterns of elliptical galaxies and their dependence on galaxy mass. The α-enhancement measured in the central regions of elliptical galaxies is observed to become increasingly super-solar for more massive galaxies. This trend has generally been interpreted as more massive ellipticals forming their stars on shorter timescales.

However, as the star-formation timescale decreases, most chemical evolution models predict that these massive elliptical galaxies should also be metal-poor, in contradiction with the observed mass-metallicity relation. Self-consistently reproducing both the mass-metallicity relation of elliptical galaxies and their observed mass-dependent α-enhancement continues to be a challenge for modern galaxy evolution simulations of all levels of complexity. As a result, recent papers have argued that these elliptical galaxy abundance patterns require that the IMF become more top-heavy in more massive ellipticals.

We investigate alternatives to a galaxy mass-dependent IMF in Chapter 3

using a similar framework as presented in Chapter 2. However, unlike the work done in Chapter 2, where the chemical tracers of the Milky Way's evolution can be measured on a star by star basis, elliptical galaxies are generally so distant that we can only study the chemical abundances of their stellar populations in integrated light. Despite the more limited constraints that these averaged abundance measurements provide, we can still infer much about the physical processes happening in elliptical galaxies.

In particular, we find that the elliptical galaxy abundance patterns and their dependence on galaxy mass can be reproduced if in addition to having a shorter star-formation timescale, more massive ellipticals also have less efficient outflows. No change to the high-mass slope of the IMF is needed for our close-correspondence models though a non-universal IMF is not precluded. We also highlight a number of uncertainties in the outcomes of stellar evolution and in the theoretical nucleosynthetic yield tables that have a substantial impact on the simulated average abundance ratios calculated by chemical evolution models. Reducing these uncertainties by improving our understanding of the late stages of stellar evolution and generating more complete theoretical yield tables will allow chemical evolution models to infer more stringent constraints on the evolution of elliptical galaxies.

In Chapter 4, we present an observational project studying the Slug Nebula. The Slug Nebula is one of the largest and most luminous Lyman-α (Lyα) nebulae discovered to date, extending over 450 kiloparsecs around the bright quasar UM287 at $z = 2.283$. It is characterized by high surface brightnesses over intergalactic scales and its Lyα emission may either trace high-density ionized gas ('clumps') or large column

densities of neutral material. To distinguish between these two possibilities, information from a non-resonant line such as Hα is crucial. Therefore, we analyzed a deep Multi-Object Spectrometer For Infra-Red Exploration (MOSFIRE) observation of one of the brightest Lyα emitting regions in the Slug Nebula with the goal of detecting associated Hα emission. We also obtained a deep, moderate resolution Lyα spectrum with [Keck-I/LRIS] of the nearby brightest region of the Slug. We succeeded in detecting Hα from this bright region of the Nebula, with a flux of $F_{\mathrm{H}\alpha} = 2.62 \pm 0.47 \times 10^{-17}$ erg cm^{-2} s^{-1} ($\mathrm{SB}_{\mathrm{H}\alpha} = 2.70 \pm 0.48 \times 10^{-18}$ erg cm^{-2} s^{-1} arcsec^{-2}) at the expected spatial and spectral location. Combining the Hα detection with its corresponding Lyα flux (determined from previous narrow-band imaging) we calculated a flux ratio of $\mathrm{F}_{\mathrm{Ly}\alpha}/\mathrm{F}_{\mathrm{H}\alpha} = 5.5 \pm 1.1$.

Our measurements argue for the origin of the Lyα emission being recombination radiation, suggesting the presence of high-density ionized gas and a more complex origin for at least some parts of the Slug Nebula. However, the presence of a skyline at the location of the Hα emission decreases the signal-to-noise ratio of the detection and our ability to put stringent constraints on the Hα kinematics.

Bibliography

Adibekyan, V. Z., Sousa, S. G., Santos, N. C., et al. 2012, A&A, 545, A32

Anders, F., Chiappini, C., Santiago, B. X., et al. 2014, A&A, 564, A115

Andrews, B. H., Weinberg, D. H., Schönrich, R., & Johnson, J. A. 2017, ApJ, 835, 224

Anglés-Alcázar, D., Davé, R., Özel, F., & Oppenheimer, B. D. 2014, ApJ, 782, 84

Anglés-Alcázar, D., Faucher-Giguère, C.-A., Kereš, D., et al. 2017, MNRAS, 470, 4698

Arrigoni, M., Trager, S. C., Somerville, R. S., & Gibson, B. K. 2010, Mon. Not. R. Astron. Soc., 402, 173

Arrigoni Battaia, F., Hennawi, J. F., Prochaska, J. X., & Cantalupo, S. 2015a, ApJ, 809, 163

Arrigoni Battaia, F., Prochaska, J. X., Hennawi, J. F., et al. 2018, MNRAS, 473, 3907

Arrigoni Battaia, F., Yang, Y., Hennawi, J. F., et al. 2015b, ApJ, 804, 26

Astropy Collaboration, Robitaille, T. P., Tollerud, E. J., et al. 2013, A&A, 558, A33

Atek, H., Kunth, D., Schaerer, D., et al. 2009, A&A, 506, L1

Baldwin, J. A., Phillips, M. M., & Terlevich, R. 1981, PASP, 93, 5

Barber, C., Crain, R. A., & Schaye, J. 2018, MNRAS, 479, 5448

Bensby, T., Feltzing, S., & Lundström, I. 2003, A&A, 410, 527

Bensby, T., Feltzing, S., & Oey, M. S. 2014, A&A, 562, A71

Bird, J. C., Loebman, S. R., Weinberg, D. H., et al. 2021, MNRAS, 503, 1815

Bland-Hawthorn, J., & Gerhard, O. 2016, ARA&A, 54, 529

Bohlin, R. C. 2014, AJ, 147, 127

Bond, J. R., Kofman, L., & Pogosyan, D. 1996, Nature, 380, 603

Borisova, E., Cantalupo, S., Lilly, S. J., et al. 2016, ApJ, 831, 39

Bouché, N., Dekel, a., Genzel, R., et al. 2010, Astrophys. J., 718, 1001

Bovy, J., Rix, H.-W., & Hogg, D. W. 2012, ApJ, 751, 131

Brinchmann, J., Kunth, D., & Durret, F. 2008a, A&A, 485, 657

Brinchmann, J., Pettini, M., & Charlot, S. 2008b, MNRAS, 385, 769

Brook, C. B., Stinson, G., Gibson, B. K., et al. 2014, MNRAS, 443, 3809

Brown, J. M., & Woosley, S. E. 2013, ApJ, 769, 99

Burstein, D., Faber, S. M., Gaskell, C. M., & Krumm, N. 1984, ApJ, 287, 586

Cai, Z., Fan, X., Yang, Y., et al. 2017, ApJ, 837, 71

Cai, Z., Hamden, E., Matuszewski, M., et al. 2018, ApJ, 861, L3

Calura, F., & Menci, N. 2009, MNRAS, 400, 1347

—. 2011, MNRAS, 413, L1

Cantalupo, S. 2017, in Astrophysics and Space Science Library, Vol. 430, Astrophysics and Space Science Library, ed. A. Fox & R. Davé, 195

Cantalupo, S., Arrigoni-Battaia, F., Prochaska, J. X., Hennawi, J. F., & Madau, P. 2014, Nature, 506, 63

Cantalupo, S., Porciani, C., Lilly, S. J., & Miniati, F. 2005, ApJ, 628, 61

Cappellari, M., McDermid, R. M., Alatalo, K., et al. 2012, Nature, 484, 485

Casagrande, L., Schönrich, R., Asplund, M., et al. 2011, A&A, 530, A138

Chapman, S. C., Lewis, G. F., Scott, D., et al. 2001, ApJ, 548, L17

Chen, M. C., Herwig, F., Denissenkov, P. A., & Paxton, B. 2014, Monthly Notices of the Royal Astronomical Society, 440, 1274

Chen, Y.-M., Tremonti, C. A., Heckman, T. M., et al. 2010, AJ, 140, 445

Chiappini, C. 2009, in The Galaxy Disk in Cosmological Context, ed. J. Andersen, Nordströara, B. m, & J. Bland-Hawthorn, Vol. 254, 191–196

Chiappini, C., Matteucci, F., & Gratton, R. 1997, 10, 765

Chiappini, C., Matteucci, F., & Romano, D. 2001, ApJ, 554, 1044

Chieffi, A., & Limongi, M. 2004, ApJ, 608, 405

Chiosi, C. 1980, A&A, 83, 206

Chisholm, J., Tremonti, C., & Leitherer, C. 2018, MNRAS, 481, 1690

Chisholm, J., Tremonti, C. A., Leitherer, C., & Chen, Y. 2017, MNRAS, 469, 4831

Chisholm, J., Tremonti, C. A., Leitherer, C., et al. 2015, ApJ, 811, 149

Chisholm, J., Tremonti Christy, A., Leitherer, C., & Chen, Y. 2016, MNRAS, 463, 541

Choi, J., Dotter, A., Conroy, C., et al. 2016, ApJ, 823, 102

Christensen, C. R., Davé, R., Governato, F., et al. 2016, ApJ, 824, 57

Conroy, C. 2013, ARA&A, 51, 393

Conroy, C., Graves, G. J., & van Dokkum, P. G. 2014, ApJ, 780, 33

Conroy, C., & Gunn, J. E. 2010, FSPS: Flexible Stellar Population Synthesis, ascl:1010.043

Conroy, C., Gunn, J. E., & White, M. 2009, ApJ, 699, 486

Conroy, C., & van Dokkum, P. 2012a, ApJ, 747, 69

Conroy, C., & van Dokkum, P. G. 2012b, ApJ, 760, 71

da Ângela, J., Shanks, T., Croom, S. M., et al. 2008, MNRAS, 383, 565

Dalcanton, J. J. 2007, ApJ, 658, 941

Davé, R., Finlator, K., & Oppenheimer, B. D. 2011, MNRAS, 416, 1354

—. 2012, MNRAS, 421, 98

de Lapparent, V., Geller, M. J., & Huchra, J. P. 1986, ApJ, 302, L1

De Lucia, G., Fontanot, F., & Hirschmann, M. 2017, MNRAS, 466, L88

De Lucia, G., Springel, V., White, S. D. M., Croton, D., & Kauffmann, G. 2006, MNRAS, 366, 499

De Masi, C., Matteucci, F., & Vincenzo, F. 2018, MNRAS, 474, 5259

Dekel, A., Birnboim, Y., Engel, G., et al. 2009, Nature, 457, 451

Dey, A., Bian, C., Soifer, B. T., et al. 2005, ApJ, 629, 654

Di Matteo, T., Springel, V., & Hernquist, L. 2005, Nature, 433, 604

Dijkstra, M. 2017, arXiv e-prints, arXiv:1704.03416

Doherty, C. L., Gil-Pons, P., Lau, H. H. B., Lattanzio, J. C., & Siess, L. 2014a, MNRAS, 437, 195

Doherty, C. L., Gil-Pons, P., Lau, H. H. B., et al. 2014b, MNRAS, 441, 582

Doherty, C. L., Gil-Pons, P., Siess, L., & Lattanzio, J. C. 2017, PASA, 34, e056

Doherty, C. L., Gil-Pons, P., Siess, L., Lattanzio, J. C., & Lau, H. H. B. 2015, MNRAS, 446, 2599

Dotter, A. 2016, ApJS, 222, 8

Dutton, A. A., van den Bosch, F. C., Faber, S. M., et al. 2011, MNRAS, 410, 1660

Eldridge, J. J., Stanway, E. R., Xiao, L., et al. 2017, PASA, 34, e058

Erb, D. K., Steidel, C. C., Trainor, R. F., et al. 2014, ApJ, 795, 33

Faber, S. M. 1973, ApJ, 179, 731

Fall, S. M., & Efstathiou, G. 1980, MNRAS, 193, 189

Farrell, E. J., Groh, J. H., Meynet, G., & Eldridge, J. J. 2020, MNRAS, 494, L53

Fishlock, C. K., Karakas, A. I., Lugaro, M., & Yong, D. 2014, ApJ, 797, 44

Fontanot, F., De Lucia, G., Hirschmann, M., et al. 2017, MNRAS, 464, 3812

Fontanot, F., De Lucia, G., Monaco, P., Somerville, R. S., & Santini, P. 2009, MNRAS, 397, 1776

Ford, A. B., Davé, R., Oppenheimer, B. D., et al. 2014, MNRAS, 444, 1260

Fox, A. J., Richter, P., Ashley, T., et al. 2019, ApJ, 884, 53

Frankel, N., Sanders, J., Rix, H.-W., Ting, Y.-S., & Ness, M. 2019, ApJ, 884, 99

Freudenburg, J. K. C., Weinberg, D. H., Hayden, M. R., & Holtzman, J. A. 2017, ApJ, 849, 17

Fuhrmann, K. 1998, A&A, 338, 161

Fumagalli, M., Mackenzie, R., Trayford, J., et al. 2017, MNRAS, 471, 3686

Gallazzi, A., Charlot, S., Brinchmann, J., & White, S. D. M. 2006, MNRAS, 370, 1106

Gallazzi, A., Charlot, S., Brinchmann, J., White, S. D. M., & Tremonti, C. A. 2005, MNRAS, 362, 41

Gallego, S. G., Cantalupo, S., Lilly, S., et al. 2018, MNRAS, 475, 3854

Gargiulo, I. D., Cora, S. A., Padilla, N. D., et al. 2015, MNRAS, 446, 3820

Geach, J. E., Alexander, D. M., Lehmer, B. D., et al. 2009, ApJ, 700, 1

Gil-Pons, P., Doherty, C. L., Gutiérrez, J. L., et al. 2018, PASA, 35, 38

Gilmore, G., & Reid, N. 1983, MNRAS, 202, 1025

Gilmore, G., Wyse, R. F. G., & Kuijken, K. 1989, ARA&A, 27, 555

Guetta, D., & Della Valle, M. 2007, ApJ, 657, L73

Hayden, M. R., Recio-Blanco, A., de Laverny, P., Mikolaitis, S., & Worley, C. C. 2017, A&A, 608, L1

Hayden, M. R., Bovy, J., Holtzman, J. A., et al. 2015, ApJ, 808, 132

Hayes, M. 2015, PASA, 32, e027

Hayes, M., Östlin, G., Schaerer, D., et al. 2010, Nature, 464, 562

Haywood, M., Di Matteo, P., Lehnert, M. D., Katz, D., & Gómez, A. 2013, A&A, 560, A109

Hennawi, J. F., Prochaska, J. X., Cantalupo, S., & Arrigoni-Battaia, F. 2015, Science, 348, 779

Henry, A., Scarlata, C., Martin, C. L., & Erb, D. 2015, ApJ, 809, 19

Heringer, E., Pritchet, C., & Kerkwijk, M. H. v. 2019, The Astrophysical Journal, 882, 52

Heringer, E., Pritchet, C., Kezwer, J., et al. 2017, ApJ, 834, 15

Hine, N. K., Geach, J. E., Matsuda, Y., et al. 2016, MNRAS, 460, 4075

Hirschi, R. 2017, Pre-supernova Evolution and Nucleosynthesis in Massive Stars and Their Stellar Wind Contribution, ed. A. W. Alsabti & P. Murdin, 1879

Hirschmann, M., De Lucia, G., & Fontanot, F. 2016, MNRAS, 461, 1760

Holden, B. P., Oesch, P. A., González, V. G., et al. 2016, ApJ, 820, 73

Hopkins, P. F., Kereš, D., Oñorbe, J., et al. 2014, MNRAS, 445, 581

Hopkins, P. F., Quataert, E., & Murray, N. 2012, MNRAS, 421, 3522

Hu, E. M., Cowie, L. L., & McMahon, R. G. 1998, ApJ, 502, L99

Hummer, D. G., & Storey, P. J. 1987, MNRAS, 224, 801

Hunter, J. D. 2007, Computing In Science & Engineering, 9, 90

Johansson, J., Thomas, D., & Maraston, C. 2012, MNRAS, 421, 1908

Jones, E., Oliphant, T., Peterson, P., et al. 2001, SciPy: Open source scientific tools for Python, [Online; accessed June 2017]

Jørgensen, I. 1999, MNRAS, 306, 607

Karakas, A. I. 2010, MNRAS, 403, 1413

Kauffmann, G., White, S. D. M., & Guiderdoni, B. 1993, MNRAS, 264, 201

Kawata, D., & Chiappini, C. 2016, Astronomische Nachrichten, 337, 976

Kennicutt, Jr., R. C. 1998, ARA&A, 36, 189

Kewley, L. J., Maier, C., Yabe, K., et al. 2013, ApJ, 774, L10

Kirby, E. N., Cohen, J. G., Guhathakurta, P., et al. 2013, ApJ, 779, 102

Kobayashi, C., Umeda, H., Nomoto, K., Tominaga, N., & Ohkubo, T. 2006, Astrophys. J., 653, 1145

Kodama, T., & Arimoto, N. 1997, A&A, 320, 41

Kormendy, J., & Ho, L. C. 2013, ARA&A, 51, 511

Kovetz, A., Yaron, O., & Prialnik, D. 2009, MNRAS, 395, 1857

Kriek, M., Shapley, A. E., Reddy, N. A., et al. 2015, ApJS, 218, 15

Kroupa, P. 2008, in Astronomical Society of the Pacific Conference Series, Vol. 390, Pathways Through an Eclectic Universe, ed. J. H. Knapen, T. J. Mahoney, & A. Vazdekis, 3

Krumholz, M. R., & Dekel, A. 2012, ApJ, 753, 16

Larson, R. B. 1972, Nature, 236, 21

—. 1974, MNRAS, 169, 229

—. 1976, MNRAS, 176, 31

Lau, M. W., Prochaska, J. X., & Hennawi, J. F. 2016, ApJS, 226, 25

Lee, S.-K., Ferguson, H. C., Somerville, R. S., Wiklind, T., & Giavalisco, M. 2010, ApJ, 725, 1644

Lehner, N., & Howk, J. C. 2011, Science, 334, 955

Lehner, N., O'Meara, J. M., Howk, J. C., Prochaska, J. X., & Fumagalli, M. 2016, ApJ, 833, 283

Lehner, N., Wotta, C. B., Howk, J. C., et al. 2019, ApJ, 887, 5

Lehner, N., Howk, J. C., Tripp, T. M., et al. 2013, ApJ, 770, 138

Leibler, C. N., Cantalupo, S., Holden, B. P., & Madau, P. 2018, MNRAS, 480, 2094

Leitherer, C., Schaerer, D., Goldader, J. D., et al. 1999, ApJS, 123, 3

Lequeux, J., Peimbert, M., Rayo, J. F., Serrano, A., & Torres-Peimbert, S. 1979, A&A, 80, 155

Leroy, A. K., Walter, F., Sandstrom, K., et al. 2013, AJ, 146, 19

Leung, S.-C., & Nomoto, K. 2018, ApJ, 861, 143

Libeskind, N. I., van de Weygaert, R., Cautun, M., et al. 2018, MNRAS, 473, 1195

Lilly, S. J., Carollo, C. M., Pipino, A., Renzini, A., & Peng, Y. 2013, ApJ, 772, 119

Lin, L., Patton, D. R., Koo, D. C., et al. 2008, ApJ, 681, 232

Lodders, K., Palme, H., & Gail, H. P. 2009, Landolt Börnstein, 4B, 712

Loebman, S. R., Debattista, V. P., Nidever, D. L., et al. 2016, ApJ, 818, L6

Ma, X., Hopkins, P. F., Faucher-Giguère, C.-A., et al. 2016, MNRAS, 456, 2140

Mac Low, M.-M., & Ferrara, A. 1999, ApJ, 513, 142

Mackereth, J. T., Bovy, J., Leung, H. W., et al. 2019, MNRAS, 489, 176

Maiolino, R., & Mannucci, F. 2019, A&A Rev., 27, 3

Maiolino, R., Nagao, T., Grazian, A., et al. 2008, A&A, 488, 463

Mandelker, N., Padnos, D., Dekel, A., et al. 2016, MNRAS, 463, 3921

Maoz, D., & Mannucci, F. 2012, PASA, 29, 447

Marino, R. A., Cantalupo, S., Lilly, S. J., et al. 2018, ApJ, 859, 53

Marquardt, K. S., Sim, S. A., Ruiter, A. J., et al. 2015, A&A, 580, A118

Martin, C. L. 1999, The Astrophysical Journal, 513, 156

Martin, C. L. 2005, ApJ, 621, 227

Martin, C. L., Shapley, A. E., Coil, A. L., et al. 2012, ApJ, 760, 127

Martin, D. C., Matuszewski, M., Morrissey, P., et al. 2015, Nature, 524, 192

Martín-Navarro, I., La Barbera, F., Vazdekis, A., Falcón-Barroso, J., & Ferreras, I. 2015, MNRAS, 447, 1033

Maseda, M. V., van der Wel, A., da Cunha, E., et al. 2013, ApJ, 778, L22

Mathews, W. G., & Baker, J. C. 1971, ApJ, 170, 241

Matsuda, Y., Yamada, T., Hayashino, T., et al. 2004, AJ, 128, 569

Matteucci, F. 1994, A&A, 288, 57

Matteucci, F., & Francois, P. 1989, MNRAS, 239, 885

Matteucci, F., & Greggio, L. 1986, A&A, 154, 279

Matthee, J., Sobral, D., Oteo, I., et al. 2016, MNRAS, 458, 449

McClure, R. D., & van den Bergh, S. 1968, AJ, 73, 1008

McKee, C. F., Parravano, A., & Hollenbach, D. J. 2015, ApJ, 814, 13

McLean, I. S., Steidel, C. C., Epps, H., et al. 2010, in Proc. SPIE, Vol. 7735, Ground-based and Airborne Instrumentation for Astronomy III, 77351E–77351E–12

McLean, I. S., Steidel, C. C., Epps, H. W., et al. 2012, in Proc. SPIE, Vol. 8446, Ground-based and Airborne Instrumentation for Astronomy IV, 84460J

McQuinn, K. B. W., van Zee, L., & Skillman, E. D. 2019, ApJ, 886, 74

Miley, G., & De Breuck, C. 2008, A&A Rev., 15, 67

Mitchell, P. D., Schaye, J., Bower, R. G., & Crain, R. A. 2020, MNRAS, 494, 3971

Muratov, A. L., Kereš, D., Faucher-Giguère, C.-A., et al. 2015, MNRAS, 454, 2691

—. 2017, MNRAS, 468, 4170

Murray, N., Quataert, E., & Thompson, T. A. 2005, ApJ, 618, 569

Nakajima, K., Ouchi, M., Shimasaku, K., et al. 2013, ApJ, 769, 3

Nelson, D., Vogelsberger, M., Genel, S., et al. 2013, MNRAS, 429, 3353

Nidever, D. L., Bovy, J., Bird, J. C., et al. 2014, ApJ, 796, 38

Nomoto, K., Iwamoto, K., Nakasato, N., et al. 1997, Nuclear Physics A, 621, 467

Nomoto, K., Kobayashi, C., & Tominaga, N. 2013, Annu. Rev. Astron. Astrophys., 51,

457

Okamoto, T., Nagashima, M., Lacey, C. G., & Frenk, C. S. 2017, MNRAS, 464, 4866

Oke, J. B., Cohen, J. G., Carr, M., et al. 1995, PASP, 107, 375

Oppenheimer, B. D., Davé, R., Kereš, D., et al. 2010, MNRAS, 406, 2325

Overzier, R. A., Nesvadba, N. P. H., Dijkstra, M., et al. 2013, ApJ, 771, 89

Pagel, B. E. J. 2009,

Pagel, B. E. J., & Patchett, B. E. 1975, MNRAS, 172, 13

Pagel, B. E. J., & Tautvaisiene, G. 1995, MNRAS, 276, 505

Pandya, V., Fielding, D. B., Anglés-Alcázar, D., et al. 2021, MNRAS, 508, 2979

Paxton, B., Bildsten, L., Dotter, A., et al. 2011, ApJS, 192, 3

Paxton, B., Cantiello, M., Arras, P., et al. 2013, ApJS, 208, 4

Paxton, B., Marchant, P., Schwab, J., et al. 2015, ApJS, 220, 15

Paxton, B., Schwab, J., Bauer, E. B., et al. 2018, ApJS, 234, 34

Pedregosa, F., Varoquaux, G., Gramfort, A., et al. 2011, Journal of Machine Learning Research, 12, 2825

Peek, J. E. G., & Graves, G. J. 2010, ApJ, 719, 415

Peeples, M. S., & Shankar, F. 2011, MNRAS, 417, 2962

Perez, F., & Granger, B. E. 2007, Computing in Science and Engg., 9, 21

Perez, J., Michel-Dansac, L., & Tissera, P. B. 2011, MNRAS, 417, 580

Péroux, C., & Howk, J. C. 2020, ARA&A, 58, 363

Pipino, A., Devriendt, J. E. G., Thomas, D., Silk, J., & Kaviraj, S. 2009, A&A, 505, 1075

Pipino, A., Lilly, S. J., & Carollo, C. M. 2014, MNRAS, 441, 1444

Pipino, A., & Matteucci, F. 2004, MNRAS, 347, 968

Podsiadlowski, P., Mazzali, P. A., Nomoto, K., Lazzati, D., & Cappellaro, E. 2004, ApJ, 607, L17

Prescott, M. K. M., Dey, A., & Jannuzi, B. T. 2009, ApJ, 702, 554

Prescott, M. K. M., Martin, C. L., & Dey, A. 2015a, ApJ, 799, 62

Prescott, M. K. M., Momcheva, I., Brammer, G. B., Fynbo, J. P. U., & Møller, P. 2015b, ApJ, 802, 32

Prochaska, J. F., Hennawai, J., & Burles, S. 2017a, XIDL, [Online; accessed 2017]

Prochaska, J. X., Naumov, S. O., Carney, B. W., McWilliam, A., & Wolfe, A. M. 2000, AJ, 120, 2513

Prochaska, J. X., Hennawi, J. F., Lee, K.-G., et al. 2013, ApJ, 776, 136

Prochaska, J. X., Werk, J. K., Worseck, G., et al. 2017b, ApJ, 837, 169

Prochaska, L. C., Rose, J. A., & Schiavon, R. P. 2005, AJ, 130, 2666

Putman, M. E., Peek, J. E. G., & Joung, M. R. 2012, ARA&A, 50, 491

Pych, W. 2004, PASP, 116, 148

—. 2012, dcr: Cosmic Ray Removal, Astrophysics Source Code Library, ascl:1207.006

Querejeta, M., Schinnerer, E., Meidt, S., et al. 2021, arXiv e-prints, arXiv:2109.04491

Recchi, S., Spitoni, E., Matteucci, F., & Lanfranchi, G. A. 2008, A&A, 489, 555

Renzini, A., & Ciotti, L. 1993, ApJ, 416, L49

Robin, A. C., Reylé, C., Fliri, J., et al. 2014, A&A, 569, A13

Roškar, R., Debattista, V. P., Stinson, G. S., et al. 2008, ApJ, 675, L65

Rubin, K. H. R., Prochaska, J. X., Koo, D. C., & Phillips, A. C. 2012, ApJ, 747, L26

Rubin, K. H. R., Prochaska, J. X., Koo, D. C., et al. 2014, ApJ, 794, 156

Rubin, K. H. R., Weiner, B. J., Koo, D. C., et al. 2010, ApJ, 719, 1503

Rudie, G. C., Steidel, C. C., Trainor, R. F., et al. 2012, ApJ, 750, 67

Rupke, D. S., Veilleux, S., & Sanders, D. B. 2005, ApJS, 160, 115

Salaris, M., Serenelli, A., Weiss, A., & Miller Bertolami, M. 2009, ApJ, 692, 1013

Salpeter, E. E. 1955, ApJ, 121, 161

Samland, M., & Gerhard, O. E. 2003, Astronomy Astrophysics, 399, 961–982

Sanders, R. L., Shapley, A. E., Reddy, N. A., et al. 2020, MNRAS, 491, 1427

Sanders, R. L., Shapley, A. E., Jones, T., et al. 2021, ApJ, 914, 19

Schiavon, R. P. 2007, ApJS, 171, 146

—. 2010, Publication of Korean Astronomical Society, 25, 83

Schmidt, M. 1959, ApJ, 129, 243

—. 1963, ApJ, 137, 758

Schönrich, R., & Binney, J. 2009, Mon. Not. R. Astron. Soc., 396, 203

Scoville, N., Sheth, K., Aussel, H., et al. 2016, ApJ, 820, 83

Segers, M. C., Schaye, J., Bower, R. G., et al. 2016, MNRAS, 461, L102

Sellwood, J. A., & Binney, J. J. 2002, MNRAS, 336, 785

Shapiro, P. R., & Field, G. B. 1976, ApJ, 205, 762

Shapley, A. E., Reddy, N. A., Kriek, M., et al. 2015, ApJ, 801, 88

Siess, L. 2010, A&A, 512, A10

Simha, V., Weinberg, D. H., Conroy, C., et al. 2014, arXiv e-prints, arXiv:1404.0402

Smith, R. J. 2020, ARA&A, 58, 577

Somerville, R. S., & Davé, R. 2015, ARA&A, 53, 51

Somerville, R. S., Hopkins, P. F., Cox, T. J., Robertson, B. E., & Hernquist, L. 2008, MNRAS, 391, 481

Steidel, C. C., Adelberger, K. L., Shapley, A. E., et al. 2000, ApJ, 532, 170

Steidel, C. C., Bogosavljević, M., Shapley, A. E., et al. 2011, ApJ, 736, 160

Steidel, C. C., Strom, A. L., Pettini, M., et al. 2016, ApJ, 826, 159

Steidel, C. C., Rudie, G. C., Strom, A. L., et al. 2014, ApJ, 795, 165

Strauss, M. A., Weinberg, D. H., Lupton, R. H., et al. 2002, AJ, 124, 1810

Strom, A. L., Steidel, C. C., Rudie, G. C., et al. 2017, ApJ, 836, 164

Sukhbold, T., Ertl, T., Woosley, S. E., Brown, J. M., & Janka, H. T. 2016, ApJ, 821, 38

Tacconi, L. J., Neri, R., Genzel, R., et al. 2013, ApJ, 768, 74

Tantalo, R., Chiosi, C., Bressan, A., & Fagotto, F. 1996, A&A, 311, 361

Taylor, P., & Kobayashi, C. 2015, MNRAS, 448, 1835

Team, T. P. D. 2019, pandas-dev/pandas: Pandas

Thomas, D., Maraston, C., Bender, R., & Al, T. E. T. 2005, 673

Thomas, D., Maraston, C., Schawinski, K., Sarzi, M., & Silk, J. 2010, MNRAS, 404, 1775

Tortora, C., Hunt, L. K., & Ginolfi, M. 2021, arXiv e-prints, arXiv:2110.06946

Trager, S. C., Faber, S. M., Worthey, G., & González, J. J. 2000, AJ, 120, 165

Trainor, R. F., & Steidel, C. C. 2012, ApJ, 752, 39

Trainor, R. F., Steidel, C. C., Strom, A. L., & Rudie, G. C. 2015, ApJ, 809, 89

Trainor, R. F., Strom, A. L., Steidel, C. C., & Rudie, G. C. 2016, ApJ, 832, 171

Tremonti, C. A., Heckman, T. M., Kauffmann, G., et al. 2004, ApJ, 613, 898

Troncoso, P., Maiolino, R., Sommariva, V., et al. 2014, A&A, 563, A58

Tumlinson, J., Peeples, M. S., & Werk, J. K. 2017, ARA&A, 55, 389

Twarog, B. A. 1980, ApJ, 242, 242

van den Bergh, S. 1962, AJ, 67, 486

van den Bergh, S. 1972, in External Galaxies and Quasi-Stellar Objects, ed. D. S. Evans, D. Wills, & B. J. Wills, Vol. 44, 1

Van Rossum, G., & Drake, F. L. 2009, Python 3 Reference Manual

Veilleux, S., Maiolino, R., Bolatto, A. D., & Aalto, S. 2020, A&A Rev., 28, 2

Veilleux, S., & Osterbrock, D. E. 1987, ApJS, 63, 295

Ventura, P., Di Criscienzo, M., Carini, R., & D'Antona, F. 2013, MNRAS, 431, 3642

Villar-Martín, M. 2007, New A Rev., 51, 194

Vincenzo, F., & Kobayashi, C. 2020, Monthly Notices of the Royal Astronomical Society, 496, 80–94

Vogelsberger, M., Genel, S., Springel, V., et al. 2014, MNRAS, 444, 1518

Voit, G. M., Bryan, G. L., O'Shea, B. W., & Donahue, M. 2015, ApJ, 808, L30

Walcher, C. J., Coelho, P., Gallazzi, A., & Charlot, S. 2009, MNRAS, 398, L44

Walt, S. v. d., Colbert, S. C., & Varoquaux, G. 2011, Computing in Science and Engg., 13, 22

Weidner, C., & Kroupa, P. 2005, ApJ, 625, 754

Weidner, C., Kroupa, P., & Pflamm-Altenburg, J. 2011, MNRAS, 412, 979

Weidner, C., Kroupa, P., Pflamm-Altenburg, J., & Vazdekis, A. 2013, MNRAS, 436, 3309

Weinberg, D. H., Andrews, B. H., & Freudenburg, J. 2017, ApJ, 837, 183

Weiner, B. J., Coil, A. L., Prochaska, J. X., et al. 2009, ApJ, 692, 187

Wes McKinney. 2010, in Proceedings of the 9th Python in Science Conference, ed. Stéfan van der Walt & Jarrod Millman, 56 – 61

White, S. D. M., & Frenk, C. S. 1991, ApJ, 379, 52

Woosley, S. E., & Weaver, T. A. 1995, ApJS, 101, 181

Worthey, G. 1994, ApJS, 95, 107

Worthey, G., Faber, S. M., & Gonzalez, J. J. 1992, ApJ, 398, 69

Worthey, G., & Ottaviani, D. L. 1997, ApJS, 111, 377

Worthey, G., Tang, B., & Serven, J. 2014, ApJ, 783, 20

Wotta, C. B., Lehner, N., Howk, J. C., et al. 2019, ApJ, 872, 81

Wotta, C. B., Lehner, N., Howk, J. C., O'Meara, J. M., & Prochaska, J. X. 2016, ApJ, 831, 95

Yan, Z., Jerabkova, T., & Kroupa, P. 2019, A&A, 632, A110

Yang, Y., Zabludoff, A., Jahnke, K., & Davé, R. 2014, ApJ, 793, 114

Yang, Y., Zabludoff, A., Tremonti, C., Eisenstein, D., & Davé, R. 2009, ApJ, 693, 1579

Yoshii, Y. 1982, PASJ, 34, 365

Yoshii, Y., Tsujimoto, T., & Nomoto, K. 1996, ApJ, 462, 266

Zhao, J. K., Oswalt, T. D., Willson, L. A., Wang, Q., & Zhao, G. 2012, The Astrophys-

ical Journal, 746, 144